ESTIMATION OF CONFINED PEAK STRENGTH FOR HIGHLY INTERLOCKED JOINTED ROCKMASSES

By

Navid Bahrani

A thesis submitted in partial fulfillment
of the requirements for the degree of
Doctor of Philosophy (PhD) in Natural Resources Engineering

The Faculty of Graduate Studies
Laurentian University
Sudbury, Ontario, Canada

THESIS DEFENCE COMMITTEE/COMITÉ DE SOUTENANCE DE THÈSE
Laurentian Université/Université Laurentienne
Faculty of Graduate Studies/Faculté des études supérieures

Title of Thesis Titre de la thèse	ESTIMATION OF CONFINED PEAK STRENGTH FOR HIGHLY INTERLOCKED JOINTED ROCKMASSES
Name of Candidate Nom du candidat	Bahrani, Navid
Degree Diplôme	Doctor of Philosophy Science
Department/Program Département/Programme	Natural Resources Engineering
Date of Defence June 18, 2015 Date de la soutenance	

APPROVED/APPROUVÉ

Thesis Examiners/Examinateurs de thèse:

Dr. P.K. Kaiser
(Supervisor/Directeur de thèse)

Dr. Ming Cai
(Committee member/Membre du comité)

Dr. D. McCreath
(Committee member/Membre du comité)

Dr. Dean Millar
(Committee member/Membre du comité)

Dr. Erik Eberhardt
(External Examiner/Examinateur externe)

Dr. Richard Smith
(Internal Examiner/Examinateur interne)

Approved for the Faculty of Graduate Studies
Approuvé pour la Faculté des études supérieures
Dr. David Lesbarrères
Monsieur David Lesbarrères
Acting Dean, Faculty of Graduate Studies
Doyen intérimaire, Faculté des études supérieures

ACCESSIBILITY CLAUSE AND PERMISSION TO USE

I, **Navid Bahrani**, hereby grant to Laurentian University and/or its agents the non-exclusive license to archive and make accessible my thesis, dissertation, or project report in whole or in part in all forms of media, now or for the duration of my copyright ownership. I retain all other ownership rights to the copyright of the thesis, dissertation or project report. I also reserve the right to use in future works (such as articles or books) all or part of this thesis, dissertation, or project report. I further agree that permission for copying of this thesis in any manner, in whole or in part, for scholarly purposes may be granted by the professor or professors who supervised my thesis work or, in their absence, by the Head of the Department in which my thesis work was done. It is understood that any copying or publication or use of this thesis or parts thereof for financial gain shall not be allowed without my written permission. It is also understood that this copy is being made available in this form by the authority of the copyright owner solely for the purpose of private study and research and may not be copied or reproduced except as permitted by the copyright laws without written authority from the copyright owner.

Abstract

The determination of rockmass strength for mining has become critically important in recent years due to the increase in the number of projects at depths exceeding 1500 m. The commonly used empirical approaches for the estimation of rockmass strength are primarily based on experiences at shallow depths (< 1500 m) and from observations of rockmass behaviours at low confinement (e.g., tunnel wall failure). Therefore, the application of these techniques for estimating the strength of rockmasses when highly interlocked and confined (e.g., pillar cores) is hypothesized to be flawed. The goal of this research is to develop reliable means of estimating the confined strength of highly interlocked jointed rockmasses.

A two-dimensional code based on the Distinct Element Method (*DEM*) and its embedded Grain-based Model (*GBM*) is used to simulate the behaviour of a highly interlocked jointed rockmass to better understand its Strength Degradation (*SD*) from intact rock with increasing confinement.

The *GBM* is first calibrated to the laboratory response of intact and granulated marble. The term "granulated" refers to a heat-treated marble where the cohesion at grain boundaries has been destroyed. The granulated marble represents an analogue for a highly interlocked jointed rockmass. The calibrated *GBMs* are then used to simulate micro-defected and defected rocks and jointed rockmasses.

The results of triaxial test simulations on the calibrated synthetic rockmass specimens are used to develop two semi-empirical approaches. In the first approach, called the *SD* approach, equations that relate the strength degradation of a jointed rockmass from intact rock to the confinement are developed. The second approach is based on adjusting the strength parameters of the Hoek-

Brown failure criterion to extend its applicability to highly interlocked jointed rockmassess. It is demonstrated that these two approaches can be used to estimate the confined strength of such rockmasses in a situation where the unconfined and confined strengths of the intact rock and the unconfined strength of the rockmass are known.

The findings of this research provides the foundation for a better characterization of the strength for highly interlocked jointed rockmasses, and increases our understanding of the influence of confinement on rockmass strength.

Keywords: defected rock, jointed rockmass, confined rockmass strength, joint persistence, joint roughness, degree of interlock, highly interlocked rockmass, Hoek-Brown failure criterion, Geological Strength Index (*GSI*), Particle Flow Code (*PFC*), Grain-based Model (*GBM*).

Acknowledgements

This research was supported by Natural Sciences and Engineering Research Council of Canada (NSERC), CEMI through its SUMIT program, Itasca Consulting Group through its IEP program, and MIRARCO.

I would like to thank my thesis advisor Dr. Peter Kaiser for providing me with the opportunity to carry out this research. His support, encouragements, skillful guidance, and critical review of this thesis were essential to its completion.

I would also like to thank Sean Maloney, my supervisor at MIRARCO, for his support during my graduate studies at Laurentian University.

A special thanks to Benoît Valley for being such a valued friend. He provided his precious insights into the initial stages of this research. I learned, through many discussions with him, how to think differently as a researcher, develop ideas, and overcome technical challenges.

I would like to acknowledge my committee members, Drs. Dougal McCreath, Ming Cai and Dean Millar, for reviewing my research documents, attending my presentations and their technical advice during the course of this research.

I am grateful to my IEP mentor Dr. Matthew Pierce for his support and technical advice and to Drs. David Potyondy and Sacha Emam for helpful guidance in the early stages of the PFC numerical simulations.

I wish to express thanks to Dr. Ted Brown for kindly mailing his only hard copy of Dr. Gerrogianopoulos's PhD thesis from Australia, which includes the details of laboratory tests

conducted on Wombeyan and Carrara marble. I would also like to acknowledge Dr. Evert Hoek for his correspondence and providing useful information on the early development stages of the Hoek-Brown failure criterion including laboratory test data on Panguna andesie.

My thanks are also extended to my friends and colleagues at MIRARCO and CEMI for being an invaluable support system, especially Rob Bewick for many technical discussions and reviewing my research documents.

I wish to express my sincere thanks to my parents Parvaneh and Hossein, and my sister Vanoosheh. I would not have started this journey if it was not for their inspiration and encouragements. I am very thankful to my in-laws Shahrzad, Majid, Kaveh, Leila and Farbod for being such a caring and loving family. Thanks to my aunts Farah and Zari for being there for me through tough times, and to Hadi and Parisa for their honest friendship.

Finally, I would like to thank my wife, my love and friend, Rana, for motivating me and for putting up with my ups and downs. This research could not have been accomplished without her continued support.

This thesis is dedicated to my beloved Rana, Parvaneh, Hossein and Vanoosheh.

Table of Contents

List of Figures

List of Tables

List of Acronyms

AASHTO	American Association of State Highway and Transportation Officials
BM	Ball Model
BPM	Bonded Particle Model
CC	Cohesive Component
CI	Confidence Interval
DEM	Distinct Element Method
DFN	Discrete Fracture Network
FC	Frictional Component
FS	Factor of Safety
GBM	Grain-based Model
GSI	Geological Strength Index
HB	Hoek-Brown
IRS	Intact Rock Strength
ISRM	International Society for Rock Mechancis
JCS	Joint-wall Compressive Strength
JRC	Joint Roughness Coefficient
LdB	Lac du Bonnet
MC	Mohr-Coulomb
MRMR	Modified Rock Mass Rating
NGI	Norwegian Geotechnical Institude
Pb	Parallel Bond
PFC	Particle Flow Code
REV	Representative Element Volume

RM_{HI}	Highly Interlocked Jointed Rockmass
RM_{I}	Interlocked Jointed Rockmass
RMR	Rock Mass Rating
RQD	Rock Quality Designation
SCR	Surface Condition Rating
SD	Strength Degradation
SEM	Scanning Electron Microscope
Sj	Smooth-joint
SR	Structure Rating
SRF	Stress Reduction Factor
SRM	Synthetic Rock Mass
UCS	Uniaxial Compressive Strength
URL	Underground Research Laboratory

Chapter 1

1 Introduction

1.1 Background

Reliable design of underground excavations such as drifts and stopes, pillars and the assessment of abutment stability require a reliable estimate of the rockmass strength. This rockmass strength is influenced by the presence of geological features at various scales including micro-cracks present at the grain scale, fractures and veins at the laboratory specimen scale, cemented joints at the rock block scale and block-forming joints at the overall rockmass scale.

In recent years, due to the increase in the number of deep mining and civil projects, the accurate determination of the strength of jointed rockmasses has gained increasing importance. For example, cave mining operations at depth require the development of hundreds of kilometers of drifts and thousands of pillars and draw points before extraction can proceed. The pillars are usually designed with a range of width-to-height ratios to provide confinement, which results in varying pillar strengths. The most commonly adopted empirical engineering approaches are based on rockmass classification systems for excavation and support design and rockmass characterization systems for estimating rockmass strength. These approaches were primarily developed from tunneling experiences at relatively shallow depths (typically less than 1500 m) and observations of rockmass behaviours at relatively low confinement (e.g., rock failure near tunnel walls where the confining pressure is in the range of only a few MPa). The application of these techniques when estimating the rockmass strength in highly confined rockmasses (e.g., for

pillar cores) at great depths (> 1.5 km) is thought to be flawed and could result in uneconomic designs.

There is encouraging evidence based on field observation and laboratory test data that jointed rockmasses are stronger at high confinement than that predicted by commonly adopted empirical approaches such as the Geological Strength Index (*GSI*; Hoek et al., 1995). Consequently, methodologies for the determination of rockmass strength must consider all confinement-dependent strength-enhancing factors in order to reduce the possibility of its underestimation. This is of particular concern when dealing with rockmasses where the rock near excavations fails in a brittle manner as the rock blocks are very strong and the degree of interlock within the rockmass plays a key role. Hence, this thesis deals with the estimation of the confined peak strength for highly interlocked jointed rockmasses consisting of hard brittle rock blocks and joints that are non-persistent and rough.

1.1.1 Brittle Failure of intact rock and massive rockmass

Changes in the failure mode of intact (unfractured) brittle rock with increasing confinement has often been documented in the literature. A well-known example is the laboratory experiments by Paterson (1958), who conducted uniaxial and triaxial compression tests on coarse-grained Wombeyan marble. The confinement in the triaxial compression tests ranged between 0 and 100 MPa (Figure 1-1).

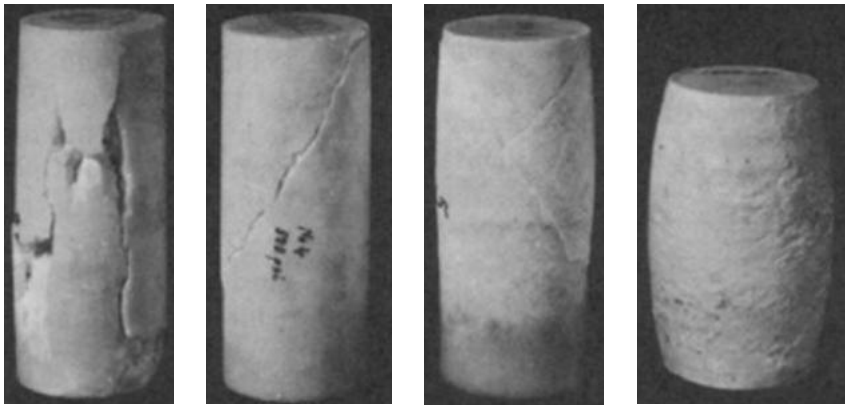

(a) (b) (c) (d)

Figure 1-1: Changes in the failure mode of Wombeyan marble with increasing confining pressure (after Paterson, 1958): a) axial splitting under unconfined condition; b) single shear band failure at 3.5 MPa confining pressure; c) conjugate shear bands at 35 MPa confining pressure; and d) ductile behavior at 100 MPa confining pressure.

Paterson (1958) observed a transition in the failure mode with increasing confinement; axial splitting or fracturing at zero confining pressure (Figure 1-1a), a well-defined single shear band formation at 3.5 MPa confining pressure (Figure 1-1b), conjugate shear banding at 35 MPa confining pressure (Figure 1-1c), and ductile behavior at a very high confining pressure of 100 MPa (Figure 1-1d).

A brittle material, when subjected to stress, breaks without significant deformation (strain). Rocks that fail in this manner are called brittle rocks. Heterogeneity at the grain scale (e.g., grain geometry and stiffness contrast) or slip on flaws (e.g., micro-cracks, grain boundaries and voids) introduces tensile stresses in brittle rocks even in an overall compressive stress field (Diederichs, 2003; Lan et al., 2010; Valley et al., 2010). Therefore, failure of brittle rocks is dominated by extensional or tensile damage including the formation and propagation of tensile cracks prior to the peak stress. In brittle rocks, there is a reduction in strength once the peak stress is reached, and the magnitude and rate of this strength reduction depends on the level of confining pressure.

The generated tensile stresses result in the initiation of tensile cracks at about 30 to 50% of the peak strength (Brace et al., 1966; Bieniawski, 1967; Holcomb and Costin, 1987; Martin, 1993; Eberhardt et al., 1999; Nicksiar and Martin, 2013). At this stress level, cracks are mostly generated parallel to the loading direction. This is reflected by the onset of the non-linearity in the lateral strain curve. The plot of axial stress versus lateral strain can therefore be used to identify the crack initiation stress, which is defined as the point of deviation from linear elasticity. The axial strain magnitude where the volumetric strain reversal occurs (on the plot of volumetric strain versus axial strain) marks the beginning of unstable crack growth. This point usually occurs between 70 and 85% of the peak strength and is called the crack damage stress (Lockner et al., 1992; Martin and Chandler, 1994; Eberhardt et al., 1999; Diederichs, 2003).

Increasing the applied load beyond the crack damage stress will lead to axial splitting of the specimen at low confinement. At high confinement, the tensile stresses are still present and while tensile cracks are still generated, they no longer propagate in an unstable manner. At high confinement, the failure is usually controlled by the coalescence of micro-cracks forming macroscopic shear bands that lead to shear rupture (Diederichs, 1999; 2003).

Griffith (1921) proposed that the strength of brittle materials is dictated by the presence of small cracks and that failure occurs when the most vulnerably oriented crack in a population of randomly oriented cracks begins to extend under the applied stress. Hoek and Bieniawski (1965) investigated the dependency of crack length on confinement. They found that the crack length under triaxial compression is sensitive to the ratio of σ_1/σ_3, where σ_1 and σ_3 are the major and minor principal stresses at failure, respectively.

As shown in Figure 1-2a, the crack length extension reduces to less than 10% of its original length for confining pressures greater than about 10% of the applied major principal stress. This rapid decrease in the length of cracks, propagated from a pre-existing crack due to the increase in the confining pressure, is schematically shown on the σ_1 versus σ_3 space in Figure 1-2b.

This tensile or extension-driven damage process plays an important role in the failure of massive rockmasses. Similar to the brittle failure of the laboratory scale rock specimen, the failure mode of a massive rockmass changes with confinement. Near excavation boundaries where the confinement is low, tensile fractures are initiated when the maximum tangential stress exceeds the crack initiation stress of the intact rock, and then propagate parallel to the excavation boundary. This results in the spalling and slabbing of the massive rockmass (compare Figure 1-3a and b).

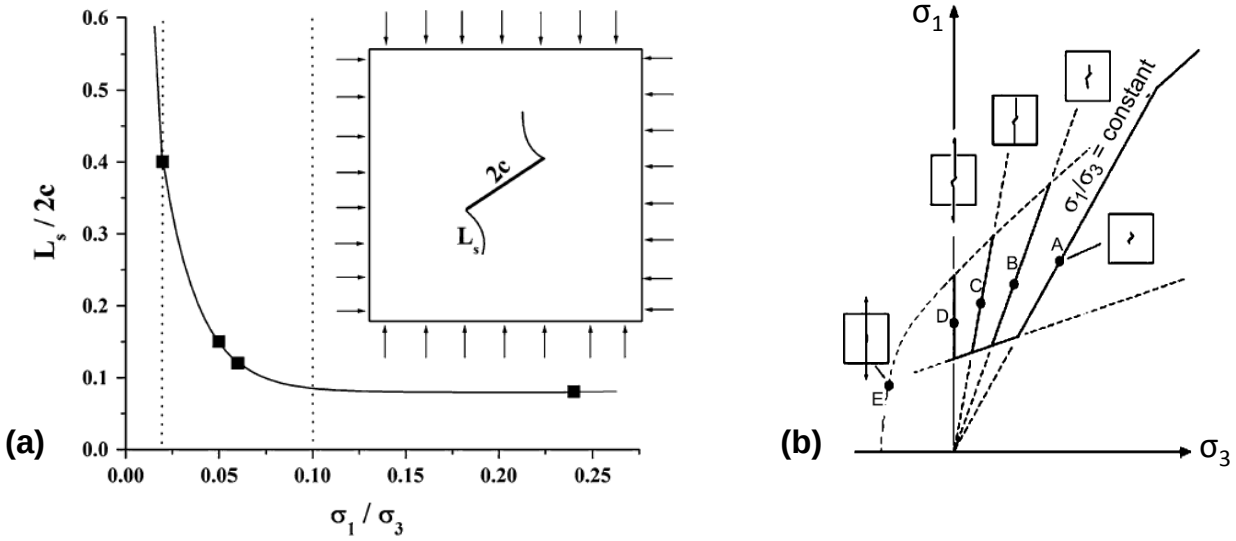

Figure 1-2: Dependency of crack length on confining pressure: a) relationship between the ratio of stable crack length (L_s) to initial crack length ($2c$) and the principal stress ratio (σ_1/σ_3) (after Hoek and Bieniawski, 1965); b) decrease in crack length and its propagation with increasing confining pressure (after Kaiser et al., 2000; Diederichs, 2003).

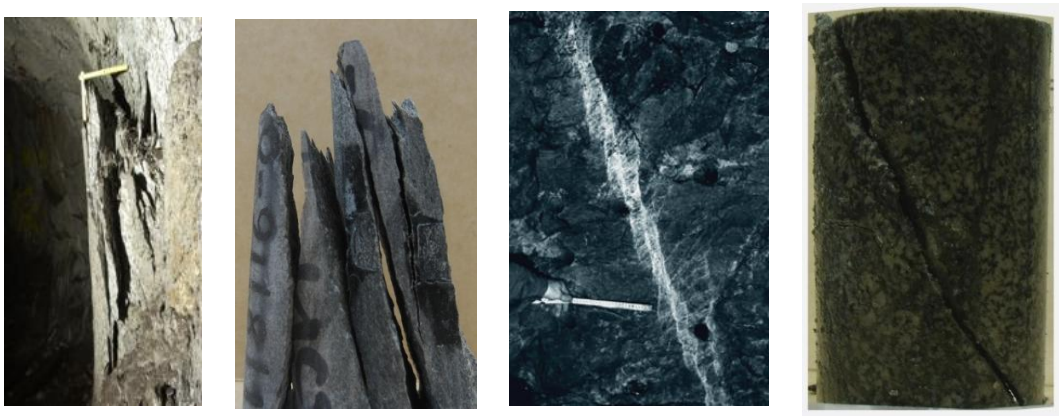

(a) (b) (c) (d)

Figure 1-3: Failure modes of brittle intact rock and massive rockmass near and away from excavation boundaries: a) unstable tensile crack propagation near excavation wall leading to spalling (Kaiser et al, 2000); b) axial splitting of a brittle rock specimen from Creighton mine tested at MIRARCO laboratory under unconfined condition; c) shear rupture zone observed in a deep South African gold mine formed as a result of accumulation of tensile fractures (Ortlepp, 1997); and d) shear failure through intact rock specimen from Nickel Rim South mine tested at MIRARCO laboratory at 10 MPa confining pressure.

At high confinement, the unstable propagation of tensile fractures is inhibited but damage can still accumulate. Away from excavation boundaries, when confinement is sufficiently high, accumulation of tensile fractures results in the formation of shear rupture zones in massive rock (compare Figure 1-3c and d).

According to Kaiser et al. (2000) and Diederichs (2003), the *in situ* strength of massive rockmasses can be represented by a tri-linear or a continuous *s*-shaped failure envelope on the principal stress space (Figure 1-4). This figure illustrates that the damage and failure mechanism of a massive rockmass can be divided into four regions depending on the stress path it experiences during excavation: no damage, shear failure, spalling and unraveling. As shown in Figure 1-4, if the stress path is below the damage initiation threshold, the rockmass remains elastic. However, if the stress path exceeds the damage threshold, seismicity or acoustic emissions are observed and damage in the form of micro-cracks accumulates. If the confinement

level is sufficiently high, the interaction and coalescence of the cumulative damage leads to macroscopic shear failure. In this case, the strength of the massive rockmass can be approximated by the long-term strength of laboratory specimens. If the stress path moves to the left of the spalling limit or into the tensile zone, the failure envelope of the massive rockmass reduces and falls back into the damage initiation threshold. This reduction in rockmass strength is due to the complex stress path and stress rotation near the excavation boundaries (Martin, 1993; Read et al., 1998; Eberhardt, 2001).

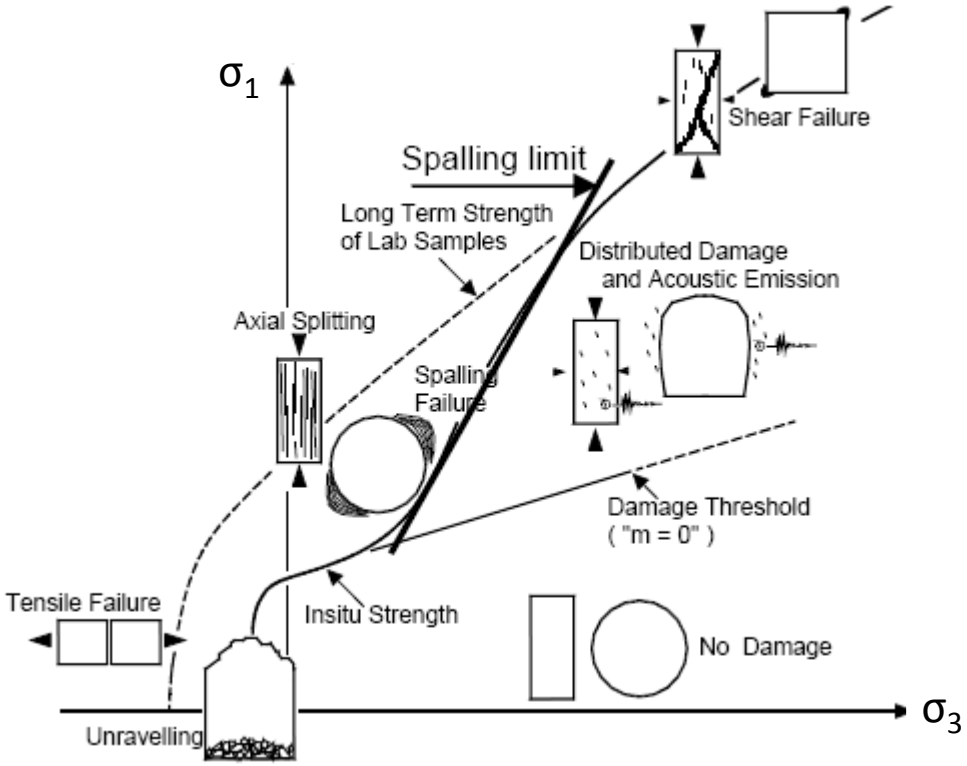

Figure 1-4: Schematic of *s*-shaped failure envelope, showing four zones of distinct rockmass failure mechanisms: no damage, shear failure, spalling and unraveling (after Diederichs, 1999; Kaiser et al., 2000).

1.1.2 Strength of jointed rockmass

A jointed rockmass consists of rock blocks defined by structural discontinuities. The presence of discontinuities within a rockmass results in a change in its strength and deformation properties as well as in the failure modes observed in unfractured laboratory scale rock specimens and massive rockmasses. Figure 1-5 illustrates the transition from an isotropic intact rock specimen to a highly anisotropic rockmass containing one or two joint sets then to an isotropic jointed rockmass with more than two joint sets.

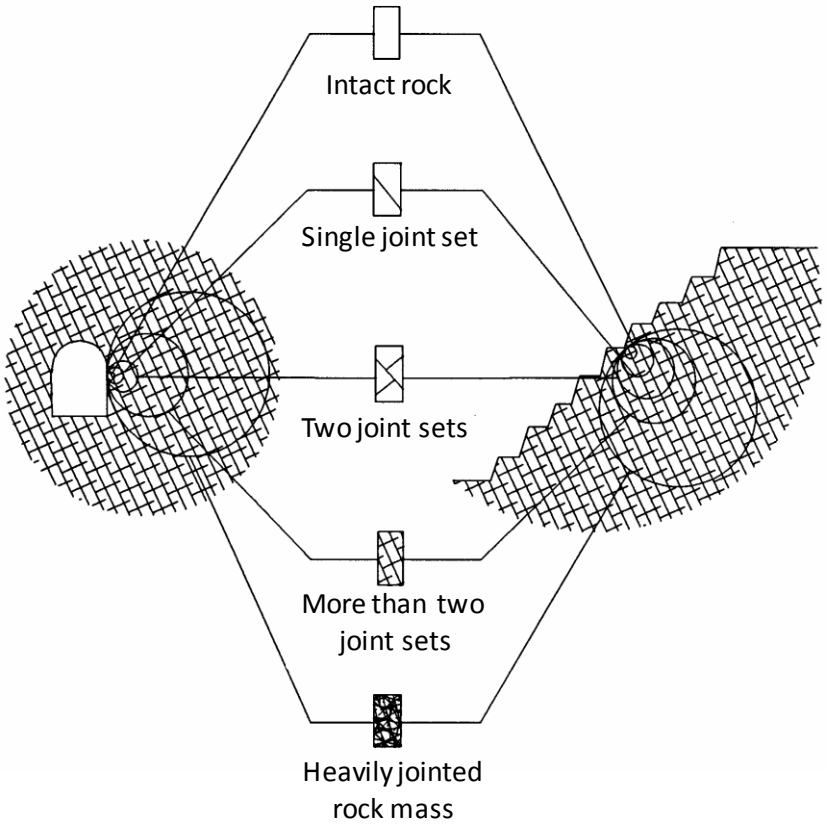

Figure 1-5: Transition from intact rock to heavily jointed rockmass with increasing scale (after Hoek et al., 1995).

When dealing with the estimation of rockmass strength, it is suggested that the scale of individual rock blocks should be sufficiently small in relation to the overall size of the structure being considered (Hoek and Brown, 1980a; Hoek and Brown, 1997). Most standard failure criteria for the estimation of rockmass strength are based on the assumption that there are sufficient numbers of closely spaced and persistent discontinuities to ensure that isotropic behavior is applicable.

1.1.2.1 Degree of interlock

According to Hoek (1994) and Hoek et al. (1995), the strength of a jointed rockmass depends on the degree of interlock between the rock blocks. The degree of interlock is defined as the kinematic freedom of the rock blocks to rotate over and slide along each other (Hoek, 1983). Various types of rockmasses in terms of the degree of interlock between their constituent rock blocks include highly interlocked, interlocked and poorly interlocked rockmasses.

Figure 1-6 schematically illustrates various degrees of block interlock. A rockmass with convex-shaped blocks (Figure 1-6a) is considered to be a highly interlocked rockmass as the joints forming the blocks terminate on other joints, but are not continouos and therefore do not generate any plane of weakness throughout the rockmass. Therefore, failure of such a rockmass is dominated by a combination of block openings along their boundaries (joints) and intra-block tensile fracturing at low confinement and shearing of the rockmass, mainly through the blocks, at high confinement.

Rockmasses made up of rectangular blocks formed by non-persistent and/or rough joints (Figure 1-6b and c) are also considered as highly interlocked jointed rockmasses. In these two

rockmasses, failure mainly occurs by fracturing of the intact rock in the case of the rockmass with non-persistent joints at both low and high confinements (Figure 1-6b), and sliding along asperities causing dilation at low confinement and shearing of asperities at high confinement in the case of the rockmass with rough joints (Figure 1-6c).

The rockmass schematically shown in Figure 1-6d consists of two joint sets; one non-persistent and one persistent. In this rockmass, block sliding along the persistent joint is the main mode of failure if the persistent joint is critically oriented. If both joint sets are persistent (i.e., the case shown in Figure 1-6e), block rotation will also be a possible mode of failure. Due to the high degree of freedom of the blocks arising from their ability to slide along and/or rotate over each other, these rockmasses (shown in Figure 1-6d and e) are considrerd as interlocked jointed rockmasses. A Further dicussion on the differences between the strengths and failure modes of highly interlocked and interlocked jointed rockmasses can be found in *Chapter 6*.

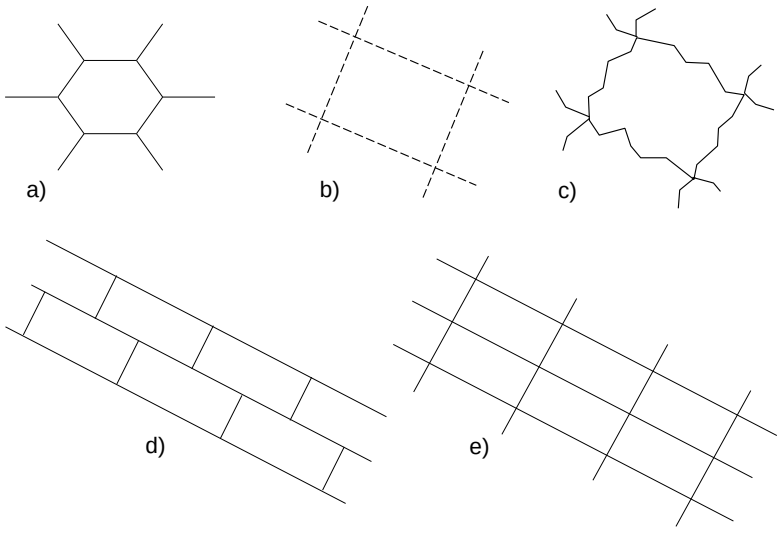

Figure 1-6: Schematic of various degrees of block interlock in 2D, assuming a third out-of-plane joint set exists: a) a convex-shaped block; b) a rectangular block with non-persistent joints; c) a rectangular block with persistent but very rough joints; d) a rockmass with rectangular blocks made up of two joint sets, one persistent and the other one non-persistent; e) a rockmass with rectangular blocks made up of two persistent joint sets.

Bahrani et al. (2014) used the grain and grain boundaries as analogues for rock blocks and block forming joints in a jointed rockmass and showed how the degree of interlock between grains increases with irregularity and surface roughness (Figure 1-7a to d). Figure 1-7a shows hexagonal close-packed circular particles with a porosity of 26%. In such a case, failure occurs through particle rotation and overriding. Figure 1-7b shows the densely packed rounded sand with a porosity of around 31 to 34% (Dusseault and Morgenstern, 1978). The failure observed in this material, which is considered as an analogue for a poorly interlocked rockmass, occurs due to particle rotation, overriding and minor shearing of asperities.

In Figure 1-7c, the interpenetrative contacts in locked sand with a porosity of 27 to 33% (Dusseault and Morgenstern, 1979) are shown with arrows. The failure of locked sand occurs mainly because of particle overriding at low confinement as well as asperity shearing and grain breakage at high confinement (Dusseault and Morgenstern, 1978). Granulated Wombeyan marble (Rosengren and Jaeger, 1968), an analogue for a highly interlocked jointed rockmas, has a porosity of 4% (Figure 1-7d). Its failure occurs mainly by grain boundary opening at low confinement and grain breakage at high confinement.

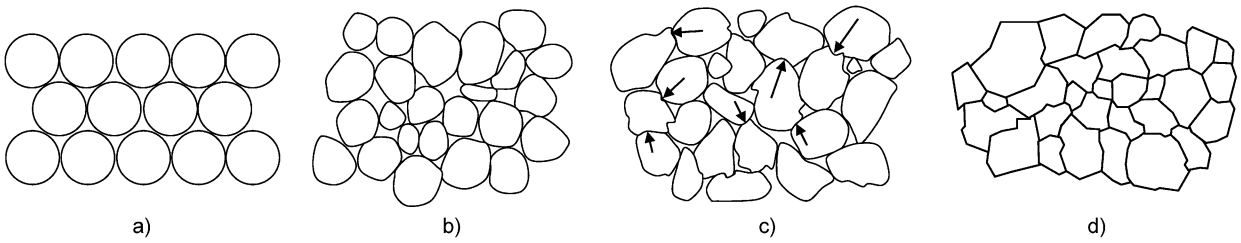

Figure 1-7: Fabric of granular assemblies with increasing interlock from left to right: a) hexagonal close-packed circular particles; b) densely packed rounded sand; c) locked sand with interpenetrative contacts shown with arrows; and d) granulated Wombeyan marble. (a) to (c) redrawn and modified from Dusseault and Morgenstern (1978), and (d) drawn from Rosengren and Jaeger (1968).

An example of a highly interlocked jointed rockmass with hexagonal blocks is a rockmass with columnar jointing, which often develops in basalts and dolerites (Figure 1-8). In this case, the rockmass is divided into columns that are typically hexagonal with side lengths in the order of a few tens of centimeters. The columns are also usually intersected by cross joints that become less regular with depth (Jaeger et al., 2007).

In such rockmasses, the columns can slide along their long axis yet, due to the high degree of interlock between these columns in the direction perpendicular to their long axis, they cannot rotate or slide without disrupting the rockmass fabric or breaking through intact rock. This leads to geometric dilation or a bulking process that precedes failure at relatively low confinement. Hence, geometric incompatibilities between rock columns generate an extremely high dilation, which leads to an initially steep failure envelope at low confining pressures (i.e., $\sigma_3 < \sim UCS_i/10$; Kaiser and Kim, 2014).

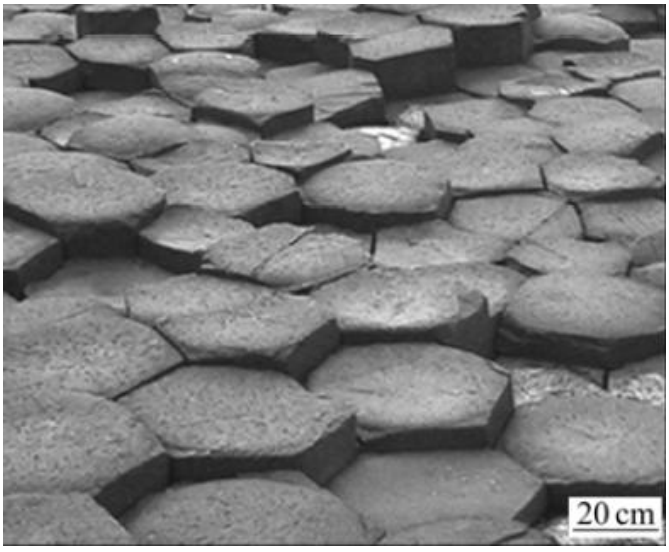

Figure 1-8: A highly interlocked columnar basaltic rockmass (after Di et al., 2011).

The following reviews factors that influence the degree of interlock in a jointed rockmass, including the joint roughness, the joint persistence and the strength of rock blocks.

1.1.2.2 Joint roughness

As used in most rockmass classification and characterization systems, factors such as separation or aperture of discontinuities, nature of infilling material present, wall condition (hard or soft) and their surface roughness influence the surface condition of discontinuities and, therefore, the strength of a jointed rockmass. Among these, the non-planarity or roughness of discontinuities contributes to the degree of interlock between the rock blocks (i.e., discontinuity surface interlock).

According to Patton's (1966) bilinear shear strength envelope for rough discontinuities (Figure 1-9), a high dilation due to roughness rapidly increases the shear strength of the discontinuities as normal stress increases. Beyond a critical normal stress, dilation due to shear deformation along the discontinuities is suppressed and failure occurs by shearing asperities and breaking through intact rock. The surface roughness decreases the ability of rock blocks to slide and rotate during the failure process by limiting kinematic freedom at the block boundary scale.

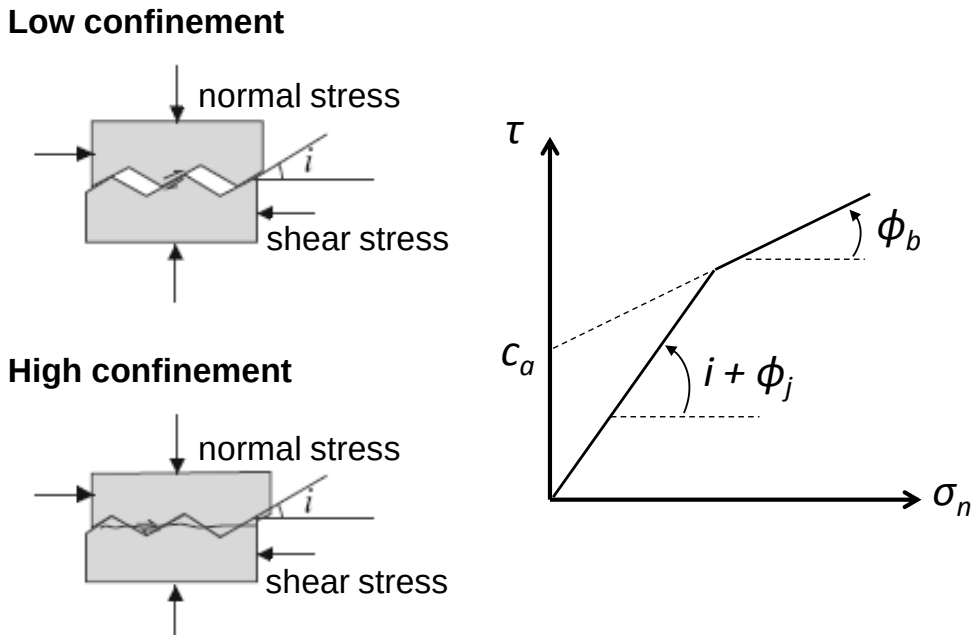

Figure 1-9: Effect of normal stress (σ_n) on joint shear strength (τ) leading to bi-linear failure envelope for joints (after Patton, 1966) with an apparent cohesion c_a (figure from Kaiser and Kim, 2014). In this figure, i refers to roughness angle, and ϕ_b and ϕ_j refer to basic friction angles of intact rock and joint, respectively.

1.1.2.3 Joint persistence

Persistence is the term used to describe the areal extent or size of a discontinuity within a plane. Persistence influences the degree of interlock between rock blocks and therefore has an important impact on the rockmass strength as the presence of rock bridges in a non-persistent jointed rockmass prevents rock blocks from sliding or falling from an excavation until the rock bridges fail. According to ISRM (1978), persistence can be crudely quantified by measuring the trace lengths of discontinuities on exposed surfaces. Joint persistence K is defined by Einstein et al. (1983) as:

$$K = \frac{\sum JL}{\sum JL + \sum RBR}$$ Equation 1-1

where *JL* is the length of a joint segment and *RBR* is the length of the rock bridge between two joint segments as shown in Figure 1-10. Rock bridges have a major influence on the shear strength of non-persistent discontinuities, particularly in hard rocks. At low confinement, unstable tensile crack propagation initiates at the tips of the discontinuities resulting in the formation of wing cracks within the rock bridge. With increasing confinement, tensile cracks can still form but their unstable propagation is inhibited.

As discussed earlier, the length of crack propagation from the tips of a pre-existing crack is highly dependent on the confinement and decreases rapidly with increasing confinement (Hoek and Bieniawski, 1965). Therefore, a much higher load is required before these short cracks are generated and accumulated within the rock bridge. The accumulation of these tensile cracks eventually results in the formation of macroscopic shear bands within the rock bridge and associated shear rupture (Bewick et al., 2015b; 2015c).

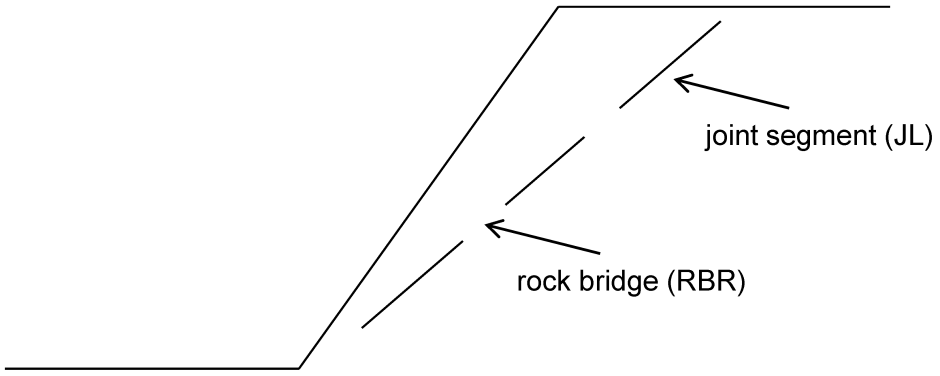

Figure 1-10: A non-persistent discontinuity showing rock bridges between joint segments (redrawn from Einstein et al., 1983).

1.1.2.4 Strength of the rock block

The strength of a rock block is influenced by the strength of the intact part of the block as well as the strength of discrete defects inside the block. In a highly interlocked rockmass, the high rock block strength forces the failure to occur by sliding along the joints at low confinement. This generates geometric dilation, which results in a rapid increase in the strength of the highly interlocked rockmass with an initial steep failure envelope, by analogue to Patton's (1966) bi-linear shear strength envelope for rough joints. However, if the blocks are weak (e.g., in a poorly interlocked rockmass), the rockmass fails by shearing through the rock block before any significant dilation along the joints occurs. Therefore, the increase in the strength of a poorly interlocked rockmass with increasing confinement is expected to be more gradual compared to that of a highly interlocked rockmass.

According to Hoek (1983), intact rock pieces are "the unfractured blocks occurring between structural discontinuities in a typical rockmass". The strength of intact rock specimens under unconfined condition is usually determined from laboratory Unconfined Compressive Strength (*UCS*) tests. According to Bewick et al. (2015a), when determining the *UCS* of a rockmass with defected rock blocks, one should differentiate between the *UCS* with failure through intact rock of predominantly homogeneous (*ho*) specimens (UCS_{ho}) and failure of heterogeneous (*he*) specimens with combined failure modes involving shear along defects and through intact rock (called UCS_{he}). Both UCS_{ho} and UCS_{he} are representative of the strength distribution in defected rock blocks forming a rockmass and need to be determined from laboratory tests. In this document, the strength of the homogeneous part of the rock is labeled UCS_i to describe the unconfined strength of the non-defected part of the rock.

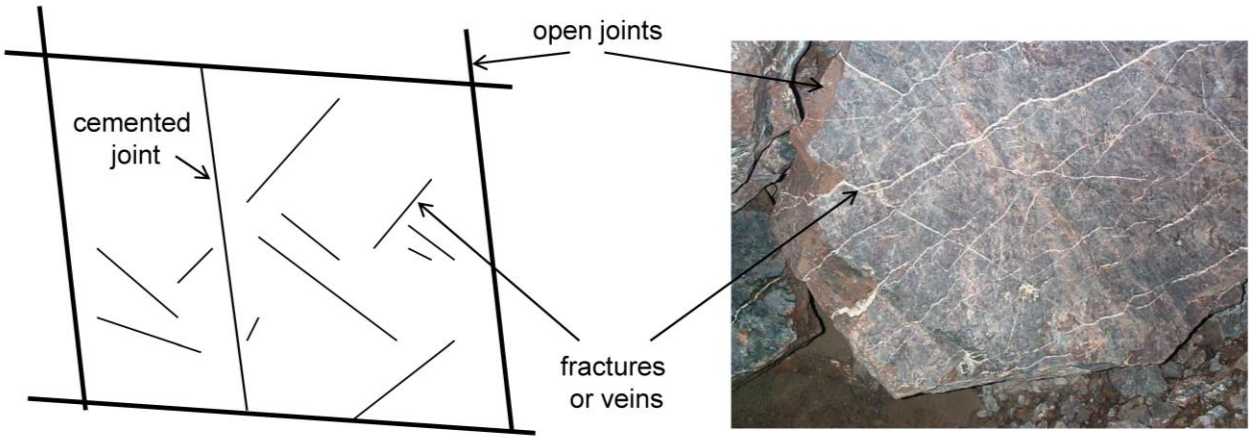

Figure 1-11: Defected rock block defined by open joints; left figure redrawn from Laubscher and Jakubec (2000), right photo courtesy of Dr. P.K. Kaiser.

It is well known that the strength of rock decreases with increasing specimen size (Bieniawski, 1967; Pratt et al., 1972; Bieniawski and Van Heerden, 1975; Hoek and Brown, 1997). The rock block strength is influenced by the presence of fractures, veins and cemented joints as the size of a rock specimen reaches that of a rock block. This is schematically shown in Figure 1-11. Laubscher (1990) and Laubscher and Jakubec (2000) in their rockmass classification system, called Modified Rock Mass Ratings (*MRMR*), introduced correction factors to account for laboratory scale features such as micro-cracks as well as rock block scale features such as fractures, veins and cemented joints to arrive at a proper assessment of the rock block strength.

1.2 Terminology

In an effort to focus on the essence of this thesis, the following terminology is adopted:

Intact rock is used to describe the non-defected rock material between discontinuities, which might be represented by a hand specimen or piece of drill core examined in the laboratory (Brady and Brown, 2007). In this document, intact rock refers to a laboratory specimen that does not

contain any strength dominating defects at the specimen scale. Note that pre-existing grain and grain boundary fractures, which cannot be seen by the naked eye, may exist in intact rock specimens. In this document, the unconfined compressive strength of such a homogeneous intact rock is labeled UCS_i.

Damaged rock refers to a laboratory scale specimen that has been damaged through an external process, for example during drilling a core from a highly stressed zone. Such a process may result in the generation of tensile micro-cracks. Other examples include heating the specimen in the laboratory and cutting the specimen using a saw to simulate specimen scale defects. In this document, the unconfined compressive strength of rock damaged by any external process is labeled UCS_d.

Micro-defects are those flaws at the grain scale (i.e., grain and grain boundary cracks), which exist in all rock types and cannot be seen by the naked eye.

Defects are cohesive or non-cohesive structures at the specimen and rock block scales such as veins and cemented joints, which may influence the failure mode or the rock strength.

Discontinuity in rock mechanics is a collective term for all fractures or features in a rockmass such as joints, faults, shears, weak bedding planes and contacts that have zero or relatively low tensile strength (Brady and Brown, 2007).

Joints are the most common and geotechnically significant structural features in a rockmass (Brady and Brown, 2007). According to ISRM (1978), a joint is a break of geological origin in the continuity of a body of rock occurring either alone or, more frequently, in a set or system. Joints typically show no signs of visible movement parallel to the joint surface.

Massive rockmass refers to a field scale rockmass that is largely free of persistent or non-persistent joints.

Jointed rockmass is the total *in situ* medium containing persistent or non-persistent discontinuities of different types such as bedding planes, faults, joints, folds and other structural features (Brady and Brown, 2007). In this document, the unconfined compressive strength of rockmass (jointed or massive) is labeled UCS_{rm}.

Non-persistently jointed rockmass is a rockmass where the joints are not continuous and terminate within the rock to generate rock bridges.

Persistently jointed rockmass is a rockmass where the joints are sufficiently continuous to generate rock blocks with open block boundaries.

Moderately jointed refers to a rockmass with persistent or non-persistent joints that do not form blocks with all-sided open block boundaries.

Rockmass characterization systems such as Geological Strength Index (*GSI*) (Hoek, 1994; Hoek et al., 1995) are indices intended to assist in obtaining rockmass strength and deformation properties. The *GSI* intends to characterize (describe) the rockmass without providing specific engineering design recommendations. Design recommendations are obtained by numerical modeling or by use of semi-empirical relationships that are based on the intact rock and rockmass parameters.

Rockmass classification systems such as Rock Mass Rating (*RMR)* (Bieniawski, 1976; Bieniawski, 1989), Modified Rock Mass Rating (*MRMR)* (Laubscher, 1990; Laubscher and

Jakubec, 2000) and Tunneling Quality Index (*Q)* (Barton et al., 1974) provide quantitative descriptions of rockmasses for the purpose of arriving at specific design recommendations (e.g., support classes, *TBM* performance, excavation stability limits, stand up time, etc.). Only recently have some attempts been made by Barton (2002) and Barton and Pandey (2011) to utilize *Q* for rockmass characterization.

Failure criteria such as the non-linear Hoek-Brown (*HB*) and the linear Mohr-Coulomb (*MC*) failure criteria are used to describe an increase in strength of rock with increasing confining pressure. Both the *HB* and *MC* criteria are shear-based criteria.

Equivalent Friction angle (ϕ_e) is defined as the combined basic angle of friction (ϕ_b) and dilation angle (i) on the principal stress space determined for a given range of confinement.

Highly interlocked jointed rockmass is a rockmass that consists of hard and brittle rock blocks and joints that are rough and non-persistent. Such a rockmass fails due to intra-block tensile fracturing or opening of the joints at low confinement and intra-block shear failure at high confinement. It is discussed and demonstrated in this document that the strength of a highly interlocked rockmass increases more rapidly with increasing confinement compared to that of an interlocked or a poorly interlocked rockmass where sliding along persistent joints and block rotation are the main modes of failure.

Strength Degradation (*SD*) is the difference between the strengths of the intact (laboratory scale) specimen and that of the damaged rock or rockmass. Thus, *SD* provides a measure for the degree of degradation a rockmass has experienced from its virgin, massive state.

The term “degradation” in rock mechanics is used for different purposes. For example, Fang and Harrison (2001) used the term “degradation” to describe the post-peak strength reduction from the peak strength. In this document, the strength degradation is related to the intensity of damage in an intact rock or structure in a jointed rockmass, not the straining beyond the peak strength.

The concept of strength degradation is schematically illustrated on the shear stress versus normal stress space in Figure 1-12 by analogue to a direct shear test. For an intact rock specimen, the failure envelope can be approximated as a line with a slope equal to the rock basic friction angle $\emptyset_b$ and a cohesion c (Figure 1-12a). If the same rock contains a smooth joint with zero cohesion (Figure 1-12b), the shear strength of the rock joint is represented by a linear envelope and a slope equal to the joint basic friction angle $\emptyset_j$. The reduction in the shear strength of the joint from that of the rock (shear strength degradation: $\Delta\tau = \tau_{rock} - \tau_{joint}$) is independent of normal stress (assuming $\emptyset_b = \emptyset_j$). For a rough joint with a roughness angle of i, as shown in Figure 1-12c, the shear strength of the rock joint can be represented by a bilinear envelope as suggested by Patton (1966), as was discussed earlier. When comparing the shear strength envelopes of intact and jointed rocks, it become evident (as shown by Figure 1-12c) that the shear strength degradation $\Delta\tau$ decreases with increasing normal stress up to a critical normal stress. Beyond this critical normal stress, the shear strength degradation remains constant independent of normal stress.

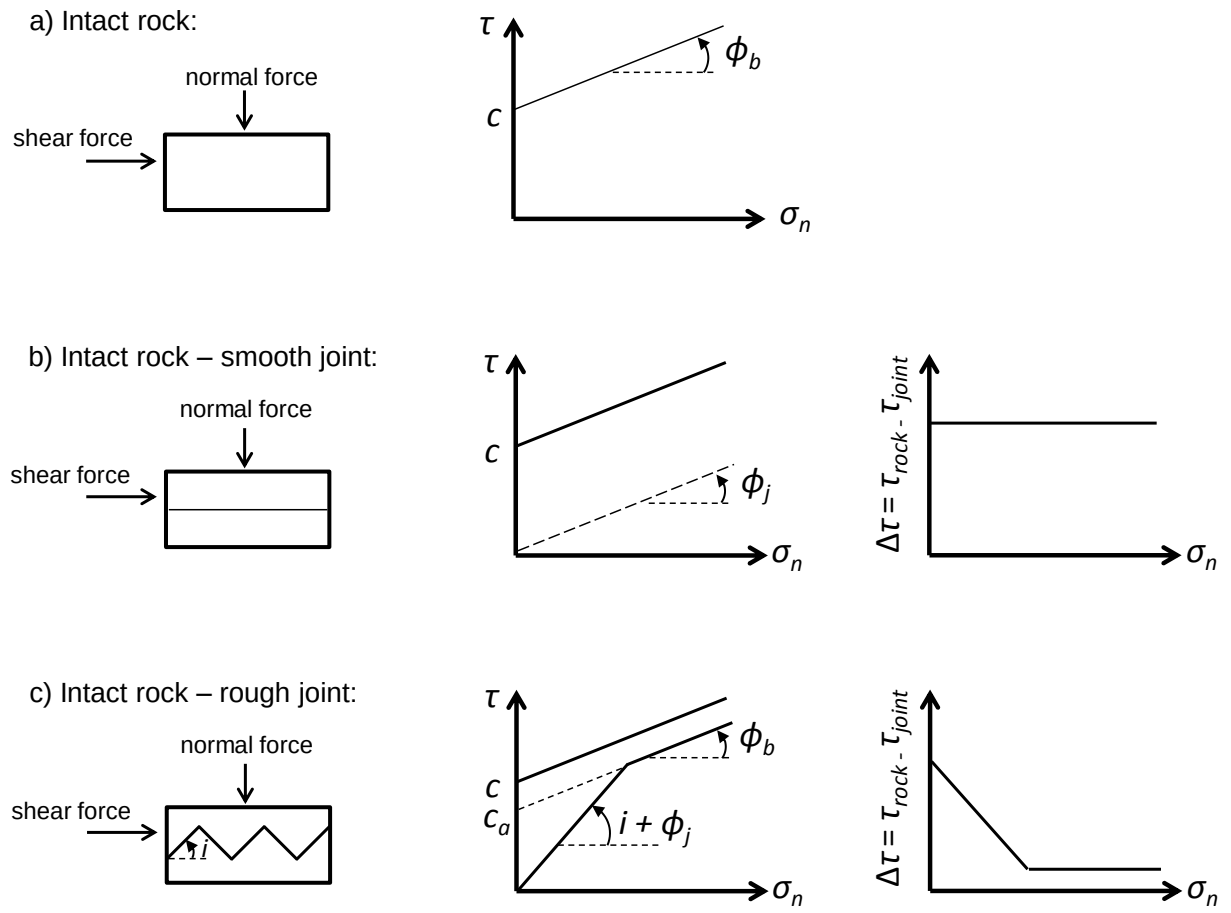

Figure 1-12: Shear strength of: a) intact rock; b) smooth joint; and c) rough joint with a roughness angle of *i*.

The concept of strength degradation in the principal stress space is schematically shown in Figure 1-13. As can be seen in Figure 1-13a, the strength of damaged rock (or jointed rockmass) increases rapidly with increasing confinement and approaches but does not reach the intact strength at high confinement. Therefore, the strength degradation ($\Delta\sigma_1$) (Figure 1-13b), which is the difference between the strength of intact rock (σ_{1i}) and the strength of damaged rock (σ_{1d}) (or the strength of jointed rockmass, σ_{1rm}), can be said to decrease rapidly at low confinement before remaining almost constant once beyond a critical confining pressure.

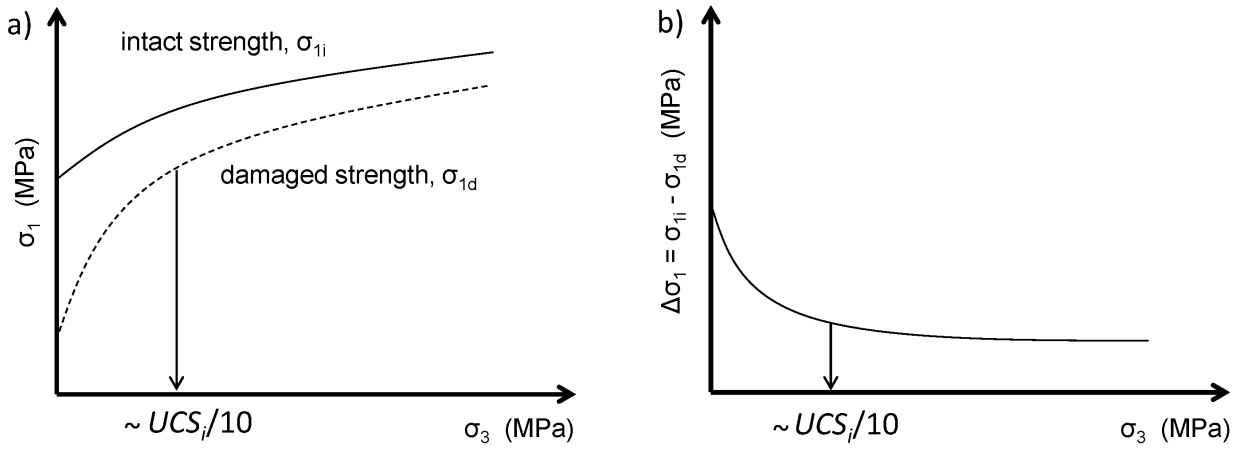

Figure 1-13: Schematic representation of: a) intact and damaged strengths; and b) strength degradation, as a function of confinement.

According to Bahrani and Kaiser (2013), this critical confining pressure is between UCS_i/20 and UCS_i /6 with a typical central value of UCS_i/10 as was suggested by Kaiser and Kim (2014). As was discussed earlier, the rapid increase in the strength of damaged rocks with confinement is due to the reduction in the length of propagated tensile cracks. When the confining pressure is greater than about 10% of the applied axial stress, ($\sigma_1/\sigma_3 > 0.1$; Hoek and Bieniawski, 1965; Diederichs, 2003) shear banding or shear rupture dominates the confined rock behavior.

1.3 Problem Statement

At great depths (e.g., > 1.5 km), the magnitude of *in situ* stresses can reach or exceed the maximum confining pressure typically applied to intact rock specimens in the laboratory. Therefore, reliable estimation of the strength of jointed rockmasses at high confinement is difficult but of paramount importance for deep underground construction and mining projects.

While rockmass classification systems such as *Q* and *RMR* were originally developed for engineering design (e.g., support selections), it is the rockmass characterization system *GSI* that

was intended to provide a semi-empirical method for estimating the unconfined and confined strengths of jointed rockmasses. Unfortunately, its applicability to confined hard rock conditions is questionable. The *MRMR* is also limited to providing a means of obtaining the unconfined rockmass strength. The following reviews the origin and application of the *HB* failure criterion and the *GSI* rockmass characterization system to put this thesis in perspective.

The *HB* failure criterion was developed to reflect the non-linear failure envelopes of both intact rock and jointed rockmasses. It was initially proposed by Hoek and Brown (1980a and 1980b) and later extended by Hoek et al. (1995) and Hoek and Brown (1997) to incorporate the rockmass properties using the *GSI* characterization system. The *HB* criterion's early development was based on the laboratory strength data of intact and jointed Panguna Andesite from the slopes of the Bougainville open pit copper mine in Papua New Guinea. Examination of the jointed rockmass (Figure 1-14a) from the description provided by Hoek and Brown (1980a and 1980b) illustrates that the rockmass near the excavation surface is disturbed with little to no interlock and with typical rock pieces measuring about 50 to 200 mm. The rockmass consists of multiple persistent joint sets with varying joint surface conditions (i.e., slightly, moderately or completely weathered).

In order to estimate the strength of the rockmass, samples from bench faces were gathered by a front end loader, dumped into large drums and transported to the laboratory where they were compacted into a 570 mm diameter rockfill triaxial cell (Figure 1-14b). Later, Bougainville copper mine constructed their own small triaxial cell (Figure 1-14c) and carried out tests on specimens with a diameter of 152 mm. Further triaxial tests were conducted by Jaeger (1970) on 25 and 50 mm cores of intact andesite and undisturbed 152 mm cores of closely jointed andesite.

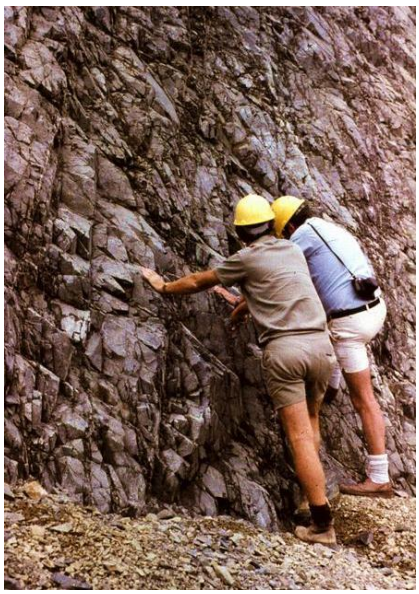

(a)

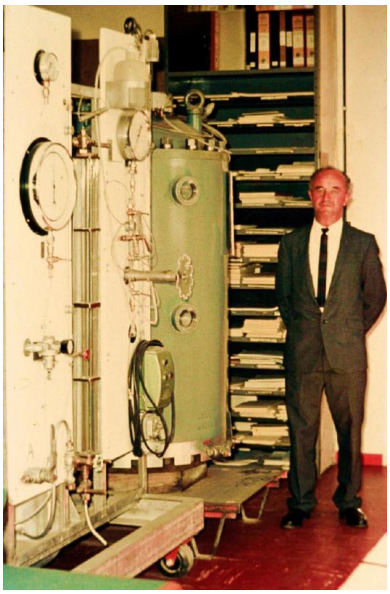

(b)

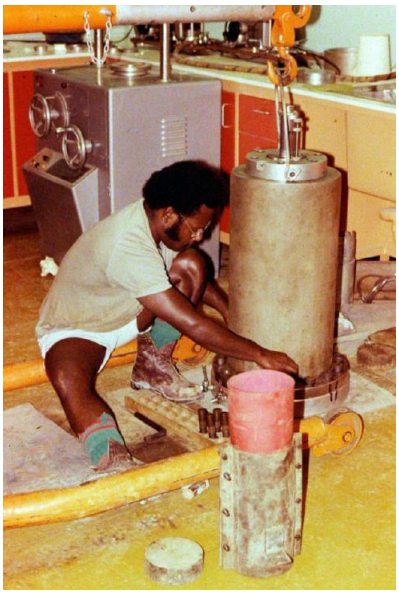

(c)

Figure 1-14: a) A typical bench face of jointed andesite in Bougainville open pit copper mine; b) traxial cell, for testing 570 mm diameter specimens; c) triaxial cell for testing 152 mm diameter specimens. Photographs provided by Dr. E. Hoek.

The results of these tests are presented in Figure 1-15. As can be seen from this figure, the strength of jointed andesite increases at a lower rate with increasing confinement compared with that of intact andesite. This suggests that the joints in the specimens of jointed andesite have a lower equivalent friction angle compared to that of intact andesite.

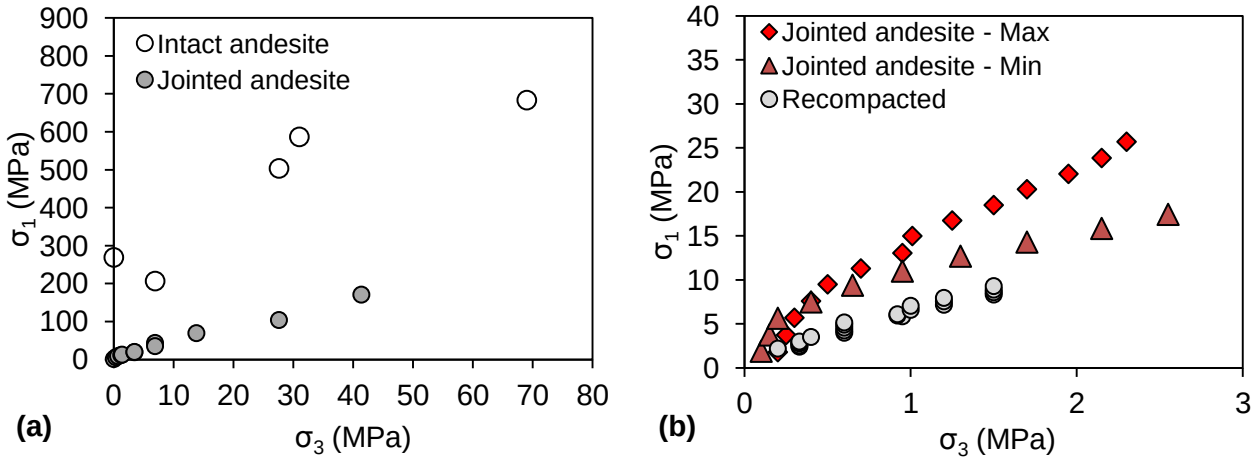

Figure 1-15: Results of triaxial tests on: a) intact and jointed specimens tested by Jaeger (1970); b) jointed andesite and recompacted rockfill tested by Bougainville Copper mine. Data provided by Dr. E. Hoek.

Table 1-1 lists some of the projects used in the development of the *HB* failure criterion and the *GSI* system. It is concluded that this criterion was verified through case studies that are dominated by rockmass behaviours in low confinement zones near excavations. As can be seen in this table the uniaxial compressive strength of the intact rock is higher than 100 MPa in only two projects, and the majority of rockmasses have a *GSI* less than 65. Therefore, it can be understood that the *GSI* approach to obtain rockmass strength parameters was originally developed on and for relatively weak rocks. Hoek et al. (1995) and Marinos et al. (2005) also mentioned that the *GSI* system was developed specifically to deal with difficult and poor quality rockmasses, situations where the *RMR* system cannot be applied.

Table 1-1: List of projects used to develop and refine the *HB* criterion and the *GSI* characterization system.

Type of project	UCS_i (MPa)	*GSI*	Reference
Mine drift	50	75	Hoek and Brown (1997)
Underground powerhouse	110	75	Hoek and Brown (1997)
Powerhouse cavern	30	65	Hoek and Brown (1997)
Tunnel	5 to 10	20	Hoek and Brown (1997)
Hydroelectric tunnel	10	6 and 45	Hoek (1999)
Highway tunnel	10 to 100	15 to 50	Goricki et al. (2006)
Water transport tunnel	15 to 110	25	Hoek et al. (2008)

As indicated by Hoek et al. (1995), the *GSI* system was intended to estimate the isotropic rockmass strength when there exists a sufficient number of closely spaced persistent joint sets that the rockmass strength is independent of the direction of the applied load. In such situations, the rockmass strength largely depends on the shape and size of the rock blocks and the surface conditions of the block-forming joints.

The *GSI* system is used when jointed rockmasses are interlocked but the degree of interlock is relatively low due to the fact that joints are persistent and relatively smooth. The applicability of the *GSI* system is schematically illustrated in Figure 1-16. As can be seen from this figure, the joint in a rockmass described by the *GSI* system is such that sliding on block boundaries dominates failure. However, in massive to moderately or non-persistently (highly interlocked) jointed rockmasses, the fundamental assumption outlined above is frequently invalid due to the very high degree of interlock between the rock blocks resulting from rock bridges and the roughness of the block forming joints as well as the high strength of the blocks.

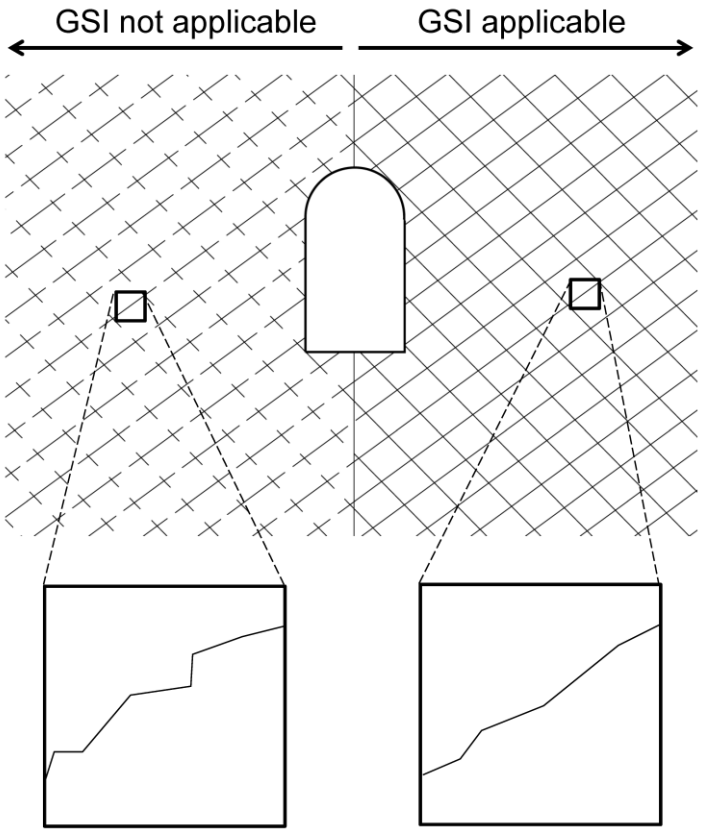

Figure 1-16: Schematic of non-persistently and persistently jointed rockmasses, showing the applicability of the *GSI* characterization system in jointed rockmasses where the joints are persistent and relatively smooth, therefore sliding on joints dominates failure.

From the review of the *HB* failure criterion including the original data and the projects used to develop and calibrate the *GSI* system, Bahrani and Kaiser (2013) concluded that the application of the *GSI* approach for strength determination of massive and non-persistently jointed rockmasses must be limited if not flawed, largely due to the implicit extrapolation beyond the experience base. This is particularly the case if the strength of the confined rockmass plays an important role in the behaviour of an underground structure such as pillars or abutments.

It was concluded that new equations or at least new parameter recommendations need to be developed to allow for the accurate estimation of the strength of jointed rockmasses made up of

interlocked, hard brittle rock blocks with non-persistent and rough joints. As such, this thesis focuses on obtaining the strength parameters for such rockmasses (i.e., for conditions where the *GSI* system is not applicable).

Figure 1-17 provides a simplified description of the various types of rockmass failure commonly observed underground (Hoek et al., 1995; Kaiser et al., 2000). This thesis deals with the strength estimation for rockmasses where failure is dominated by intra-block fracturing (rather than shearing of block boundaries) at intermediate to high stress levels and in massive to moderately or non-persistently jointed rockmasses with high rock block strength (i.e., elements shaded in Figure 1-17).

Therefore, this thesis does not deal with low *in situ* stress conditions where gravity-driven failure and raveling of blocks from the excavation surfaces occurs nor does it touch upon strength estimation for weak rocks and squeezing ground. It also does not address strength determination for blocky, very blocky or disintegrated rockmasses, as these are all situations in which the *GSI* system is applicable.

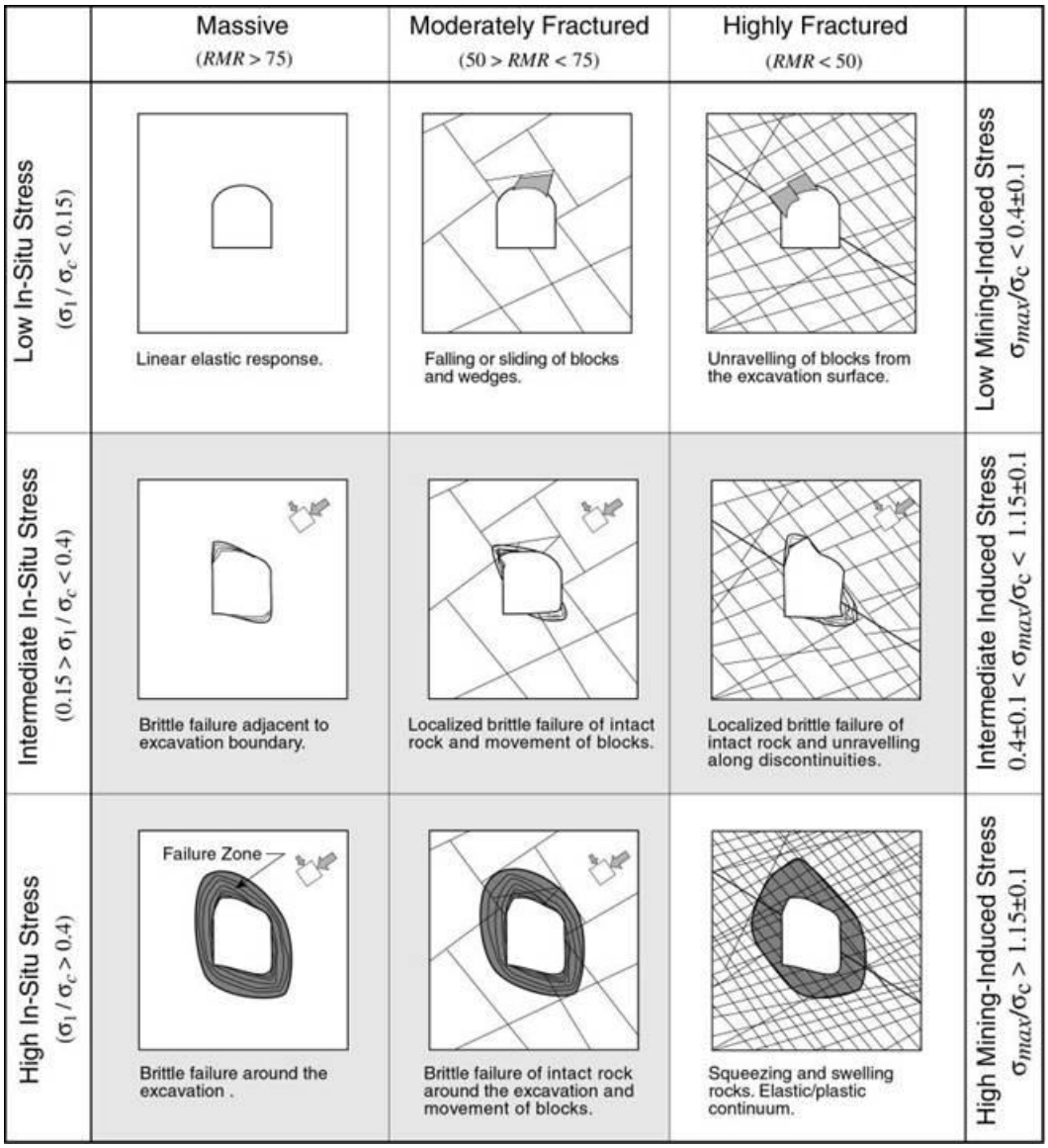

Figure 1-17: Rockmass behavior matrix (Kaiser et al., 2000).

1.4 Hypothesis and Objectives

Based on the considerations presented in the introductory sections, it is hypothesized that the strength of a highly interlocked jointed rockmass increases more rapidly with increasing confinement compared to that of an interlocked or a poorly interlocked jointed rockmass. Thereofre, it is hypothesized that the existing empirical approaches, which were developed based

on experiences from observation of rock behavior near excavation boundaries in poorly interlocked rockmasses, tend to underestimate the confined strength of highly interlocked rockmasses made up hard brittle rock blocks and joints that are rough and non-persistent.

Based on this hypothesis, the primary objective of this research is to develop an approach that will make it possible to more accurately estimate the confined strength of highly interlocked rockmasses. For this purpose, semi-empirical equations that relate the strength reduction of a jointed rockmass from an intact rock to confinement have been developed based on the results of numerical simulations. This approach is called the Strength Degradation (*SD*) approach for confined strength of jointed rockmasses. The following are the prevailing assumptions for the *SD* approach:

- *UCS* and triaxial test results of intact rock are available and indicate "high rock strength" according to the classification by Bieniawski (1973)[1]; thus UCS_i > 100 MPa and
- the unconfined compressive strength of the jointed rockmass can be reliably estimated using one of the existing empirical approaches, or from back analysis of rockmass strength by monitoring its behavior near excavation boundaries (e.g., tunnel wall failure).

This research also aims at providing insight into the influence of confinement, rock defects, joint persistence and joint roughness on the strength and failure modes of intact rocks, micro-defected rocks, defected rock blocks and jointed rockmasses. Detailed objectives include:

- developing a methodology for calibration of a distinct element grain-based model to laboratory properties of intact and damaged (micro-defected) rocks;

[1] Intact rock strength was classified by Bieniawski (1973) into five categories: 1. Very low strength (UCS_i = 1 – 25 MPa); 2. Low strength (UCS_i = 25 – 50 MPa); 3. Medium strength (UCS_i = 50 –

- developing a methodology to simulate a damaged (micro-defected) rock specimen with various damage densities;
- developing a semi-empirical approach to estimate the confined strength of micro-defected rocks;
- developing an approach to simulate defected rocks;
- developing a semi-empirical approach to estimate the confined strength of highly interlocked jointed rockmasses made up of hard brittle rock blocks and joints that are rough and non-persistent; and
- suggesting adjusted *HB* strength parameters for such rockmasses.

1.5 Indirect Evidence in Support of Hypothesis

Unfortunately, the author did not have access to the detailed field observations and load and deformation histories of rockmasses that would have allowed systematic back-analyses to be undertaken in order to investigate the hypothesis. The following summarizes some indirect evidence that is consistent with the hypothesis advanced in this thesis.

1.5.1 Failure of massive to moderately jointed rockmasses

Extensive research on brittle failure around underground openings in massive to moderately jointed rockmasses conducted by Martin (1997), Martin et al. (1999), Diederichs (1999; 2003), Kaiser et al. (2000) and Hadjiabdolmajid et al. (2002) concisely indicate a higher rock strength at high confinement than what would be anticipated when projecting from rock behavior under low confinement (i.e., near excavation boundary). They showed that the strength of such rockmasses is not properly estimated by the linear *MC* or the non-linear *HB* failure criteria.

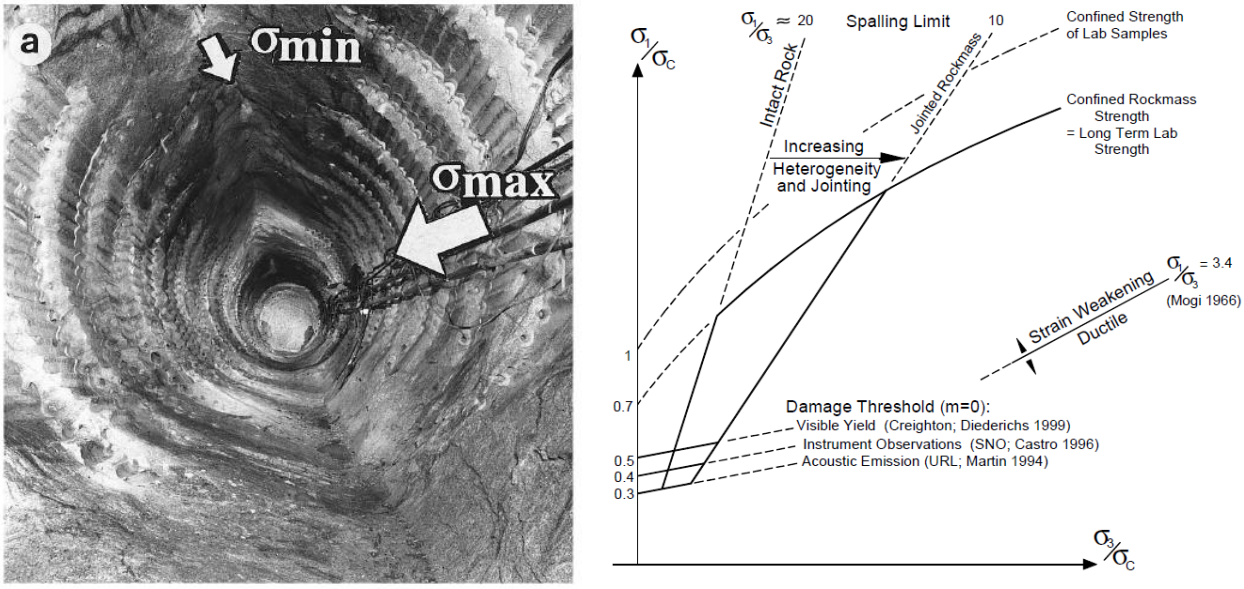

(a) (b)

Figure 1-18: a) V-shaped notch observed around the mine-by-experiment tunnel (Martin, 1997); b) bi-linear cut-off failure envelope for brittle failure in massive to moderately jointed rockmass (after Kaiser et al., 2000). σ_c in (b) is the intact rock strength under unconfined condition.

Figure 1-18a shows brittle failure in the form of v-shaped notching observed around the mine-by-experiment tunnel at the 420-level of the Underground Research Laboratory (*URL*) in Manitoba, Canada. Although the stress anisotropy at this depth was very high (the maximum and minimum principal stresses are 60 MPa and 11 MPa in magnitude, respectively) the maximum depth of the v-shaped notch was measured to be only 0.5 m. The main factor that stopped the propagation of failure beyond this depth is interpreted to be due to the rapid increase in the strength of the massive to moderately jointed rockmass with increasing confinement.

Based on field measurements and observations of near excavation failure in massive to moderately jointed rockmasses, including the case of the *URL*, Kaiser et al. (2000) introduced a bi-linear cut-off failure envelope for brittle rocks as presented in Figure 1-18b. The first linear section of this envelope, which is equal to the crack initiation stress of intact rock under

unconfined condition, accounts for unstable crack propagation at low confinement, and is obtained by introducing the *HB* brittle parameters by Martin et al. (1999). The second linear section of the criterion, known as the spalling limit, is defined by the constant σ_1/σ_3 ratio ranging from 5 to 20 depending on the level of heterogeneity. At high confinement, the conventional nonlinear Hoek-Brown failure criterion is assumed to be applicable.

1.5.2 Pillar strength

Evidence of a significant increase in rockmass strength at higher confinement can be found in the pillar stability graph developed by Lunder and Pakalnis (1997) based on the data collected by Potvin et al. (1989), which is extensively used by mine engineers for the design of mine pillars. This graph, shown in Figure 1-19, summarizes failed, transitional (unstable) and stable pillars and suggests that no failed pillar can be identified at pillar width-to-height ratios greater than 1.8. This is interpreted here as an indication that the core of wider pillars is highly confined and thus did not fail.

Hedley and Grant (1872) suggest a criterion that flattens with increasing pillar width-to-height ratio for pillar strength normalized by the unconfined strength of intact rock (shown with the dashed line in Figure 1-19). Intuitively, by considering the rise in the rockmass strength with confinement, it would be expected that wide pillars with high confinement in their cores should have strengths that exceed the unconfined intact rock strength if non-persistently joined and highly interlocked, thus suggesting a criterion that steepens with increasing the width-to-height ratio.

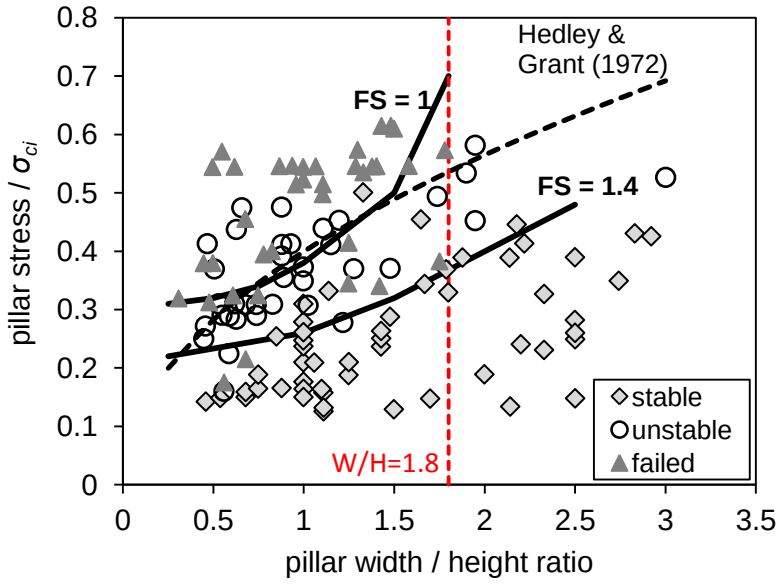

Figure 1-19: Pillar stability graph showing stable, unstable and failed pillars together with one of many empirical stability criteria (Hedley and Grant, 1972), and stability limits obtained by continuum modeling using the *HB* brittle parameters (Martin et al., 1999). *FS* stands for factor of safety.

Such an increase in the pillar strength with increasing confinement (pillar width) was also suggested by Martin and Maybee (2000) (solid black lines for factors of safety of 1 and 1.4). They used the *HB* brittle parameters suggested by Martin et al. (1999) and elastic models to arrive at the conclusion that the data should be fitted by convex functions. Their approach basically assesses the potential for pillar wall failure and considers the depth of failure as a measure of pillar wall degradation and results in a good agreement with the field data presented in Figure 1-19. Indirectly, their work also shows that the pillar cores for width-to-height ratios exceeding about 1.8 are sufficiently stable to prevent further propagation of wall spalling. If this was not the case and pillar cores were yielding, failed pillars should be found at width-to-height ratios greater than 1.8.

1.6 Methodology

The confined strength of a jointed rockmass can be determined from back-analyses of wide, marginally stable pillars and abutments, by *in situ* tests on large scale rock blocks or by extrapolation from laboratory models of jointed rockmasses or damaged rocks.

Unfortunately, data for such back analyses are extremely limited and conducting *in situ* experiments to back analyze rockmass strength requires extensive investment and planning. Moreover, such experiments are usually conducted at the production stages of mining projects when the design of underground excavations and infrastructure has already been completed and largely implemented. Conducting tests on large scale specimens is both expensive and time consuming and, furthermore, most facilities cannot test large scale hard brittle rocks at high confining pressures. On the other hand, the results of laboratory tests on physical models of jointed rockmasses and damaged rocks cannot typically be generalized to rockmasses with varying degrees of interlock (e.g., block strength, joint persistence and joint roughness).

Recently, numerical methods have been used extensively as an alternative approach to simulate jointed rockmasses at different scales. However, most numerical models of jointed rockmasses are based on calibrations of rock behavior at low confinement and this may lead to incorrect estimation of the confined strength of jointed rockmasses.

A promising approach to assess the strength of a jointed rockmass, which is the methodology used in this research, is to numerically simulate laboratory tests on materials that are considered to be analogues for jointed rockmasses. The results of numerical simulations, once calibrated, can then be utilized to extrapolate the strength of rockmasses with varying degrees of block

interlock. For this purpose, the Distinct Element Method (*DEM*) implemented by Itasca (2008) in the commercially available Particle Flow Code (*PFC*) in two-dimensions (*PFC2D* v.4.00) is chosen to generate synthetic rock specimens. The Grain-based Model (*GBM*) implemented in *PFC2D* by Potyondy (2010), is used to generate synthetic specimens with polygonal grain structures (called grain-based specimens here), in which the grains are allowed to deform and break.

The grain-based specimen is calibrated to the mechanical properties of intact and granulated Wombeyan marble reported by Gerrogiannopoulos (1976) and Gerrogiannopoulos and Brown (1978). The term "granulated" refers to a heat-treated marble where the cohesion at grain boundaries was destroyed due to anisotropy of thermal expansion of calcite grains. The granulated marble was suggested to serve as an analogue for a randomly jointed rockmass by Rosengren and Jaeger (1968). Due to the random locations and orientations of the grain boundaries, the grain geometry and the roughness of grain boundaries, the granulated marble was demonstrated to be an analogue for a highly interlocked, non-persistently jointed rockmass by Bahrani and Kaiser (2013) and Bahrani et al. (2014).

The calibrated grain-based specimens are then used to investigate:

- the influence of micro-defects on rock strength under unconfined and confined conditions;
- the influence of scale and defects on rock strength under unconfined condition; and
- the influence of the degree of interlock between rock blocks on rockmass strength under unconfined and confined conditions.

The results of laboratory tests simulated on synthetic micro-defected specimens and synthetic rockmass specimens are used to develop semi-empirical equations that relate the strength reduction of micro-defected rocks and jointed rockmasses from intact rock to confinement. This approach, as mentioned earlier, is called the Strength Degradation (*SD*) approach.

It will be shown that the *SD* approach for micro-defected rocks can be used to estimate the confined strength of a micro-defected rock in a situation where the unconfined and confined strengths of intact rock and the unconfined strength of micro-defected rock are known. Similarly, the *SD* approach for jointed rockmasses can be used to estimate the confined strength of a jointed rockmass in a situation where the unconfined and confined strengths of intact rock are known from laboratory triaxial tests and the unconfined strength of jointed rockmass can be reliably estimated using existing empirical approaches or from back analysis of rockmass behavior at relatively low confinement (e.g., rock failure near tunnel walls).

A method within the framework of the *SD* approach is proposed to estimate the variability of the confined strengths of micro-defected rocks and jointed rockmasses. The capability of the *SD* approach for estimating the confined strengths of micro-defected rocks and jointed rockmasses and the variability in the strength data is investigated on the published laboratory data on damaged, micro-defected and defected rocks, and physical models of jointed rockmasses.

As mentioned earlier, the *SD* approach for jointed rockmasses is applicable when the rockmass is highly interlocked and consists of hard brittle rock blocks with rough joints that are non-persistent. This research ends with semi-empirical equations for the *HB* strength parameters for such rockmasses, which can be directly used in commercially available continuum codes.

1.7 Scope and Structure

The research is described and the results are summarized in eight chapters.

This introductory chapter (*Chapter 1*) presents the hypothesis, overall goals, terminologies, objectives, and the methodology applied to test the hypothesis.

In *Chapter 2*, various methods for estimating the strength of a jointed rockmass are reviewed. These include empirical, analytical and numerical approaches. The results of laboratory tests on damaged, micro-defected and defected rocks (which are considered to be analogues for jointed rockmasses and physical models of jointed rockmasses) are presented.

Chapter 3 provides the background on the laboratory properties of intact and granulated Wombeyan marble, the methodology applied to simulate Wombeyan marble using the *GBM* and its calibration assumptions and results. Uniaxial and triaxial test simulations on the calibrated grain-based specimens are conducted to investigate the influence of confinement on the strength, deformation modulus, stress-strain curve and the number and nature of micro-cracks. The results of simulations in terms of the change in the failure mode with increasing confinement are compared with those of Wombeyan marble specimens tested in the laboratory.

In *Chapter 4*, the calibrated grain-based specimens are used to simulate micro-defected rocks. The influence of damage, simulated in the form of grain boundary micro-cracks, on the strength, deformation modulus, stress-strain curve and failure modes are investigated. The data concerning the strength of undamaged and damaged grain-based specimens are then used to develop semi-empirical equations that can be used to estimate the confined strength of micro-defected rocks. This approach, called the Strength Degradation (*SD*) approach for micro-defected rocks, is tested

on the results of laboratory tests on rock specimens that were damaged by various means in the laboratory. It is demonstrated that the *SD* approach is capable of estimating the confined strength of micro-defected rocks and its variability.

Chapter 5 describes how the grain-based specimens calibrated in the previous chapter are used to investigate the influence of specimen size on the strength of intact and defected rocks under unconfined condition. This chapter demonstrates a realistic simulation of defected rock specimens by combining a grain-based specimen consisting of deformable and breakable grains and a Discrete Fracture Network (*DFN*) model to simulate defects. The applicability of the *SD* approach, developed in *Chapter 4* for micro-defected rocks, is then tested to obtain estimations of the confined strength of defected rocks.

Chapter 6 provides an introduction to the influence of the degree of interlock between rock blocks on the rockmass strength. In this chapter, the grain-based specimen calibrated to the properties of granulated Wombeyan marble is treated as a highly interlocked jointed rockmass. This model is then used to investigate the influence of block shape, joint roughness and joint persistence on the strength of jointed rockmasses. For this purpose, the influence of confinement on the peak strength, failure mode, number and nature of intra-block fracturing at peak stress and stress-strain curves is discussed. This chapter also includes a discussion on the applicability and limits of applicability of the *HB* failure criterion and the *GSI* system for estimating the confined strength of highly interlocked rockmasses.

In *Chapter 7*, the results of simulations of highly interlocked jointed rockmasses from *Chapter 6* are adopted to develop a series of semi-empirical equations, similar to those presented in *Chapter 4*, to estimate the confined strength of such rockmasses. This approach, called the

Strength Degradation (*SD*) approach for jointed rockmasses, is investigated on the published laboratory test data on jointed rock specimens. This is followed by development of semi-empirical equations to obtain the values of *HB* strength parameters for highly interlocked rockmasses made up of hard brittle rock blocks and joints that are rough and non-persistent.

Chapter 8 presents a discussion and summary of this document including its major conclusions, the implications for pillar design and recommendations for future research.

Chapter 2

2 Review of Methods for Rockmass Strength Estimation

2.1 Introduction

In this chapter, the results of laboratory experiments on damaged and defected rocks, which are considered to be analogues for jointed rockmasses, and physical models of jointed rockmasses are reviewed. The objective of this review is to demonstrate how the strength of jointed rockmasses rapidly increases with increasing confinement, and to investigate the factors contributing to this elevated rockmass strength.

Next, the currently available methods for the estimation of the strength of jointed rockmasses are reviewed. For this purpose, the following are evaluated:

- empirical methods including rockmass classification and characterization systems;
- analytical methods based on the theory of plane of weakness; and
- numerical methods where Discrete Fracture Network (*DFN*) models are used to simulate jointed rockmasses.

The essence of this chapter is to investigate the applicability of these methods for the estimation of the unconfined and confined strengths of interlocked jointed rockmasses. It will be discussed in this chapter how the deficiencies in the existing empirical, analytical and numerical methods have led to this research.

2.2 Rockmass Strength from Physical Model Tests

Physical modeling has been used by many researchers to investigate the influence of factors such as joint persistent, joint orientation, and block shape on the strength of jointed rockmasses. In

this section, laboratory tests on physical models of jointed rockmass and damaged and defected rocks are reviewed. The focus of this section is on the laboratory models that represent isotropic rockmasses. Therefore, models made for investigation of anisotropic behavior of jointed rockmasses such as those by Ramamurthy and Arora (1994) and Prudencio and Van Sin Jan (2007) are not discussed here. Most of the laboratory test data presented in this section are used later to assess the applicability of the proposed Strength Degradation (*SD*) approaches for the estimation of the confined strengths of micro-defected and defected rocks and jointed rockmasses.

The results of laboratory experiments are analyzed by calculating equivalent angles of friction and cohesive strengths at low ($\sigma_3 < \sim UCS_i/10$) and high ($\sigma_3 > \sim UCS_i/10$) confinements using the following equation and by plotting the equivalent Mohr-Coulomb criterion on the principal stress space according to Hoek et al. (2002):

$$\sigma_1 = \frac{2c_e \cos \emptyset_e}{1 - \sin \emptyset_e} + \frac{1 + \sin \emptyset_e}{1 - \sin \emptyset_e}\sigma_3 \qquad \text{Equation 2-1}$$

where c_e and ϕ_e are equivalent friction angle and cohesion, respectively, and σ_1 and σ_3 are the major and minor principal stresses at failure, respectively. The change in the magnitudes of these two parameters with increasing confinement is schematically shown in Figure 2-1. This figure demonstrates how the equivalent (apparent) cohesion of the rockmass increases as its equivalent friction angle, including a dilational component of shear resistence, decreases with increasing confinement.

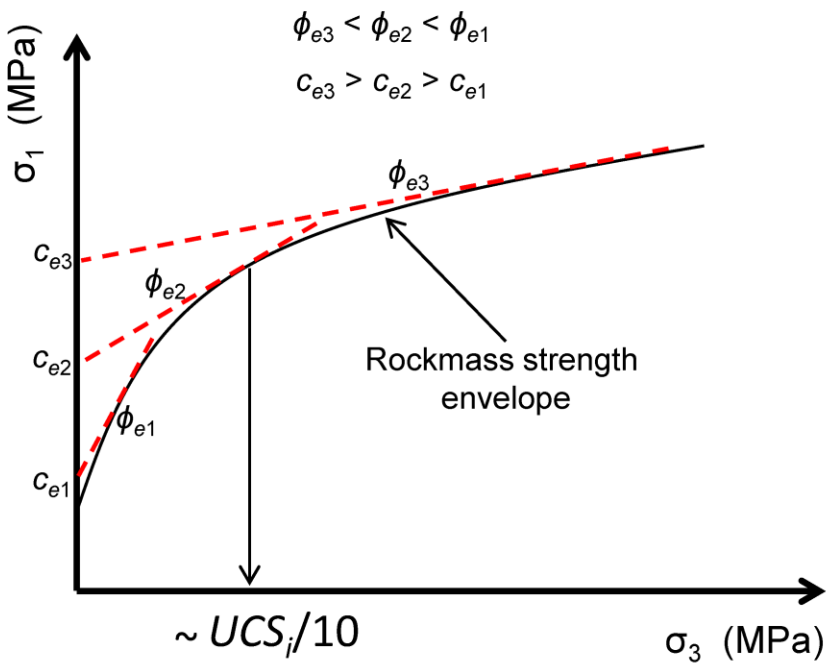

Figure 2-1: Change in the magnitudes of equivalent friction angle and cohesion with increasing confinement.

It is shown in the following sections that at low confinement ($\sigma_3 < \sim UCS_i/10$), the equivalent friction angle of a jointed rockmass consisting of a basic friction angle (ϕ_b) and a dilation angle (i) is higher than that of intact rock. At high confinement ($\sigma_3 > \sim UCS_i/10$), when the dilation is suppressed, the equivalent friction angle of the jointed rockmass is reduced and becomes comparable to that of intact rock.

Models of jointed rockmass by Rosengren and Jaeger (1969)

Rosengren and Jaeger (1969) found that when a specimen of coarse-grained Wombeyan marble is heated up to ~600° C, the anisotropy of thermal expansion of calcite grains causes complete separation of the grains at their boundaries. They mentioned that during heating, the specimen initially emitted a continuous "pinging" sound, which was probably caused by the tensile failure

of the grain boundaries. This was confirmed by microscopic examination of this material, which showed that the grain boundaries were opened (Figure 2-2a). The heat-treated marble had a very low direct tensile strength of 0.03 MPa (compared to 7 MPa before treatment), wherein failure occurred by fracturing along the grain boundaries. This very tightly interlocked material, referred to as "granulated" marble, with randomly oriented grain boundaries was presented by Rosengren and Jaeger (1969) as an analogue for a randomely jointed rockmass, as shown in Figure 2-2a[2].

As illustrated in Figure 2-2b, heating the marble reduced its unconfined compressive strength (UCS_d) to about a quarter of its intact strength (UCS_i). However, a small amount of confinement rapidly increases the confined strength (or equivalent/apparent cohesion) with an initial equivalent friction angle of 65°.

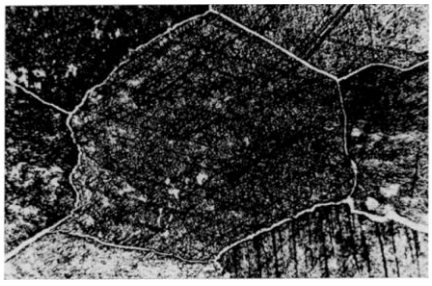

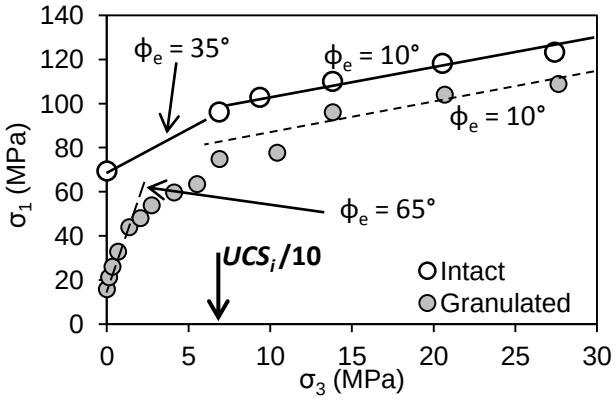

(a) (b)

Figure 2-2: a) Photomicrograph showing details of open grain boundaries in granulated marble (width of picture is 2.4 mm); b) comparison between the strengths of intact and granulated Wombeyan marble tested by Rosengren and Jaeger (1969).

[2] This structure actually resembles a rockmass with non-persistent joint sets as each joint or grain boundary is of limited length. While each grain boundary is open and forms blocks without rock bridges, the joint sets are actually not persistent. As a consequence, this structure either has to be extremely dilatant at low confinement or fail by fracturing through grains. In other words, the granulated rock is an analogue of a non-persistently jointed rockmass but one with highly interlocked blocks with continuous block boundaries.

The equivalent friction angle gradually decreases (and equivalent cohesion increases) with increasing confinement and reaches about 10° for confining pressures greater than 10% of its intact strength ($\sigma_3 > \sim UCS_i/10 = 7$ MPa). Beyond this critical confining pressure, the dilation is inhibited and the confined strength is about 65% of the marble's intact strength[3].

Models of jointed rockmass by Brown (1970)

Brown (1970) conducted triaxial tests on 4 in × 4 in × 8 in gypsum plaster specimens, containing various discontinuity configurations as shown in Figure 2-3. The confining pressure for these experiments was 0, 1.2, 3, 6 and 12 MPa.

The results of triaxial tests are shown in Figure 2-4. As can be seen, the unconfined compressive strengths of jointed specimens are less than those of intact specimens (typically greater than 50% of UCS_i). With increasing confinement, the strengths of jointed specimens increase rapidly (typically at $\phi_e = \phi_b + i = 45°$ to 60°) and approach those of intact specimens (near $\sigma_3 = UCS_i/10$ or 2 MPa). Interestingly, the confined strengths of jointed specimens pass those of intact specimens at confining pressures of 14 MPa in *T60*, *T45* and *H60* specimens and 6.9 MPa in *H45* and *H30* specimens. The rapid increase in the strength of jointed specimens with increasing confinement is due to the very high degree of interlock between these blocks.

[3] At more than about 12 MPa confining pressure this marble exhibits a rapidly flattening failure envelope, which is a characteristic of a collapsing marble structure.

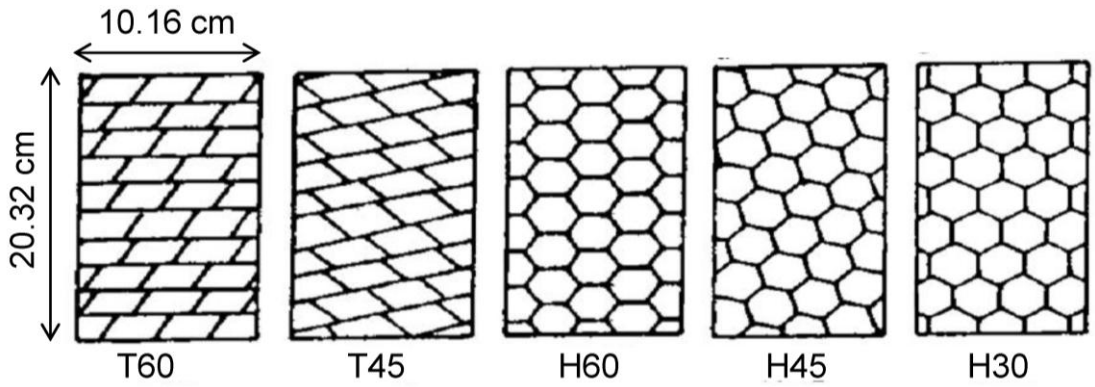

Figure 2-3: Different configurations of jointed gypsum specimens (Brown, 1970).

The reason for the higher strength of jointed specimens compared to that of unjointed (intact) specimens at high confining pressures (i.e., 14 MPa) is unknown, but interpreted here to be due to the higher strength of the individual blocks compared to the strength of unjointed specimens resulting from laboratory testing condition. Since it is unlikely that the strength of a jointed rockmass is higher than the strength of the intact rock, the results of laboratory tests on plaster models conducted by Brown (1970) and Brown and Trollope (1970) (discussed later in this chapter) were excluded from the future analyses presented in this document.

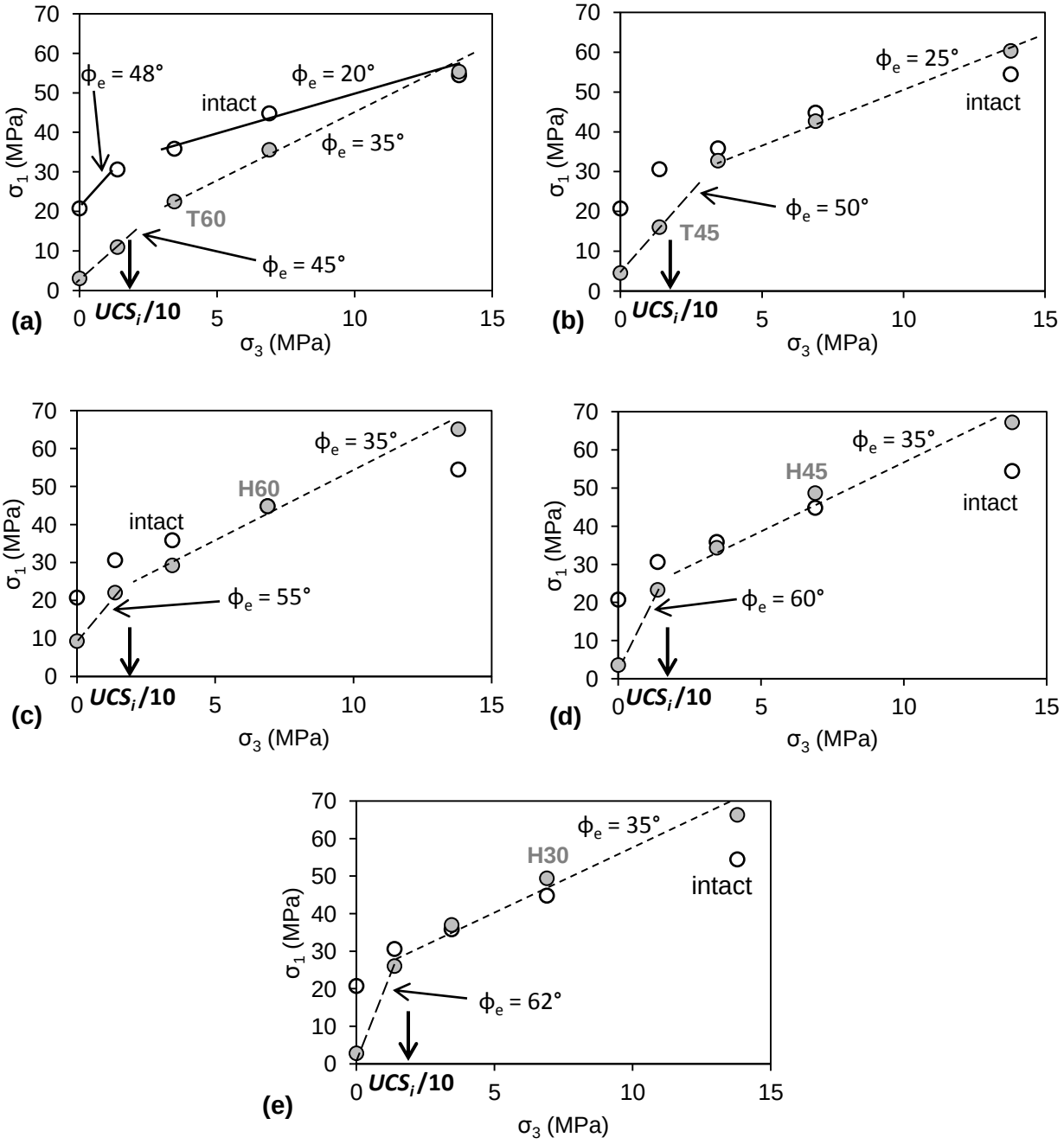

Figure 2-4: Strength of intact and jointed gypsum specimens tested by Brown (1970): a) strengths of unjointed and *T60* jointed specimens; b) strengths of unjointed and *T45* jointed specimens; c) strengths of unjointed and *H60* jointed specimens; d) strengths of unjointed and *H45* jointed specimens; e) strengths of unjointed and *H30* jointed specimens.

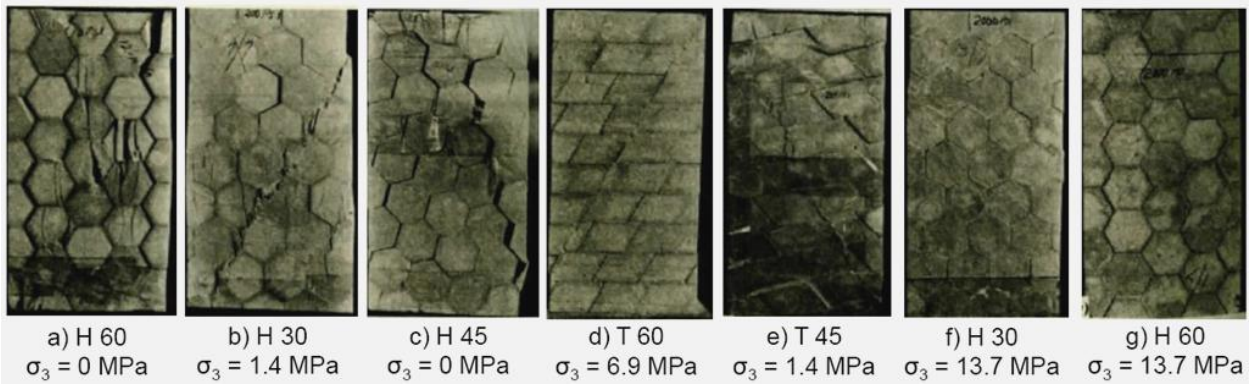

Figure 2-5: Typical modes of failure of physical models of jointed rockmass (after Brown, 1970).

Brown (1970) described the failure mechanisms of these specimens: axial splitting of the plaster in a brittle manner under unconfined condition (Figure 2-5a), shear failure of the plaster along an approximately planar surface independent of joints at intermediate confining pressures (Figure 2-5b), collapse as a result of block movement involving the opening of joints and dilation of the specimen (Figure 2-5c), formation of a single shear plane partly through plaster and partly along joints (Figure 2-5d), formation of complex non-planar shear failure surfaces partly through plaster and partly along joints (Figure 2-5e), formation of conjugate shear planes through the plaster at high confining pressures (Figure 2-5f), and formation of multiple conjugate shear planes partly through plaster and partly along joints at high confining pressures (Figure 2-5g).

Models of jointed rockmass by Brown and Trollope (1970)

Brown and Trollope (1970) reported the results of a series of triaxial compression tests on 4 in × 4 in × 8 in specimens made up of assemblies of 1 inch cubes of gypsum plaster arranged in such a manner that three sets of mutually perpendicular joint planes were formed, as shown in Figure 2-6.

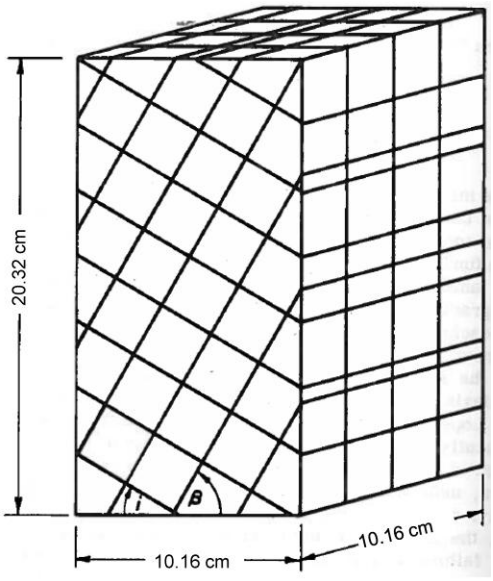

Figure 2-6: Geometry of a physical model of jointed rockmass (Brown and Trollope, 1970).

In preparing the jointed rockmass models, the cubes were arranged so that two joint sets were inclined at angles of 0° and 90°, 15° and 75°, 30° and 60°, as well as at 45° and 45° to the specimen axes, while the third set remained vertical in each case. These specimen types are referred to as the 0/90, 15/75, 30/60 and 45/45. The results of triaxial tests are presented in Figure 2-7. Similar to the results of tests on plaster models reported by Brown (1970), the strength of jointed specimens increases rapidly with increasing confinement and eventually reaches and passes the strength of unjointed specimens at high confining pressure (typically at σ_3 > 12 MPa). For all except for the 30/60 specimen, the initial dilation angle is greater than 20°.

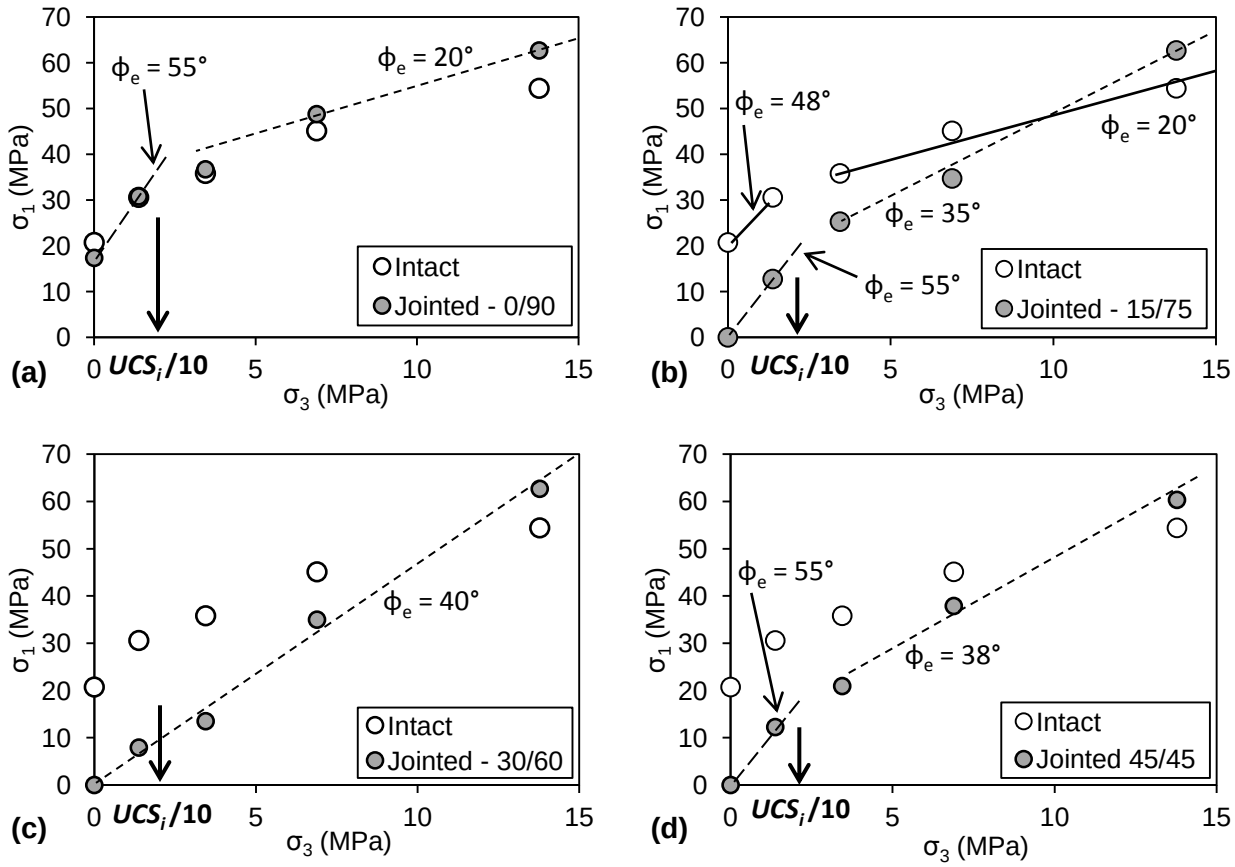

Figure 2-7: Strength of intact and jointed gypsum specimens tested by Brown and Trollope (1970).

Brown and Trollope (1970) mentioned that the majority of the specimens failed by sliding on one or more of the joints at low confinement and by forming one or more shear fracture planes at high confinement. As can be seen in Figure 2-7a, the strength of the 0/90 specimen is very close to that of an unjointed specimen for its entire range of confinement. In the 0/90 specimen, similar to the unjointed specimen, failure occurred by the appearance of vertical fractures (spalling) at low confining pressures and formation of shear planes at high confining pressures (see Figure 2-8).

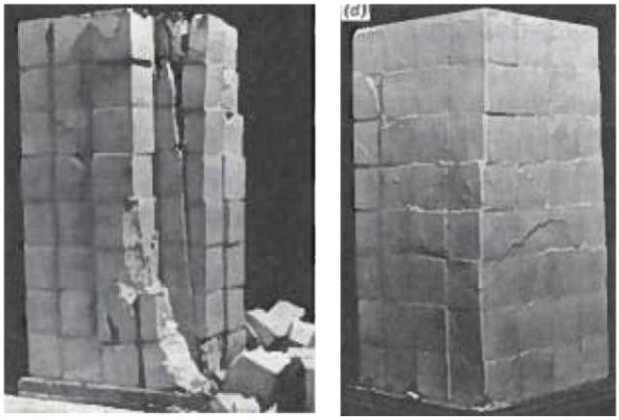

a) 0°/90°
σ_3 = 0 MPa

b) 0°/90°
σ_3 = 6.9 MPa

Figure 2-8: Failure modes 0/90 jointed specimens at 0 MPa and 6.9 MPa confining pressures (after Brown and Trollope (1970).

In other specimens, slip along joints was the main mode of failure under unconfined condition and it is for this reason that the *UCS* values are nearly zero. In the 45/45 and 15/75 specimens, the strength rapidly increases at low confinement ($\sigma_3 < \sim UCS_i/10$) with an equivalent friction angle of about 55°. The failure mode at low confinement involved a combination of sliding along joints and fracturing of individual blocks. At high confinement ($\sigma_3 > \sim UCS_i/10$), when the dilation is suppressed, these specimens failed by fracturing through the blocks which resulted in the generation of single or multiple shear planes. The 30/60 specimens failed by sliding along joints at all confining pressures and it is for this reason that the failure envelope is relatively linear.

Models of jointed rockmass by Ladanyi and Archambault (1972)

Ladanyi and Archambault (1972) constructed physical models of jointed rockmass from rods with a square cross-section of 12.7 mm and a length of 63.5 mm that had been sawn from commercial compressed concrete bricks.

Figure 2-9 shows the configurations of one of the 'brickwall' models. As can be seen, the model consists of two joint sets; a primary joint set inclined at an angle of β to the major principal stress direction and a cross joint set inclined at an angle of α to the major principal stress direction. Ladanyi and Archambault (1972) conducted a series of triaxial tests on the brickwall models with varying joint orientations and the results are summarized in Figure 2-10.

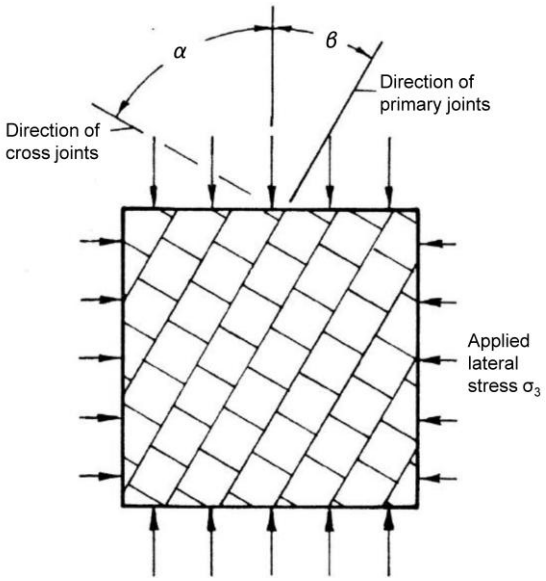

Figure 2-9: Configuration of the brickwall model tested by Ladanyi and Archambault (1972).

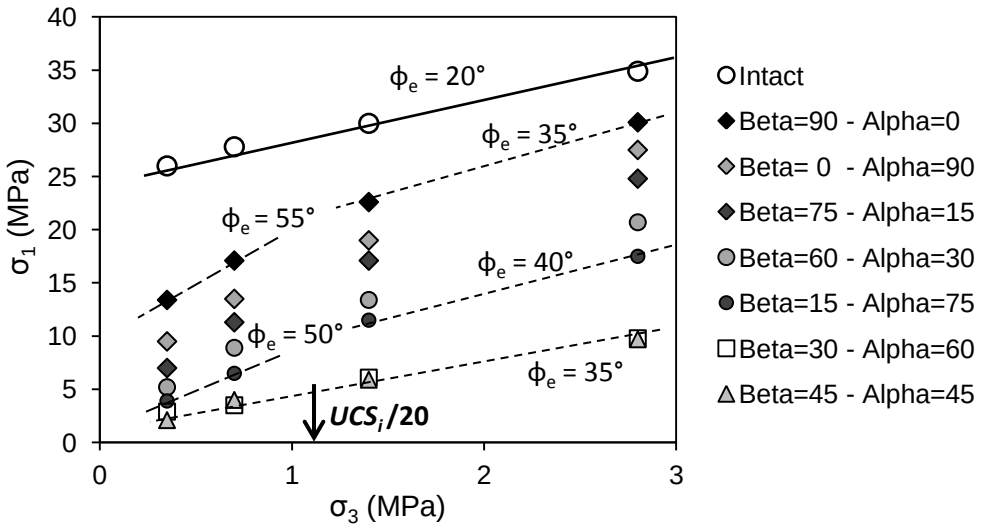

Figure 2-10: Strength of brickwall models tested by Ladanyi and Archambault (1972).

Figure 2-10 shows that the jointed specimens, with the primary joint sets being perpendicular and parallel to the major principal stress, present the highest strengths. In these specimens, the strength rapidly increases with increasing confinement with an equivalent friction angle of $\phi_e = 55°$ for $\sigma_3 < \sim UCS_i/20$. Beyond this confining pressure ($\sigma_3 > \sim UCS_i/20$), the equivalent friction angle decreases to about 35°. This behavior can also be seen in other specimens, but with lower apparent cohesion, except for those where the primary joint set is at 30° and 45° to the major principal stress direction. Such two specimens represent pure frictional behavior (i.e. linear failure envelope) with no or very small initial dilation and a cohesive strength of nearly zero, which suggests that the failure of these two specimens involved sliding along the joints.

As discussed by Hoek (1983), the degree of interlock between the model blocks is highly relevant for the behavior of the brickwall model since it controls the freedom the blocks to slide and rotate. Figure 2-11 shows photographs of different failure modes including shear plane failure in the model with horizontal primary joints (Figure 2-11a), shear failure of the blocks in the model with the primary joints inclined at > 45° to the major principal stress direction (Figure 2-11b), and kink-band failure resulting from block sliding along boundaries and block rotation in the model with the primary joint at < 45° to the major principal stress direction (Figure 2-11c).

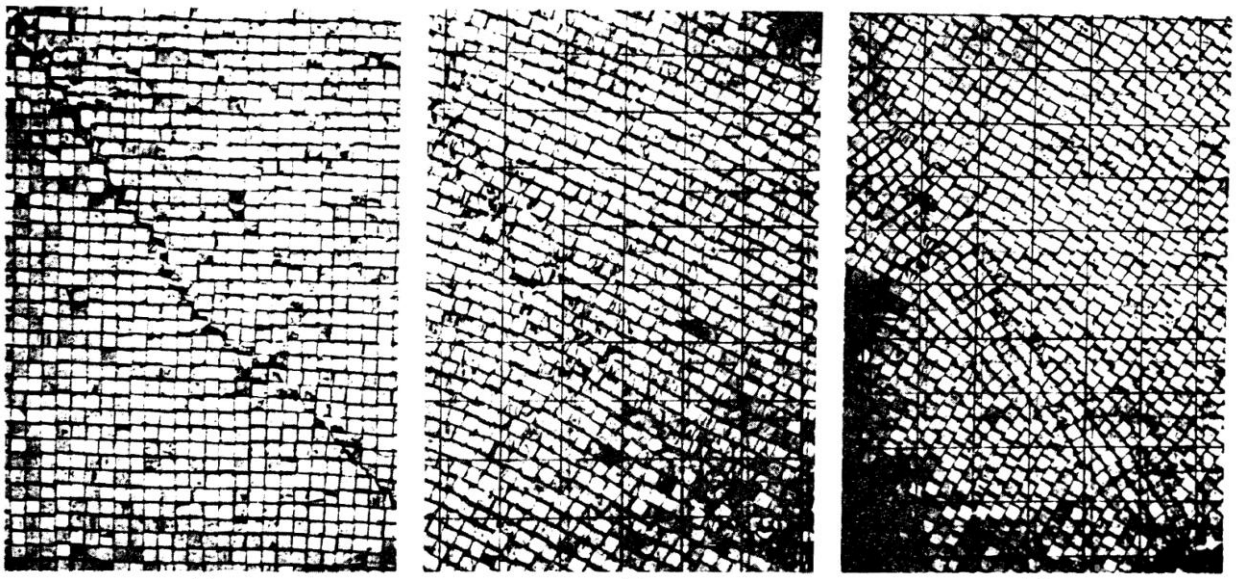

Figure 2-11: Failure modes of brickwall models tested by Ladanyi and Archambault (1972).

Models of jointed rockmass by Einstein and Hirschfield (1973)

Einstein and Hirschfeld (1973) reported the results of experiments on jointed gypsum specimens. They investigated the influence of joint orientation, joint spacing and number of joint sets on the strength of jointed rockmasses. The specimens failed in uniaxial compression tests by axial splitting of intact material. At low values of confining pressure, the shear failure along joints or failure of intact material was observed. At high confining pressures, the failure was due to the formation of many almost parallel shear planes, mainly within the intact material. At low confining pressures ($\sigma_3 < \sim UCS_i/10$), the behavior of specimens was brittle and at high confining pressure it was ductile. Einstein and Hirschfeld (1973) observed that the strength of the specimens depended on the joint dip angle except at high confining pressures, wherein the strength of the specimens was nearly equal to that of the intact material.

The results of tests on specimens with two orthogonal sets of joints parallel and perpendicular to the maximum principal stress direction (Figure 2-12a) are presented in Figure 2-12b. Similar to the investigation by Brown (1970) and Brown and Trollope (1970), the strengths of jointed specimens are less than that of the intact specimens at zero confining pressure. At low confinement ($\sigma_3 < \sim UCS_i/10$), the strength envelopes of specimens with the joint spacings of 1 cm and 0.5 cm represent equivalent friction angles of 50° and 42°. At high confinement ($\sigma_3 > \sim UCS_i/10$), the equivalent friction angles of the jointed specimens with the joint spacings of 1 cm and 0.5 cm reduce to about 25° and 20°, respectively. As opposed to the results of tests by Brown (1970) and Brown and Trollope (1970), the strength of jointed specimens never exceeds those of intact specimens.

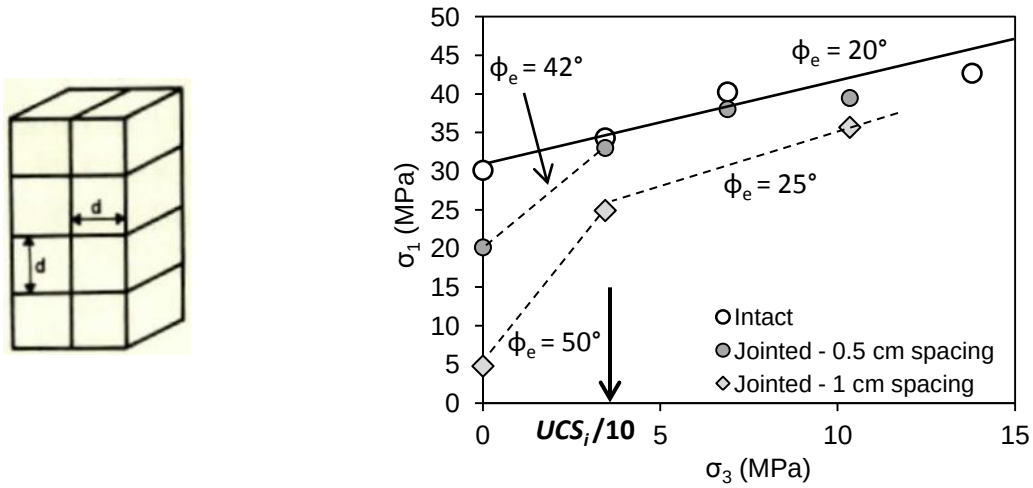

Figure 2-12: a) Configuration of the jointed plaster specimens tested by Einstein and Hirschfeld (1973); and b) strength envelopes of intact and jointed gypsum specimens.

Models of jointed rockmass by Gerrogiannopoulos (1976) and Gerrogiannopoulos and Brown (1978)

In an attempt to investigate the behavior of jointed rockmasses, Gerogiannopoulos (1976) and Gerrogiannopoulos and Brown (1978) conducted a series of laboratory triaixial tests on intact and granulated coarse-grained Wombeyan marble and fine-grained Carrara marble, similar to those of Rosengren and Jaeger (1969). They also observed a rapid increase in the strength of granulated marble with increasing confinement as shown in Figure 2-13a and b. This rapid increase in the strength at low confinement is due to the high degree of interlock between the independent grains, which leads to a high dilation angle equal to or greater than 25° for $\sigma_3 < \sim UCS_i/10$. Beyond this confining pressure ($\sigma_3 > \sim UCS_i/10$), the equivalent friction angle of the granulated marble becomes comparable to that of intact marble in both cases.

Note that the results of experiments on intact and granulated Wombeyan marble presented in Figure 2-13a are used as the basis for model calibration and the simulation of intact, micro-defected, and defected rock specimens and jointed rockmasses throughout this thesis.

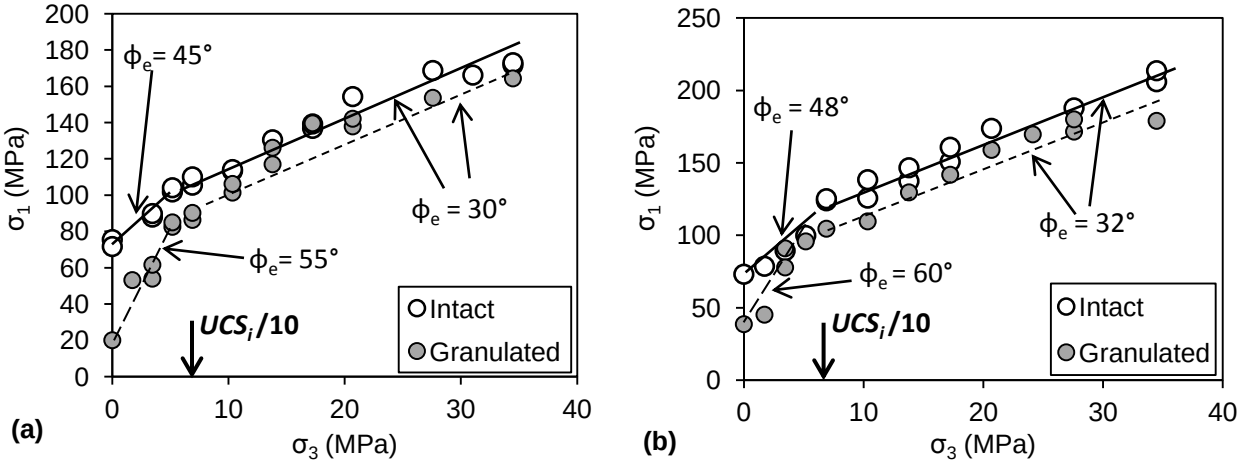

Figure 2-13: Strength of intact and granulated: a) Wombeyan marble; b) Carrara marble, tested by Gerogiannopoulos (1976).

Models of jointed rockmass by Ribacchi (2000)

Ribacchi (2000) conducted a series of triaxial tests on 84 mm × 168 mm laboratory specimens of fine-grained limestone specimens made up of various degrees of fracturing due to intense shear tectonic deformation. The purpose of these experiments were to investigate the influence of fracture intensity and confinement on the strength and elastic modulus of fractured rock, which can be considered as a small scale model of a jointed rockmass. The specimens tested were classified into the four following groups:

- *IN*: seemingly intact specimens;
- *IF*: specimens with rare and mostly healed fractures;
- *FR*: specimens with diffused fracturing; and
- *SH*: specimens having multiple shear surfaces.

The results of triaxial tests are presented in Figure 2-14 (a-c). The scatter in the strength values is due to the qualitative and subjective classification of rock specimens. Ribacchi (2000) mentioned that some pre-existing weakness planes could be seen after failure of the intact specimens. As can be seen in Figure 2-14, the strength variations between different groups were found to be in agreement with the qualitative classification. Indeed, the unconfined and confined strengths and the equivalent friction angle of fractured specimens were discovered to decrease with increasing fracture intensity from *IF* to *SH* specimens. Unfortunately, no information on the mechanical properties of the defects or the failure modes of different classes of defected rock is available.

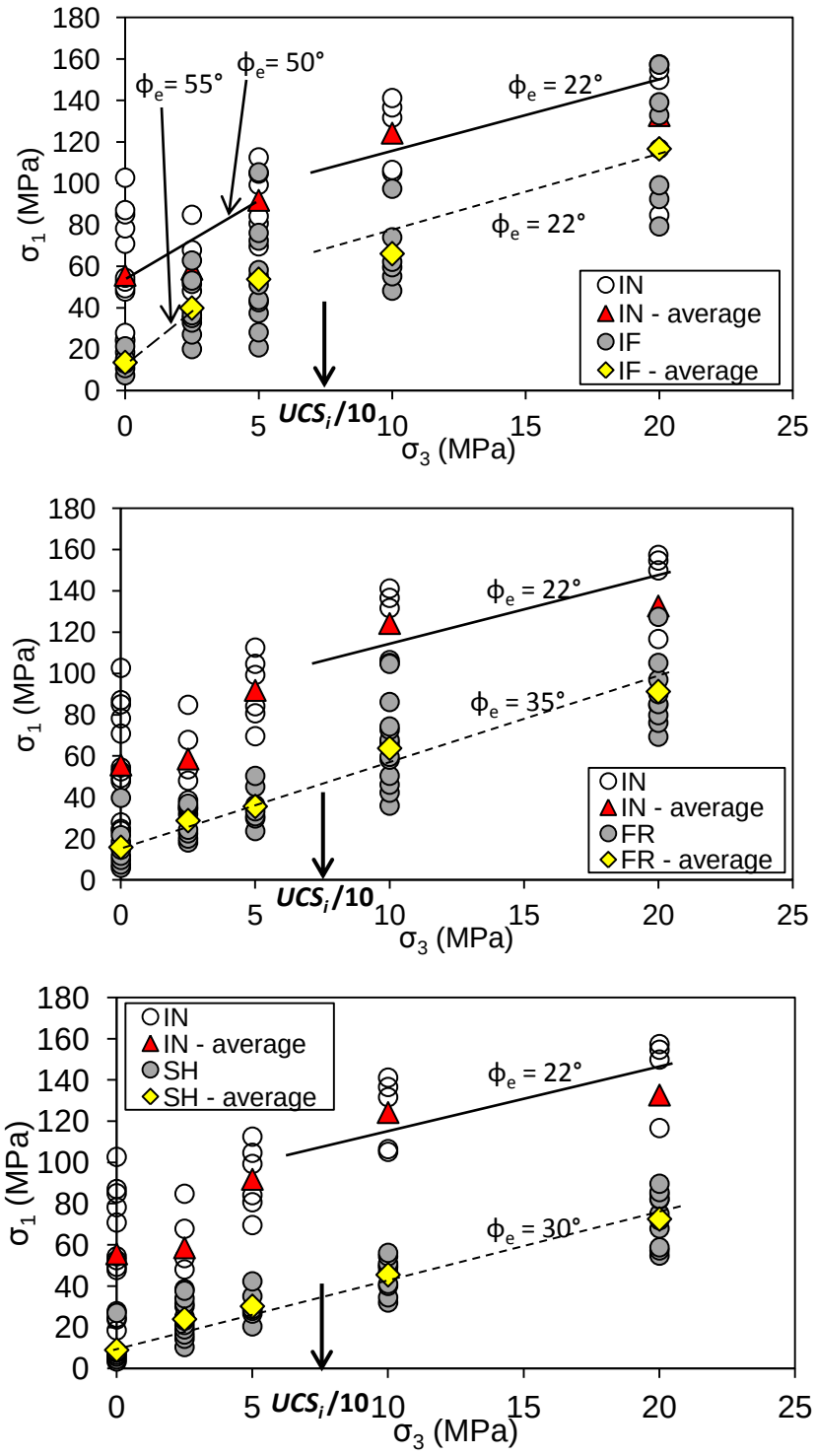

Figure 2-14: Strengths of intact and defected limestone tested by Ribacchi, (2000): a) intact (*IN*) versus *IF* specimens; b) intact (*IN*) versus *FR* specimens; c) intact (*IN*) versus *SH* specimens. Red triangles refer to the average strength of *IN* specimens, and yellow diamonds refer to the average strengths of *IF*, *FR* and *SH* specimens.

It is shown in Figure 2-14a that the equivalent friction angle of *IN* specimens at high confinement ($\sigma_3 > \sim UCS_i/10$) is about 22°. At low confinement ($\sigma_3 < \sim UCS_i/10$), the strength of *IF* specimens increases with an equivalent friction angle of 50°, indicating that the dilation angle at this confinement is about 28°. Beyond this confinement, the equivalent friction angle becomes comparable to that of *IN* specimens, suggesting that at high confinement, the failure occurs through the intact part of the *IF* specimens. The strength envelopes of *FR* and *SH* specimens represent frictional behavior (i.e., linear failure envelope with no or very small initial dilation and cohesive strength), as shown in Figure 2-14a and b. This suggests that the main failure mode of *FR* and *SH* specimens were shearing along defects.

Models of defected rock by Yang et al. (2008)

Yang et al. (2008) investigated the mechanical properties of marble specimens containing two filled machined slots. The marble specimens were classified into two groups: fine-grained marble with an average grain size of 1.5 mm and coarse-grained marble with an average grain size of 5.0 mm. A high-speed electric cutting machine was used to cut planar flaws in the intact marble with different angles relative to the specimen axis. The slot thickness was about 0.3 to 0.5 mm. The slots were then filled with gypsum to form closed flaws (i.e., cohesive defects). The specimens were divided into four types depending on their slot orientation: Type A is intact with no slots while Types B, C and D are slotted with angles of 30°, 45° and 60° to the specimen axis, respectively (Figure 2-15a). Figure 2-15b shows the failure modes of all the four types under unconfined condition.

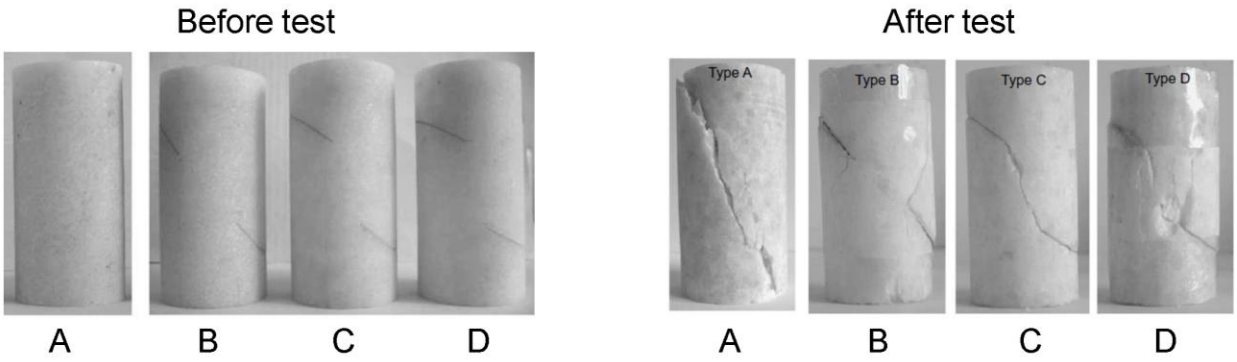

Figure 2-15: Geometry and failure modes of intact and slotted marble specimens under unconfined condition (Yang et al., 2008).

Under unconfined condition, the slots were directly involved in the failure of the specimens and caused the specimens to fail at a lower strength. As can be seen in Figure 2-15, the fractures nucleated from the tips of these slots and propagated to the boundaries of the specimens (e.g., Type B) or towards the tips of the other slot (e.g., Type C and Type D). Yang et al. (2008) indicated that both the intact and slotted specimens failed by shearing through the intact part of the specimens at high confinement.

Figure 2-16a and b show that at low confinement ($\sigma_3 < \sim UCS_i/7$ in coarse grained marble, and $\sigma_3 < \sim UCS_i/10$ in fine grained marble), the equivalent friction angles of the coarse- and fine-grained slotted specimens are about 45° and 50°, respectively. At high confinement ($\sigma_3 > \sim UCS_i/7$ in coarse-grained marble, and $\sigma_3 > \sim UCS_i/10$ in fine-grained marble), the dilation is suppressed and the equivalent friction angles become similar to those of intact marble.

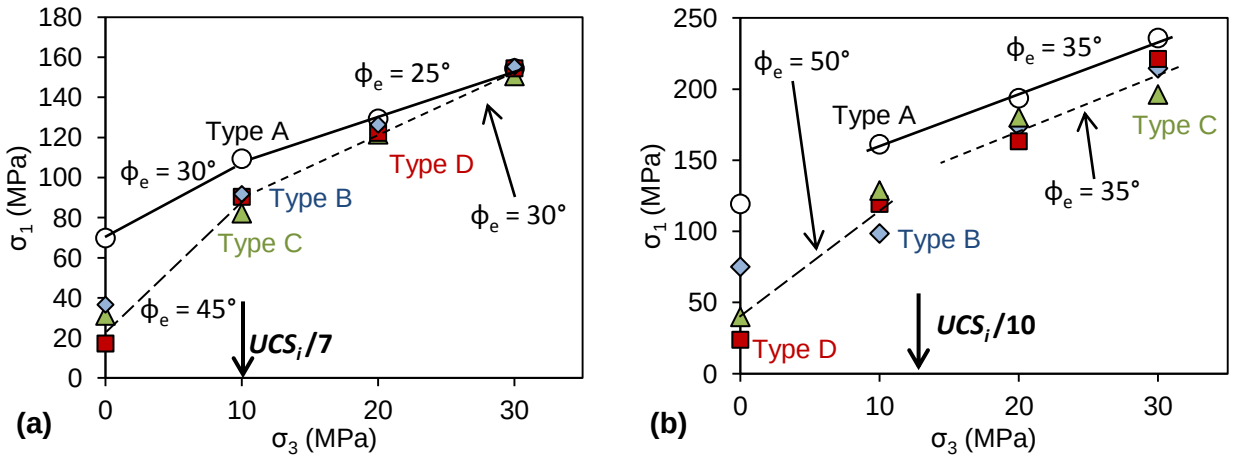

Figure 2-16: Strengths of intact and slotted specimens of: a) coarse-grained marble; and b) fine-grained marble, tested by Yang et al. (2008). Circles refer to intact marble, and diamonds, triangles, and squares refer to Type B, C and D slotted marble, respectively.

Models of fractured rock by Yang et al. (2011)

Yang et al. (2011) conducted a series of triaxial compression tests on coarse-grained marble under different loading and unloading stress paths to investigate the influence of confinement on the strength of intact and fractured (damaged) specimens. In these experiments, the specimens were loaded axially and laterally, unloaded axially or laterally to generate damage (unloading-induced fractures) and then reloaded axially under different values of confining pressure until failure.

Figure 2-17a and b compare the failure modes of intact and damaged specimens. The failed damaged specimen consists of two parallel shear fractures; one generated during the first loading-unloading cycle and the other one generated when reloading the damaged specimen. The failed intact specimen, however, contained only one shear fracture.

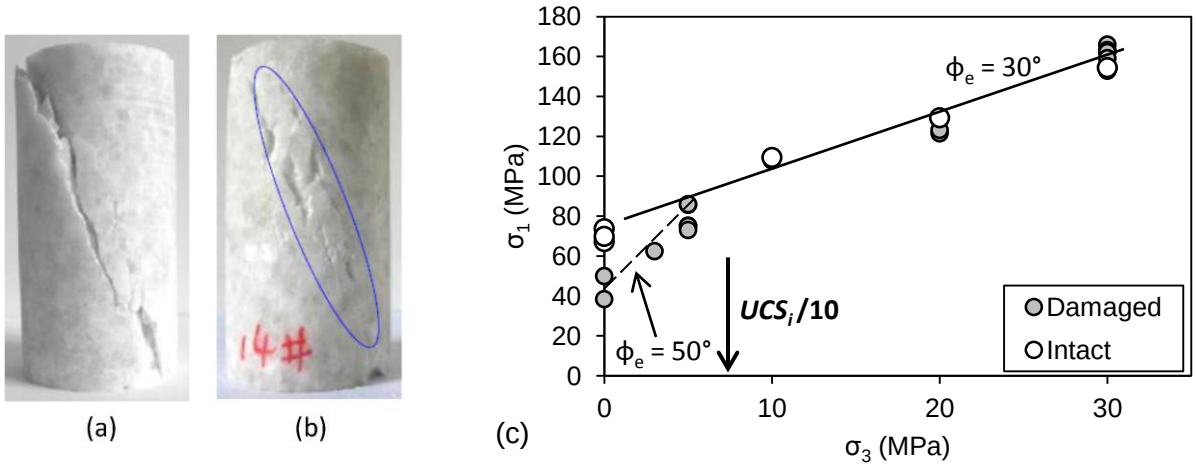

Figure 2-17: Comparison between failure modes of: a) intact and b) damaged marble specimens. c) Strengths of intact and damaged specimens tested by Yang et al., (2011).

Figure 2-17c compares the unconfined and confined strengths of intact and damaged specimens, and indicates that the results are similar to those of most experiments reviewed in this chapter. This means that, once more, the unconfined strength of damaged specimen is less than that of intact specimen, the strength of damaged specimens rapidly increases with increasing confinement (with an equivalent friction angle of about 50°, which is greater than that of intact specimens) and approaches the intact strength at a confining pressure of about 10% of the intact UCS_i. The dilation is inhibited beyond this critical confining pressure ($\sigma_3 > \sim UCS_i/10$) and the equivalent friction angle of the damaged marble decreases to that of intact marble (about 30°), whicle its equivalent cohesion increases and approaches but never reaches that of intact marble.

Models of jointed rockmass by Arzua et al. (2014)

More recently, Arzua et al. (2014) investigated the complete stress-strain response, strength, deformability and dilation of artificially jointed granitic rock specimens with two joint sets. They prepared jointed specimens in order to simulate rockmass behavior at the laboratory scale. All

cores tested contained the same three joints belonging to two joint sets: one sub-vertical and two sub-horizontal joints as shown in Figure 2-18a. The jointed specimens were created by cutting the specimens and using adhesive tape to rejoin the pieces of the cores. The cut surfaces were planar and smooth with a friction angle of about 26° (Alejano et al., 2012). The mean dip angles of the joint sets were measured as 23.5 ± 0.8° for the sub-horizontal joints, and 85 ± 2° for the sub-vertical joints.

Arzua et al. (2014) conducted a total of 28 confined compression tests on intact cores and 22 confined compression tests on jointed cores. Triaxial testing was set up for confining pressures in the range of 0.5 to 12 MPa. The test results in Figure 2-18b demonstrate how the strength reduces from the intact specimens to that of jointed specimens. The equivalent friction angle at low confinement ($\sigma_3 < \sim UCS_i/15$) is about 65° which is higher than that of the intact specimens. Note that the maximum confining pressure applied to both intact and jointed specimens is about $UCS_i/10$. Therefore, it was not possible to assess the strength, strength degradation or the change in the equivalent friction angle and cohesion of the jointed specimens at high confining pressures (i.e., $\sigma_3 > \sim UCS_i/15$).

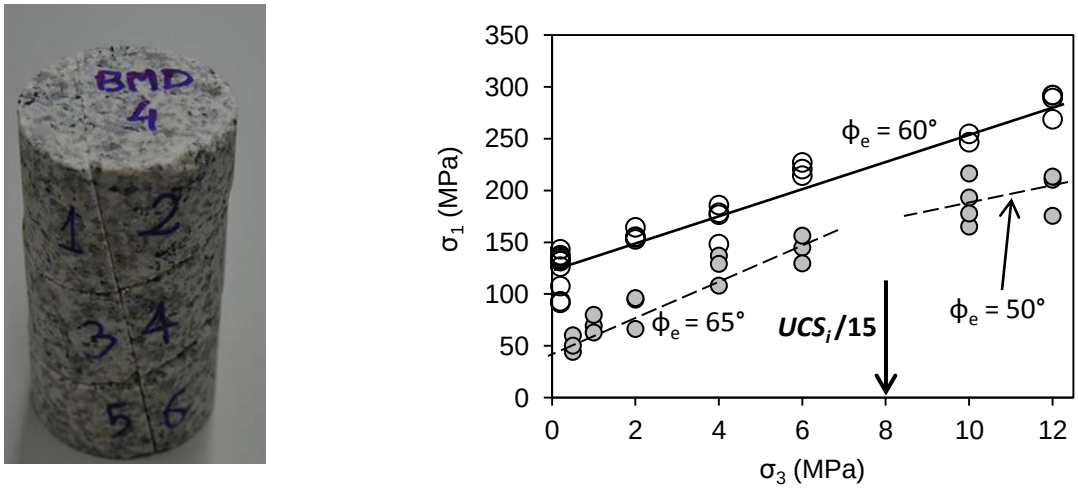

(a) (b)

Figure 2-18: a) Artificially jointed granitic specimen; b) results of triaxial tests on intact and jointed specimens (Azrua et al., 2014).

Damaged Lac de Bonnet (LdB) granite as a model of jointed rockmass

Evidence of core damage has been documented at the Underground Research Laboratory (*URL*) in Manitoba (Canada) by Martin and Stimpson (1994) and Eberhardt et al. (1999). They suggested that the observed difference between the laboratory properties of specimens is due to the increase in the amount of stress-induced damage in the specimens taken from increasing depth (i.e. in-situ stress level). The disturbed specimens can be identified from the change in the material's response when subjected to uniaxial compression; undamaged specimens respond in a linear elastic manner whereas damaged specimens initially exhibit a strongly non-linear response due to their micro-crack closures.

These observations were consistent with the results of Scanning Electron Microscope (*SEM*) analyses by Eberhardt et al. (1999), who noted that visible cracks were difficult to find in the thin sections of the specimens from the 130- and 240-levels, whereas numerous cracks were visible in

the 420-level specimens. Figure 2-19a shows how the drilling-induced fractures end within the intact part of the core to generate rock bridges. Therefore, it is possible to consider the damaged specimens as analogues for non-persistently jointed rockmasses.

Figure 2-19b shows the results of triaxial tests on undamaged and damaged specimens and reveals that the strength of damaged specimens increases up to a confining pressure of about $UCS_i/20$ = 10 MPa with a higher equivalent friction angle of 63° compared to that of intact specimens. Beyond the confining pressure of about 10 MPa, the strength of damaged specimens increases with an equivalent friction angle of 50°, which is similar to that of undamaged specimens.

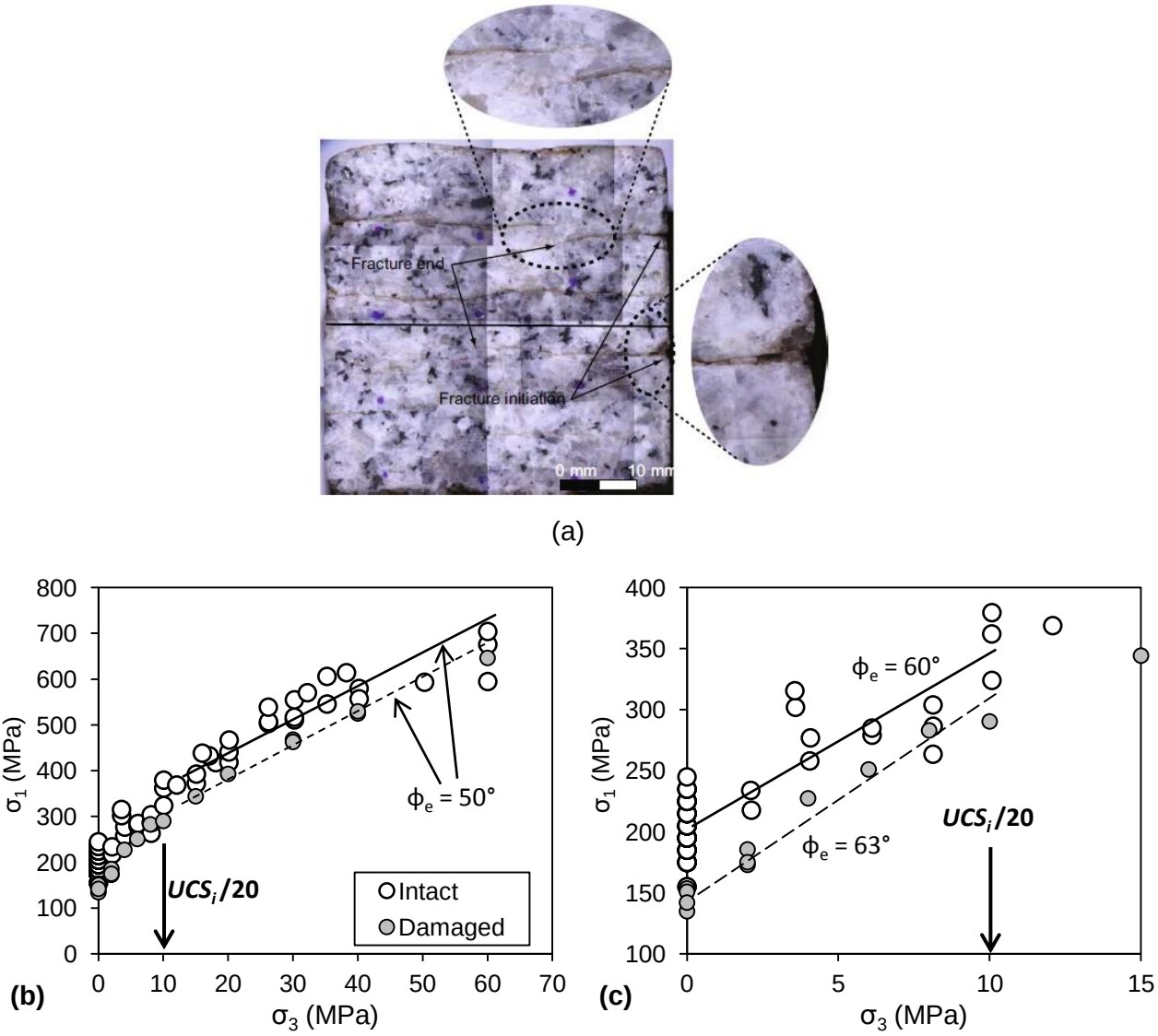

Figure 2-19: a) Example of a damaged *LdB* granite specimen (Lim and Martin, 2010); b) strength envelopes of intact and damaged specimens of *LdB* granite for the entire range of confinement; c) strength envelopes of intact and damaged specimens of *LdB* granite up to the confining pressure of 15 MPa.

Summary of rockmass strength from physical model tests

After analyzing the results of laboratory tests on damaged and defected rocks and physical models of jointed rockmasses, the following can be concluded:

- the strengths of damaged, defected or jointed specimens can be as low as 10% of their intact strengths under unconfined condition;
- at low confinement ($\sigma_3 < \sim UCS_i/10$), the strengths of damaged, defected or jointed specimens increase more rapidly as confinement increases than they do when compared to their intact strength;
- the initial equivalent friction angle of the strength envelope of damaged, defected or jointed specimens (when $\sigma_3 < \sim UCS_i/10$) is higher than that of their intact specimens;
- therefore, at low confinement ($\sigma_3 < \sim UCS_i/10$) the strength degradation decreases rapidly with increasing confinement;
- at high confinement ($\sigma_3 > \sim UCS_i/10$), when the dilation is suppressed, the strengths of damaged or jointed specimens approach their intact strengths;
- the equivalent friction angle of the strength envelope of damaged, defected or jointed specimens at high confinements is close to that of their intact specimens; and
- therefore, at high confinement ($\sigma_3 > \sim UCS_i/10$), the strength degradation remains relatively constant (typically less than 20% of intact strength).

2.3 Methods of Strength Estimation of Jointed Rockmasses

2.3.1 Empirical methods

Empirical rockmass classification and characterization systems are used at different stages of civil and mining projects to provide information on the composition and characteristics of a jointed rockmass. These systems provide initial estimates of support requirements for excavations (classification systems) and estimates of the anticipated strength and deformation properties of the rockmass (characterization systems). Such empirical information is particularly important during the early stages of a project, when direct access to the rockmass and observations of rockmass behaviour are not possible.

Rockmass classification and characterization systems should be used within the bounds of applicability that are largely dependent on the case histories from which they were developed. These bounds include not only the rockmass characteristics but also the prevailing *in situ* stress and mining-induced stress change conditions. Users of rockmass classification and characterization systems must be cautious when collecting appropriate parameters and in applying resulting rockmass classes and properties to rock engineering problems. Therefore, it is of importance to understand the origin and underlying assumptions behind the commonly used classification and characterization systems before applying them.

In the application of all rockmass classification and characterization systems, the first step is to divide the rockmass into a number of structural domains (regions with consistent characteristics) in such a way that certain features are more or less uniform within each domain. Major geological features such as faults, dykes and shear zones are characterized separately. Changes in rock type and significant changes in discontinuity spacing or characteristics within the same rock type are also used to define the domain boundaries. The most widely used methods for estimating the rockmass strength are the rockmass classification systems *RQD*, *Q*, *RMR* and *MRMR* as well as the rockmass characterization system *GSI*, which will be briefly reviewed in the following pages.

2.3.1.1 Rockmass classification and characterization systems

Rock Quality Designation Index (RQD)

The Rock Quality Designation index (*RQD*) was developed by Deere (1964) to provide a quantitative estimate of rockmass quality from drill core logs. *RQD* is defined as the percentage of intact core pieces longer than 100 mm (4 inches) in the total length of the core. Palmström

(1982) suggested that when no core is available but discontinuity traces are visible in surface exposures or exploration adits, the *RQD* may be estimated from the number of discontinuities per unit volume. The suggested relationship for clay-free rockmasses is:

$$RQD = 115 - 3.3J_v \qquad \text{Equation 2-2}$$

wherein the volumetric joint count J_v, is the sum of the number of joints per unit length for all joint sets. The value of *RQD* may change significantly depending on the orientation of the borehole relative to the dominant joint sets. Thus, the use of the volumetric joint count can be quite useful in reducing this directional dependence.

Rock Mass Rating (RMR)

Bieniawski (1973) proposed an engineering classification for jointed rockmasses called the Geomechanics Classification system, which was intended for the selection of primary support in tunnel design. This classification system was based on a detailed study of existing major rock classification systems for tunnel design including those by Terzaghi (1946), Lauffer (1958) and Deere (1964) as well as Bieniawski's personal experience gained from numerous visits to construction sites in South Africa and elsewhere. The Geomechanics Classification introduced by Bieniawski (1973) formed the basis of the well-known *RMR* classification system (Bieniawski, 1976). The underlying data came from a number of mining and mostly civil engineering case histories. *RMR* was developed for the design of support in tunnels and for the assessment of unsupported span and stand-up time. Bieniawski (1976; 1979; 1988) demonstrated applications of the *RMR* system to civil engineering projects such as tunnels, caverns, slopes, and

foundations as well as to haulages and chambers in mining (e.g., roof stability assessment in a number of coal mines).

Even though some guidance on rockmass strength is given[4] (i.e., ranges for cohesion and friction angles of rockmasses of various classes) by Bieniawski (1976), the common applications of the *RMR* system is support design for tunnels. Bieniawski (1989) published a set of guidelines for support of horseshoe-shaped tunnels with a span of up to 15 m constructed using the drill and blast method in a rockmass subjected to a vertical stress of less than 25 MPa (equivalent to a depth below surface of less than 1000 m). Six cumulative parameter ratings are used to obtain the *RMR:* i.e. ratings of the uniaxial compressive strength of intact rock (UCS_i), *RQD*, spacing of discontinuities, condition of discontinuities, groundwater conditions and orientation of discontinuities relative to the tunnel alignment. As the *RMR* does not include stress as a rockmass characterization parameter, the impact of stress on rockmass behavior has to be assessed separately when extrapolated to high stress conditions.

Modified Rock Mass Rating (MRMR)

Laubscher (1975) introduced *MRMR* to adjust the *in situ* rockmass ratings (*RMR*) to fit the mining environment so that the *MRMR* ratings can be used for mine design. In this regard, the ratings for *RMR* are adjusted to account for weathering (30 to 100%), mining-induced stresses (60 to 120%), joint orientation (63 to 100%) and blasting effects (80 to 100%). Practical applications of the *MRMR* system as summarized by Laubscher (1990; 1993) include support

[4] The proposed relationship of *RMR* to strength was derived from a limited number of rock types and thus is not generally applicable.

design, determination of cavability (cavability diagrams), stability of open stopes, pillar design, extent of caves and failure zones, caving fragmentation, mining sequence, potential for massive wedge failure and design of pit slopes.

Laubscher (1990) and Laubscher and Jakubec (2000) described a procedure to determine the intact rock strength (*IRS*) from the *UCS* values of the weak and strong rock components that make up the *UCS* range on the basis that the weaker rock will have greater influence on the average value. The values of weak and strong rock *UCS* as well as the percentage of weak rocks present are used with the aid of an empirical chart to obtain the "corrected" value for the average intact rock strength. This corrected strength is then used to determine the rock block strength by considering some adjustment factors to account for the scale effect and the influence of defects (hardness and their frequencies) on rock block strength. Using the *MRMR* system, it is then possible to obtain an estimate of the rockmass strength. Following this, the *in situ* rockmass strength is adjusted to offer a design rockmass strength following the procedure described by Laubscher and Jakubec (2000).

Tunneling Quality Index (Q)

Barton et al. (1974) proposed the Tunneling Quality Index (*Q*) for the determination of rockmass characteristics and tunnel support design. The six parameters in the *Q* system are: *RQD*, the joint set number (J_n), the joint roughness number (J_r), the joint alteration number (J_a), the joint water reduction factor (J_w) and the stress reduction factor (*SRF*). The numerical value of the index *Q* varies on a logarithmic scale from 0.001 to a maximum of 1000. While the *Q* system considers stress via the *SRF*, it is not suitable for situations where mining-induced stress changes alter the

rockmass behaviour. In mining, Q is often used without J_w and SRF in the form of Q' to provide an indication of the rockmass before it is affected by the stress of water.

The Q system was originally based on an evaluation of over 200 case records obtained from visiting and mapping a wide variety of civil engineering tunnel conditions in igneous, metamorphic and sedimentary rocks (Barton et al., 1974). Many of the case records involved clay mineral joint fillings of various kinds, including swelling clay occurrences. However, most commonly joints were unfilled and the joint walls were unaltered or only slightly altered. Grimstad et al. (1986) and Grimstad and Barton (1993) added over 1000 case records from road tunnels in Norway and updated the support design chart. This chart provides a relationship between different Q-values, excavation equivalent dimensions and different types of permanent support. The most recent version of the Q system and the accompanying support design charts were published by NGI (2013).

Geological Strength Index (GSI)

The *GSI* system, introduced by Hoek (1994) and Hoek et al. (1995), provides a means for characterizing a jointed rockmass. The main purpose of the *GSI* system is to serve as an index for estimating the rockmass strength by degrading the intact rock strength, described by the *HB* failure criterion, for different geological conditions. According to the *GSI* system, the peak strength of a jointed rockmass is a function of the strength of intact rock blocks and the freedom of these blocks to slide and rotate under different stress conditions.

This freedom (or degree of interlocking) in the rockmass depends on two primary characteristics: the geometrical shape and size of the intact rock blocks (V_b) and the joint surface condition (J_c)

(Hoek et al., 1995; Cai et al., 2004). This classification system is presented in Figure 2-20a. In an effort to overcome some of the subjectivity found in the use of the *GSI* chart while maintaining its overall simplicity. Cai et al. (2004) presented a quantitative approach wherein the degree of interlock is supplemented with the joint spacing and the quantitative block volume and the descriptive joint condition is supplemented with the quantitative joint condition factor, as shown in Figure 2-20b.

Cai et al. (2007) also conducted back-analyses of a small number of large excavations and developed a means for estimating the residual strength of the rockmass based on *GSI*. However, because of their limited verification efforts and the multitude of possible post-peak stress-stain behaviours, their proposed relationship between peak and residual strengths demands further investigation.

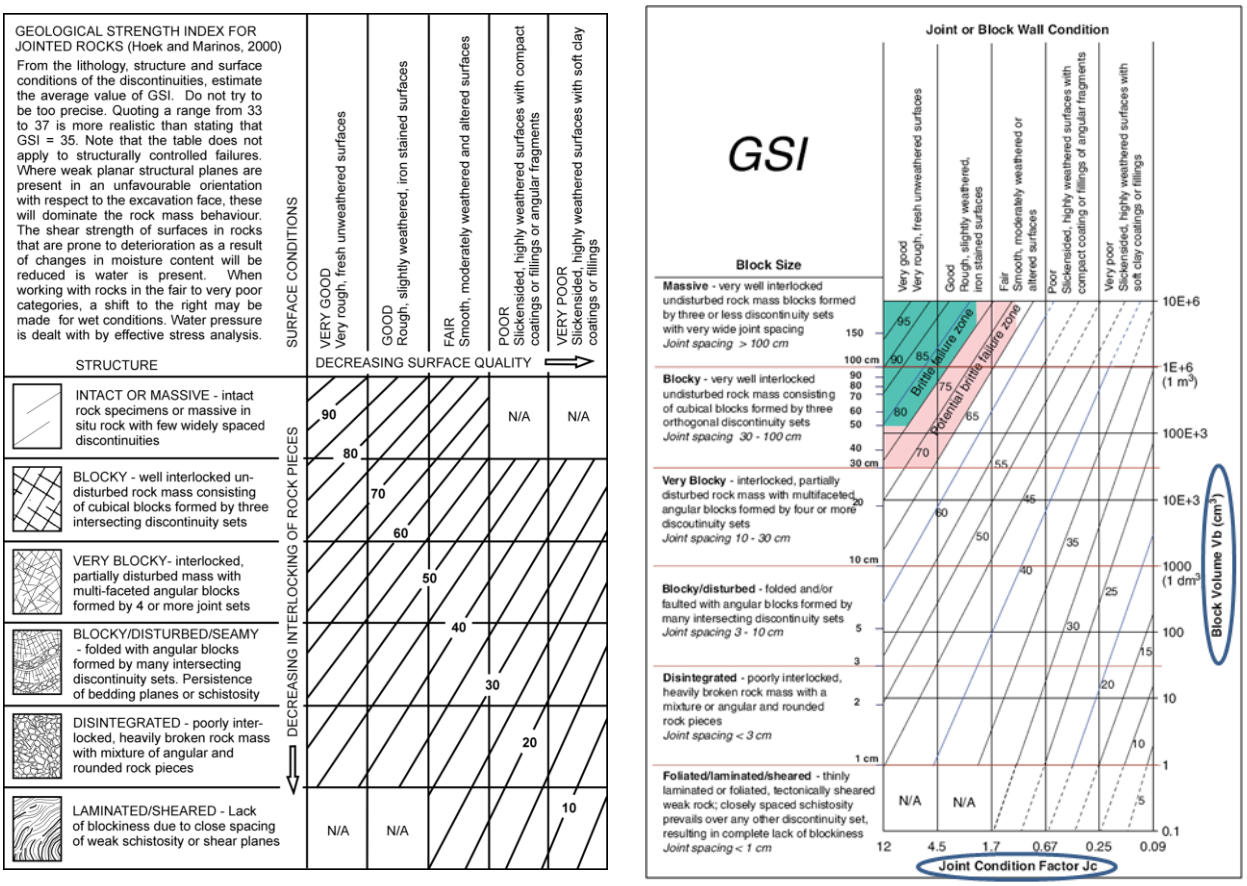

(a) (b)

Figure 2-20: a) Original *GSI* chart (after Hoek and Brown, 1997); b) modified *GSI* chart (after Cai et al., 2004).

In the next section, the empirical methods and equations based on rockmass classification and characterization systems for the determination of Mohr-Coulomb and Hoek-Brown strength parameters are reviewed.

2.3.1.2 Empirical equations for strength estimation of jointed rockmasses

The Mohr-Coulomb (*MC*) failure criterion represents a linear envelope that is obtained from a plot of the shear strength of a material versus the applied normal stress. According to this criterion, failure of a material takes place when the shear stress exceeds a yield function defined by a cohesive and a frictional strength component:

$$\tau = c_i + \sigma_n \tan \emptyset_i$$ Equation 2-3

where, σ_n and τ are the normal and shear stresses in the failure plane, $\emptyset_i$ is the basic friction angle and c_i is the cohesive or intrinsic strength of the intact rock. The inherent assumption in this criterion is that the frictional and cohesive components are simultaneously mobilized throughout the failure process. Though this assumption is applicable to cohesive soils, it cannot be applied to brittle failing rocks where the cohesion is lost through the crack damage process before the frictional strength can be mobilized (Martin and Chandler, 1994; Martin, 1997).

Although many researchers (e.g., Hadjiabdolmajid et al., 2002) have shown that the *MC* failure criterion is not applicable for the design of underground openings in massive brittle rockmasses, many practitioners still use this criterion in such a manner, often without realizing the inherent deficiencies when used in continuum models. The laboratory triaxial test data can be used to obtain the values of cohesion and friction angle for intact rock. For jointed rockmasses, however, these parameters must be estimated. Bieniawski (1976), based on *RMR*, provided some guidance for the estimation of rockmass cohesion and friction angle (Table 2-1).

Table 2-1: Rockmass cohesion and friction angle suggested by Bieniawski (1976), and calculated rockmass strength.

RMR rating	81 to 100	61 to 80	41 to 60	21 to 40	Less than 21
Rockmass cohesion (kPa)	> 400	300 - 400	200 - 300	100 - 200	< 100
Rockmass friction angle (°)	> 45	35 - 45	25 - 35	15 - 25	< 15
Calculated UCS_{rm} (MPa)	> 2	1 - 2	0.6 - 1	0.3 - 0.6	< 0.3

The rockmass strength UCS_{rm}, calculated based on the suggested values of rockmass cohesion and friction angles, is presented in Table 2-1. As can be seen, for rockmasses with *RMR* > 81, the UCS_{rm} is calculated to be above 2 MPa. This suggests that *RMR* was originally developed for weak rocks.

Many researchers have proposed empirical equations for the estimation of unconfined compressive strength of jointed rockmasses (UCS_{rm}) based on the *RMR* rating. Some of these empirical equations are listed below (Equation 2-4 to Equation 2-9). A comparison of these empirical relationships with the results of *in situ* tests on sedimentary rocks (Aydan and Dalgic, 1998) is presented in Figure 2-21. It can be seen that most of the empirical equations provide a reasonable estimate of the rockmass strength UCS_{rm}, especially those suggested by Aydan and Dalgic (1998) and Sheorey (1997).

Hoek and Brown (1980a):

$$UCS_{rm}/UCS_i = \sqrt{e^{((RMR-100)/9}} \quad \text{Equation 2-4}$$

Yudhbir and Prinzl (1983):

$$UCS_{rm}/UCS_i = e^{7.65(RMR-100)/100} \quad \text{Equation 2-5}$$

Ramamurthy et al. (1985):

$$UCS_{rm}/UCS_i = e^{(RMR-100)/18.75} \quad \text{Equation 2-6}$$

Kalamaras and Bieniawski (1993):

$$UCS_{rm}/UCS_i = e^{(RMR-100)/24} \quad \text{Equation 2-7}$$

Sheorey (1997):

$$UCS_{rm}/UCS_i = e^{(RMR-100)/20} \quad \text{Equation 2-8}$$

Aydan and Dalgic (1998):

$$UCS_{rm}/UCS_i = RMR/(RMR + 6(100 - RMR)) \quad \text{Equation 2-9}$$

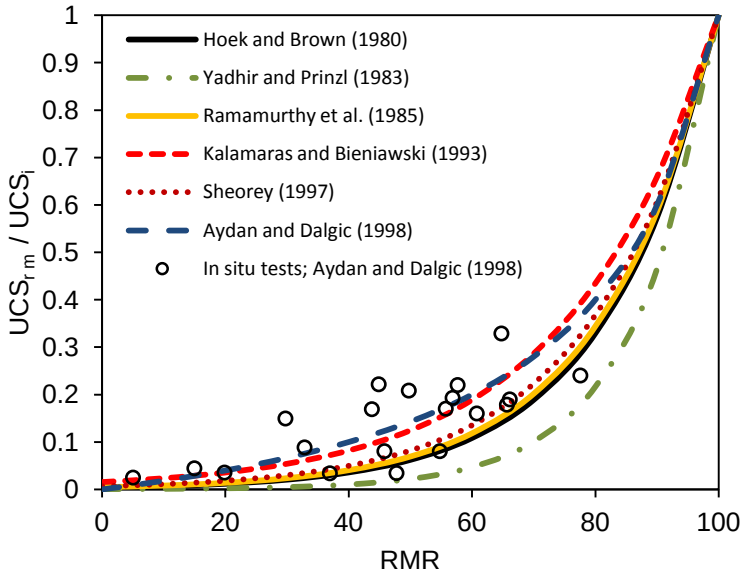

Figure 2-21: Estimates of the ratio of rockmass strength to intact rock strength based on *RMR*.

Singh et al. (1997) and Barton (2002) proposed the following equations for estimating the unconfined compressive strength of jointed rockmasses based on the tunneling quality index *Q*:

$$UCS_{rm} = 7\gamma Q^{1/3} \qquad \text{Equation 2-10}$$

$$UCS_{rm} = 5\gamma (Q\sigma_c/100)^{1/3} \qquad \text{Equation 2-11}$$

where γ is the rock density in g/cm^3. Kulhawy and Goodman (1987) suggested that the unconfined compressive strength of a rockmass can be taken as $0.33UCS_i$ when *RQD* is less than 70% and then increases linearly to $0.8UCS_i$ for *RQD* values between 70 to 100%. A similar relationship was suggested by the American Association of State Highway and Transportation Officials (AASHTO, 1996). According to this method, UCS_{rm}/UCS_i is 0.15 for *RQD* less than 64% and linearly increases to about 0.8 as *RQD* increases to 100%. Note that this is not consistent with the experience in massive to moderately jointed rockmasses (i.e., *GSI* > 75),

where the unconfined rockmass strength was estimated to be about $0.3UCS_i$ (Martin, 1997; Martin et al., 1999).

Zhang (2011) proposed an empirical relationship for the unconfined compressive strength of rockmasses by combining the existing relationship between the rockmass to intact rock compressive strength ratio (UCS_{rm}/UCS_i) and rockmass to intact rock deformation modulus ratio (E_{rm}/E_i) proposed by Ramamurthy (1993), Singh et al. (1998) and Singh and Rao (2005) and the *RQD*-E_{rm}/E_i empirical relationship derived by Zhang and Einstein (2004). This empirical *RQD*-based relationship is defined by:

$$UCS_{rm}/UCS_i = 10^{0.013RQD-1.34} \qquad \text{Equation 2-12}$$

Figure 2-22 compares the Zhang (2011) empirical relationship with those suggested by Kulhawy and Goodman (1987) and AASHTO, (1996). As can be seen, this method covers the entire range of *RQD* continuously and is in close agreement with the previous *RQD*-based equations, especially for situations where *RQD* > 70%. Zhang (2011) applied this empirical equation to six sites and found that the estimated unconfined compressive strength values were essentially in the middle of those estimated using the existing empirical rockmass strength equations. Note that the majority of the *GSI* values calculated for these sites were less than 70 and the majority of the intact rock strengths (UCS_i) were determined to be less than 100 MPa. This indicates that the *RQD*-based equation suggested by Zhang (2011) is only applicable to weak rocks. Therefore, it is not suggested to use Equation 2-12 to estimate the unconfined compressive strength of hard brittle rockmasses.

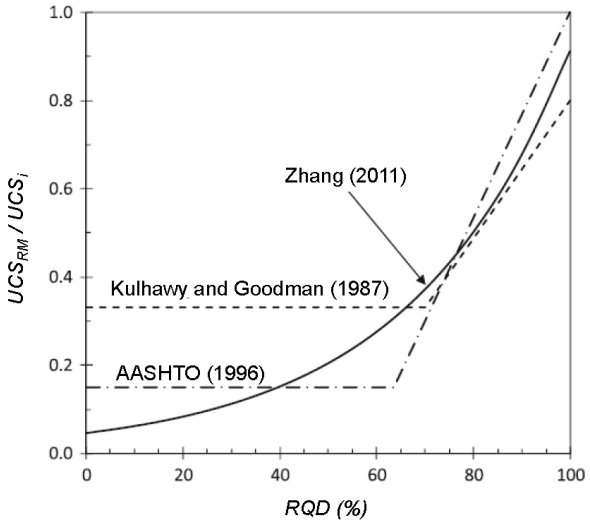

Figure 2-22: Comparison between *RQD*-based methods for the estimation of rockmass unconfined compressive strength (after Zhang, 2011).

All the empirical equations reviewed above provide an estimate of the strength of jointed rockmasses under unconfined condition. However, both the unconfined and confined strengths of a rockmass are required for simulation of jointed rockmasses using continuum codes.

To overcome the limitation of the above empirical equations in terms of estimating the confined rockmass strength, Barton and Pandey (2011) suggested the following equations, to obtain values of friction angle (Frictional Component, *FC*) and cohesion (Cohesive Component, *CC*) of a jointed rockmass:

$$FC = \tan^{-1}[(J_r/J_a)J_w] \qquad \text{Equation 2-13}$$

$$CC = (RQD/J_n)(1/SRF)(UCS_i/100) \qquad \text{Equation 2-14}$$

In Equation 2-13, the friction angle of the jointed rockmass (*FC*) is a function of the frictional properties of the joints (J_r, J_a, and J_w). This assumption is not realistic as the frictional properties of both the joints and rock blocks influence the overal friction angle of the jointed rockmass. In

Equation 2-14, the rockmass cohesive strength is a function of *SRF*; it decreases with increasing the *SRF* value. *SRF* is a parameter that describes the relation between stress and rock strength around underground openings (i.e., low confinement). Therefore, Equation 2-14 is only applicable to the estimation of cohesive strength of the rockmass at low confinement, but not at high confinement relevant for the design and stability analysis of cores of pillars and abutments. Barton and Pandey (2011) investigated the applicability of Equation 2-13 and Equation 2-14 for simulating the behavior of the rockmass near stope walls (which is a low confinement problem).

The *HB* failure criterion for estimating the strength of jointed rockmasses was originally developed by Hoek and Brown (1980a) to provide input for design of underground excavations (Hoek and Marinos, 2007). Since then, this criterion was modified by Hoek (1983), Hoek and Brown (1988), Hoek et al. (1992) and Hoek (1994). Its current version, known as the generalized *HB* failure criterion proposed by Hoek et al. (1995) and Hoek and Brown (1997) to estimate both the unconfined and confined strengths of rockmasses, is defined by:

$$\sigma_1' = \sigma_3' + \sigma_{ci}\left(m_b\frac{\sigma_3'}{\sigma_{ci}} + s\right)^a \qquad \text{Equation 2-15}$$

where σ_1' and σ_3' are the maximum and minimum effective stresses at failure, m_b is the value of the Hoek-Brown "slope" constant for the rockmass, and *s* and *a* are constants that depend upon the rockmass characteristic, where *a* controls the curvature of the failure envelope. The constants m_b and *s* are related in a general sense to the angle of internal friction of the rockmass and the rockmass cohesive strength, respectively. For intact rock, m_i is used instead of m_b, and $s = 1$ while $a = 0.5$. As per recommendation by Hoek and Brown (1997), both *HB* parameters m_i and

σ_{ci} are determined by statistical analysis of the triaxial test data covering a confinement range up to half of UCS_i in five equal increments. Therefore, the unconfined intact rock strength σ_{ci} as a *HB* parameter is not obtained from unconfined compression tests, but obtained by back projection or extrapolation from confined test data by means of regression analysis (Hoek and Brown, 1997). Note that UCS_i is often lower than σ_{ci}. The parameters m_b, s and a are all functions of *GSI* according to the following equations:

$$s = exp\left(\frac{GSI - 100}{9}\right) \quad \text{Equation 2-16}$$

$$m_b = m_i exp\left(\frac{GSI - 100}{28}\right) \quad \text{Equation 2-17}$$

$$a = \frac{1}{2} + \frac{1}{6}\left[exp\left(-\frac{GSI}{15}\right) - exp\left(-\frac{20}{3}\right)\right] \quad \text{Equation 2-18}$$

Carter et al. (2008) divided the *GSI* chart into three main domains (Domain 1: *GSI* < 30; Domain 2: 30 < *GSI* < 65; and Domain 3: *GSI* > 65) and proposed an approach for estimating the unconfined rockmass strength for each domain. They argued that, at the low and high ends of the *GSI* chart (i.e., *GSI* < 30 with 0.5 < UCS_i < 15 MPa, and *GSI* > 65 with m_i > 15), discontinuities play less of a role and the rockmass strength is dominated more by the properties of rock blocks than by the discontinuities. They further suggested that between these two limits (i.e., 30 < *GSI* < 65), the *HB* failure criterion provides a reasonable estimate of the rockmass strength. Figure 2-23, which plots the ratio of unconfined rockmass strength to intact rock strength (UCS_{rm}/UCS_i) against *GSI*, illustrates the transition from a nonlinear *HB* curve in mid-range of the rockmass competency scale (i.e. UCS_i > 15 MPa) to linear *MC* lines in soil-like materials (i.e., weak rocks with UCS_i < 15 MPa).

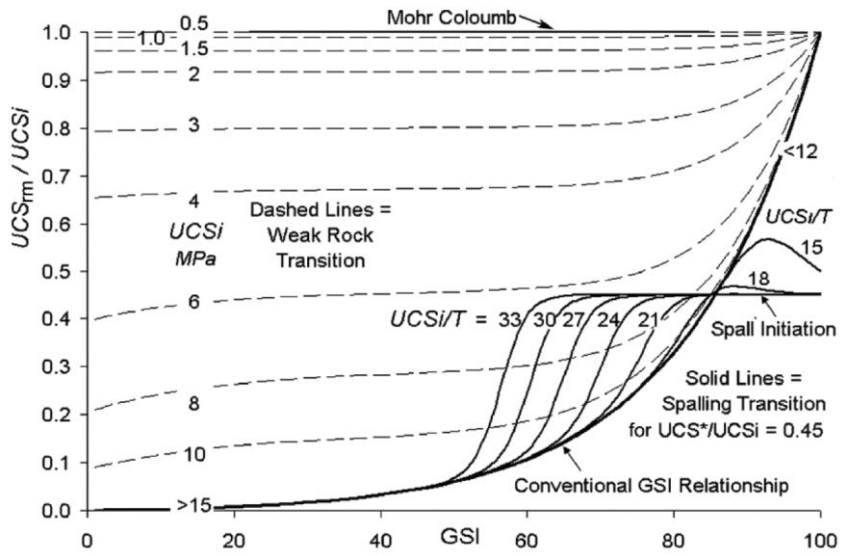

Figure 2-23: Normalized rockmass strength as a function of *GSI* illustrating the conventional *HB* behavior as well as weak and strong rockmass transition functions (Carter et al., 2008). In this figure, *T* refers to tensile strength (σ_t) and $UCS^* = 0.45UCS_i$ defines the spall transition threshold.

Also, noticeable in Figure 2-23 is the influence of the ratio of intact rock strength to tensile strength on the strength of rockmasses for *GSI* values greater than 50. Carter et al. (2008) suggested that, for $UCS_i/\sigma_t > 17$, the unconfined rockmass strength reduces to about $0.4UCS_i$. This conclusion is mainly based on the experience in massive rockmasses such as those mentioned above, that spalling begins when the maximum tangential stress at the excavation boundary exceeds 30 to 50% of the intact rock strength.

This approach seems to be very promising as it integrates the experience from sedimentary rocks (where sliding along the joints and block shearing dominate the failure) and massive to moderately jointed rockmasses consisting of hard brittle rock blocks (where tensile fracturing leading to spalling and slabbing at low confinement dominates the failure).

Recently, Dinc et al. (2011) proposed an empirical approach for the estimation of strength of jointed rockmasses based on the Structure Rating (*SR*) and Surface Condition Rating (*SCR*)

proposed by Sonmez and Ulusay (1999). These two empirical parameters define the blockiness and joint surface conditions of a rockmass, respectively. Using this approach, the rockmass strength is obtained using the generalized *HB* failure criterion but with a series of complex equations added to determine the *HB* strength parameters s, m_b and a. The proposed empirical equations were only calibrated to five slope failures and four sets of uniaxial compressive strength data of rockmasses (all zero to low confining pressure). Therefore, this approach is not applicable for the estimation of rockmass strength at high confinement (e.g., pillar design and stability of abutments at depth). Table 2-2 summarizes the rockmass classification and characterization systems and their capabilities for the estimation of unconfined and confined strengths of jointed rockmasses.

Table 2-2: Application of classification and characterization systems for rockmass strength estimation.

Classification/ characterization system	Origin & application	Joint persistence	Applicability for estimation of	
			Unconfined strength	Confined strength
RMR	civil tunnel & mine haulage	persistence & non-persistence	applicable	not applicable
Comment:		only 6 point rating difference between persistence & non-persistence rockmasses		
Q	civil tunnel	persistence	applicable	not applicable
Comment:		discontinuous joints are considered as random & therefore minimal impact on rating		provides rockmass c and ∅, however, only applicable to low confinement problems.
MRMR	mine environments	persistence	applicable	not applicable
Comment:				
GSI	mine slope & drift	persistence	applicable	applicable
Comment:				for *GSI* < 65 in poorly interlocked rockmasses

The following can be concluded from the review of the currently available empirical approaches for estimating the strength of jointed rockmasses:

- the *RMR*-based equations and the *MRMR* system can only be used to estimate the unconfined rockmass strength;
- the *RQD*-based equations were developed based on data from weak rockmasses and can only be used to estimate the unconfined rockmass strength;
- the *Q*-based equations can be used to estimate the rockmass strength parameter c and ∅ for use in numerical modeling. However, the equation for the determination of the cohesive strength of the rockmass is only applicable to low confinement problems as *SRF* (which is not a rockmass parameter yet is still required in the *Q*-based equation) is used to describe the relation between stress and rock strength at low confinement (i.e., around underground openings). On the other hand, the equation for the determination of the friction angle the jointed rockmass is only a function of the frictional properties of the joints, but not those rock blocks, and this is not a realistic assumption. Therefore, the *Q*-based equations need further investigation as the data supporting its validity are limited to low confinement problem.

Therefore, among all the empirical methods reviewed in this section, it is the *GSI* approach that provides estimates of the confined rockmass strength for use in numerical modeling. Unfortunately, this approach was calibrated to near excavation behaviour in poorly interlocked, persistently jointed and weak rockmasses.

2.3.2 Analytical methods

The influence of single discontinuities or planes of weakness and their orientations on the strength of rock specimens has been widely investigated. The single plane of weakness theory, developed by Jaeger et al. (2007) for the case shown in Figure 2-24a, assumes that there exist two independent failure modes. They include slip on the discontinuity and shear fracture of the

intact rock, either one of which can be identified depending on the orientation of the discontinuity in relation to the principal stress directions. This theory was expanded to the three-dimensional space by Amadei (1988) by taking into account the effect of intermediate principal stress.

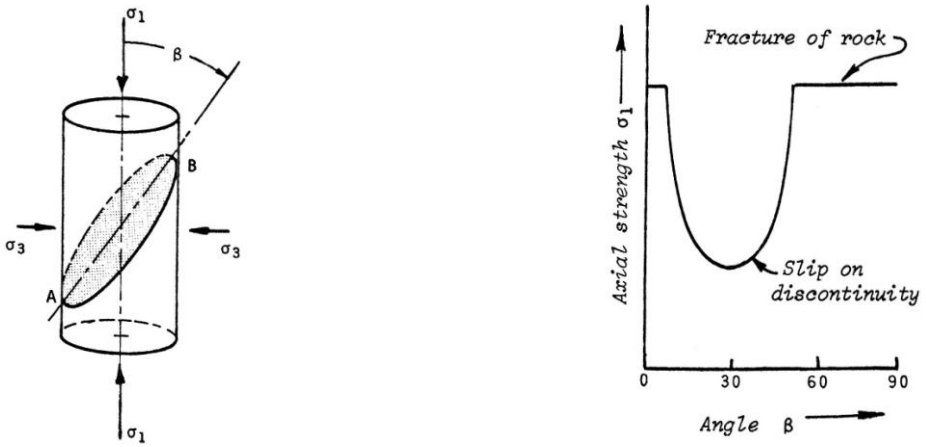

(a)

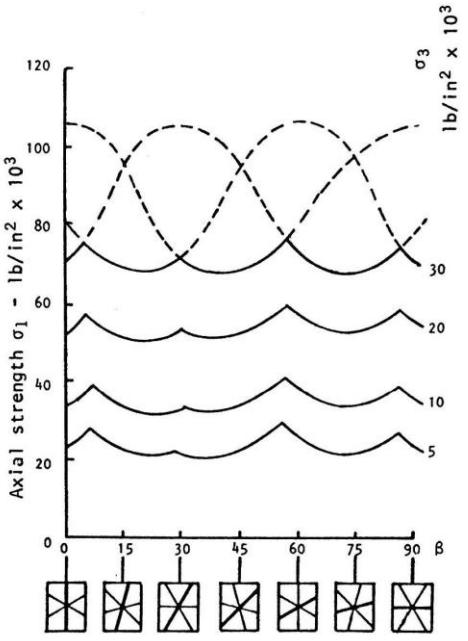

(b)

Figure 2-24: a) Strength of rock containing a single joint as a function of joint orientation; b) hypothetical strength characteristics of a specimen containing four identical weakness planes (Figures from Hoek and Brown, 1980b).

According to Jaeger's single plane of weakness theory for two-dimensional space, the shear stress (τ) and normal stress (σ_n) acting on a single discontinuity with a dip angle of β from the specimen axis (Figure 2-24a) can be obtained as a function of major (σ_1) and minor (σ_3) principal stresses according to the following equations:

$$\tau = \frac{1}{2}(\sigma_1 - \sigma_3)\sin 2\beta \qquad \text{Equation 2-19}$$

$$\sigma_n = \frac{1}{2}(\sigma_1 + \sigma_3) + \frac{1}{2}(\sigma_1 - \sigma_3)\cos 2\beta \qquad \text{Equation 2-20}$$

Hoek and Brown (1980b) demonstrated the application of Jaeger's theory for the estimation of the strength of a jointed rockmass consisting of a number of identical continuous weakness planes oriented at equal angles to each other. The solution for the case of four identical planes of weakness is shown in Figure 2-24b. In this case, failure always takes place by slipping on one of the planes of weakness. As demonstrated in Figure 2-24b, the failure envelope of this rockmass can be constructed using the minimum strength envelope shown with the solid line. From this analysis, Hoek and Brown (1980b) concluded that the strength of a rockmass containing four or more sets of continuous joints of similar properties can be considered to be isotropic.

The strength of the specimen consisting of a single plane of weakness can be represented using the *MC* strength parameters after replacing Equation 2-19 and Equation 2-20 in the *MC* failure criterion with the following:

$$(\sigma_1 - \sigma_3)_{f,\ joint} = \frac{2(c_j + \sigma_3 tan\emptyset_j)}{(1 - |\cot\beta\,|\tan\emptyset_j)\,|\,\sin 2\beta|}$$ Equation 2-21

where, c_j and $\emptyset_j$ are the cohesion and angle of internal friction of joints. Figure 2-24b shows that the strength of a rock specimen varies with the dip of the discontinuity.

Harrison and Hudson (2000) suggested that the strength of a non-persistently jointed rockmass can also be estimated analytically using the theory of weakness plane by considering the equivalent shear strength of a persistent discontinuity, which includes a percentage of the strength of the original discontinuity and a percentage of the strength of the intact rock. The equivalent shear strength of the persistent discontinuity is expressed as:

$$\tau = c_j + \sigma_n tan\emptyset_j = [K.c_w + (1-K).c_i] + \sigma_n.[K.tan\emptyset_w + (1-K).tan\emptyset_i]$$ Equation 2-22

where, c_w and $\emptyset_w$ are the cohesion and angle of internal friction of the non-persistent discontinuity, c_i and $\emptyset_i$ are the cohesion and angle of internal friction of the intact rock and *K* is the persistence of the discontinuity according to Equation 2-2.

Halakatevakis and Sofianos (2010) extended the theory of plane of weakness by using the non-linear Barton-Bandis (*BB*; Barton, 1973) failure criterion for rough joints instead of the linear *MC* failure criterion to account for discontinuities with different levels of joint roughness. The *BB* failure criterion is expressed as:

$$\tau = \sigma_n \tan\left[JRC\ log\left(\frac{JCS}{\sigma_n}\right) + \emptyset_j\right]$$ Equation 2-23

where *JRC* is the joint roughness coefficient and *JCS* is the joint wall compressive strength (Barton, 1973). By substituting Equation 2-19 and Equation 2-20 in Equation 2-23, the strength of a rock specimen consisting of a rough joint can be expressed as:

$$(\sigma_1 - \sigma_3)sin2\beta = [(\sigma_1 + \sigma_3) + (\sigma_1 - \sigma_3)\cos 2\beta] \cdot tan\left[JRC.\log\left(\frac{2.JCS}{(\sigma_1 + \sigma_3) + (\sigma_1 - \sigma_3)\cos 2\beta}\right) + \emptyset_j\right]$$ Equation 2-24

Note that the solution of the extended theory of weakness plane (Equation 2-24) is possible only by using an iterative solver. Halakatevakis and Sofianos (2010) mentioned that the extended theory of one plane of weakness can be employed for any number of crossing joints. For this purpose, similar to the approach described by Hoek and Brown (1980b), the extended theory is applied to each discontinuity separately and then the rock strength is determined as a lower strength envelope. Halakatevakis and Sofianos (2010) found a reasonable agreement between analytical and numerical methods in terms of the unconfined strength of jointed rockmass, which varies as a function of joint orientation as shown in Figure 2-25.

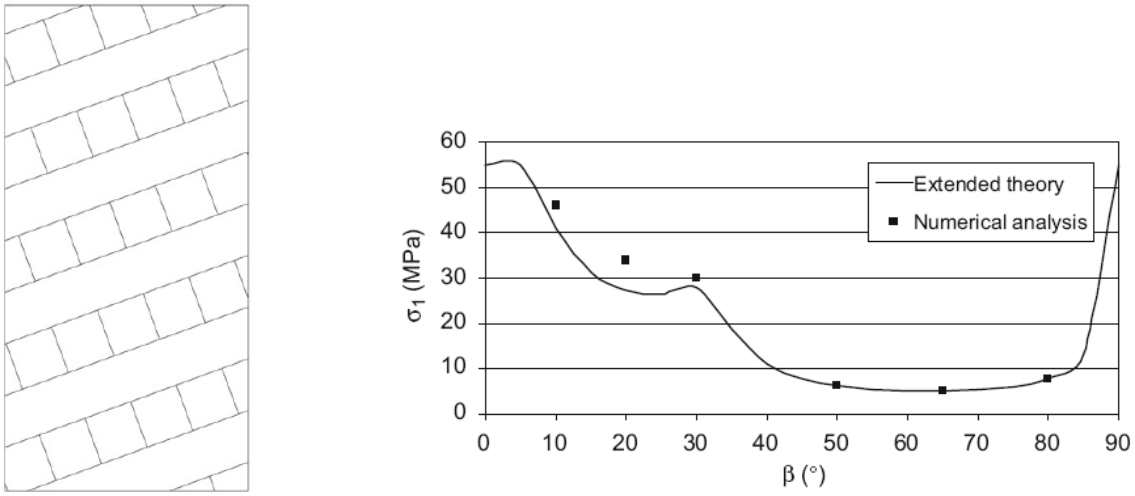

(a) (b)

Figure 2-25: a) Numerical specimen crossed by two discontinuity sets and with rock bridges; b) comparison between the unconfined strength of numerical specimen with that predicted by the extended theory (figures from Halakatevakis and Sofianos, 2010).

Halakatevakis and Sofianos (2010) also investigated the application of the original plane of weakness theory and its extension by simulating the response of laboratory experiments on jointed rockmass models conducted by Brown (1970) and Ladanyi and Archambault (1972). As shown in Figure 2-26a, the failure envelope estimated by the original theory diverges from Brown's (1970) experimental results with increasing confinement. However, the failure envelope based on the extended theory agrees well with the experimental results for confining pressures greater than 3 MPa. As such, it can be said that the extended plane of weakness theory overestimates the strength of jointed rockmass models at low confining pressures ($\sigma_3 < 3$ MPa).

Figure 2-26b compares the results of the experimental study by Ladanyi and Archambault (1972) and those of the original and extended plane of weakness theories. It becomes clear that the original theory overestimates the strength of jointed rockmass models over the entire range of confinement. However, the envelopes with low values of *JRC* based on the extended theory best

fit the experimental results for higher values of confining pressures (σ_3 > 1.4 MPa) and overestimate the strength of jointed rockmass models at low confinement (σ_3 < 1.4 MPa).

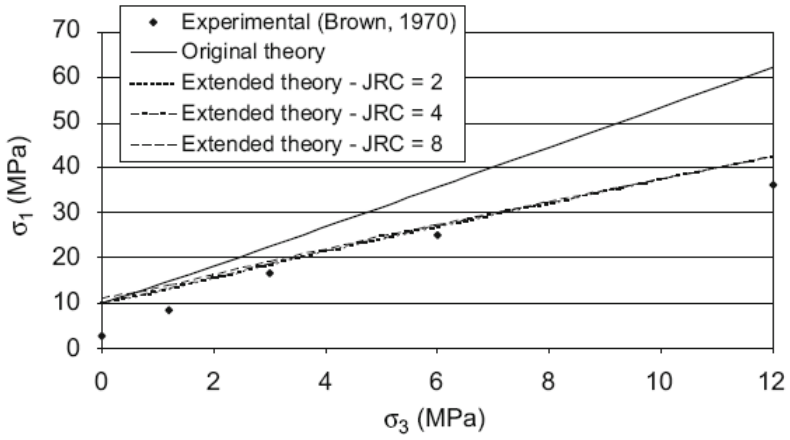

(a)

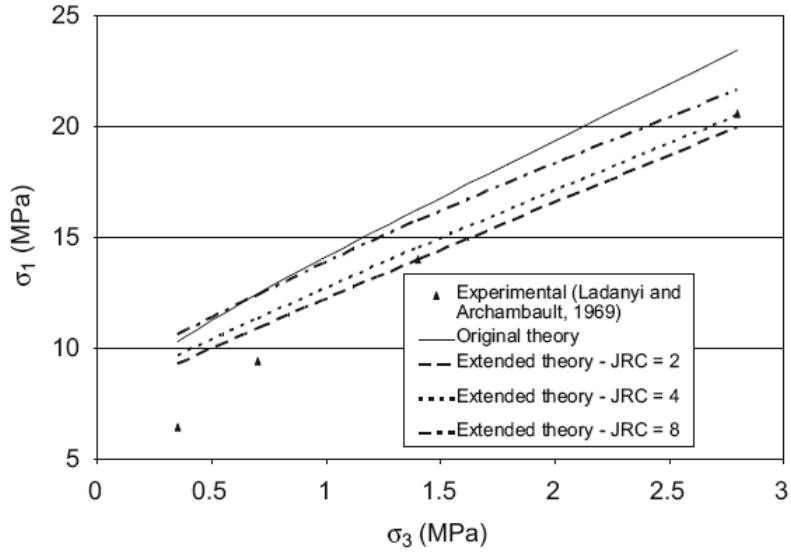

(b)

Figure 2-26: Comparison between the failure envelopes estimated by the original and extended theories of weakness plane and experimental results of jointed rockmass models by: a) Brown (1970); and b) Ladanyi and Archambault (1972) (figures from Halakatevakis and Sofianos, 2010).

The following can be concluded from the review of analytical methods for estimating the strength of jointed rockmasses:

- the theory of single plane of weakness is applicable to persistently jointed rockmasses, where failure is dominated by slip on joints;
- The theory of single plane of weakness can be extended to non-persistently jointed rockmasses, however, this approach is not practical as it was only investigated on a few jointed rockmass models;
- the extended theory of plane of weakness has not been sufficiently verified on case studies; and
- the extended theory tends to overestimate the strength of models of jointed rockmasses at low confining pressures when it is matched with the strength of jointed models at high confining pressures.

2.3.3 Numerical methods

This section briefly reviews the newest developments in estimating the rockmass strength using numerical modeling. Pierce et al. (2007) introduced a methodology to simulate a jointed rockmass within the framework of *PFC3D* known as the Synthetic Rock Mass (*SRM*) approach. The *SRM* specimens are three-dimensional models and simulate a rock medium as an assembly of spheres bonded at their contact points with an embedded discrete network of disc-shaped flaws (i.e., joints). The discrete fractures are included in the bonded-particle assembly by locating contacts between particles on opposite sides of a user-defined plane. The contact used to simulate the joint is smooth and therefore removes the "bumpiness" associated with the spherical shape of particles and enforces a *MC* shear criterion (Pierce et al., 2007).

The three main input parameters required for the construction of an *SRM* specimen are the rock block properties (*UCS* and elastic modulus), a Discrete Fracture Network (*DFN*) and the joint

properties (i.e., stiffness, cohesion and friction angle). The application of this approach is to derive rockmass properties such as deformation modulus, peak strength and post-peak behavior for later use in continuum codes.

Mas Ivars (2010) used the *SRM* approach and conducted uniaxial compression tests on 1 m × 2 m cylinders in *PFC3D* and matched their strengths to the mean strength of *in situ* rock blocks at the Rio Tinto's Northparkes mine. The *DFN* generated from borehole and tunnel scanline mapping information of the Northparkes mine was applied to an 80 m cube specimen in *PFC3D* (Figure 2-27). The generic specimen was carved into smaller specimens with heights of 80 m, 40 m and 20 m and a height-to-width ratio of 2 in different directions. The *SRM* specimens were subjected to unconfined and confined compression tests and the results are presented in Figure 2-28.

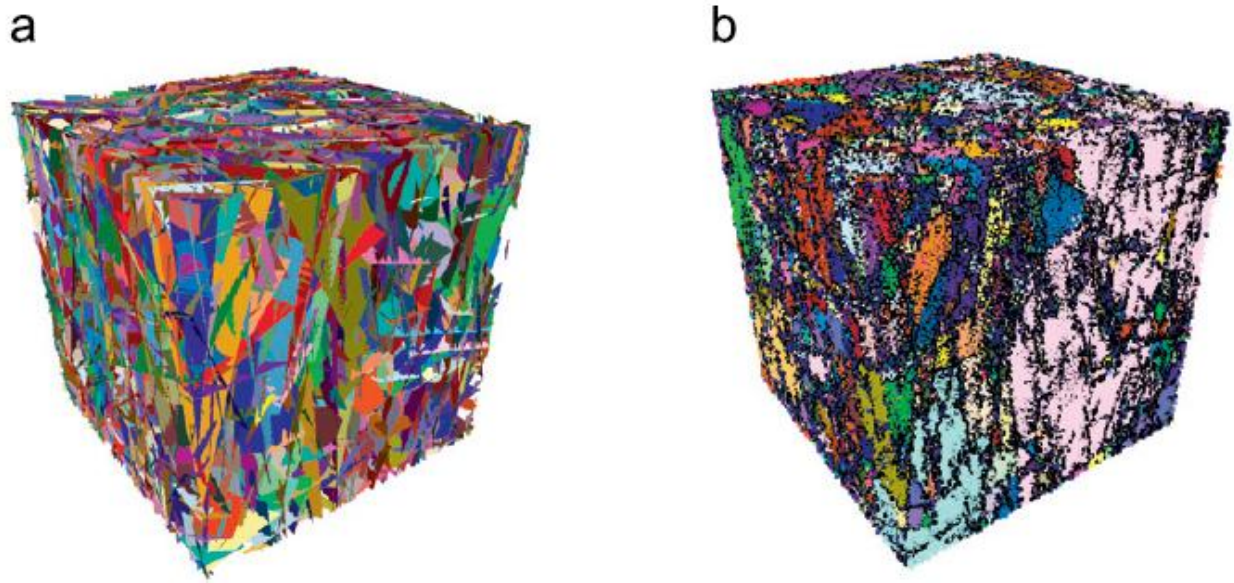

Figure 2-27: a) Three-dimensional *DFN* model; and b) corresponding three-dimensional *SRM* specimen (after Mas Ivars, 2010).

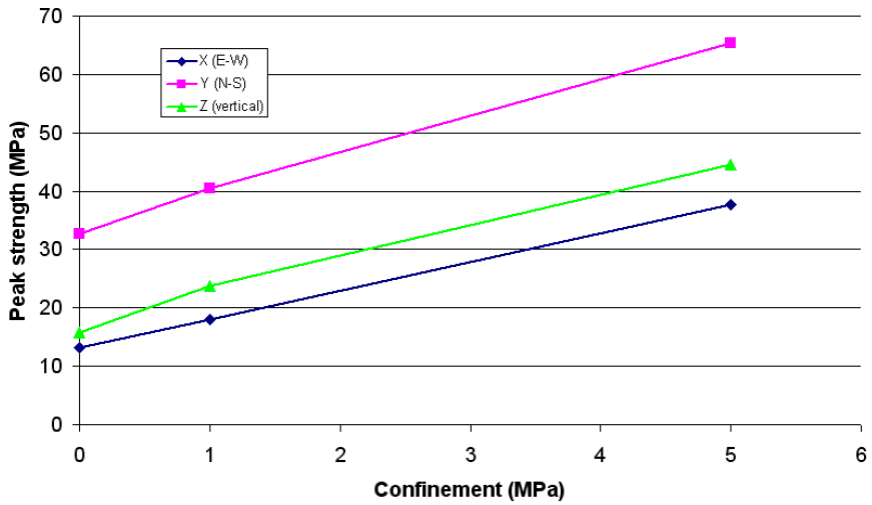

Figure 2-28: Unconfined and confined strengths of three 40 m × 40 m × 80 m *SRM* specimens in three orthogonal directions (after Mas Ivars, 2010). The mean bond normal and shear strengths used in the *SRM* specimens were 170 MPa, and the smooth joint cohesion and friction angle were 0 MPa and 30°, respectively.

Elmo and Stead (2009) combined *DFN* models with the hybrid finite-discrete element code *ELFEN* (Rockfield, 2007) and simulated jointed rockmasses of different sizes. Figure 2-29a and b show a comparison between the strength envelopes estimated by the *GSI* approach and the numerically estimated strength of slender pillars with a W/H = 2.8 / 7 with an areal fracture intensity (the ratio of total fracture length to area) of 1.8 and 2.6, respectively, up to a low confining pressure of 4 MPa. The *GSI* curves are determined assuming that m_i = 12 (typical of limestone) and σ_{ci} = 48. The properties of the joints used in the *ELFEN* model were c_j = 0.2 MPa and $\emptyset_j$ = 35°.

Note that the correspondence between the results of numerical simulations and the strength envelope of the rockmass estimated by the *GSI* approach is valid up to a confining pressure of 4 MPa. Beyond this confinement, the strength of the *ELFEN* model seems to underestimate the strength estimated by the *GSI* of 70 and overestimate the strength estimated by the *GSI* of 50.

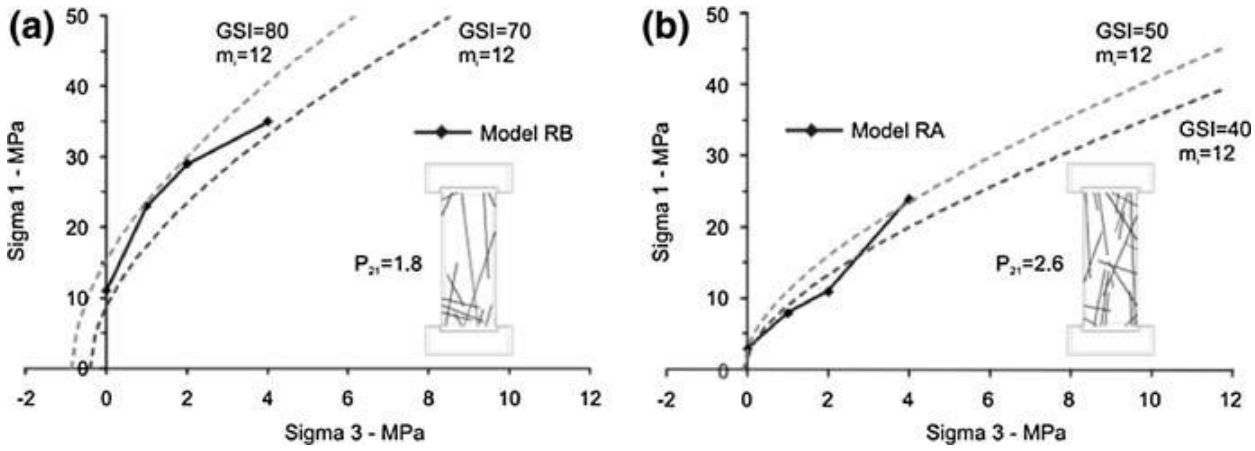

Figure 2-29: Comparison between the *ELFEN* modeled response and the *GSI* approach for two pillars with different fracture intensities (Elmo and Stead, 2009).

Moreover, the unconfined compressive strength of intact rock used in the model is 48 MPa. This indicates that the rockmass is relatively weak, and, therefore, that the *GSI* system would be an ideal approach to characterize its strength, especially at low confinement (i.e., $\sigma_3 < UCS_i/10 = 4$ MPa).

It should be noted that the rough nature of the discontinuities and its dilatant characteristics are usually ignored in simulations of jointed rockmasses using *DFN* models implemented in *SRM* specimens (Bahrani et al., 2011a). Therefore, calibration of numerical models to low confinement problems (e.g., tunnel wall instability) and when the rough nature of the discontinuities is not considered, tends to underestimate the strength of highly confined rockmasses such as pillar cores and abutments at great depths.

Numerical models, when combined with a *DFN* model have shown promising results in determining the strength and deformation properties of a rockmass. However, this approach should only be used after proper calibration of intact rock and rock block strength has been made with a *DFN* model that closely matches the characteristics of discontinuities observed in the

field. The application of the *SRM* approach for simulating defected rock blocks and estimating their strengths with increasing scale will be discussed in *Chapter 5*.

It is suggested that the *SRM* approach needs to be tested on a number of case histories and that further research is required to develop standard procedures for estimating the strength of jointed rockmasses using the *SRM* approach.

2.4 Summary and Conclusions

The review of the experiments on intact and damaged rock specimens and unjointed and jointed physical models of jointed rockmasses reveals the most about the differences between unconfined and confined rock behaviour and their related rockmass strength. The following general observations illustrate the need for a means to arrive at meaningful rockmass strength parameters at high confinement, i.e., for the establishment of peak rockmass strength for pillar design and for abutment capacity assessments:

- The strengths of damaged and jointed specimens under unconfined condition are lower than those of intact specimens due to the influence of tensile or extensional failure induced by heterogeneities and flaws and failure along defects and joints. This strength can be as little as 10% or as high as 80% of UCS_i.
- The strengths of damaged and jointed specimens increase rapidly with increasing confinement; in the principal stress space, the initial equivalent friction angle (i.e., $\phi_e = \phi_b + i$), when $\sigma_3 < \sim UCS_i /10$, can be as high as 50° to 65°.
- At high confinement (when $\sigma_3 > \sim UCS_i/10$), the failure envelopes of the damaged and jointed speciemsn tend to approach the equivalent friction angle of intact specimens.
- The strengths of damaged and jointed specimens in general approach the intact strength at high confining pressures. In some cases, it even seems to exceed the intact strength but this is likely an artifact of the laboratory testing conditions.

- As a consequence, the strength degradation in the low confinement zone ranges from 90% to 20% of intact strength while it is typically up to about 20% of intact strength under high confinement.

Various approaches including empirical, analytical and numerical methods for estimating the strength of jointed rockmasses were critically reviewed in this chapter. The goal of this review was to assess current limitations of these approaches for estimating the unconfined and confined strengths of jointed rockmasses and to build the foundation for the development of means to establish the rockmass strength in confined conditions. The main points drawn from the review of the empirical rockmass classification and characterization systems *RMR*, *MRMR*, *Q*, and *GSI* are summarized next.

With respect to each classification/characterization system's origin:

- *RMR* was originally developed based on experiences in civil tunnels and mine haulages. Its applications were later extended to situations other than tunneling such as rock slopes, foundations and haulage drifts and roof stability in coal mines.
- *MRMR* adjusts *RMR* for weathering, mining induced stresses, joint orientation and blasting effects based on mine case records.
- *Q* was developed for the determination of tunnel support requirements. Its origin and modifications have been largely based on the evaluation of a number of civil engineering case records.
- *GSI* was developed based on experiences in slopes and tunnels, mainly in weak rockmasses.

It is therefore concluded that most systems were originally developed based on experiences from low confinement problems (i.e., to describe the rockmass behavior and properties near the excavation). Furthermore, while the *MRMR* system was primarily developed for cave mining, its

application for high confinement problems such as design of cores of pillars has not been verified.

With respect to joint persistence:

- While non-persistent joints are considered in the *RMR* system, the impact of only 6 points on *RMR* likely results in an underestimation of the quality of non-persistently jointed rockmasses.
- In the *MRMR* system, the block forming joints are considered to be continuous but the effects of non-persistent defects are respected.
- Non-persistent joints are only indirectly considered in the *Q* system. When short joints do not take part in the formation of blocks, they are considered as random for the determination of the J_n value and this only slightly impacts the *Q* value. This suggests that *Q* tends to underestimate the quality of non-persistently jointed rockmasses.
- *GSI* was developed for persistently jointed rockmasses consisting of at least three block-forming joint sets.

The review of the literature revealed that the following methods have been proposed for estimating the confined strength of jointed rockmasses. However, it was also found that none of the methods provides a reliable means of estimating the strength of a rockmass when it is highly confined ($\sigma_3 > \sim UCS_i/10$). In summary, it became evident that:

- The empirical equations based on *RMR* were developed for estimating the unconfined strength of jointed rockmasses.
- The empirical *Q* approach has recently been expanded to give guidance for the estimation of the *MC* parameters cohesion and friction angle for jointed rockmasses. However, it has not been widely tested and thus needs further investigation and development. Since the *Q*-system is primarily aimed at rock support, the respective rockmass strength parameters

are, at best, applicable to low confinement problems. Therefore, this approach should not be used to describe the strength of confined rockmasses.

- The semi-empirical *GSI* approach is the most commonly used approach to arrive at rockmass strength parameters for input to numerical models. It has been evaluated on case studies and is applicable to moderately to highly fractured ground and weak rockmasses. As mentioned above, the *GSI* is applicable as long as joints are persistent and block-forming. It is not applicable in cases where massive to moderately jointed rockmasses are present, especially when they are highly confined.
- The analytical methods based on the extended plane of weakness theory, which can be applied to non-persistently jointed rockmasses, is not practical as it was only investigated on a few jointed rockmass models. It was found that the extended theory tends to overestimate the strength of models of jointed rockmasses at low confining pressures when its confined strength is matched with the strength of jointed models at high confinement.
- The *SRM* numerical approach requires high computing power and demanding calibration processes. It is very promising but in its infancy and needs further development and verification on more case histories. When not properly calibrated or only calibrated to low confinement situations, it seems to underestimate the confined rockmass strength.

In summary, this literature review supports the hypothesis that the confined rockmass strength is higher than predicted by conventional means. This is primarily the case because the failure mode changes, often drastically, when moving from low to high confinement conditions. In the former, tensile failure processes reduce the strength. In the latter, shear failure and eventually shear rupture through rock blocks and intact rock has to occur and this drastically increases the rockmass strength. It was discussed in this chapter that the existing methods for the estimation of confined strength of jointed rockmasses are limited and flawed, particularly when the rockmass is highly interlocked and consists of joints are dilatant and non-persistent, and when rock blocks are hard and brittle. This thesis aims at overcoming these deficiencies.

In this research, numerical models are calibrated on the results from laboratory tests on damaged rocks and the findings are utilized to extrapolate to rockmasses with different joint conditions (friction angle and persistence). Based on related parametric studies, an approach called the Strength Degradation (*SD*) approach was developed and is presented to estimate the confined strength of micro-defected and defected rocks and highly interlocked, non-persistently jointed rockmasses. This thesis also presents suggestions for obtaining the *HB* strength parameters for such rockmasses and their strength variability for later use in continuum modeling and probabilistic design.

In the next chapter, a grain-based distinct element model is introduced and used to simulate the laboratory behavior of intact and granulated Wombeyan marble reviewed earlier in this chapter (*Section 2.2*) and the results of simulations in terms of the change in the strength, stress-strain curves, failure modes and micro-cracking with increasing confinement are discussed.

Chapter 3

3 Grain-based Model for Intact Rock and Highly Interlocked Jointed Rockmass

3.1 Introduction

In this chapter, the grain-based model (*GBM*) embedded in *PFC2D*, is used to simulate the laboratory response of intact and heat-treated (granulated) marble reported by Gerogiannopoulos (1976), and Gerogiannopoulos and Brown (1978). The essence of the two-dimensional analyses using the *GBM* is to understand the processes that lead to the rapid increase in the confined strength of a homogeneous rock having the same properties and behavior in all directions. It is postulated that the lessons learnt from the *2D* simulations can be used to identify key parameters contributing to this rapid strengthening effect (e.g., block shape, joint roughness, joint persistence) to be able to more realistically simulate the field-scale behaviour of jointed rockmasses in three dimensions (e.g., *SRM* approach in *PFC3D*).

As discussed earlier, the granulated marble represents an analogue for a highly interlocked jointed rockmass; specifically a rockmass with relatively short joints that terminate on other joints such as those observed in columnar jointing (Dershowitz and Einstein, 1988). Therefore, the *GBM* used to simulate such a material can be considered to be a model of a highly interlocked jointed rockmass. The challenge is to calibrate the models to laboratory properties of both intact and granulated marble in such a manner that the simulation results are independent of the applied stress path; simulation results match direct tensile, unconfined and confined compressive strengths of both intact and granulated marble.

After reviewing the laboratory properties of intact and granulated Wombeyan marble including their unconfined and confined strengths and Young's moduli, various techniques for simulating an intact rock using *PFC2D*, their calibration procedures and results are discussed. The essence of this section is to confirm that the grain-based modeling (*GBM*) approach provides an appropriate technique for simulating brittle rocks and their fracturing processes.

Next, the calibration assumptions to choose the micro-properties of the *GBM* are explained in details. Once the *GBM* is calibrated, it is adopted to investigate the transition in the failure mode with increasing confinement, and the results are compared with those observed in the laboratory. Finally, the stress-strain response and the evolution of inter- and intra-grain micro-cracks with increasing axial strain and confinement predicted by the *GBM* are discussed.

3.2 Laboratory Properties of Intact and Granulated Wombeyan Marble

The laboratory behavior of coarse-grained Wombeyan marble studied by Gerogiannopoulos (1976), and Gerogiannopoulos and Brown (1978) were briefly reviewed in *Chapter 2*. The direct tensile strength of granulated marble is nearly zero, suggesting that the bonds between the grains along their boundaries were lost during heat treatment up to 600° C. As shown in Figure 3-1a, the unconfined compressive strength of the granulated marble (UCS_d) is about 30% of the intact strength (UCS_i). The strength of the granulated marble rapidly increases with increasing confinement and approaches, but never reaches that of intact marble. It is illustrated in Figure 3-1a that at low confinement ($\sigma_3 < \sim UCS_i/10$), the strength envelope of the granulated marble has an equivalent friction angle of 55°. The equivalent friction angle of the intact marble for this range of confinement is about 45°, suggesting that the inter-grain dilation is in the order of 55° -

45° = 10°. Beyond this confining pressure threshold ($\sigma_3 \geq \sim UCS_i/10$), the strength envelopes exhibit a frictional behaviour with a (dilation free) basic friction angle of 30° for both intact and granulated marble. Figure 3-1b shows the strength degradation of granulated Wombeyan marble ($\Delta\sigma_1 = \sigma_{1i} - \sigma_{1d}$) as a function of confinement. As can be seen, up to a confining pressure of about $\sigma_3 = UCS_i/10$, the strength degradation of granulated marble decreases rapidly, and then remains almost constant beyond this threshold.

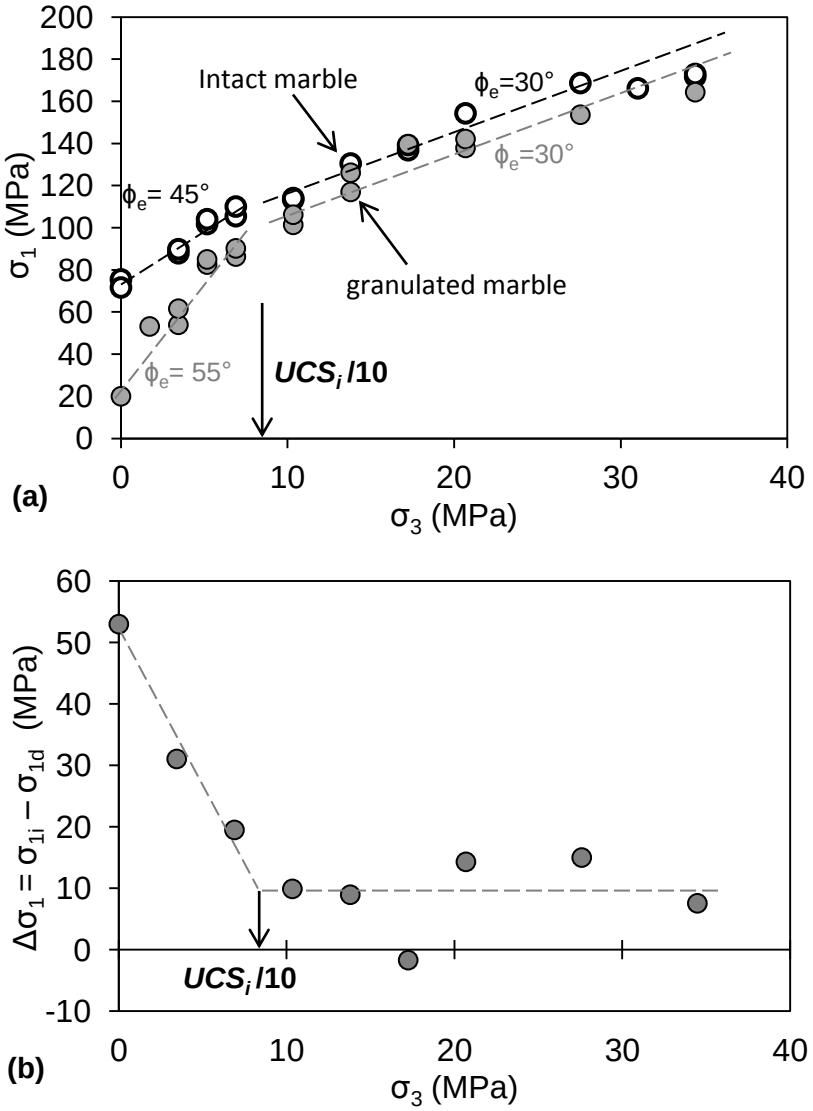

Figure 3-1: a) Strength of intact and granulated Wombeyan marble; b) strength degradation $\Delta\sigma_1$ of granulated Wombeyan marble as a function of confinement (after Gerogiannopoulos, 1976).

Figure 3-2 shows that the Young's modulus of the granulated marble increases with increasing confinement and reaches a plateau of around 30 GPa at a confining pressure greater than 15 MPa (around $UCS_i/5$). Rosengren and Jaeger (1969) and Martin and Stimpson (1994) observed a similar behavior on granulated Wombeyan marble and damaged *LdB* granite, respectively.

Martin and Stimpson (1994) found that the Young's modulus of specimens damaged during coring from highly stressed ground is strongly confinement-dependent; it increases from about 35 GPa under unconfined condition to about 63 GPa at 10 MPa (about $UCS_i/15$) confining pressure and remains relatively constant beyond this confinement, but never reaches that of intact specimens, which have an average Young's modulus of 68 GPa over the entire range of confinement.

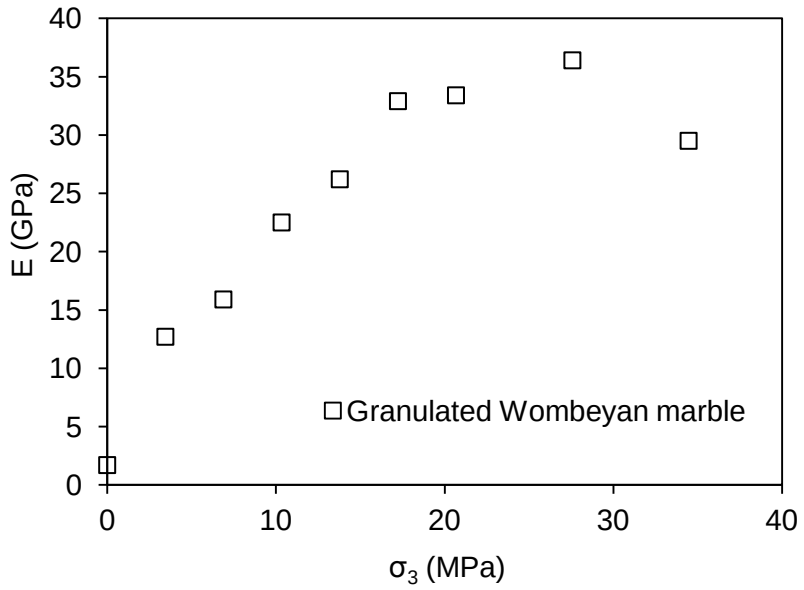

Figure 3-2: Dependency of Young's modulus of granulated Wombeyan marble on confinement (Gerogiannopoulos, 1976).

In this chapter, the *GBM* embedded in *PFC2D* is used to numerically generate a synthetic specimen with polygonal grain structure, similar to that of Wombeyan marble. The grain-based synthetic specimen is then calibrated to the laboratory properties of intact and granulated Wombeyan marble presented in Figure 3-1a and Figure 3-2.

3.3 Introduction to Adopted Distinct Element Method

The *DEM* developed by Cundall (1971) is a numerical method that is capable of simulating irregular shaped particles for the analysis of rock mechanics problems. It was first applied to soils with circular particles by Cundall and Strack (1979). One of the applications of the *DEM* is the simulation of rock by considering it as an assemblage of circular or spherical particles, cemented at their contact points. This method, which is called the Bonded Particle Model (*BPM*), has been implemented in two- and three-dimensional codes *PFC2D* and *PFC3D* (Itasca, 2008a and b). The *PFC* has been extensively used over the past two decades to study a wide range of rock mechanics phenomena as reviewed by Potyondy and Cundall (2004) and Potyondy (2015). They illustrate that such a modeling approach can simulate many aspects of the mechanical behavior and failure processes of brittle rocks from the laboratory to rockmass scale.

The main advantage of the *BPM* over conventional continuum codes is that pre-defined complex empirical constitutive relations are replaced with simpler particle contact logic without requiring plasticity rules (Potyondy and Cundall, 2004). Cracking in this method is explicitly simulated as bond breakage. Once a bond breaks, the displacement field and transition to the residual strength are controlled by particle geometry and friction at particle-particle contacts. This explicitly captures a fundamental characteristic of brittle failing rocks known as cohesion-weakening frictional-strengthening (Martin and Chandler, 1994; Hajiabdolmajid et al., 2002). The concept

of cohesion-weakening frictional-strengthening for brittle rocks was captured in the damage-controlled tests by Martin and Chandler (1994), who showed that the cohesional strength component is gradually lost and the frictional strength component mobilizes with increasing damage.

3.3.1 Approaches for simulating intact rock in PFC2D

One of the applications of the *BPM* is the micro-mechanical simulation of brittle rock failure processes at the laboratory scale. Several approaches have been proposed in this regard including the conventional ball model, the clustered particle model, the clumped particle model and the grain-based model, which are briefly reviewed before the grain-based model is adopted as the preferred model for this investigation.

3.3.1.1 Conventional ball model

The conventional ball model in *PFC* is based on the assumption that rock consists of circular or spherical particles (balls) bonded together at their contact points. The particles and bonds can then be considered as rock grains and grain boundaries, respectively. Contact and parallel bonds are the two basic bond models in the ball model. A contact bond behaves as glue between two particles, connecting them at their contact point (Figure 3-3a). A parallel bond acts as an additional cement-like material deposited over a finite area (a cylinder) between the two particles (Figure 3-3b). Cho et al. (2007) suggested that the parallel bond model as opposed to the contact bond model is a more realistic option for simulating rocks since the bond breakage results in stiffness reduction.

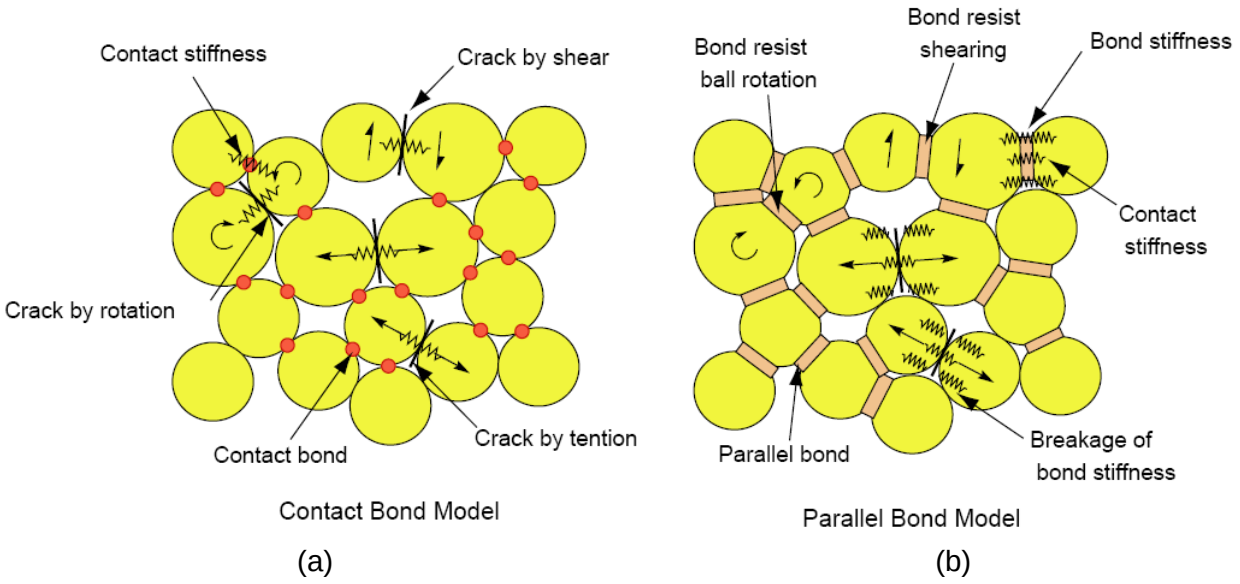

Figure 3-3: Illustration of *PFC* bond models; a) contact bond; and b) parallel bond (after Cho et al., 2007).

Conventionally, the calibration of micro-properties in the ball model is performed on the *UCS* tests. Diederichs (1999) showed that ball models calibrated to the *UCS* significantly over-predicts the tensile strength of brittle rocks and produce a linear rather than a curved failure envelope. This implies that the calibration of the ball model to the tensile strength will underestimate the rock's *UCS*. Potyondy and Cundall (2004) established the hypothesis that this limitation is due to the lack of interlocking (freedom to freely rotate) between the circular or spherical particles forming the ball model, which does not reflect the highly interlocked fabric of crystalline rocks. The three-dimensional *DEM* code developed by Wang and Tonon (2009) showed some improvement in the calibration result of the ball model in terms of friction angle. However, the tensile strength of their *DEM* model was still too high compared to that of experimental results.

3.3.1.2 Clustered particle model

Potyondy and Cundall (2004) introduced an algorithm in *PFC2D*, which generates particle clusters of complex shapes. The size of the clusters is defined by the maximum number of particles in a cluster. Figure 3-4a shows an example of a clustered particle model with a cluster size of 7. Potyondy and Cundall (2004) used unbreakable clusters, which force the cracks to occur along cluster boundaries, and showed that the *UCS* and the slope of the strength envelope exceeded those of *LdB* granite when the cluster size increased (i.e., the number of particles inside the clusters increased from 1 to 10).

Cho et al. (2007) performed a sensitivity analysis on the cluster size in an unbreakable clustered particle model and found that the σ_t/UCS ratio decreases to about 0.1 for a cluster size of 14 from 0.3 for a cluster size of 1 (clustered particle model with a cluster size of 1 corresponds to the conventional ball model). The strength ratio of 0.1 is still too high compared to the measured $\sigma_t/UCS \leq 0.05$ for *LdB* granite. Such a high strength ratio led them to use an alternative approach called the clumped particle model, which is described next.

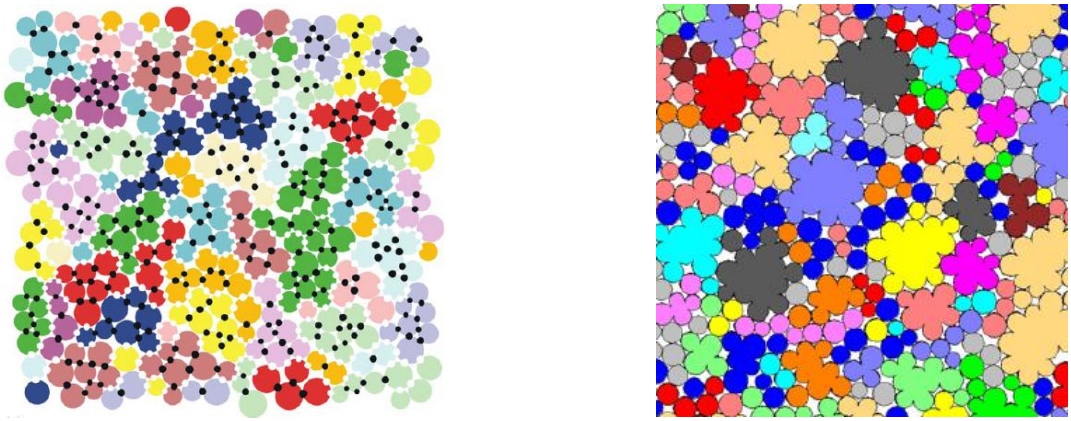

(a) (b)

Figure 3-4: a) A clustered particle model with 7 particles bonded inside each cluster. Black circles refer to intra-cluster bonds and white circles refer to inter-cluster bonds (after Potyondy and Cundall, 2004); b) a clumped particle model (after Yoon et al., 2012).

3.3.1.3 Clumped particle model

A clump consists of more than one particle but moves as a single rigid object (Figure 3-4b). Cho et al. (2007) used the clumped particle model and were able to overcome the limitations of the conventional ball and clustered particle models mentioned earlier.

Cho et al. (2007) showed that dilation significantly increased with increasing clump size. However, the strength ratio (σ_t/UCS) remained close to 0.07, similar to that of a crystalline rock. Moreover, they found an excellent agreement between the failure envelope predicted by the clumped particle model and that of *LdB* granite. The clumped particle model was later used by Bahrani et al. (2011a; 2012a; 2012b), to simulate drilling-induced core damage and Yoon et al. (2012) to simulate fracturing of Aue granite under confined asymmetric loading.

3.3.1.4 Grain-based model

A major practical limitation of the clumped particle model is that the grains are rigid and unbreakable. Laboratory tests show that this is not a realistic assumption as grain crushing occurs in compression tests (Mosher et al., 1975; Erarsalan and Williams, 2012), especially at high confinement (Gatelier et al., 2002). Similarly, rock blocks, and not just block boundaries, fail when a rockmass fails. To resolve this issue, Potyondy (2010) developed a methodology in *PFC2D*, called the grain-based model (*GBM*), which generates a synthetic material that simulates a rock with an assembly of deformable, breakable, polygonal grains. The grain structure generation procedure is described by Potyondy (2010).

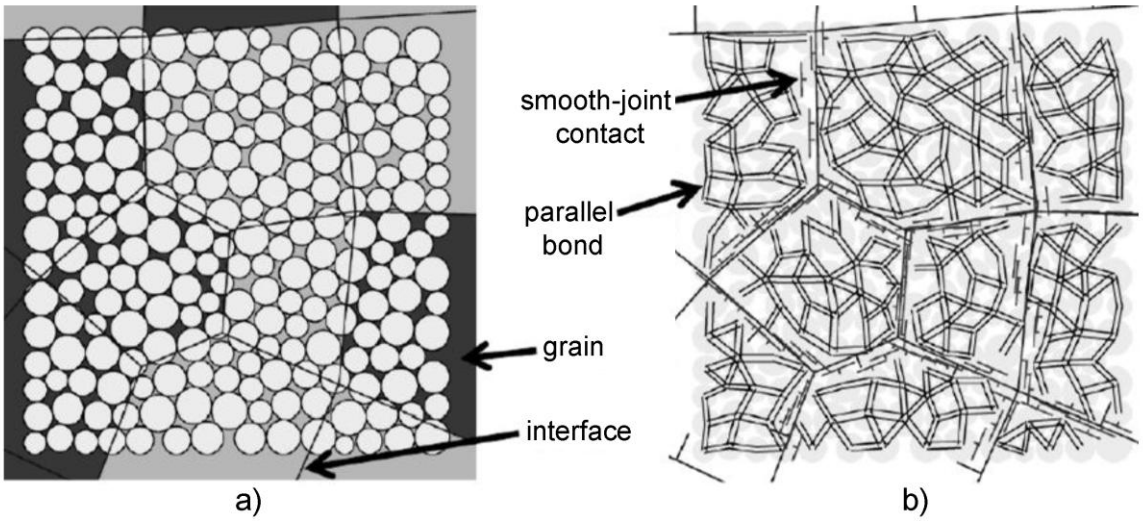

Figure 3-5: a) Grain structure overlaid on a ball model; b) *GBM* consisting of balls bonded together with parallel bonds inside the grains and smooth-joint contacts along the grain boundaries (after Potyondy, 2010).

The *GBM* is generated by overlaying the grain structure on a conventional ball model, with a number of smaller balls to fill the grains. The balls inside the grains are bonded using parallel bonds and this produces deformable and breakable grains. The grain structure is replaced by smooth-joint contacts (described below). An illustration of a grain assembly with parallel bonds and smooth-joint contacts in a *GBM* is shown in Figure 3-5a and b.

The smooth-joint contact simulates the behavior of an interface regardless of the local particle contact orientation along the interface. The use of smooth-joint contacts to simulate the behavior of joints in a rockmass has been investigated by Hadjigeorgiou et al. (2009), Esmaieli et al. (2010), Mas Ivars et al. (2011), Chiu et al. (2013), and Zhang and Stead (2015).

Figure 3-6a and b shows a parallel bond and a smooth-joint contact before bond breakage. Ball movements after breakage of the parallel bond and smooth-joint contact are shown in Figure 3-6c and d. The strength of parallel bond and smooth-joint contact is defined by the tensile

strength, cohesion and friction angle. When a parallel bond breaks (either in shear or tension), the residual strength is controlled by the friction coefficient of the balls in contact and the ball size, which generates a local dilation and causes the balls to move around each other (Figure 3-6c). However, when a smooth-joint contact breaks (either in tension or shear), its residual strength is defined by the smooth-joint friction coefficient. The balls that are located on opposite sides of a smooth-joint plane can overlap to allow particle sliding along the joint plane (with no local geometric dilation as shown in Figure 3-6d) rather than forcing the balls to move around one another. The movements of particles along a joint plane simulated with smooth-joint contacts during the seating process of a specimen in *PFC2D* and *PFC3D* are presented in Figure 3-7a and b, respectively.

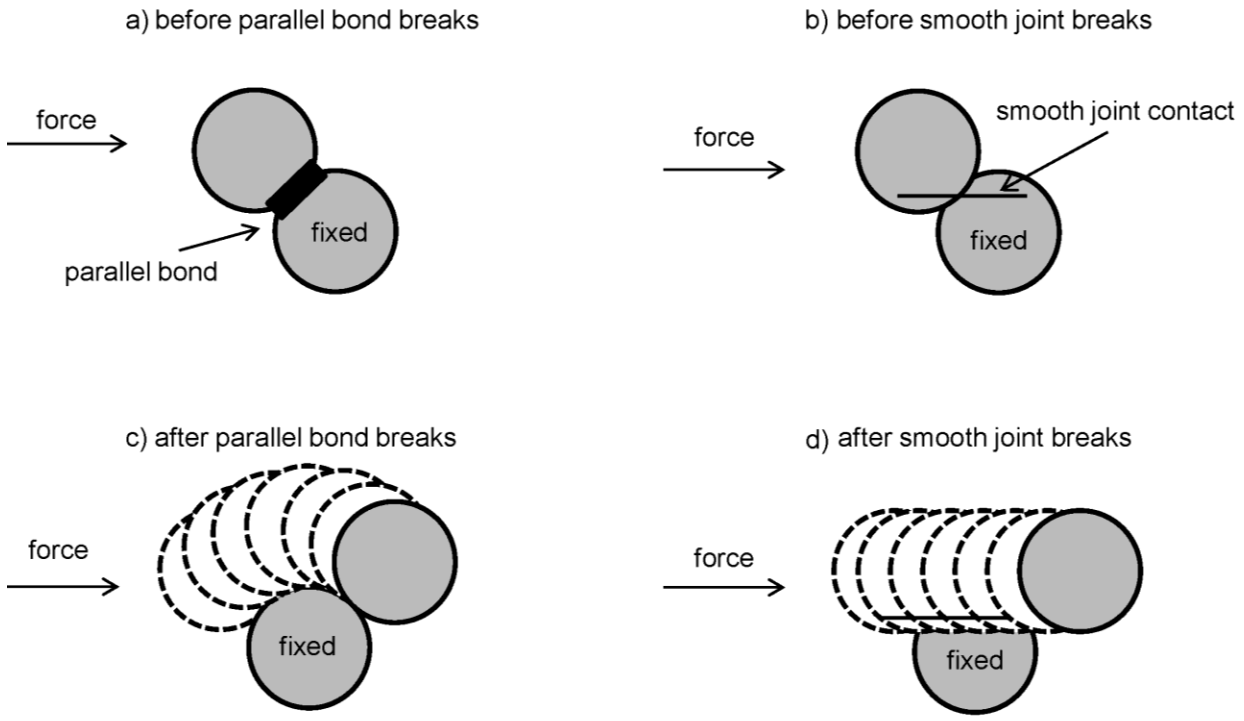

Figure 3-6: Movements of balls after breakage of parallel bond and smooth-joint contact (after Bahrani et al., 2013).

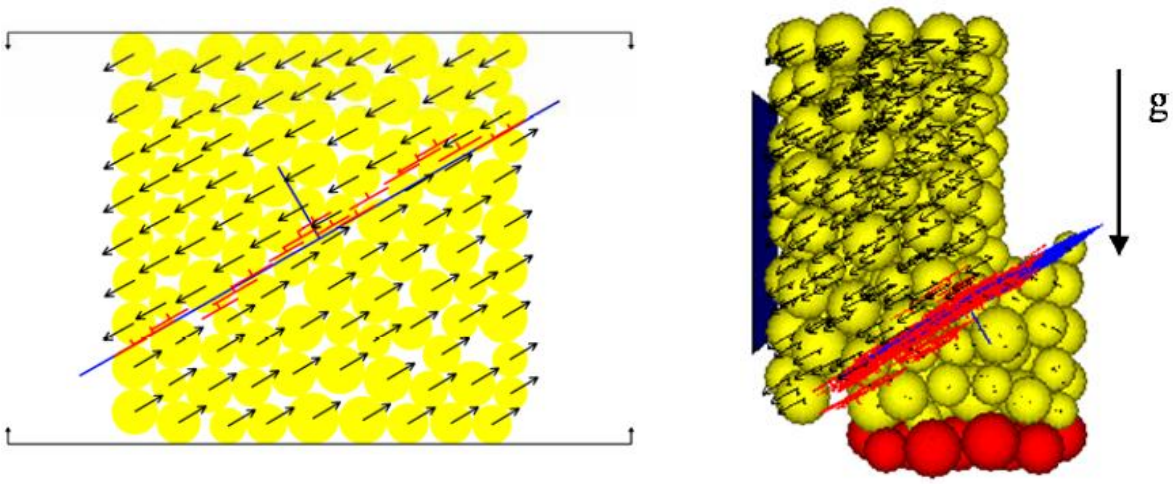

(a) (b)

Figure 3-7: Velocity field while seating a specimen consisting of an inclined joint plane simulated using smooth-joint contacts in: a) *PFC2D*; and b) *PFC3D* (after Itasca, 2008a; 2008b).

Once the smooth-joint contact is created, its stiffness properties are inherited from the contact and the two contacting balls, according to the following equations:

$$\bar{k}_n = (k_n / A) + \bar{k}^n \qquad \text{Equation 3-1}$$

$$\bar{k}_s = (k_s / A) + \bar{k}^s \qquad \text{Equation 3-2}$$

$$A = 2\bar{R}t, \quad t = 1.0 \qquad \text{Equation 3-3}$$

$$\bar{R} = \bar{\lambda} \min(R^A, R^B) \qquad \text{Equation 3-4}$$

where, $\bar{k}_n$ and $\bar{k}_s$ are the smooth-joint contact normal stiffness and shear stiffness, respectively; k_n and k_s are the contact normal stiffness and shear stiffness, respectively; and $\bar{k}^n$ and $\bar{k}^s$ are the parallel bond normal stiffness and shear stiffness, respectively. *A* is the cross sectional area of the smooth-joint contact, *t* is the ball thickness, $\bar{R}$ is the smooth-joint contact radius (i.e., half

length of the smooth-joint contact) which is a multiple, $\bar{\lambda}$, of the two particle radii, R^A and R^B. The ball thickness and radius multiplier have a value of 1 by default.

Note that the smooth-joint normal stiffness and shear stiffness are assigned as a factor of the stiffness inherited from the contact and the two contacting balls. This factor controls the Young's modulus of the *GBM* and is called the stiffness factor.

3.3.2 Calibration of PFC model to laboratory properties of intact rock

The calibration of a *BPM* is usually carried out by manually adjusting the micro-properties of the particles and the bonds until the macroscopic properties of the *BPM* match those of rock specimens. Yoon (2007), Wang and Tonon (2009; 2010) developed methodologies for calibrating 2D and 3D *BPM*s based on an optimization process, and by obtaining relationships between micro-properties and macro-properties through parameter sensitivity analyses. Yoon (2007) showed the applicability of his method for calibrating the *BPM* to laboratory properties of rock materials with *UCS* ranging from 40 MPa to 170 MPa, Young's modulus ranging from 20 GPa to 50 GPa, and Poisson's ratio ranging from 0.19 to 0.25. The calibration process suggested by Wang and Tonon (2010) showed a reasonable agreement between simulated and experimental results in terms of deformability and unconfined and confined strengths.

Cho et al. (2007) questioned the calibration process which is based on matching the *UCS* and suggested that such a calibrated model would only be adequate for simulating materials under unconfined conditions and only for tests in compression. The clumped particle model has also been used by Yoon et al. (2011; 2012) to reproduce not only the *UCS*, Young's modulus, and Poisson's ratio, but also crack initiation and crack damage stresses of Aue granite.

Since the clumps are unbreakable and rigid, the calibration of the clumped particle model requires adjustment of the micro-properties representing those of rock grain boundaries (i.e., strength and stiffness), but not the grains. However, due to the number of micro-parameters the solution is in general not unique and different combinations of micro-properties can result in the same macro-properties. As a means to reduce the number of possible solutions Bahrani et al. (2011b) proposed an approach, whereby the clumped particle model macro-properties are calibrated to laboratory properties of intact and damaged rock specimens (i.e., *LdB* granite) through an iterative adjustment of the micro-properties.

For the *GBM* with breakable grains, the micro-properties of both grains and grain boundaries must be defined. Therefore, the number of micro-properties in the *GBM* with breakable grains is about two times that of the clumped particle model. This drastically increases the non-uniqueness of the solution, when the *GBM* with breakable grains is used. The results of calibration of the *GBM* to laboratory properties of Äspö Diorite, *LdB* granite, Wombeyan marble, Lodève sandstone have been reported by Potyondy (2010), Bahrani et al. (2011a; 2011b); Bahrani et al. (2014), and Bewick et al. (2015a; 2015b), respectively.

Table 3-1 compares the four approaches in *PFC2D* including the ball model, the clustered and clumped particle models and the grain-based model, and evaluates their applicability for simulating brittle rocks.

Table 3-1: Comparison between approaches in *PFC2D* for simulating brittle rocks (e.g., LdB granite).

Model type	Bond model		Breakable grain	Is model capable of matching		
	Grain	Grain boundary		σ_t/UCS = 0.05	Non-linear envelope	Friction angle
Ball	-	Parallel bond	No	No	No	No
Clustered	Parallel bond	Parallel bond	Yes	No	Yes	Yes
Clumped	-	Parallel bond	No	Yes	No	Yes
Grain-based	Parallel bond	Smooth-joint	Yes	Yes	Yes	Yes

As can be seen in Table 3-1, the *GBM* is the most appropriate approach and therefore is chosen for simulating the laboratory response of intact and granulated Wombeyan marble, which is described next.

3.4 PFC2D Grain-based Model for Wombeyan Marble

3.4.1 Model geometry

A 20 mm × 50 mm grain-based synthetic specimen was generated to simulate the laboratory behavior of intact and granulated Wombeyan marble. The synthetic specimen is therefore smaller than the laboratory specimens reported by Gerogiannopoulos (1976). This was required to reduce the calculation time while matching the grain-based specimen grain size with actual rock grain size. According to Potyondy and Cundall (2004), scale effects are not significant when simulating rocks in compressive loading conditions in *PFC*, provided the ball size is relatively small compared to the size of the synthetic specimen.

The average grain size of Wombeyan marble according to Gerogiannopoulos (1978) and Rosengren and Jaeger (1969) is between 1 and 2 mm. A grain structure containing two different-sized equally and randomly distributed polygonal grains with average grain size of 1 and 2 mm was generated (Figure 3-8a) according to the procedure described by Potyondy (2010). No

attempt was made to match the grain size distribution of the grain-based specimen to that of Wombeyan marble. Moreover, to simplify the calibration process, only one grain type was considered. Note that the ratio of the largest grain to specimen diameter used in the simulation is 0.1, which is in agreement with that suggested by the *ISRM* (Bieniawski and Bernede, 1979). Furthermore, in the grain-based specimen (Figure 3-8b), each grain is made of multiple balls with a maximum diameter of 0.4 mm. This ensures that the maximum ball size is smaller than the minimum grain size and that each grain is made of more than 5 balls. An example of the micro-structure of Wombeyan marble is shown in Figure 3-8c.

The *GBM* used to simulate intact Wombeyan marble is called "intact (or undamaged) grain-based specimen", and the *GBM* used to simulate granulated Wombeyan marble is called "fully damaged grain-based specimen".

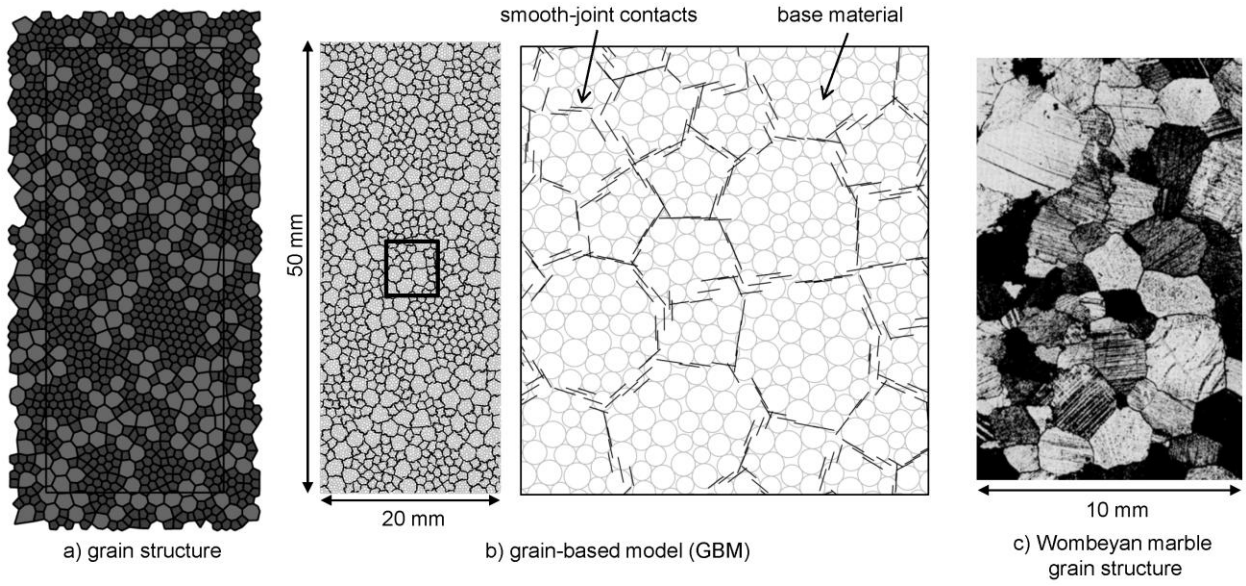

Figure 3-8: a) Grain structure containing polygonal grains with average grain size of 1 mm (dark gray grains) and 2 mm (light gray grains); b) grain-based specimen in which the grain structure is replaced by smooth-joint contacts. The parallel bonds joining the balls inside the grains are not shown in this figure; c) micro-structure of Wombeyan marble (from Rosengren and Jaeger, 1969).

It should be noted that in the numerical simulation of a laboratory compression test using the *DEM*, the strength of synthetic specimen is dependent on the loading rate, similar to a rock specimen tested in the laboratory. In this case, the loading rate is chosen that is slow enough to ensure quasi-static response (Itasca, 2008a). The quasi-static response is the response obtained when the test has been conducted under quasi-static conditions. This means that the loading has been slow enough that the system has time to adjust to the force redistribution that accompanies each nonlinear event (slip or bond breakage). In *PFC*, the quasi-static response can be obtained by reducing the strain rate until the strength is independent of the strain rate. In a compression test simulation in *PFC*, the synthetic specimen is loaded by moving the platens (frictionless walls) toward one another at a final velocity, υ_p, determined by specifying the strain rate, $\varepsilon_{p,}$ according to:

$$\upsilon_p = \frac{1}{2}\varepsilon_p L_0 \qquad \text{Equation 3-5}$$

where, L_0 is the initial specimen length. According to this equation, the strain rate is inversely proportional to the specimen length. Therefore, for a given platen velocity, the strain rate should be reduced as the specimen length is increased. All the compression tests discussed in this chapter were simulated with the strain rate of 1.0, as it was determined that running the grain-based specimens at a smaller strain rate would not impact the macroscopic strength.

3.4.2 Calibration assumptions

A calibration procedure was developed by Bahrani et al. (2014) to match the unconfined and confined strengths of the grain-based models to those of intact and granulated Wombeyan marble. The main assumptions made by Bahrani et al. (2014) are summarized as follows:

1) Heating intact Wombeyan marble affected the mechanical properties of the grain boundaries, but not the grains (i.e., by destroying the bonds between the grains). Therefore, components of grains (parallel bonds and balls) were assigned the same micro-properties in the undamaged (i.e., intact) and fully damaged (i.e., granulated) grain-based specimens.

2) The grain boundaries in the granulated Wombeyan marble have zero tensile strength and cohesion in shear. Therefore, tensile strength and cohesion of all the smooth-joint contacts in the fully damaged grain-based specimen were set to zero.

3) Heating intact Wombeyan marble had no impact on the frictional properties of the grains and grain boundaries. Therefore, the smooth-joint contacts were assigned the same value of friction angle in the undamaged (i.e., intact) and fully damaged (i.e., granulated) grain-based specimens.

Figure 3-9a and b show the adopted shear strength envelopes for smooth-joint contacts (grain boundaries) in the undamaged and fully damaged grain-based specimens, respectively. In the undamaged grain-based specimen, the strength of smooth-joint contacts is represented by tensile strength and cohesion (Figure 3-9a).

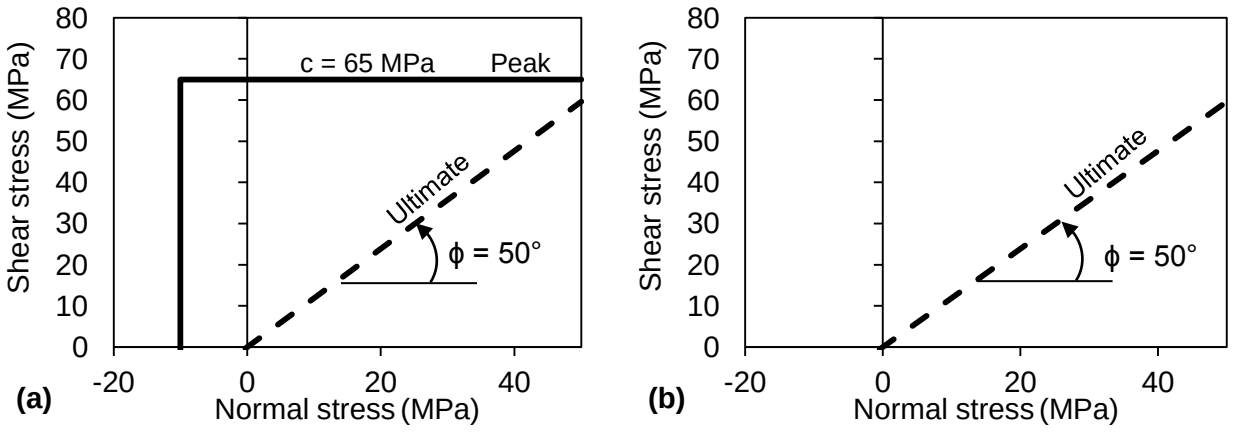

Figure 3-9: Strength envelopes for smooth-joint contacts in: a) intact (or undamaged) grain-based specimen; and b) fully damaged grain-based specimen.

When a smooth-joint contact fails either in tension or shear, its strength is defined by the friction coefficient with a value of 1.2 (i.e., equivalent friction angle of 50°). In the fully damaged grain-based specimen, the strength of smooth-joint contacts is only defined by its frictional property (i.e., equivalent friction angle of 50°) as illustrated in Figure 3-9b. As mentioned above, the friction angle of the damaged smooth-joint contacts in the fully damaged grain-based specimen is the same as that of failed smooth-joint contacts in the undamaged grain-based specimen.

3.4.3 Calibration Procedure

Based on the assumptions mentioned above, the numbers of independent unknown micro-properties are: 1 for the grain boundaries and 3 for the grains in the fully damaged grain-based specimen, and 3 for the grain boundaries and 3 for the grains in the undamaged grain-based specimen. The calibration process was started by adjusting the micro-properties of the fully damaged grain-based specimen in a systematic manner as described in the following steps and shown in the flow chart shown in Figure 3-10.

1) Calibration to granulated Wombeyan marble tensile and unconfined compressive strengths, and Young's modulus: As a starting point, arbitrary micro-properties had to be chosen for the unknown parameters. The nearly zero tensile strength of the granulated marble was automatically achieved by assigning zero normal (tensile) strength to the smooth-joint contacts. Since the values of the smooth-joint cohesion and friction coefficient have been defined in the assumptions for the fully damaged grain-based specimen, the only micro-parameters that control the *UCS* of fully damaged grain-based specimen were parallel bond normal (tensile) strength and cohesion (i.e., grain strength micro-properties).

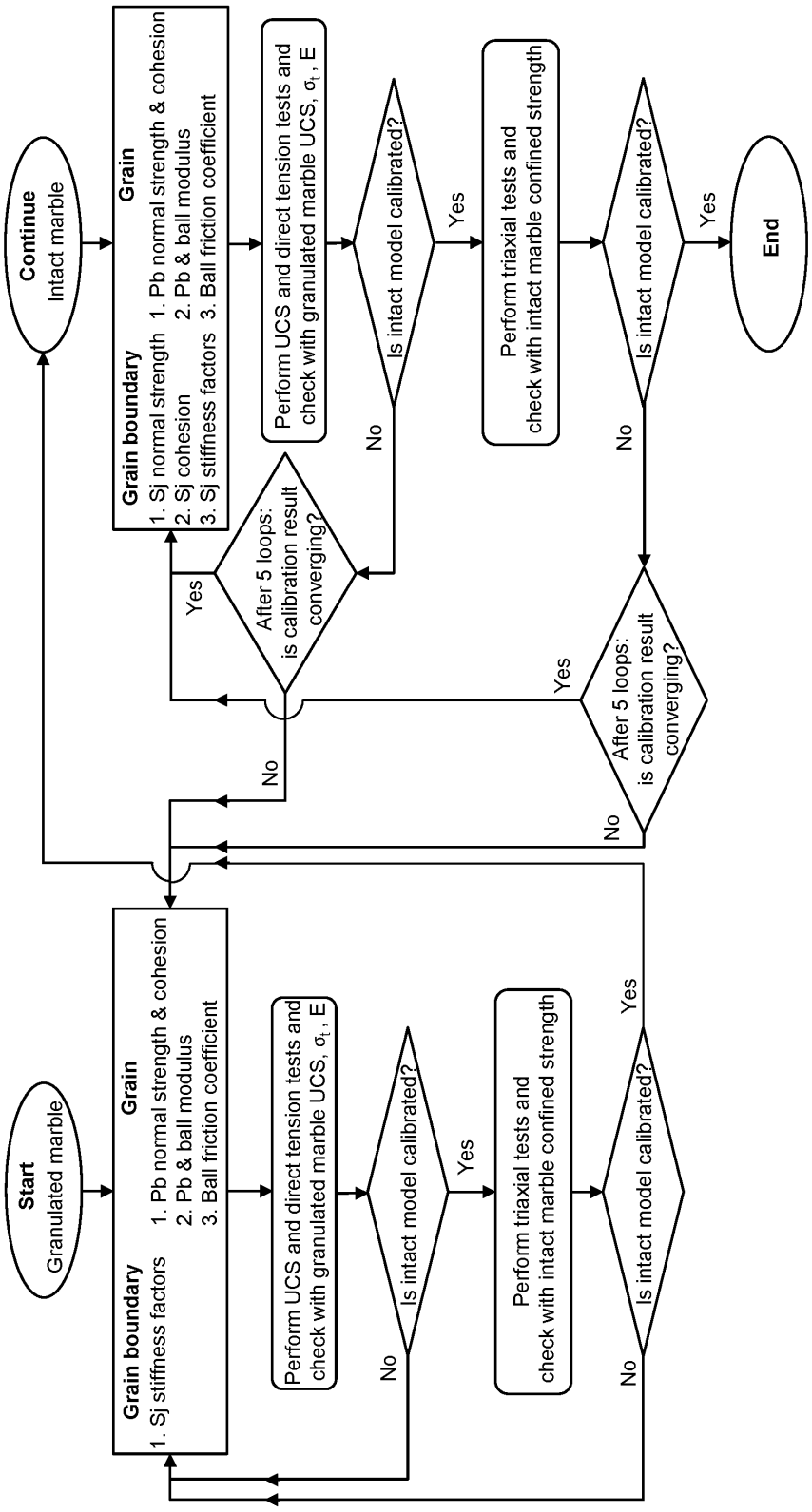

Figure 3-10: Procedure for calibrating the grain-based model to laboratory properties of intact and granulated Wombeyan marble (*Sj* stands for smooth-joint and *Pb* stands for parallel bond).

The Young's modulus of the granulated marble was obtained by adjusting the stiffness factor of smooth-joint contacts. These parameters were manually adjusted until the tensile and unconfined compressive strengths, and Young's modulus of the fully damaged grain-based specimen were matched with those of granulated Wombeyan marble (first internal loop for granulated marble in Figure 3-10).

2) Calibration to granulated Wombeyan marble confined strength: Triaxial test simulations were then carried out with the parameters obtained from step one. The micro-properties of the grains including the parallel bond normal strength and cohesion, and ball friction coefficient affect the confined strength of the fully damaged grain-based specimen. Once changes in these parameters were made, step one was repeated to ensure calibration with respect to the strength and Young's modulus of granulated Wombeyan marble (second internal loop for granulated marble in Figure 3-10).

3) Calibration to intact Wombeyan marble tensile and uniaxial compressive strengths and Young's modulus: The tensile strength of the undamaged grain-based specimen was matched by adjusting the smooth-joint normal strength (Wombeyan marble tensile strength is 7 MPa). The *UCS* of the undamaged grain-based specimen was found to be correlated to the smooth-joint cohesion, parallel bond normal strength and cohesion, and ball friction coefficient. The Young's modulus of the undamaged grain-based specimen was also found to be correlated with the parallel bond and ball modulus as well as the smooth-joint stiffness factor. At this stage, if a match with the properties of intact marble was not achieved (the micro-properties did not converge to target properties after five internal loops), calibration had to be redone from step 1 (first external loop in Figure 3-10).

4) Calibration to intact marble confined strength: The grain-based specimen which was previously calibrated to the *UCS* of intact marble was tested for its confined strength. The confined strength of the undamaged grain-based specimen is correlated to parallel bond normal strength, cohesion and ball friction coefficient. Similar to the previous step, if after five internal loops the model properties did not converge to the target properties, the calibration had to be redone from step 1 (second external loop in Figure 3-10).

As discussed by Bahrani et al. (2014), the adopted calibration procedure is an iterative procedure whereby, at each step, the number of trials to achieve an acceptable macro-property was kept to a manageable number by choosing one key micro-property (e.g., smooth-joint tensile strength to match model tensile strength). However, due to the large number of micro-properties included in the *GBM* and despite the number of imposed constraints explained above, the system is still indeterminate. This means that multiple combinations of micro-properties can lead to equivalently well calibrated but not unique calibration result. The solution presented here represents such a model that is qualitatively equivalent to other possible solutions. This lack of uniqueness, however, is not seen as a deficiency as combinations of materials with different properties in nature (e.g., different mineralogical assemblage) can also lead to similar behaviors in terms of failure mechanisms, strength and deformability. The *GBM* presented here is thus considered a valid model for investigating different aspects of confinement-dependent rock and rockmass failure processes as long as they remain within the scope, for which the *GBM* was calibrated.

3.4.4 Calibration results

The confined Young's modulus rather than unconfined Young's modulus of the granulated marble was matched during the calibration process because the opening of the grain boundaries in the granulated marble caused by heating is not explicitly simulated. As a consequence, re-closure along the grain boundaries as a result of increasing confinement and applying axial load in unconfined and confined compression tests is not captured by the *GBM* for the fully damaged grain-based specimens.

A smooth-joint stiffness factor of 0.2 was required to match the confined Young's modulus of granulated marble. As a consequence and as shown in Figure 3-11, the resulting Young's modulus of the fully damaged specimen corresponds with that of granulated Wombeyan marble at confining pressures greater than 17 MPa.

It was found that only in this case can the unconfined and confined strengths of the undamaged and fully damaged grain-based specimens be matched with those of intact and granulated Wombeyan marble as shown in Figure 3-12. This figure also demonstrates that all the calibration criteria discussed earlier including the direct tensile strength, the uniaxial compressive strength, the friction angle and the non-linear failure envelope can be captured well with the *GBM*.

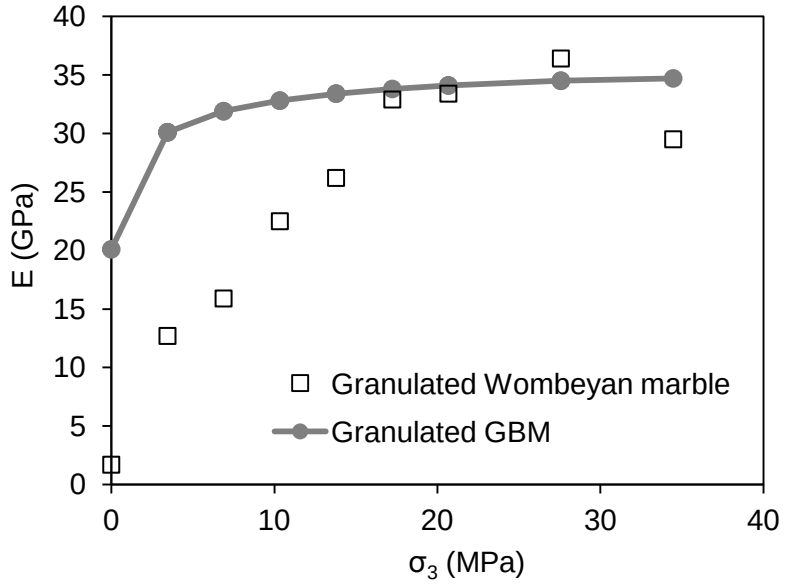

Figure 3-11: Confined Young's modulus of granulated Wombeyan marble considered for calibration. In this case, the Young's modulus at low confinement is significantly overestimated by the *GBM*.

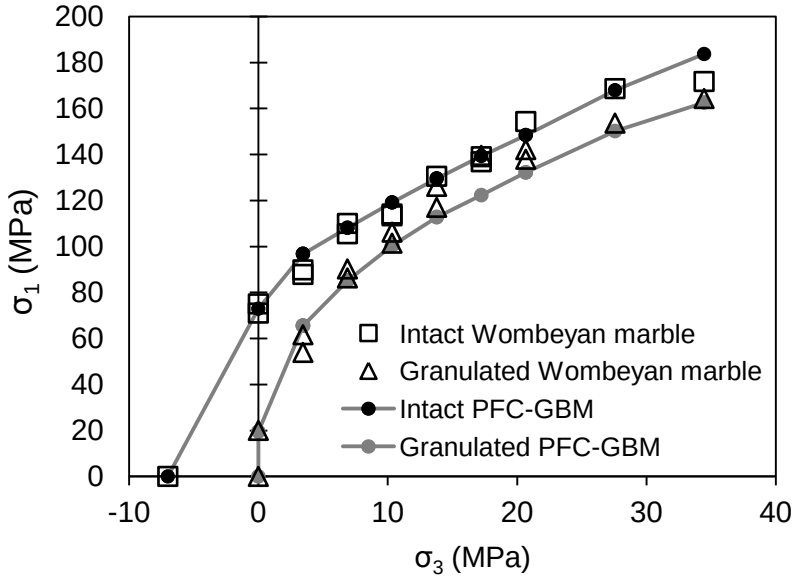

Figure 3-12: Illustration of correspondence between unconfined, confined and tensile strengths of numerical simulation and laboratory test results of intact and granulated marble, when confined Young's modulus of granulated marble is matched during calibration.

Table 3-2 and Table 3-3 summarize the micro-properties of the grains and grain boundaries in the undamaged and fully damaged grain-based specimens obtained through the calibration

process. As presented in Table 3-2, the grains in both undamaged and fully damaged grain-based specimens were assigned the same micro-properties, based on the assumption that heating the intact marble did not affect the mechanical properties of the grains. Only changes in the smooth-joint properties, representing the grain boundaries, were required to simulate the transition from intact to granulated marble (Table 3-3). The smooth-joint contacts have the same frictional properties in the undamaged and fully damaged grain-based specimens.

Table 3-2: Calibrated micro-properties of the grains (balls and parallel bonds) in the undamaged and fully damaged grain-based specimens.

Micro-properties	Undamaged and fully damaged
minimum particle (ball) radius	0.12 mm
ratio of maximum to minimum ball radius	1.66
contact normal to shear stiffness ratio	2.5
parallel bond normal to shear stiffness ratio	2.5
contact modulus	50 GPa
parallel bond modulus	50 GPa
ball friction coefficient	0.5
parallel bond radius multiplier	1
parallel bond normal (tensile) strength	110 MPa
parallel bond cohesion	110 MPa
parallel bond friction angle	0°

Table 3-3: Calibrated micro-properties of the grain boundaries (smooth-joint contacts) in the undamaged and fully damaged grain-based specimens.

Micro-properties	Undamaged	Fully damaged
smooth-joint normal to shear stiffness ratio	2.5	2.5
smooth-joint stiffness factor	0.8	0.2
smooth-joint normal (tensile) strength	10 MPa	0 MPa
smooth-joint cohesion	65 MPa	0 MPa
smooth-joint friction angle	0°	0°
smooth-joint friction coefficient	1.2	1.2

3.4.5 Failure mode and micro-cracking

The location, orientation, and type of both inter- and intra-grain micro-cracks (tensile and shear) in the undamaged and fully damaged synthetic specimens simulated in uniaxial and triaxial compression with 3.5 MPa and 34.5 MPa confining pressures are illustrated in Figure 3-13. This figure shows all of the micro-cracks that formed from the beginning of the test to the point when a 20% and 10% stress drop occurred in the post-peak response of unconfined and confined compression tests, respectively.

Undamaged grain-based specimen: in the uniaxial compression test (Figure 3-13a), the micro-cracks are oriented approximately parallel to the axial load direction. Most of the fractures are inter-grain tension cracks. When the micro-crack density was sufficiently high, the interaction of the sub-vertical micro-cracks resulted in a macroscopic axial fracture. In the confined compression tests (Figure 3-13b and c), the interaction between inter- and intra-grain micro-cracks formed macroscopic shear bands. This is more pronounced at higher confinement (with 34.5 MPa confining pressure for Figure 3-13c), where conjugate shear rupture zones consist of several intra-grain tensile cracks. The failure modes predicted by the *GBM* at 0 MPa, 3.5 MPa and 34.5 MPa confining pressures are representative of those observed by Paterson (1958) in the laboratory as shown in Figure 3-13.

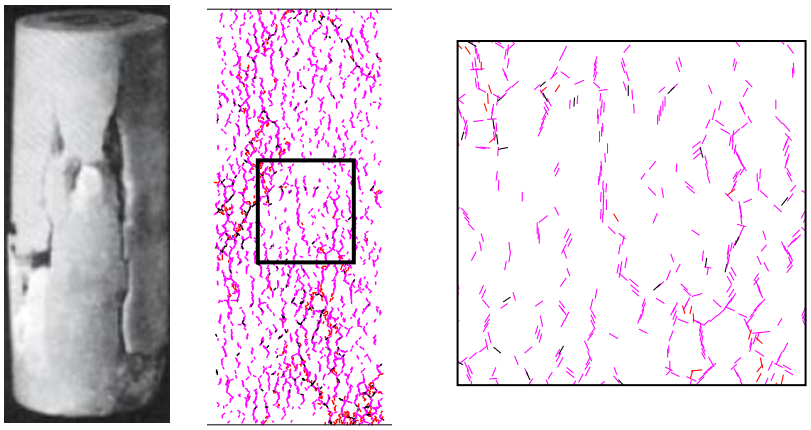

(a) σ_3 = 0 MPa

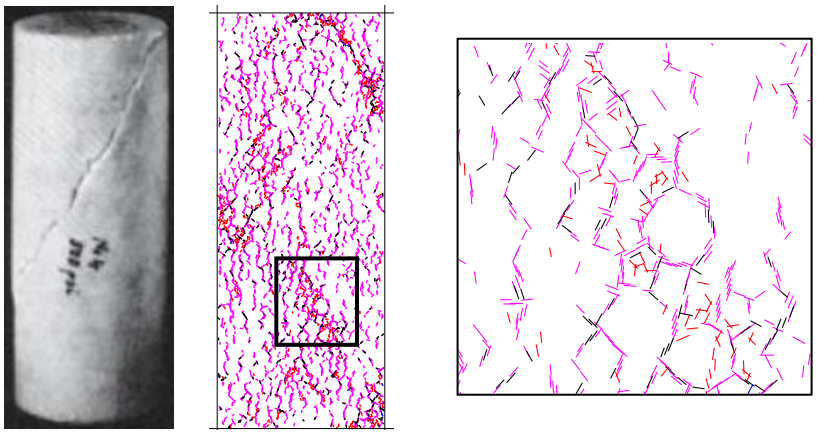

(b) σ_3 = 3.5 MPa

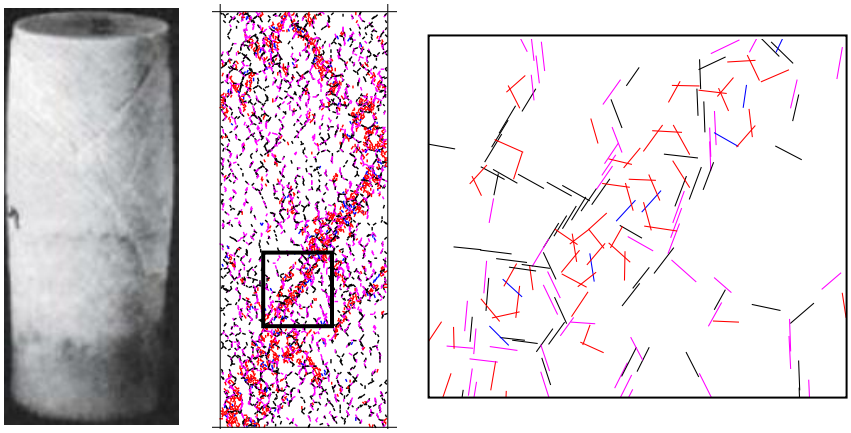

(c) σ_3 = 34.5 MPa

Figure 3-13: Comparison between failure modes of intact Wombeyan marble tested by Paterson (1958) and those predicted by the *GBM* in: a) unconfined compression; b) 3.5 MPa confined; and c) 34.5 MPa confined tests. Pink and black refer to inter-grain tensile and shear micro-cracks, respectively, and red and blue refer to intra-grain tensile and shear cracks, respectively.

Fully damaged grain-based specimen: as mentioned in *Section 3.4.2*, due to the frictional state of the grain boundaries only micro-cracks inside the grains can be seen during these simulations. In the uniaxial compression test (Figure 3-14a), the fully damaged grain-based specimen fails mainly by opening of the grain boundaries and sliding along them, which generates large amounts of geometric dilation as can be seen in Figure 3-15.

Relatively few intra-grain tensile cracks are developed at zero confinement. However, a small amount of confining pressure (i.e., 3.5 MPa in Figure 3-14b) prevents the grains from opening and freely sliding along their boundaries. As a result, the number of intra-grain tensile micro-cracks rapidly increases with increasing confinement. This is more pronounced at a confining pressure of 34.5 MPa (Figure 3-14c), where the interaction between several intra-grain tensile micro-cracks and a number of intra-grain shear micro-cracks generates macroscopic shear fractures similar to those seen in the undamaged synthetic specimen (compare Figure 3-13c and Figure 3-14c).

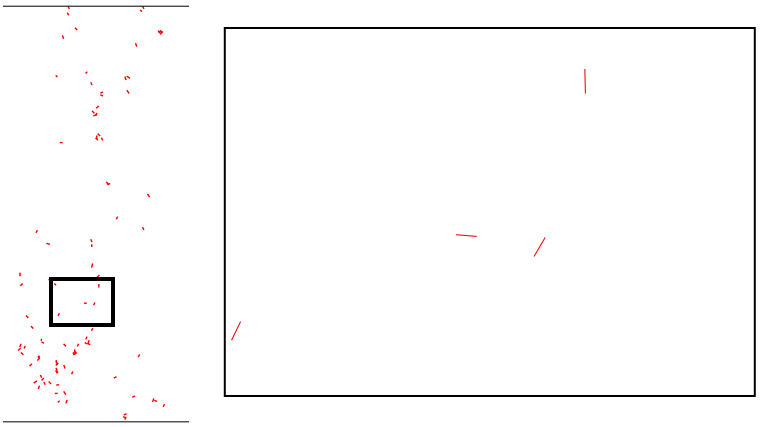

(a) σ_3 = 0 MPa

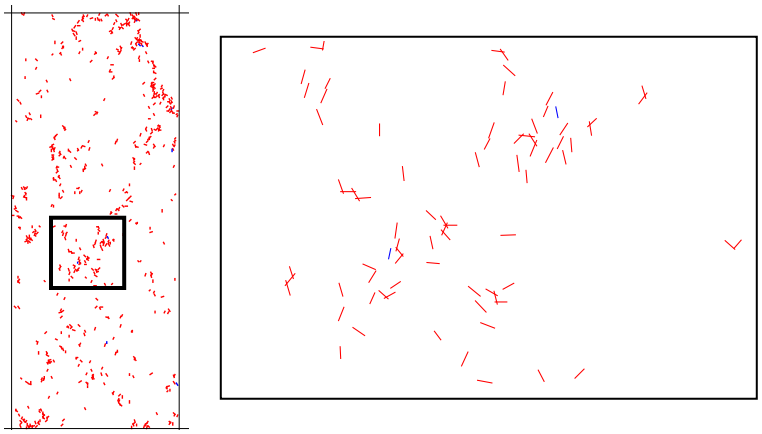

(b) σ_3 = 3.5 MPa

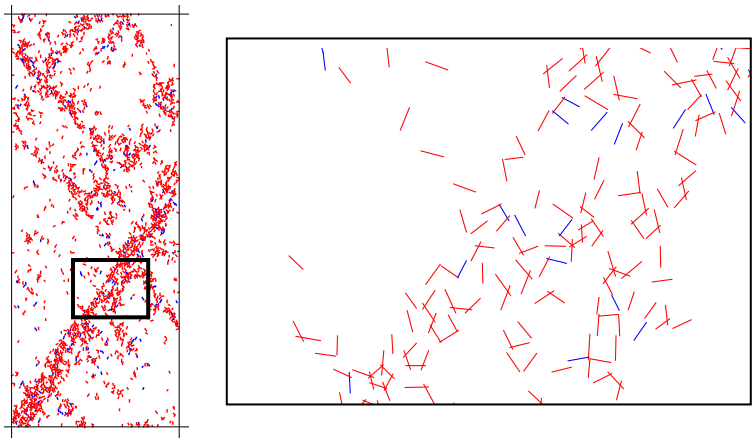

(c) σ_3 = 34.5 MPa

Figure 3-14: Failure modes of the fully damaged grain-based specimen in: a) unconfined; b) 3.5 MPa confined; and c) 34.5 MPa confined tests. Red and blue refer to intra-grain tensile and shear micro-cracks, respectively.

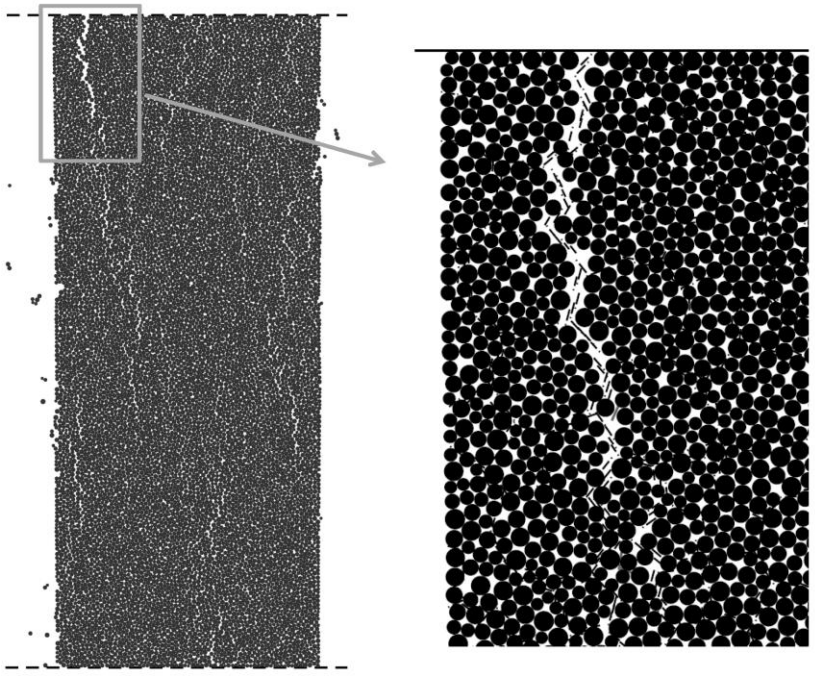

Figure 3-15: Macroscopic fractures and large geometric dilation due to opening of grain boundaries in the fully damaged grain-based specimen in the unconfined compression test (smooth-joint contacts are shown with black lines in the right figure).

The stress-strain curves as well as the number of micro-cracks generated in the undamaged and fully damaged grain-based specimens deformed in uniaxial and triaxial compression with 3.5 and 34.5 MPa confining pressures are presented in Figure 3-16. The following observations can be made from these graphs:

- the transition from brittle, at zero or low confinement, to more ductile with much reduced post-peak strength reduction at high confinement, is evident from the stress-strain curves, especially in the case of the undamaged grain-based specimen;
- failure starts by tensile cracking; inter-grain tensile micro-cracks in the undamaged grain-based specimen and intra-grain tensile micro-cracks in the fully damaged grain-based specimen;
- the number of shear micro-cracks (inter-grain or intra-grain cracks) increases with increasing confinement;

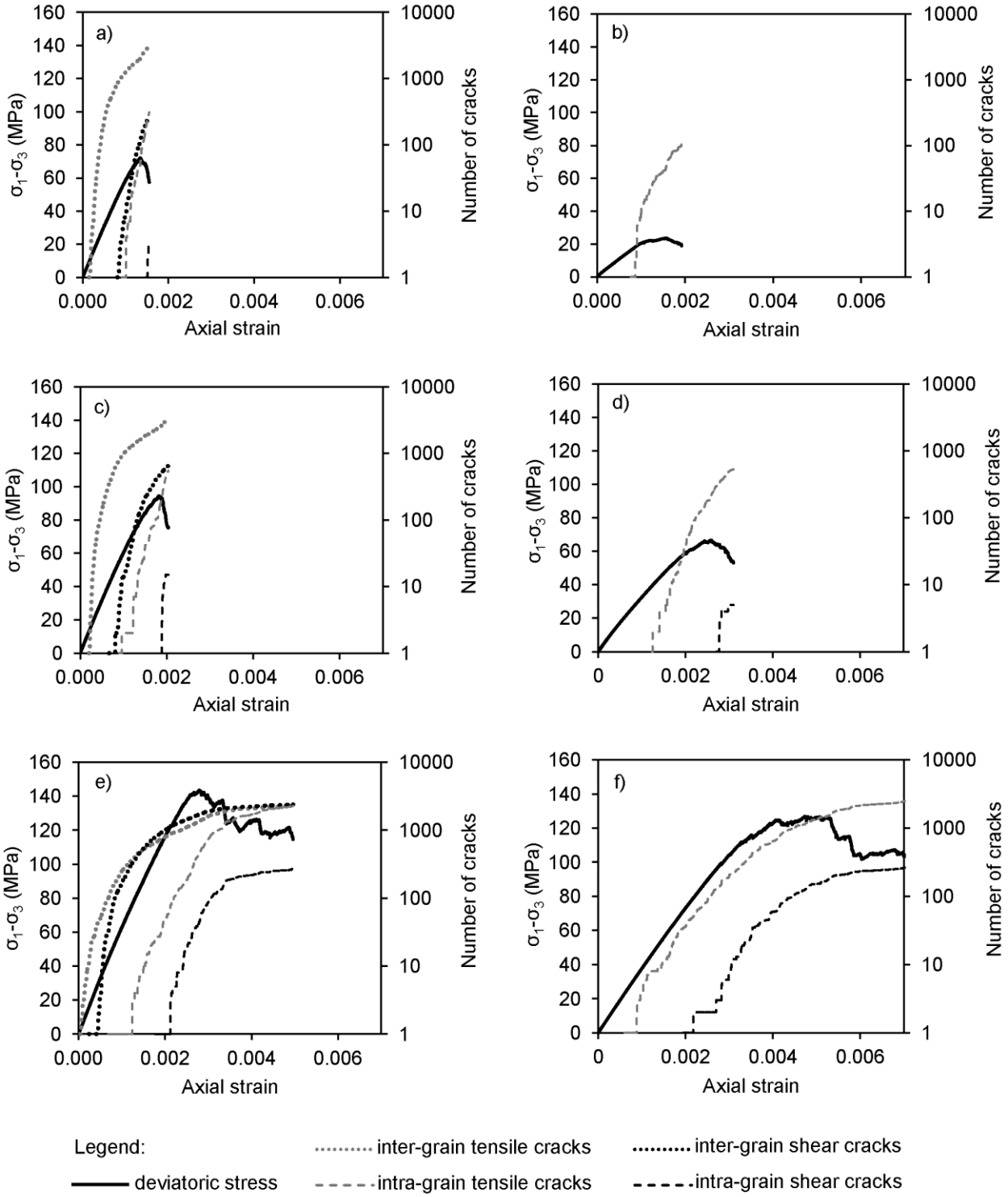

Figure 3-16: Stress-strain curves and numbers of inter- and intra-grain tensile and shear micro-cracks for: a) undamaged grain-based specimen at σ_3 = 0 MPa; b) fully damaged grain-based specimen at σ_3 = 0; c) undamaged grain-based specimen at σ_3 = 3.5 MPa; d) fully damaged grain-based specimen at σ_3 = 3.5 MPa; e) undamaged grain-based specimen at σ_3 = 34.5 MPa; f) fully damaged grain-based specimen at σ_3 = 34.5 MPa.

- inter- or intra-grain tensile micro-cracks always initiate before inter- or intra-grain shear micro-cracks;
- in the undamaged grain-based specimen, intra-grain tensile micro-cracks initiate before the peak strength is reached, and intra-grain shear micro-cracks initiate in the post-peak region; and
- In the fully damaged grain-based specimen, the intra-grain shear micro-cracks initiate before peak stress, but only at high confinement (i.e., 34.5 MPa).

In summary, the *GBM* calibrated to the properties of intact and granulated Wombeyan marble was confirmed to be a suitable numerical method for simulating the characteristics of hard brittle rocks in terms of strength, failure mode and stress-strain response under different stress paths, and was therefore used to simulate micro-defected and defected rocks and jointed rockmasses, which will be demonstrated in the following chapters.

3.5 Summary and Conclusions

The grain-based model embedded in *PFC2D* was successfully applied to simulate the laboratory response of intact and granulated Wombeyan marble. After calibrating the undamaged and fully damaged grain-based specimens to the properties of intact and granulated Wombeyan marble, the following can be concluded:

- the *GBM* captures the observed transition in the failure mode of brittle rocks from axial fracturing at low confinement to shear failure at high confinement;
- the *GBM* captures the observed stress-strain response of brittle rocks from brittle behavior (stress drop after peak) at low confinement to more ductile behavior (less step post-peak slopes and maintenance of strength post-peak) with increasing confinement;
- the *GBM* captures the observed tensile to compressive strength ratio of less than 0.05 for brittle failing rocks;
- the *GBM* captures the non-linear failure envelope of brittle failing rocks;

- the *GBM* captures known rock failure processes including fracturing which mainly initiates along the grain boundaries and continues by breaking through the grains as the axial stress reaches and passes the peak stress; and
- the rock failure process is dominated by tensile cracking, and the number of shear cracks increases with increasing confinement.

In the next chapter, the calibrated grain-based specimens are used to simulate damaged rocks containing various damage densities. The results of laboratory test simulations on undamaged and damaged grain-based specimens will be used to develop a semi-empirical approach for estimating the confined strength of micro-defected rocks.

Chapter 4

4 Estimation of Confined Strength of Micro-defected Rocks

4.1 Introduction

In this chapter, the grain-based specimens calibrated in *Chapter 3* to the laboratory properties of intact and granulated Wombeyan marble, are used to simulate rock specimens with varying densities of micro-defects. The micro-defects are simulated in the form of grain boundary frictional micro-cracks, and their influence on the strength, Young's modulus, stress-strain curve and failure mode at different confinement levels is investigated. The results of numerical simulations are then used to develop semi-empirical equations that relate the strength degradation between intact and micro-defected grain-based specimens to the confinement. The applicability of this approach, called the Strength Degradation (*SD*) approach for the estimation of the confined strength of micro-defected rocks is then investigated on the published laboratory test results reviewed in *Chapter 2*.

4.2 Review of the Influence of Micro-defects on Rock Strength

It is known that the presence of micro-defects (e.g., grain and grain boundary micro-cracks) reduces the unconfined compressive strength of laboratory scale rock specimens. For example, Martin and Stimpson (1994) and Eberhardt et al. (1999) found that the observed decrease in the rock strength obtained from cores of *LdB* granite with increasing depth is due to the increase in the density of stress-induced micro-cracks. A similar observation was made by Watson et al. (2009) on samples taken from deep mines in South Africa. Lanaro et al. (2009) reported a strong

negative correlation between rock strength and *in situ* stresses, and explained this observation by the presence of micro-cracks in the samples taken from high stress zones associated with faults. Holt et al. (2000) generated synthetic rocks cured under initial stress and applied an approximate coring stress path to generate damage in the form of micro-cracks in the specimens. The damaged specimens exhibited lower unconfined compressive strength than undamaged specimens. The investigations reviewed above have been focused on the strength of micro-defected rocks under unconfined condition. Unfortunately, the influence of micro-defects on the confined strength of rock has not received as much attention.

It is well known that the rock strength decreases with increasing specimen scale. Hoek and Brown (1997) suggested that the reduction in rock strength with increasing specimen scale is due to the greater opportunity for failure along grain boundaries with pre-existing micro-cracks, as more and more of these features are included in the larger specimens. Eventually, when a sufficiently large number of grains and micro-cracks are included in a specimen, the strength reaches a constant value. The majority of laboratory tests on the influence of scale on rock strength were conducted under unconfined condition. Few investigations conducted on the influence of scale and therefore the presence of micro-defects on the confined strength of rock are limited to very low confining pressures (e.g., Medhurst and Brown, 1998).

The rock strength is also influenced by the presence of veins and cemented joints as the scale of a rock specimen reaches that of a rock block. In the *MRMR* classification system, Laubscher (1990) and Laubscher and Jakubec (2000) introduced correction factors to account for the laboratory scale features (micro-cracks) and the rock block scale features (fracture, veins and cemented joint) to estimate the rock block strength from the strength of the non-defected (or

homogeneous) part of the intact rock block. Again, their approach is limited to the estimation of rock strength under unconfined condition.

The literature reviewed above and in *Chapter 2* reveals that the influence of defects at the grain scale such as grain boundary micro-cracks, and at the specimen scale including fractures and veins on the confined strength of rock specimens has not received much attention in rock engineering. This chapter deals with the confined strength of micro-defected rocks. In the following, various densities of micro-defect, simulated in the form of grain boundary micro-cracks are introduced to the undamaged grain-based specimen calibrated to the properties of intact Wombeyan marble, and the results of triaxial test simulations are used to develop a semi-empirical approach to estimate the confined strength of micro-defected rocks.

4.3 Simulation of Micro-defected Rock

As mentioned in *Chapter 3*, the calibration of the *GBM*s was based on the assumption that heating intact marble affected the mechanical properties of all of the grain boundaries. Based on this assumption, all of the smooth-joint contacts, representing grain boundaries in the model of intact marble were simulated to be cohesive, and all of the smooth-joint contacts in the model of granulated marble were simulated to be frictional. For these reasons, the models of intact and granulated Wombeyan marble are called undamaged and fully damaged grain-based specimens, respectively. In nature, a rock specimen may consist of a combination of cohesive and frictional grain boundaries. Therefore, a partially damaged grain-based specimen should consist of a combination of cohesive and frictional smooth-joint contacts. In terms of strength, the undamaged specimen is the strongest, the fully damaged specimen is the weakest, and the partially damaged specimens are expected to fall between these two strength limits.

Such partially damaged specimens were simulated by assigning the properties of damaged grain boundaries (Figure 3-9) to a number of grain boundaries. For this purpose, the properties of the damaged smooth-joint contacts were assigned in increments of 10% from 0% to 90% of all the smooth-joint contacts. In this thesis, SJ_d refers to the percentage of damaged smooth-joint contacts in a *GBM*. For example, Figure 4-1 shows a partially damaged grain-based specimen, where the properties of the damaged smooth-joint contact were assigned to 50% of all the smooth-joint contacts (i.e., SJ_d = 50%). The damaged and undamaged smooth-joint contacts are shown with green and black lines, respectively.

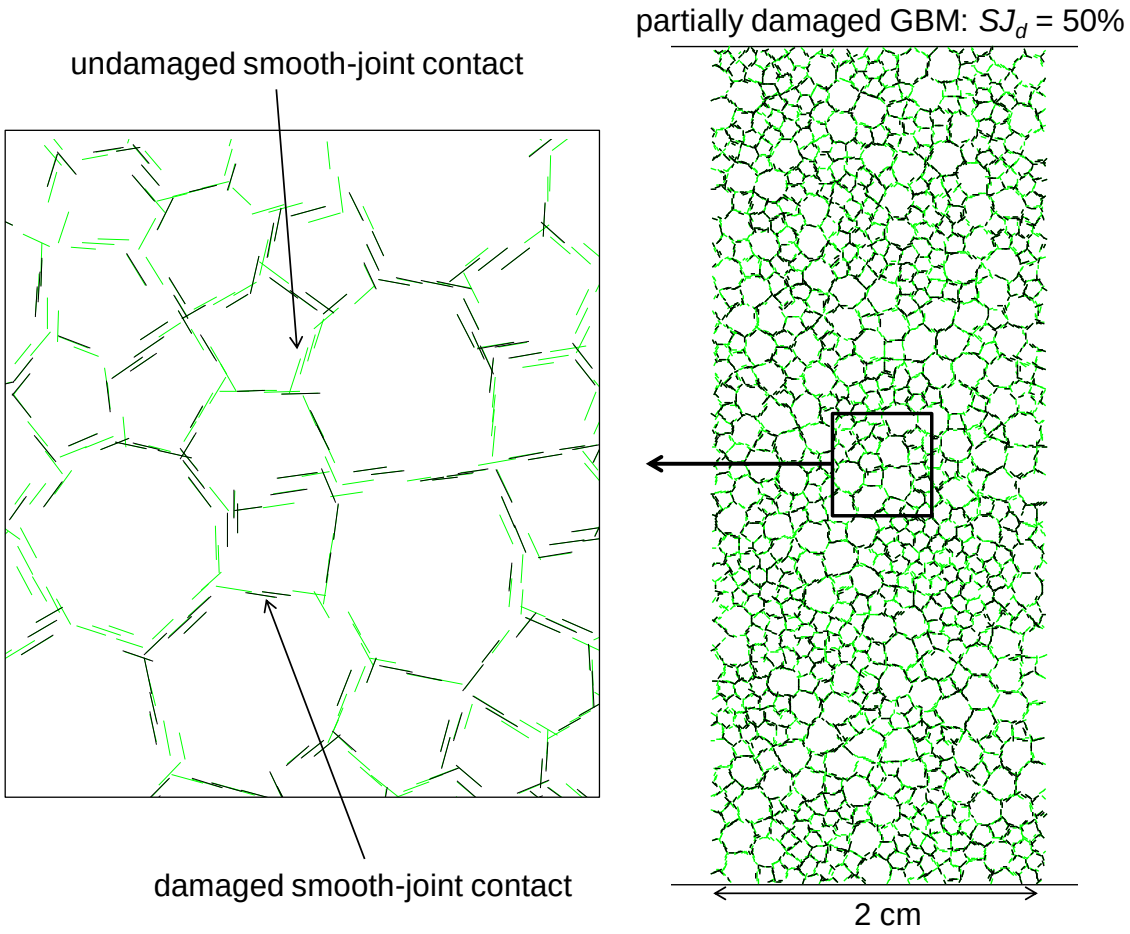

Figure 4-1: A partially damaged grain-based specimen where 50% of the smooth-joint contacts are damaged (SJ_d = 50%). Green and black lines refer to undamaged (cohesive) and damaged (frictional) smooth-joint contacts.

As can be seen from Figure 4-1, the partially damaged grain-based specimens is isotropic as the damaged grain boundaries are randomly oriented and located inside the synthetic specimen and therefore do not generate planes of weakness in specific orientations. Moreover, the damaged grain boundaries have no tensile or cohesive strength and are in a frictional state. For these reasons the partially and fully damaged grain-based specimens are considered as reasonable models of micro-defected rocks.

4.3.1 Peak strength

Three *GBM*s with different realizations for the grain structure and particle arrangement were built for each partially damaged grain-based specimen. Uniaxial and triaxial compression tests were simulated on all the specimens. Figure 4-2a shows the unconfined strengths of intact (UCS_i) and damaged (UCS_d) specimens as a function of damage density (i.e., percentage of damaged smooth-joint contacts, SJ_d). The variability in the *UCS* is due to the geometric heterogeneity, which arises from the difference in the grain structure and particle arrangement of the three model realizations. It can be seen from Figure 4-2a that the decrease in the *UCS* with increasing damage density can be represented by a linear function with a high coefficient of determination of 0.96.

Figure 4-2b shows the unconfined and confined strengths of the grain-based specimens with the percentage of damaged smooth-joint contacts ranging from 0% (i.e., undamaged grain-based specimen as a model of intact marble) to 100% (i.e., fully damaged grain-based specimen as a model of granulated marble) on the σ_1 versus σ_3 stress space. Each point in this graph represents an average of three numerical simulation test results. The plots of the strength degradation ($\Delta\sigma_1$) as a function confinement in Figure 4-2c indicates that the strength degradation of damaged

grain-based specimens decreases with increasing confinement up to the confining pressure of about $UCS_i/10$ = 7.5 MPa. The strength degradation remains below 20 MPa beyond the confining pressure of 7.5 MPa. This confinement dependency of strength degradation causes the failure envelope of the damaged grain-based specimens to be more non-linear with a high initial slope, compared to that of undamaged grain-based specimen, and the non-linearity of the failure envelope increases with increasing the damage density (SJ_d).

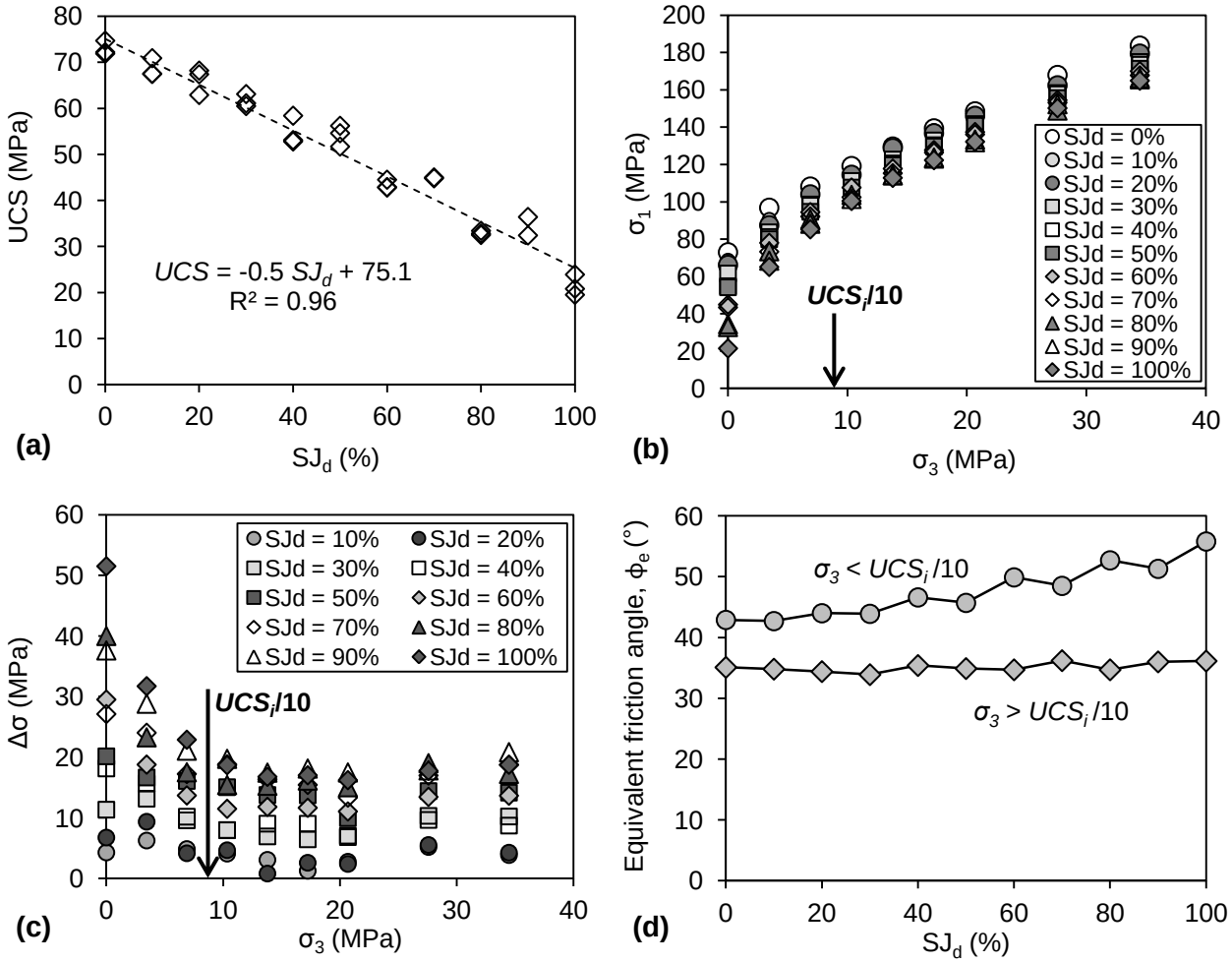

Figure 4-2: a) Correlation between unconfined strength and percentage of damaged smooth-joint contacts; b) unconfined and confined strengths of undamaged (intact), partially damaged, and fully damaged (granulated) grain-based specimens; c) strength degradation ($\Delta\sigma_1$) of damaged grain-based specimens as a function of confinement. Each point in these graphs represents the average of strength or strength degradation values; d) Influence of damage density on the equivalent friction angle of damaged grain-based specimens at low ($\sigma_3 < UCS_i/10$) and high ($\sigma_3 > UCS_i/10$) confinements.

Figure 4-2d shows the equivalent friction angles calculated for the low ($\sigma_3 < UCS_i/10$) and high ($\sigma_3 > UCS_i/10$) confinement portions of the strength envelopes as a function of damage density. This figure indicates that the equivalent friction angle at low confinement increases with increasing damage density, while it remains independent of damage density at high confinement.

4.3.2 Stress-strain response

The stress-strain curves during compression are presented in Figure 4-3 for the grain-based specimens with damage densities of 0%, 20%, 50%, 80% and 100% and confining pressures of 0 MPa, 6.9 MPa and 34.5 MPa. At zero confinement, as shown in Figure 4-3a, both the strength and the Young's modulus decrease with increasing damage density. The axial strain at peak strength is not sensitive to the damage density. The initial post-peak response becomes more ductile with increasing damage density. This is due to the increase in the number of damaged grain boundaries, which are at the frictional state.

The stress-strain curves of grain-based specimens at confining pressures of 6.9 MPa and 34.5 MPa presented in Figure 4-3b and c, suggest that the damaged grain-based specimens become more ductile with increasing damage density and confinement. The axial strain at peak strength increases with increasing damage density. The influence of damage becomes less significant in terms of the strength degradation at high confinement, while the reduction in the value of Young's modulus due to the presence of micro-cracks is almost independent of confinement.

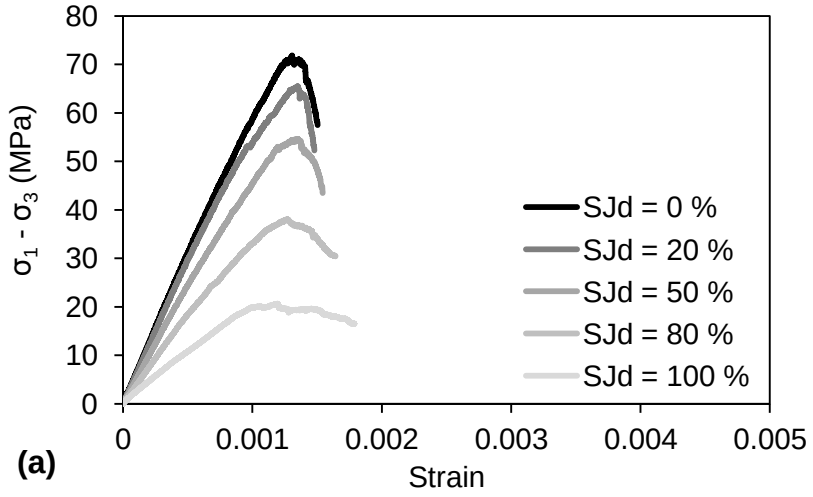

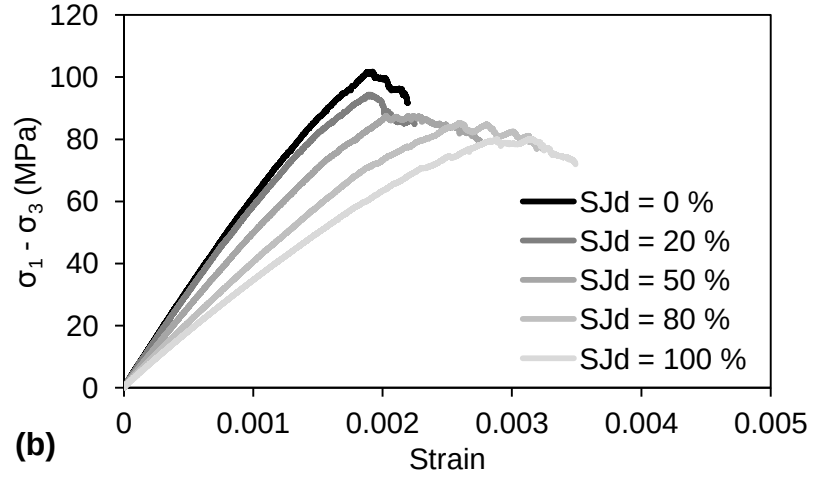

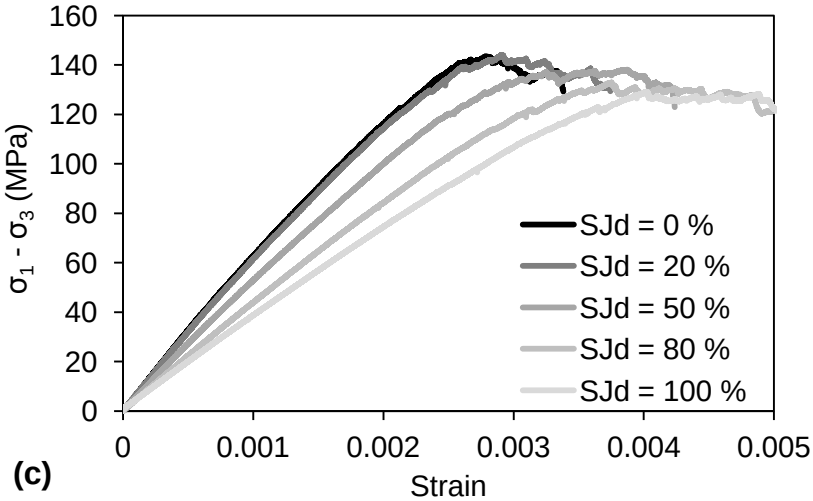

Figure 4-3: Stress-strain curves of undamaged, partially damaged and fully damaged grain-based specimens at: a) σ_3 = 0 MPa; b) σ_3 = 6.9 MPa; and c) σ_3 = 34.5 MPa.

Figure 4-4 shows the influence of confinement on the Young's modulus of the grain-based specimens (calculated at 50% of the peak strength from the stress vs. strain curve) with various damage densities. The Young's modulus is independent of confinement, except for the fully damaged grain-based specimen (SJ_d = 100%). In this case, the Young's modulus increases from 20 GPa under unconfined condition to about 34 GPa at the confining pressure of 10 MPa and remains relatively constant beyond this confining pressure.

Previous studies by Martin and Stimpson (1994) and Eberhardt et al. (1999) on *LdB* granite and Rosengren and Jaeger (1968) on Wombeyan marble have shown that the Young's modulus of damaged rocks is confinement dependent, and increases with increasing confinement. This is due to the closure of open cracks with increasing confinement in actual rock. As discussed in the previous chapter, micro-cracks were not simulated to be open and therefore their closure at high confinement was not captured. For this reason, the values of Young's modulus remained relatively constant independent of confinement in the damaged grain-based specimens.

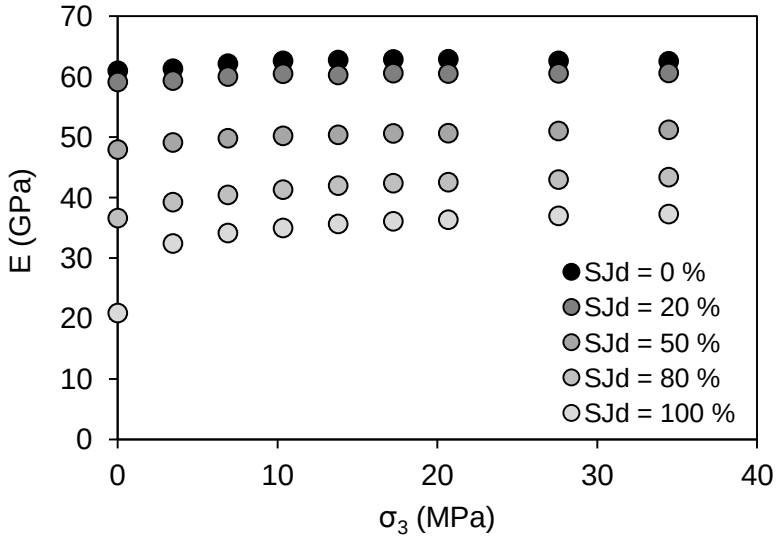

Figure 4-4: Young's moduli of undamaged, partially damaged and fully damaged grain-based specimens as a function of confinement. Each point in this graph represents the average of three moduli.

4.3.3 Failure mode

The failure modes including the location, orientation and types of inter- and intra-grain micro-cracks (tensile and shear) in the grain-based specimens with the damage densities of SJ_d = 0%, 50% and 100% at confining pressures of 0 MPa, 6.9 MPa and 34.5 MPa are shown in Table 4-1. Note that the damaged smooth-joint contacts are in the purely frictional state since they are considered to be broken before the test and therefore cannot be seen in these figures. For this reason, no inter-grain micro-crack can be seen in the fully damaged grain-based specimen (i.e., SJ_d = 100%).

The known transition in the failure mode in brittle rocks from axial splitting at low confinement to shear failure at high confinement is observed in the grain-based specimens with various damage densities. As shown in Table 4-1, at zero confinement failure is dominated by sub-vertical grain boundary tension micro-cracks. A number of these micro-cracks connect to generate relatively long macroscopic sub-vertical fractures. The intra-grain cracks are mainly formed during the post-peak stage of the test. Clusters of these micro-cracks generate macroscopic shear fractures. Examples of this type of fracture can be seen in the top left corners of the specimens with the damage densities of SJ_d = 0% and 50%. The failure mode of the fully damaged grain-based specimen (SJ_d = 100%), as discussed in the previous chapter, cannot be distinguished from the observation of micro-cracks, as failure occurs mainly by opening of or sliding along the frictional grain boundaries.

Table 4-1: Failure modes of synthetic specimens with damage densities of 0%, 50%, and 100%, at 0 MPa, 6.9 MPa and 34.5 MPa confining pressures. Magenta and black refer to inter-grain tensile and shear cracks, respectively, and red and blue refer to intra-grain tensile and shear cracks, respectively.

SJ_d	σ_3 = 0 MPa	σ_3 = 6.9 MPa	σ_3 = 34.5 MPa
0%	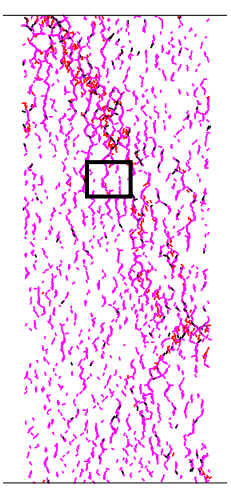	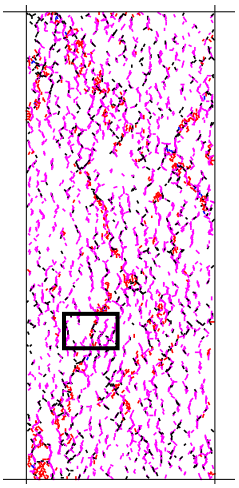	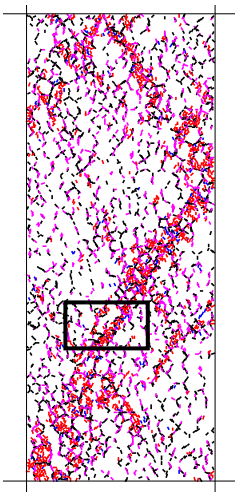
50%	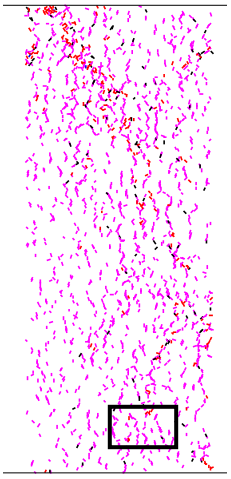	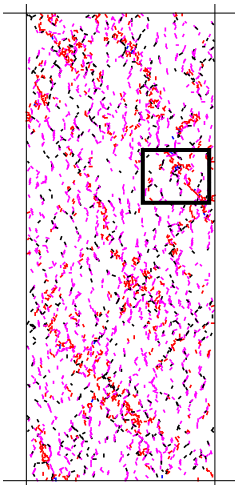	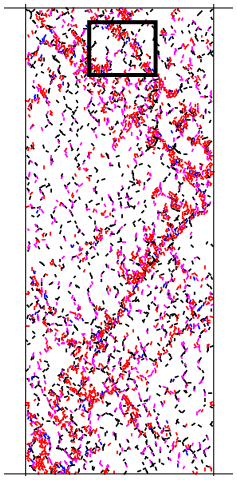
100%	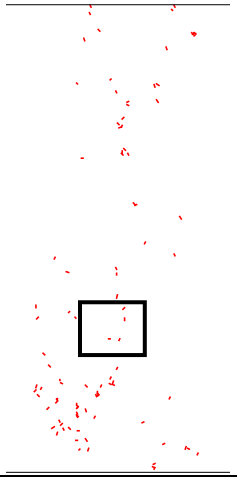	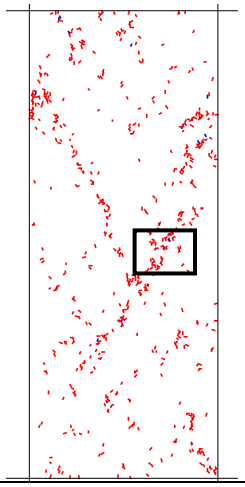	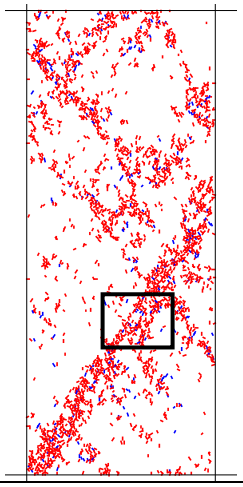

The number of inter-grain micro-cracks decreases and the number of intra-grain micro-cracks increases with increasing confinement. At the confining pressure of 6.9 MPa, the sub-vertical fractures are smaller in length and the inclined fractures are longer compared to those at zero confinement. The failure modes of the grain-based specimens with the damage densities of SJ_d = 0% and 50% are similar. In the fully damaged grain-based specimen, two inclined fractures consisting of a number of intra-grain tension micro-cracks can be distinguished.

At the confining pressure of 34.5 MPa, the failure modes of the grain-based specimens with varying damage densities are very similar. At this confining pressure, the sub-vertical fractures are very short and the failure is dominated by two or more macroscopic and conjugate shear fractures. The macroscopic shear fractures are the result of interaction between intra-grain tensile and shear micro-cracks. These macroscopic shear fractures are thicker than those at lower confining pressures (e.g., 0 and 6.9 MPa).

Close-up views of the boxed areas in Table 4-1 are presented in Table 4-2. Particle velocity vectors along with the grain boundaries and micro-cracks are shown in these figures to better understand the failure modes at the grain scale. Three main modes of failure can be distinguished from the velocity vectors; opening, direct shearing, and combined opening-shearing. In the opening mode, the directions of velocity vectors are opposite, and they are nearly perpendicular to the direction of applied load (e.g., SJ_d = 0% and σ_3 = 0 MPa). Direct shearing occurs when the direction of velocity vectors of two groups of particles is opposite, and the resulting shear fracture is steep relative to the direction of applied load (e.g., SJ_d = 0% and σ_3 = 34.5 MPa). Combined opening-shearing contains components of these two failure modes (e.g., SJ_d = 0% and σ_3 = 6.9 MPa).

Table 4-2: Grain scale failure modes of synthetic specimens with damage densities of 0%, 50%, and 100%, at 0 MPa, 6.9 MPa and 34.5 MPa confining pressures. Green refers to undamaged grain boundaries, magenta and black refer to inter-grain tensile and shear cracks, respectively, and red and blue refer to intra-grain tensile and shear cracks, respectively.

SJ_d	σ_3 = 0 MPa	σ_3 = 6.9 MPa	σ_3 = 34.5 MPa
0%	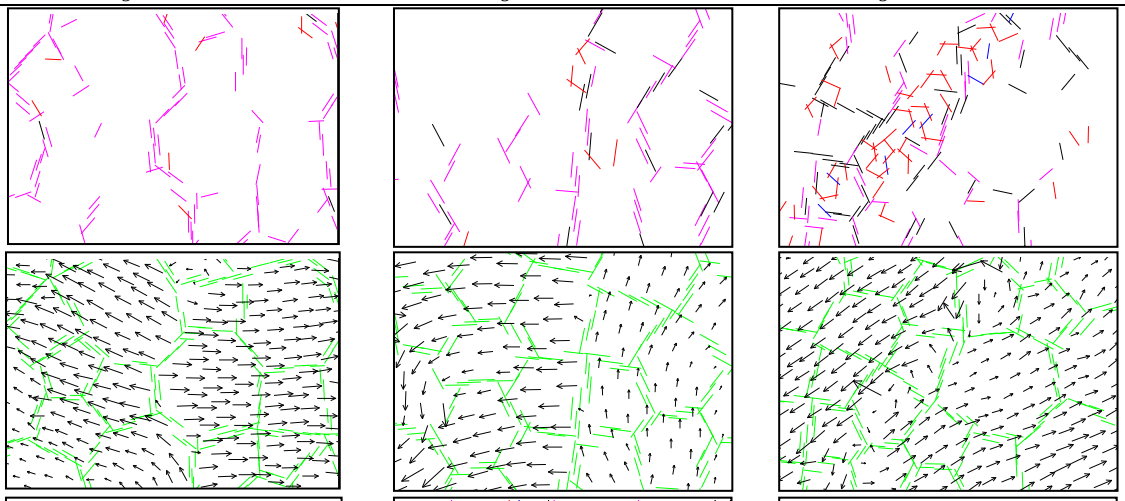		
50%	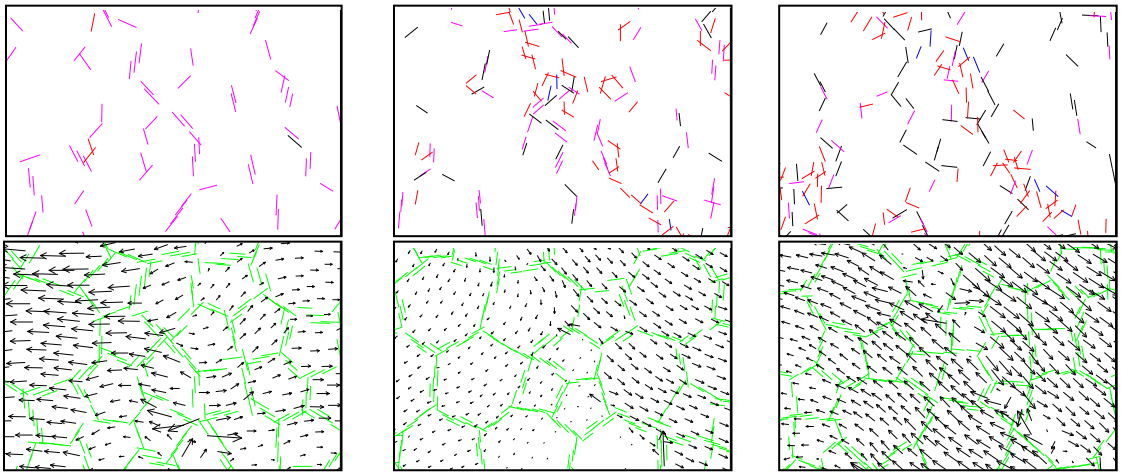		
100%	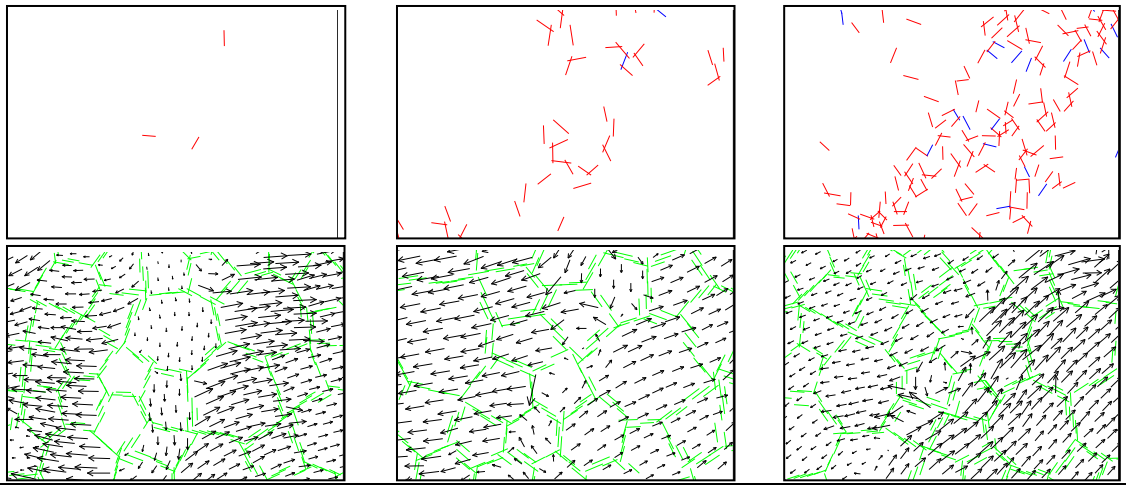		

At zero confinement, the failure mode at the grain scale mainly consists of a combination of opening and combined opening-shearing, with opening being the dominant failure mode. Opening, as shown in Table 4-2 occurs mainly along the nearly vertical grain boundaries, which have been failed in tension. At the 6.9 MPa confining pressure, a combination of all the three modes can be seen, with combined opening-shearing being the dominant mode. The combined opening-shearing can occur along the grain boundaries or through the grains. The main mode of failure at the 34.5 MPa confining pressure is direct shearing, which occurs by failing through the grains. Failure mechanisms described above were observed in all other partially damaged grain-based specimens.

In summary, the results of numerical simulations suggest that the presence of micro-defects (i.e., frictional grain boundary micro-cracks) in a rock specimen results in the decrease in its cohesive strength under unconfined condition. This loss of cohesion decreases with increasing confinement, as the dilation along the grain boundaries is inhibited and shearing through the grains is enforced. The equivalent friction angle of micro-defected rocks at low confinement (initial slope of the failure envelope) increases with increasing the density of micro-defects. The equivalent friction angle of micro-defected rocks at high confinement is close to that of intact specimen (with no micro-defects), and remains relatively constant independent of the density of micro-defects.

In the next section, the results of numerical simulations, in terms of the peak strength, are used to develop semi-empirical equations that can be used to estimate the confined strength of micro-defected rocks.

4.4 Strength Degradation (SD) Logic for Micro-defected Rocks

Bahrani and Kaiser (2013) defined a degradation parameter (*DP*), based on laboratory test results on intact and damaged rocks, which determines the reduction in the strength of damaged rock from that of intact rock ($\Delta\sigma_1 = \sigma_{1i} - \sigma_{1d}$) as a percentage of intact rock strength (σ_{1i}) according to

$$DP = \left(\frac{\Delta\sigma_1}{\sigma_{1i}}\right) \times 100 = [(\sigma_{1i} - \sigma_{1d})/(\sigma_{1i})] \times 100 \qquad \text{Equation 4-1}$$

The degradation parameter *DP* values for different damaged rocks are plotted against confinement normalized to the average unconfined compressive strength of intact rock (σ_3/UCS_i) in Figure 4-5a. It indicates a rapid declining trend in *DP* for all tests. It can be seen from this figure that independent of the amount of degradation at zero confinement, ranging from *DP* = 35% to 75%, the *DP* is less than 20% (typically 10 ± 5%) when confinement is greater than about 10% of UCS_i.

The results of laboratory tests on intact and granulated Wombeyan marble by Gerogiannopoulos (1976), included in the strength degradation graph (Figure 4-5a), nicely follow the strength degradation behavior described above. Therefore, the strength degradation of the fully damaged grain-based specimen (i.e., SJ_d = 100%) calibrated to the strength of granulated Wombeyan marble as well as the strength degradation of the partially damaged grain-based specimens with damage densities ranging from SJ_d = 10% to 90% are expected to be consistent with the trend of the *DP* described above. This is shown in Figure 4-5b, where the *DP* of the grain-based specimens with various damage densities are plotted as a function of confinement normalized to the unconfined compressive strength of undamaged grain-based specimen (σ_3/UCS_i). In this

figure, the *DP* ranges from 5% to 70% at zero confinement, rapidly decreases to below 20% at a confining pressure equal to $UCS_i/10$, and remains below 15% beyond this limit (i.e., for $\sigma_3 > UCS_i/10$). Note that the data points in Figure 4-5a were determined by first averaging the strengths of undamaged and damaged specimens at different values of confining pressure and then calculating the *DP* values using Equation 4-1.

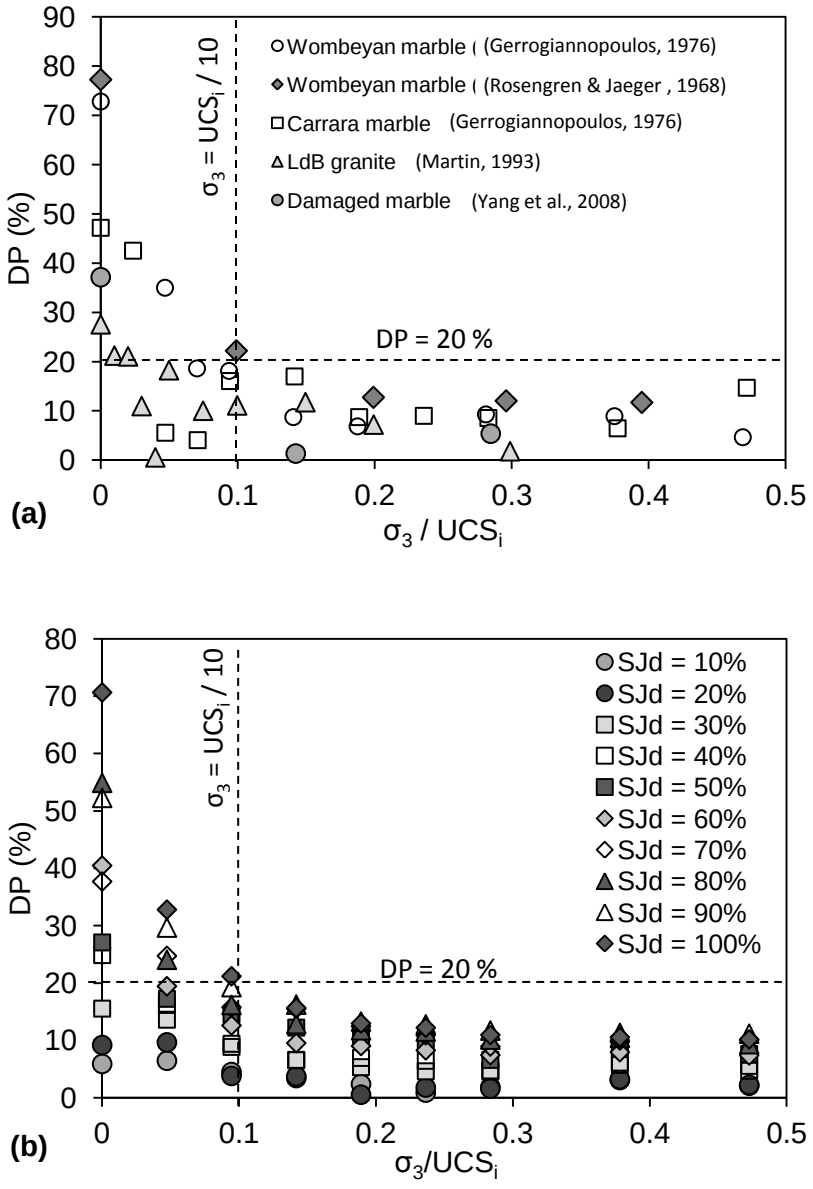

Figure 4-5: Strength degradation graph showing *DP* for: a) actual damaged rocks; and b) damaged grain-based specimens.

In the following, a series of semi-empirical equations are developed to fit the strength degradation behavior (*DP* vs. σ_3/UCS_i) of the damaged grain-based specimens shown in Figure 4-5b. Such semi-empirical equations can be used to estimate the confined strengths of micro-defected rocks, as demonstrated later in this chapter.

4.4.1 Determination of degradation parameters for micro-defected rocks

The results of numerical simulations presented in Figure 4-5b were used to develop a series of semi-empirical equations to estimate the confined strength of micro-defected rocks. This approach, which is based on determining the strength degradation of micro-defected rock from intact rock, is referred to as the Strength Degradation (*SD*) approach for micro-defected rock throughout this document. The *SD* approach provides a means for estimating the confined strength of a micro-defected rock in a situation where the unconfined and confined strengths of the intact rock as well as the unconfined strength of the micro-defected rock are known.

An exponential function was used to fit to the results of numerical simulations. The general form of this function is expressed as:

$$y = \mathrm{A}e^{\mathrm{Bx}} + \mathrm{E} \qquad \text{Equation 4-2}$$

where, the values of *A* and *E* define the limits of the trendline in the y-axis, and the sign of *B* defines whether the curvature decreases or increases exponentially. Least square regression analyses were conducted to determine these fitting parameters. The following three steps are undertaken to develop the *SD* approach.

Step 1: the *DP* values of the grain-based specimens with the damage densities ranging from SJ_d = 10% to 100% were first plotted against σ_3. The negative exponential function used to fit to the data is expressed as:

$$DP = (Du - Dc)e^{[100(-\sigma_3/\sigma_{ci})/c]} + Dc \qquad \text{Equation 4-3}$$

where, *Du* (unconfined degradation) is the value of *DP* at zero confinement, *Dc* (confined degradation) is the value of *DP* at high confinement where *DP* becomes independent of confining pressure, and *c* controls the curvature of the trend line. An example of this exercise is shown in Figure 4-6 for the grain-based specimen with the damage density of SJ_d = 50%. The fitting parameters *Du*, *Dc* and *c* for all the damaged grain-based specimens, which were obtained from the least square regression analysis, are listed in Table 4-3. As can be seen in this table, the least square regression analysis resulted in relatively high coefficients of determination (R^2) for most of the cases.

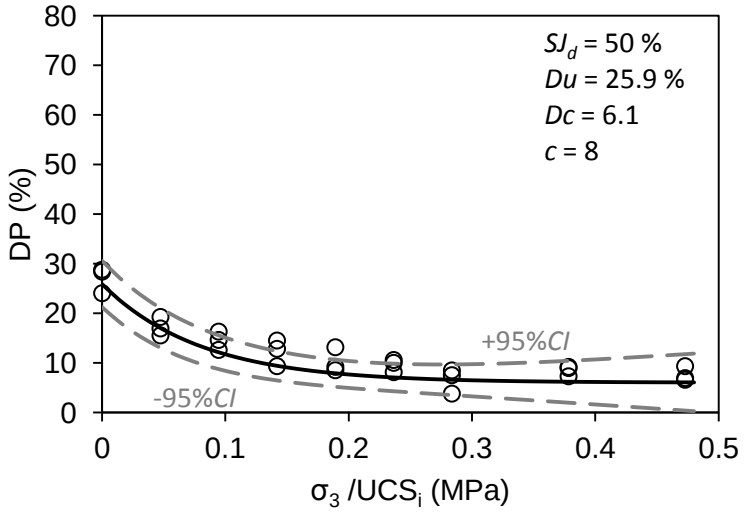

Figure 4-6: Parameters D_u, D_c and *c* for the grain-based specimen with a damage density of SJ_d = 50% obtained from the least square regression analysis. The ± 95% confidence intervals are shown with the dashed grey lines.

Table 4-3: Degradation parameters and coefficient of determination obtained from the least square regression analysis.

SJ_d (%)	*Du* (%)	*Dc* (%)	c	R^2
10	6.7	1.7	12.8	0.52
20	10.3	1.6	9.2	0.32
30	16.4	4.7	9.1	0.72
40	25.1	5.1	6.9	0.87
50	25.9	6.1	8.0	0.91
60	40.4	7.9	4.7	0.88
70	37.6	9.7	6.7	0.98
80	54.7	10.8	4.1	0.97
90	52.1	11.3	5.5	0.98
100	70.3	11.1	5.0	0.99

The ± 95% confidence interval (*CI*) curves are also plotted to represent the variability. The *CI* provides a visual measure of the dispersion of data around the best fit curve. It gives an estimate of an interval within which the mean is expected to occur for a given set of data. The *CI* for the predicted *y* value for a given value of independent variable *x* was determined according to the following equation:

$$CI = y \pm (s)(t_{\alpha/2,DOF})\sqrt{\frac{1}{n} + \frac{(x_i - \bar{x})^2}{\sum_{i=1}^{n}(x_i - \bar{x})^2}} \qquad \text{Equation 4-4}$$

where, $t_{\alpha/2,DOF}$ is the critical *t*-distribution value corresponding to half of the desired α level (here α/2 = 0.05/2 = 2.5%) at $n - 3$ degrees of freedom (*DOF*), since there are three variables (*Du*, *Dc*, and *c*); *n* is the number of observations used in the regression analysis; *s* is the standard error of the estimate; x_i is the given value of *x*; and $\bar{x}$ is the average of the *x* values.

Step 2: As was mentioned earlier, the unconfined compressive strengths of intact and micro-defected rocks and the confined strength of intact rock are the known parameters for the

estimation of confined strength of micro-defected rocks in the *SD* approach. Therefore, *Du* (i.e., *DP* value at zero confinement) can be directly determined from laboratory test data according to the following equation:

$$Du = [(\sigma_{ci} - UCS_d)/\sigma_{ci}] \times 100 \qquad \text{Equation 4-5}$$

where, σ_{ci} is the uniaxial compressive strength of intact rock obtained from triaxial test results according to the procedure described by Hoek and Brown (1997), and UCS_d is the average unconfined compressive strength of micro-defected rocks obtained from laboratory compression tests.

Du is in fact a measure of the level of damage (micro-defects) in a specimen; the higher the amount of damage in a specimen, the higher the *Du* value. The parameters *Dc* and *c* are unknown parameters in this approach. Therefore, equations that correlate these two parameters to *Du* had to be developed. For this purpose, the values of *c* and *Dc* were plotted against *Du* in Figure 4-7a and b, respectively. These figures indicate that *Dc* increases non-linearly with increasing *Du*. The rate of increase in *Dc* decreases with increasing damage density, especially for *Du* values greater than 50%. Figure 4-7b shows that the curvature parameter *c* decreases rapidly as *Du* increases and tends to level off for *Du* > 50%.

In Figure 4-7a, the exponential function was forced to pass through the origin as the strength degradation in a specimen with no damage is zero. Therefore, *A* and *E* in the general exponential function ($y = Ae^{Bx} + E$) had to be equal in magnitudes. The confined degradation *Dc* was determined to be in the form of:

$$Dc = -17.3e^{-0.017D_u} + 17.3$$ Equation 4-6

In determining the equation for the curvature parameter *c* (Figure 4-7b), no constraint was implemented in defining the fitting parameters. The curvature parameter *c* was found to be correlated to *Du* according to:

$$c = 10.8e^{-0.055D_u} + 4.5$$ Equation 4-7

The least square regression analyses resulted in relatively high coefficients of determination of 0.93 and 0.82 for *Dc* and *c*, respectively. The ± 95% *CI* curves are also plotted in Figure 4-7a and b. As can be seen from this figure, the ± 95% *CI* curves widen out for *Du* greater than 50%. It is suggested that since there is only one data point for *Du* greater than 70%, Equation 4-6 and Equation 4-7 should be used with care when dealing with micro-defected rocks of very high *Du* values (*Du* > 70%). Note that this point corresponds to the grain-based specimen with the damage density of SJ_d = 100%. A higher *Du* value can be obtained in materials consisting of less interlocked grains or micro-defected rocks where the micro-defects are not limited to the grain boundaries but also exist inside the grains. Such materials can represent a lower dilation at low confinement and therefore a higher degradation and a lower strength at high confinement.

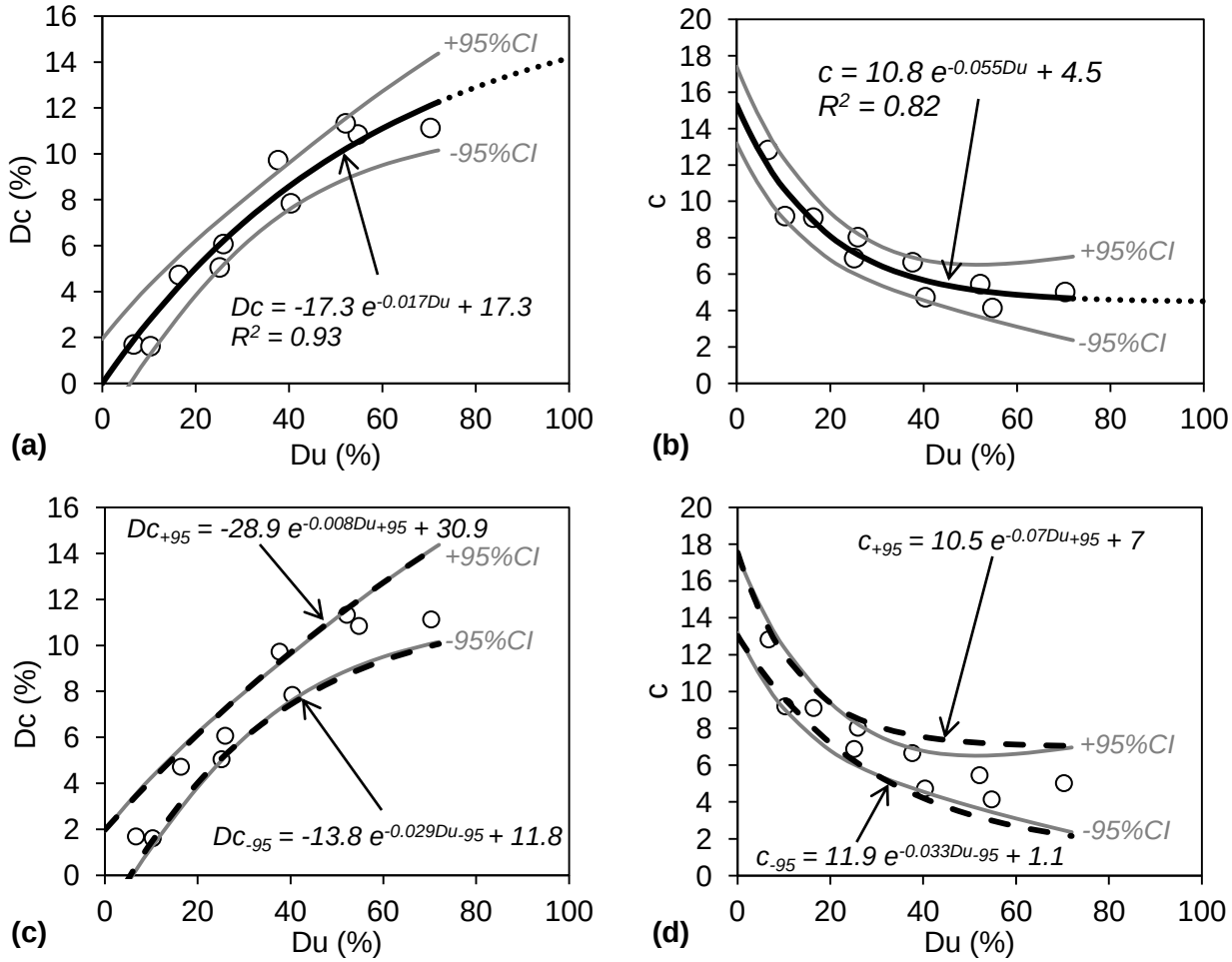

Figure 4-7: Relationships between: a) D_c and D_u; and b) c and D_u. Grey lines are calculated ± 95% confidence intervals (*CI*), and dashed lines are approximated ± 95% *CIs* of degradation parameters: c) *Dc*; and d) *c*.

Step 3: Exponential functions similar to Equation 4-6 and Equation 4-7 were also used to approximate the ± 95% *CI*s. The least square regression analysis was conducted to define the fitting parameters *A*, *B* and *E* in the general exponential function (i.e., $y = Ae^{Bx} + E$). The dashed lines in Figure 4-7c and d represent the exponential curves fitted to the ± 95% *CI* curves defined in the previous steps. The values of confidence intervals at zero confinement were defined to be 5.8 from step 1, and found to be independent of damage density. Therefore, the upper and lower

unconfined degradation (Du_{+95CI} and Du_{-95CI}) were approximated by adding 5.8 to and subtracting 5.8 from the unconfined degradation (Du).

Equation 4-8 to Equation 4-11 can be used to approximate the upper confidence intervals (+ 95% *CI*) of the degradation parameters.

$$Du_{+95CI} = Du + 5.8 \quad \text{Equation 4-8}$$

$$Dc_{+95CI} = -28.9\, e^{-0.008 Du_{+95CI}} + 30.9 \quad \text{Equation 4-9}$$

$$c_{+95CI} = 10.5\, e^{-0.07 Du_{+95CI}} + 7 \quad \text{Equation 4-10}$$

$$DP_{+95CI} = (Du_{+95CI} - Dc_{+95CI}) e^{[100(-\sigma_3/\sigma_{ci})/c_{+95CI}]} + Dc_{+95CI} \quad \text{Equation 4-11}$$

Equation 4-12 to Equation 4-15 can be used to approximate the lower confidence intervals (-95% *CI*) of the degradation parameters.

$$Du_{-95CI} = Du - 5.8 \quad \text{Equation 4-12}$$

$$Dc_{-95CI} = -13.8\, e^{-0.029 Du_{-95CI}} + 11.8 \quad \text{Equation 4-13}$$

$$c_{-95CI} = 11.9\, e^{-0.033 Du_{-95CI}} + 1.1 \quad \text{Equation 4-14}$$

$$DP_{-95CI} = (Du_{-95CI} - Dc_{-95CI}) e^{[100(-\sigma_3/\sigma_{ci})/c_{-95CI}]} + Dc_{-95CI} \quad \text{Equation 4-15}$$

4.4.2 Approach to estimate confined strength of micro-defected rocks

Now that the strength degradation of micro-defected rocks can be estimated as a function of confinement, the confined strength of micro-defected rocks can be estimated after rearranging Equation 4-1 in the form of:

$$\sigma_{1d} = \sigma_{1i} \times [1 - (DP/100)]$$ Equation 4-16

The following steps are taken to estimate the confined strength of micro-defected rocks using the *SD* approach:

Step 1: The *HB* failure envelope is fitted through the unconfined and confined strengths of intact rock following the procedure explained by Hoek and Brown (1997) and Hoek et al. (2002).

Step 2: *Du* is determined from the unconfined compressive strength of intact rock (σ_{ci}) obtained from triaxial compression tests and the average unconfined strength of micro-defected rocks (UCS_d) using Equation 4-5.

Step 3: The values of *Dc*, *c* and *DP* are determined from Equation 4-6, Equation 4-7, and Equation 4-3, respectively.

Step 4: The confined strength of micro-defected rock is then estimated using Equation 4-16.

Step 5: Equation 4-8 to Equation 4-11 are used to approximate the upper confidence interval (+ 95% *CI*) of the degradation parameters, and Equation 4-12 to Equation 4-15 are used to approximate the lower confidence interval (- 95% *CI*) of the degradation parameters.

Step 6: DP_{-95CI} determined from step 5 replaces *DP* in Equation 4-16 to obtain the upper bound confined strength, and DP_{+95CI} determined from step 5 replaces *DP* in Equation 4-16 to obtain the lower bound confined strength. Note that a lower degradation parameter results in a higher strength and vice versa.

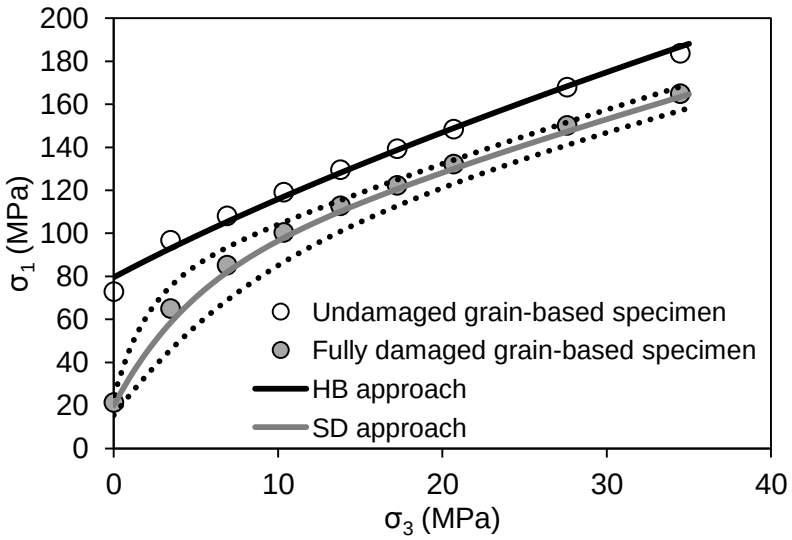

Figure 4-8: Confined strength of fully damaged grain-based specimen estimated using the *SD* approach. The dotted curves show the estimated variability determined using the *SD* approach.

The applicability of the *SD* approach for estimating the confined strength of micro-defected rocks is first examined on the results of numerical simulations from which the semi-empirical equations were derived (Figure 4-8). This of course is a circular argument as the inputs were obtained from the eventual outputs, but is presented here to demonstrate and verify the approach. Figure 4-8 shows the correspondence between the confined strength of the fully damaged grain-based specimen and that estimated by the *SD* approach. The variability estimated by the upper and lower bounds for the data obtained from approximating the ± 95% *CI*s of the degradation parameters is shown with the dotted curves.

As indicated above, the *SD* approach, which is based on the results of simulation of granulated Wombeyan marble was expected to provide a reasonable estimate of the confined strength of other damaged rocks. This hypothesis was investigated on the published laboratory data on damaged (micro-defected) rock specimens reviewed in *Chapter 2*. In the following, the

applicability of the *SD* approach for estimating the confined strength of granulated Wombeyan and Carrara marble, and damaged *LdB* granite and marble is investigated.

4.5 Case Examples

4.5.1 Granulated Wombeyan and Carrara marble

The results of laboratory tests on intact and granulated Wombeyan marble reported by Gerrogiannopoulos (1976) are shown in Figure 4-9a. As can be seen, the *SD* approach reasonably predicts the rapid increase in the strength of granulated marble up to a critical confining pressure with a value of about $UCS_i/10$ (i.e., 7.5 MPa), however it tends to underestimate the confined strength beyond this limit. The upper and lower strength envelopes reasonably capture the strength variability of the granulated marble up to the confining pressure of 10 MPa. Beyond this point, the strength of granulated marble is slightly underestimated even by the upper strength envelope.

Figure 4-9b and Figure 4-9c show the results of laboratory tests on Wombeyan and Carrara marble reported by Rosengren and Jaeger (1968) and Gerrogiannopoulos (1976), respectively, and their strength envelopes estimated by the *SD* approach. It can be seen that the *SD* approach captures the rapid increase in the strengths of granulated Wombeyan and Carrara marble at low confinement and, considering the inherent variability in strength data, reasonably predicts their confined strengths at high confinement. This is more evident in the case of Wombeyan marble (Figure 4-9b) as the variability of the data is reasonably estimated by the upper and lower bound strength envelopes.

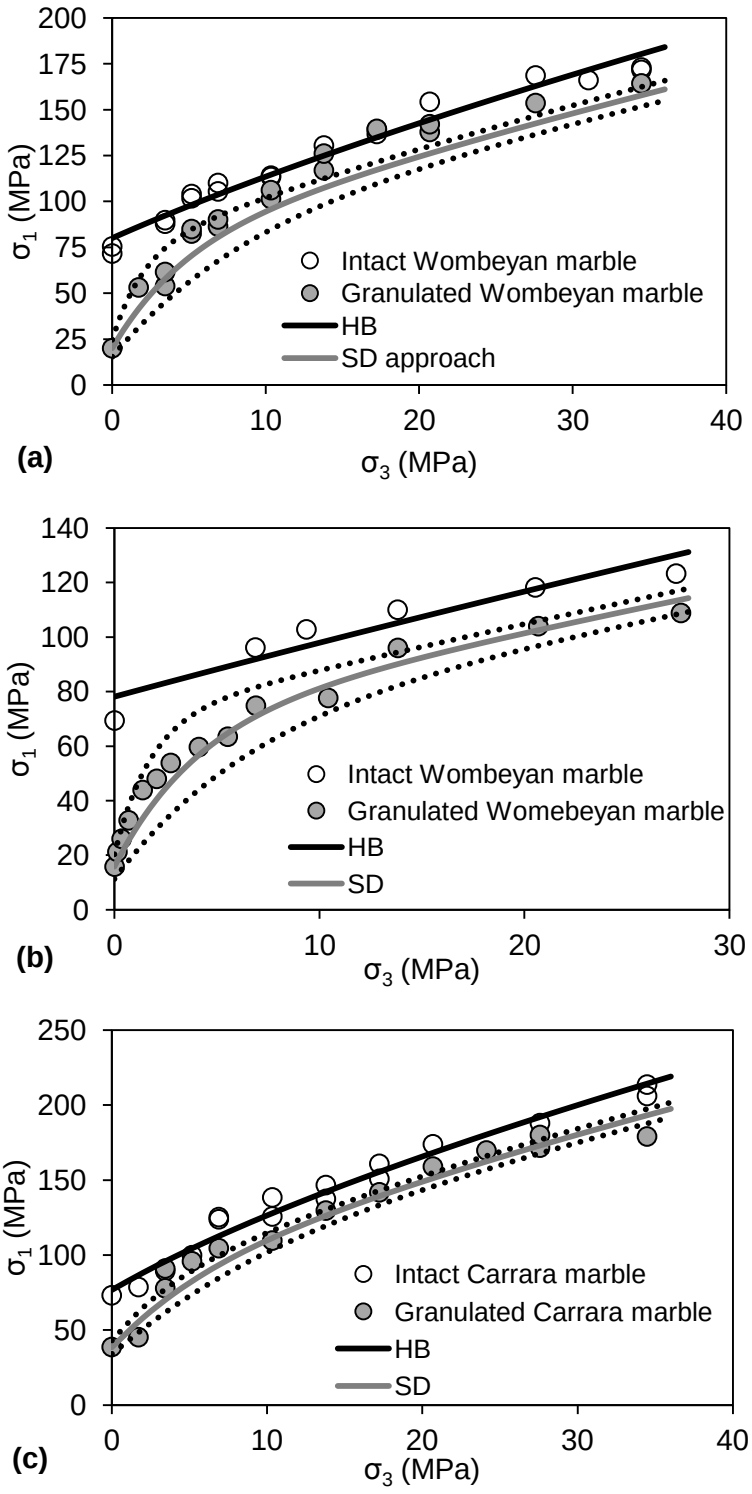

Figure 4-9: Laboratory data of intact and granulated: a) Wombeyan marble tested by Gerrogiannopoulos (1976); b) Wombeyan marble tested by Rosengren and Jaeger (1968); c) Carrara marble tested by Gerrogiannopoulos (1976), and their confined strengths estimated using the *SD* approach. The dotted curves show the estimated variability determined using the *SD* approach.

4.5.2 Damaged Lac du Bonnet granite

Figure 4-10 shows the laboratory test results on undamaged (130-level) and damaged (420-level) specimens of *LdB* granite, and indicates that the *SD* approach, when matched with the average UCS_d of damaged *LdB* granite, provides a reasonable fit to its strength up to the confining pressure of 20 MPa, but slightly overestimates the confined strength for confining pressures greater than 30 MPa (Figure 4-10). The results up to the confining pressure of 20 MPa and beyond are zoomed out and shown in Figure 4-10b and c, respectively. As can be seen, the strength variability is very well captured by the upper and lower bound strength envelopes.

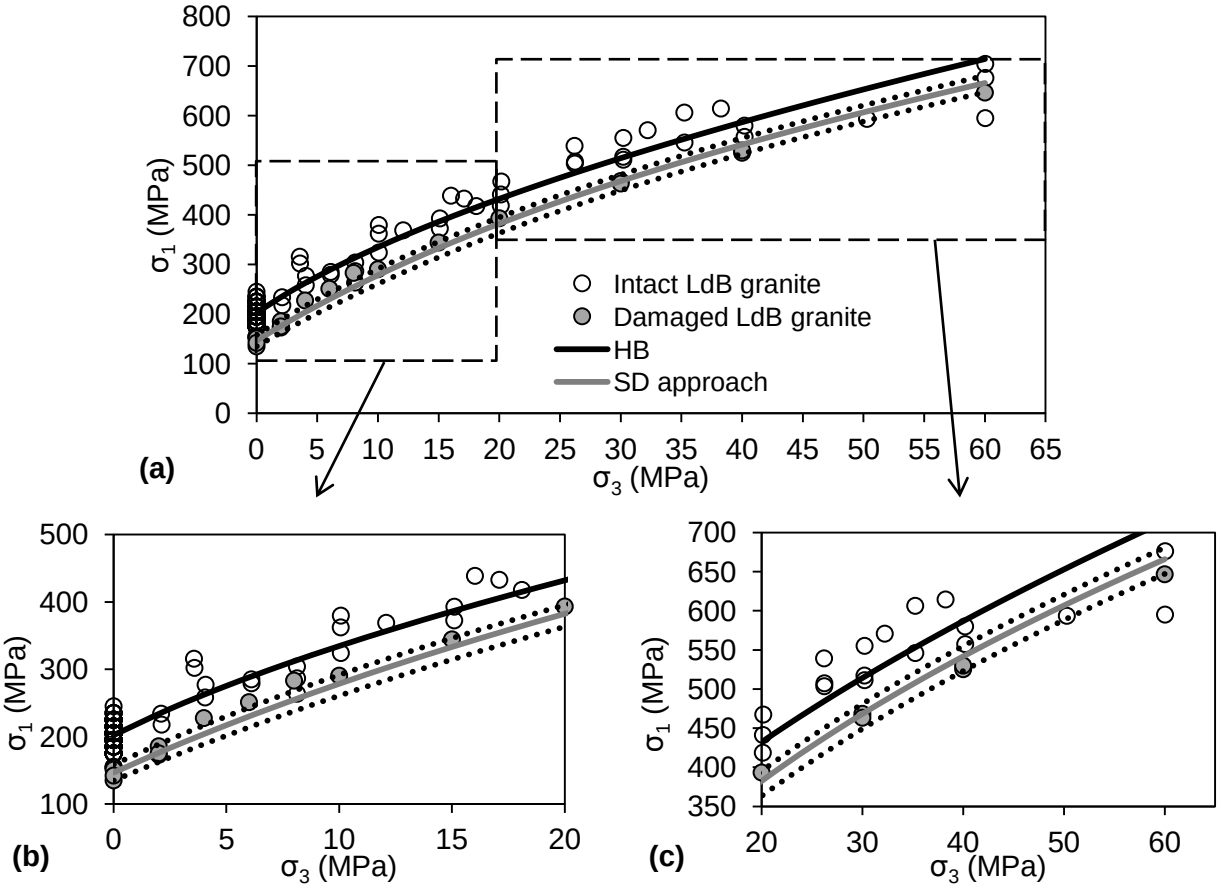

Figure 4-10: Laboratory data on undamaged (intact) and damaged *LdB* granite and the strength envelope predicted by the *SD* approach: a) for the entire range of confinement; b) for confining pressures less than 20 MPa; and c) for confining pressures greater than 20 MPa. The dotted curves show the estimated variability determined using the *SD* approach (Data from Martin, 1993).

4.5.3 Damaged marble

The results of laboratory tests on intact and damaged marble by Yang et al. (2011) are shown in Figure 4-11, along with the confined strengths predicted by the *SD* approach and the upper and lower bounds obtained by approximating the ± 95% *CI* of the degradation parameters. It can be seen that the *SD* approach provides a reasonable estimate of the confined strengths of the damaged marble; it captures the rapid increase in the strength with increasing confinement, however, it fails to properly estimate the strength at 30 MPa confining pressure. This is due to the fact that the strengths of damaged marble at this confining pressure is equal or higher than that of intact marble.

Bewick et al. (2011) and Langford and Diederichs (2015) discussed the importance of the determination of variability for the triaxial test data, respectively. Bewick et al. (2011) explained how the *HB* failure envelope can be fitted to the confidence intervals and later be used in numerical stress modeling to constrain potential stable and yielding conditions.

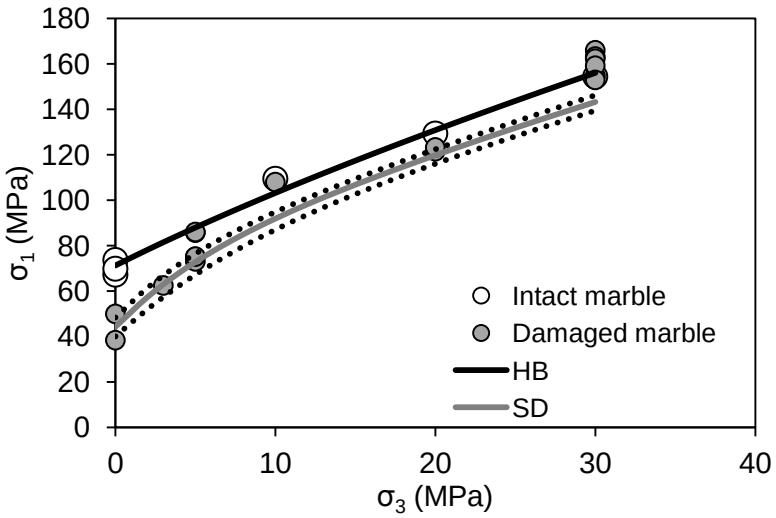

Figure 4-11: Laboratory data of intact and re-fractured marble, and the estimation of the confined strength of re-fractured marble using the *SD* approach (laboratory data from Yang et al., 2011). The dotted and dashed curves show the predicted variability which were obtained from approximating the ± 95% *CI*.

Table 4-4 compares the percentage of triaxial test data within the variability range (upper and lower bounds) estimated by the curves obtained from approximating the ± 95% confidence intervals of the degradation parameters. For three of the five cases, over 50% of the data points are determined to fall between the estimated upper and lower strength envelopes. In granulated Carrara marble (Gerrogiannopoulos, 1976) and damaged marble (Yang et al., 2011), only 36% and 28% of the data points are determined to fall between the upper and lower strength envelopes, respectively. This is due to the high variability of the strength data in these two cases, which resulted in strengths of damaged specimens that are equal or even higher than their intact strengths at some values of confining pressures (e.g., 10 MPa and 30 MPa confining pressures in the case of damaged marble).

The confidence interval is a useful tool when trying to constrain a data set and provide upper and lower bounds. Such intervals can be used for probabilistic analysis of different geotechnical problems. Valley et al. (2010) and Cai (2011) demonstrated the application of combining probabilistic methods such as point estimate (Rosenblueth, 1981) and Monte Carlo methods with finite element method for stability analysis of tunnels and caverns and support design.

Table 4-4: Percentage of laboratory test data within the upper and lower strength envelopes estimated using the *SD* approach.

Rock type	Percentage of data
Granulated Womebeyan marble (Rosengren and Jaeger, 1968)	93
Granulated Wombeyan marble (Gerrogiannopoulos, 1976)	50
Granulated Carrara marble (Gerrogiannopoulos, 1976)	36
Damaged *LdB* granite (Martin, 1993)	78
Damaged marble (Yang et al., 2011)	28

The *SD* approach and the methodology to estimate the upper and lower strength envelopes developed in this chapter will provide an opportunity to combine finite element method and probabilistic analysis for a more reliable assessment of uncertainty in rockmass characterization for rock engineering design.

4.6 Summary and Conclusions

The grain-based specimens previously calibrated to the laboratory properties of intact and granulated Wombeyan marble was used to simulate micro-defected rock specimens. Micro-defects were simulated by assigning damage properties to a percentage of the smooth-joint contacts representing the grain boundaries (i.e., SJ_d = 10% to 100%). The following can be concluded from the results of triaxial tests simulated on undamaged, partially damaged and fully damaged grain-based specimens:

- the unconfined compressive strength of damaged specimens decreases linearly with increasing damage density;

- the unconfined and confined strengths of the specimens with damage densities ranging from SJ_d = 10% to SJ_d = 90% fall between those of undamaged (i.e., intact; SJ_d = 0%) and fully damaged (i.e., granulated; SJ_d = 100%) specimens;
- the confined strength of partially and fully damaged specimens initially increases rapidly with increasing confinement to about 10% of the *UCS* of the undamaged specimen (i.e., about $\sigma_3 = UCS_i/10$);
- at higher confining pressures (i.e., $\sigma_3 > \sim UCS_i/10$), the strength envelope runs nearly parallel to the envelope of the intact specimen but with a degradation of between 5 and 15% (unless grains are very weak and less interlocked, which is not demonstrated here);
- the amount of damage in a specimen does not influence the overall failure mode at different levels of confinement; it is predominantly dilatant up to about $\sigma_3 = UCS_i/10$, and shear dominated at $\sigma_3 > \sim UCS_i/10$;
- at the specimen scale, the failure mode changes from axial splitting at low confinement to shear band formation at high confinement and this is independent of damage density;
- at the grain scale, three modes of failure are opening, combined opening-shearing and direct shearing; and
- grain boundary opening is dominant under low confinement or unconfined condition, combined opening-shearing is dominant at low confinement, and direct shearing which occurs through the grains is dominant at high confinement.

The simulation test results including the unconfined and confined strengths of undamaged, partially damaged and fully damaged grain-based specimens were used to develop a set of semi-empirical equations, which describe the strength degradation from intact to damaged rock as a function of confinement. Therefore, having knowledge of the unconfined and confined strengths of intact rock and the unconfined strength of micro-defected rock, the confined strength of micro-defected rock can be estimated.

The applicability of this approach, called the Strength Degradation (*SD*) approach for estimating the confined strength of micro-defected rocks, was assessed on the published laboratory tests on

damaged rock specimens. It was found that the confined strength of damaged specimens can be reasonably estimated using the *SD* approach. The *SD* approach was expanded to estimate strength variability by determining the upper and lower strength envelopes based on ± 95% confidence intervals of the degradation parameters.

In the next chapter, the grain-based model is integrated with *DFN* models to simulate defected specimens, specimens that contain defects that are much larger than the grains. The undamaged grain-based specimen is used to investigate the influence of specimen scale on the strength of intact and defected rocks under unconfined condition. The purpose of this first extension is to arrive at strength envelopes for defected rock blocks, e.g., a rock block with a stockwork of veins.

Chapter 5

5 Influence of Scale on Unconfined Compressive Strength of Defected Rocks

5.1 Introduction

In this chapter, the grain-based specimen calibrated to the properties of intact Wombeyan marble (*Chapter 3*) is used to investigate the influence of specimen size on the unconfined compressive strength of intact and defected rocks. Discrete Fracture Network (*DFN*) models are used to simulate the defects. For this purpose, the numerical simulations consist of two stages:

- Stage 1: the grain-based model (*GBM*) is used to simulate intact rocks and then integrated with *DFN* models to simulate defected rocks. The *DFN* models include two sets for defects with different orientations relative to the loading direction. The scale effect investigation at this stage is conducted on intact (not defected, nor damaged) and defected grain-based specimens with widths ranging from 1 to 5 cm, and a constant height-to-width ratio of 2.5.
- Stage 2: the ball model (*BM*) is used to simulate intact rocks and then integrated with the *DFN* models to simulate defected rocks. First, the intact and defected ball specimens with a width of 5 cm and a height-to-width ratio of 2.5 are calibrated to the strengths of intact and defected grain-based specimens of the same geometry and defect configurations from stage 1. The scale effect investigation is continued by generating two more ball specimens with widths of 8 and 12 cm and a height-to-width ratio of 2.

Prior to simulating defected rock specimens of different sizes, previous *in situ*, laboratory and numerical investigations on the influence of specimen size on rock strength are reviewed. It will be discussed that the unconfined compressive strength of rocks may either increase or decrease, or remain constant with increasing specimen size.

5.2 Review of Scale Effect on Rock Strength

As discussed in *Chapter 1*, the rock block strength is an important parameter that directly impacts the strength of jointed rockmasses as the strength of the blocks affects the degree of interlock and thus the freedom the blocks will have to rotate and dilate. A rock block is an intact part of the rockmass that is defined by open joints. A rock block may contain structural features at different scales such as micro-defects, fractures, veins and cemented joints, all of which may influence its strength and failure mode under different loading conditions. Figure 5-1 illustrates how the strengths of cores taken for laboratory strength tests are highly dependent on their locations within the rock block.

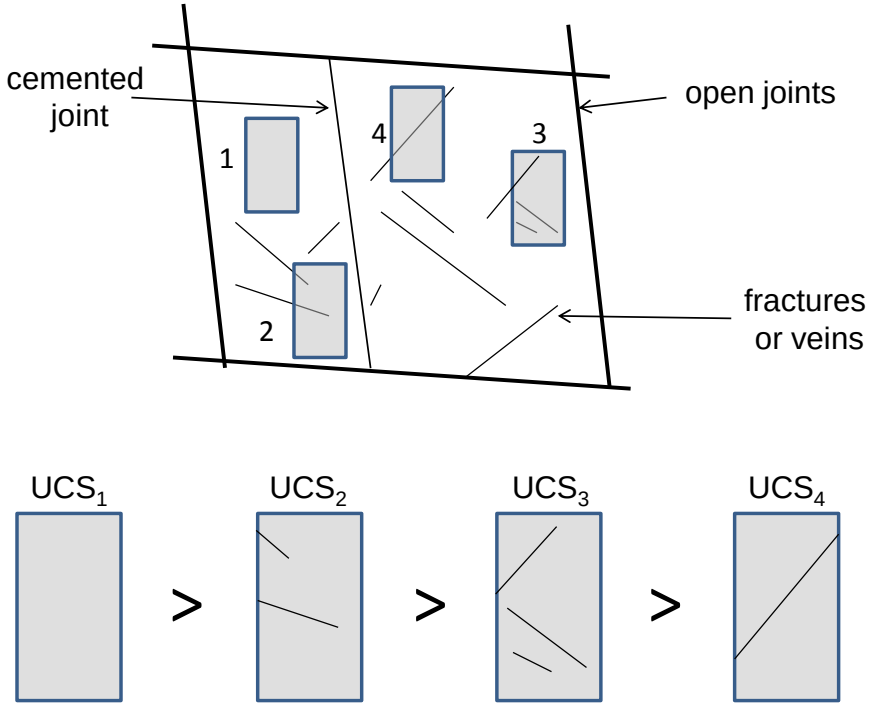

Figure 5-1: Influence of defect density and orientation on the strength variability of cores taken from a defected rock block.

Homogenous cores (e.g., sample #1 in Figure 5-1), represent the strongest part of the rock block. The cores that contain defects are weaker and their strengths decrease as the densities of the defects increase (e.g., samples # 2 and 3 in Figure 5-1). The weakest cores are those that contain defects that are continuous and critically oriented (e.g., sample # 4 in Figure 5-1).

Laubscher and Jakubec (2000) describe a method developed to determine the intact rock strength from weak and strong rock *UCS* values. They discuss how the intact rock specimen may be homogenous or have weaker materials mixed in, and the cores selected for strength testing are usually the strongest pieces of the rock block and do not necessarily reflect the average strength value of homogenous and heterogeneous cores. Therefore, an average value is determined on the assumption that the weaker rock will have a greater influence on the estimation of the average value. The values of weak and strong rock *UCS* as well as the percentage of weak rocks present in a rockmass are used to obtain the 'corrected' value for the average intact rock strength with the aid of an empirical chart. The corrected intact rock strength is then used to determine the rock block strength for homogeneous and non-homogeneous rock blocks.

The aforementioned authors suggest that the long-term strength of a homogenous rock block that does not contain veins or fractures is 80% of the corrected intact rock strength. This reduction accounts for the influence of micro-defects on the rock block strength, which corresponds with the scale effect relationship proposed by Hoek and Brown (1980a). Laubscher and Jakubec (2000) mention that veins and fractures reduce the strength of a rock block based on the frequency with which they occur and their frictional properties. Therefore, to obtain the strength of a non-homogeneous rock block, the corrected intact rock strength adjusted for the influence of

micro-defects is multiplied by the adjustment factor determined for hardness and defect frequency per meter.

A direct approach to estimate the strength of a rock block is to conduct scale effect tests. In these tests, the rock strength varies with increasing size until the strength becomes independent of the specimen size. The scale where the density of different types of defects becomes independent of the size is called the representative element volume (*REV*). According to Hudson and Harrison (1997), the *REV* is the smallest volume at which the size of tested specimens contains a sufficient number of defects that the average value will be reasonably consistent under repeated testing. Schultz (1995) suggested a rockmass *REV* of 5 to 10 times more than the mean joint spacing in a basaltic rock. Pariseau et al. (2008), in accordance with this advice, selected an *REV* size of a cube with an edge length of 10 times the maximum joint set spacing for the simulation of a rock slope using a finite element model. The strength of the rock block *REV* usually lies between the strength of the intact part of the block and the strength of the specimen failed along a single discrete defect (Figure 5-2).

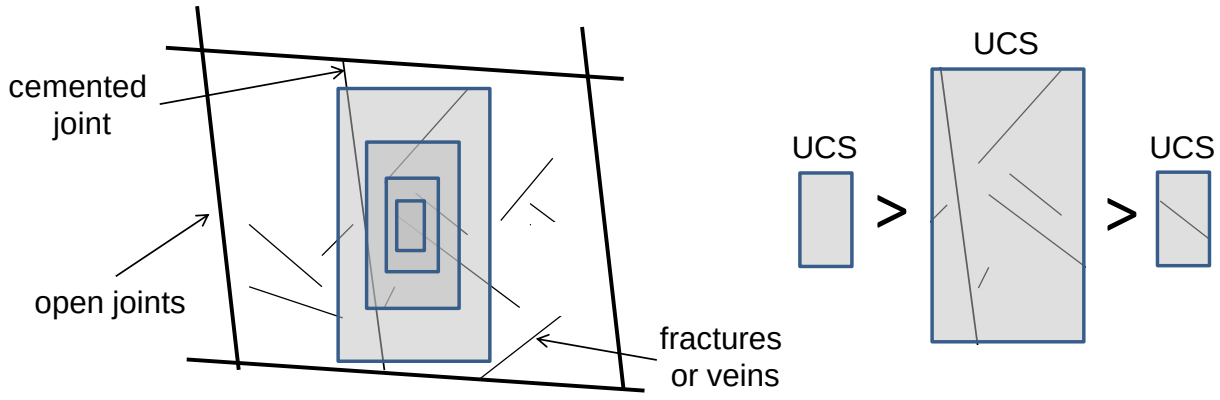

Figure 5-2: Increase in the size of sample to obtain rock block strength.

The following section reviews some laboratory and *in situ* tests as well as numerical simulations conducted to investigate the influence of specimen size on rock strength.

5.2.1 Laboratory and in situ investigations of scale effect on rock strength

One of the first investigations on the influence of specimen size on rock strength was conducted by Bieniawski (1968). He described tests on three classes of cubical coal specimens including small-size specimens up to 0.02 m, medium-size specimens up to 0.5 m and large-size specimens up to 2 m. All the tests were conducted underground to avoid environmental influences such as changes in temperature and humidity. All the specimens were carefully prepared and loaded in uniaxial compression with the loading direction being perpendicular to the bedding planes. The results from over sixty underground tests are shown in Figure 5-3 and indicate a rapid decrease in the strength with increasing specimen size until about 1.5 m, after which the strength remained essentially constant. Bieniawski (1968) suggests that the presence of discontinuities of various types including cracks, cleats and bedding planes in coal resulted in this scale effect.

Bieniawski and Van Heerden (1975) review large scale *in situ* tests conducted by various researchers on different rock types including coal, granite, iron ore, sandstone, shale, marl, and quartz diorite. The results of all these tests revealed that the strength of rocks at the laboratory scale can be between 2 and 16 times greater than that of those at the *in situ* scale. The variation in rock strength at the *in situ* scale compared to their strength at the laboratory scale was again interpreted as being due to structural differences in rockmasses, which may differ substantially from one location and rock type to another.

Pratt et al. (1972) performed uniaxial compressive tests on specimens of quartz diorite ranging in height from 0.08 to 2.7 m in the field and in the laboratory. All specimens had a height-to-width ratio of 1.5 or greater. Additional data on 0.025 m × 0.051 m cylinders by Brown and Swanson (1970) and Walsh et al. (1970) on specimens taken from cores less than 150 m from the site of the *in situ* samples provided even smaller specimens for comparison with the larger *in situ* specimens. As shown in Figure 5-3, the strength of quartz diorite decreases by a factor of ten as the specimen height increases, and asymptotically approaches a constant value for specimens with the height of 0.9 m and greater. This figure also includes the data from Jahns (1966), which shows a reduction in the strength of iron ore with increasing specimen size.

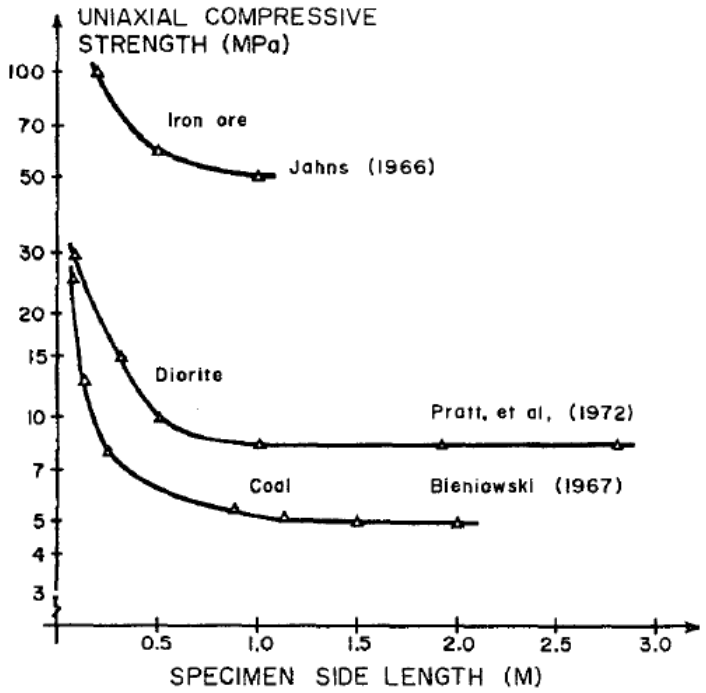

Figure 5-3: Influence of specimen scale on rock strength under unconfined condition. Note that the y-axis is on log scale (figure from Bieniawski, 1968).

Based on published data, Hoek and Brown (1980a) suggest that the uniaxial compressive strength (UCS_i) of a rock specimen with a diameter of d (mm) be related to the uniaxial compressive strength of a 50 mm (UCS_{50}) diameter specimen by the following relationship:

$$UCS_i = UCS_{50}\left(\frac{50}{d}\right)^{0.18} \qquad \text{Equation 5-1}$$

This relationship, together with the data upon which it was based (i.e., 30 to 200 mm diameter rock cylinders), is shown in Figure 5-4. Hoek and Brown (1997) suggest that this reduction in strength is due to the increase in the probability of failure around rock grains with increasing specimen size.

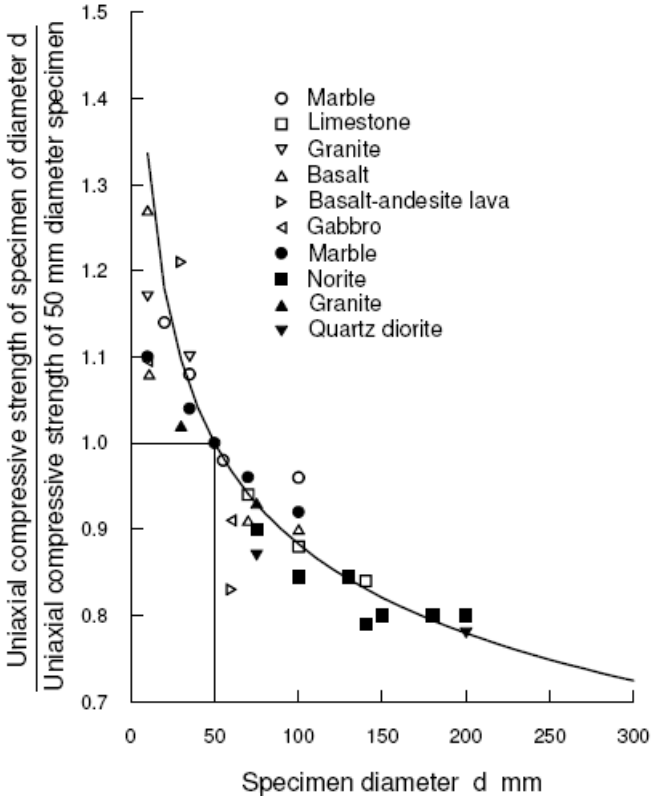

Figure 5-4: Influence of specimen size (diameter) on rock strength (after Hoek and Brown, 1980a).

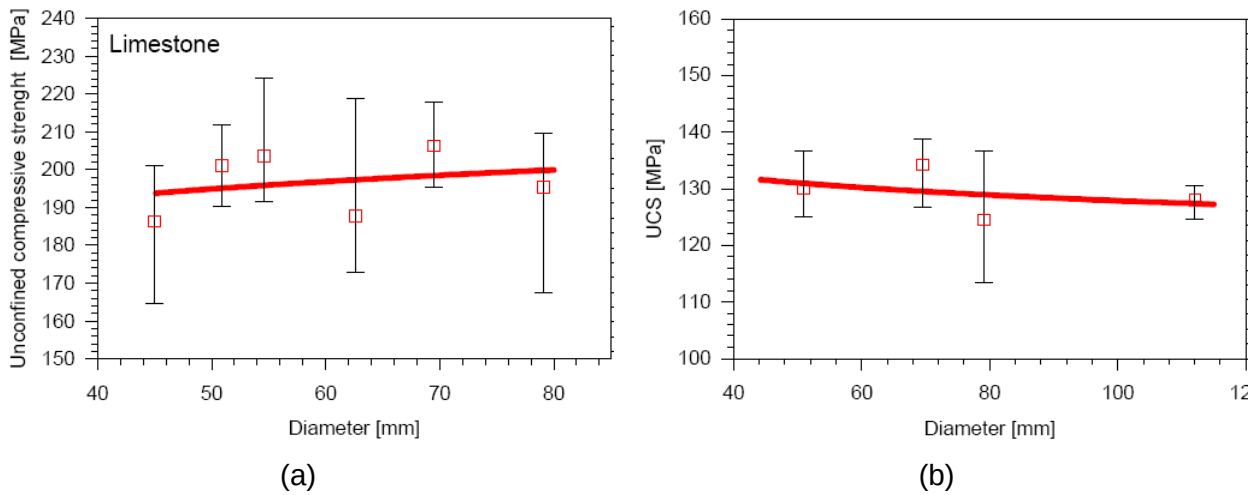

Figure 5-5 Influence of specimen diameter on *UCS* of: a) limestone; and b) granite (after Thuro et al., 2001).

Thuro et al. (2001) performed uniaxial compressive tests using a servo-controlled testing machine to investigate the influence of specimen size on rock strength for two rock types including a fine-grained pyroxene and amphibole-rich kersantite of the south Bohemian massif in Austria and a fine to medium-grained clastic limestone of the northern Alps, also in Austria. The diameter of the cores varied between 45 and 80 mm for the limestone and 45 and 110 mm for the granite with a constant height-to-diameter ratio of 2.0 for both rock types. Figure 5-5 summarizes the results of scale effect tests on these rock specimens. As can be seen, the specimen size had a minor effect on the strength of these rock types; the *UCS* of limestone slightly increases with an increasing specimen scale (Figure 5-5a), while the *UCS* of granite slightly decreases with an increasing specimen scale (Figure 5-5b).

Hawkins (1998), Yoshinaka et al. (2008) and Darlington et al. (2011) also performed a comprehensive literature review on the influence of specimen size on rock strength. The data they collected came from cylindrical specimens of various rock types including cementitious,

sedimentary, igneous and metamorphic rocks. Some of the data indicated a reduction in rock strength with increasing specimen size (e.g., Blanks and McNamara, 1935) while some did not show any clear or significant trend (e.g., Symons, 1970). A few even showed an increase in strength with increasing specimen size (e.g., Hoskins and Horino, 1969), and interestingly, others showed an increase and then a decrease in strength with increasing specimen size (e.g., Hoskins and Horino, 1969; Hawkins, 1998).

Figure 5-6 illustrates the results of scale effect test reported by Hawkins (1998) on sedimentary rocks with core diameters ranging from 15 to 150 mm. The results show a rapid increase in strength up to a core diameter of about 50 mm followed by a gradual decrease in strength with further increase in specimen size. Unfortunately, Hawkins (1998) did not provide any explanation on the strength behavior observed with increasing specimen size.

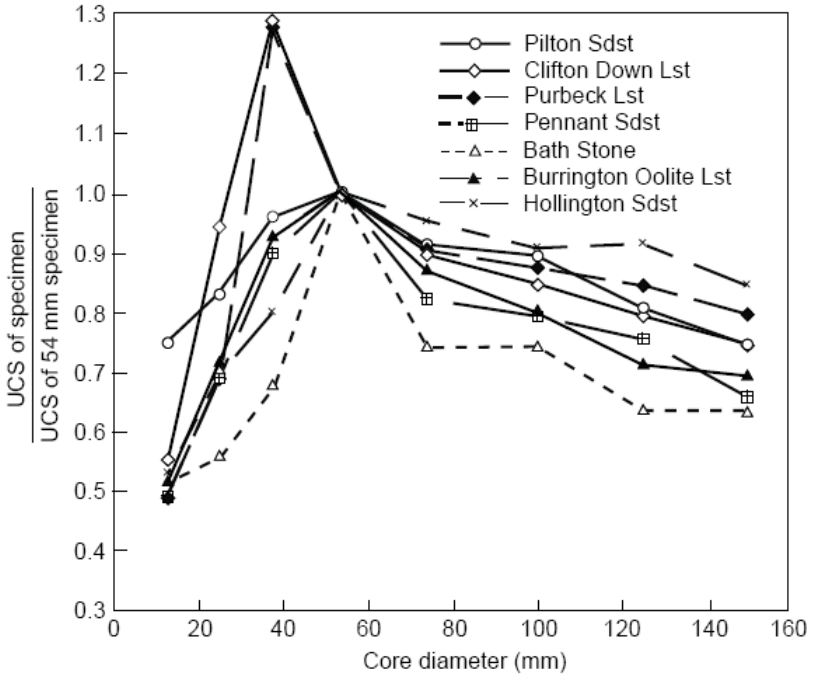

Figure 5-6: Influence of specimen diameter on the strength of sedimentary rocks (after Hawkins, 1998)

The influence of specimen size on the confined strength of defected rocks has not received considerable attention in rock engineering. Figure 5-7 present the results from a series of triaxial compression tests conducted by Medherst and Brown (1998) on 61, 101, 146 and 300 mm diameter coal specimens from Moura Pit 17DU in Australia. Their experiment did not include any *UCS* tests and the applied confining pressure ranged between 0.2 and 10 MPa. Medherst and Brown (1998) indicate that the failure mode changed from axial splitting at confining pressures of less than 1 MPa to shear failure at confining pressures greater than 1 MPa.

Figure 5-7a shows the results of triaxial tests on 61 to 300 mm diameter specimens in the principal stress space. From this figure, it follows that the rock strength decreases with increasing specimen size and the general trends indicated in *Chapter 2* can be found to occur here as well. At low confinement ($\sigma_3 < \sim UCS_i/10$), the 61 and 101 mm diameter specimens follow a 55° equivalent friction angle trend. The 61 mm diameter specimen shows a frictional behavior with an equivalent friction angle of 40° at high confinement ($\sigma_3 > \sim UCS_i/10$). The strengths of the 146 and 300 mm diameter specimens can be represented with high equivalent friction angles of 55° and 62°, respectively, at very low confinement ($\sigma_3 < \sim UCS_i/16$). The equivalent friction angle of the 146 mm diameter specimen is reduced to 45° at $\sigma_3 > \sim UCS_i/16$. Unfortunately, no tests were conducted on the 300 mm diameter specimen at high confinement.

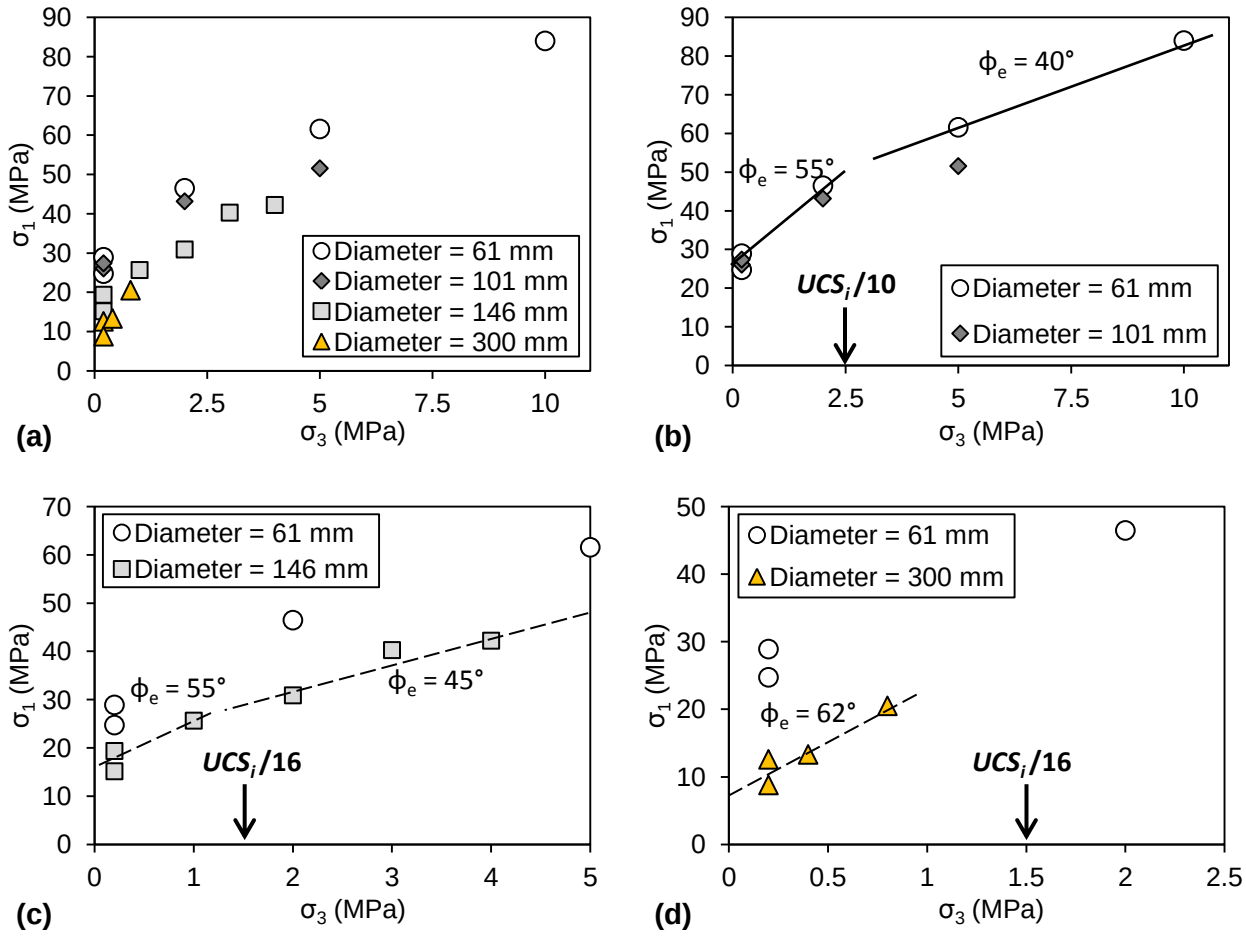

Figure 5-7: a) Influence of specimen size on the confined strength of coal from Moura Pit 17DU: a) all data; b) strengths of 61 mm and 101 mm diameter specimens; c) strengths of 61 mm and 146 mm diameter specimens; and d) strengths of 61 mm and 300 mm diameter specimens (data from Medherst and Brown, 1998).

5.2.2 Numerical investigation of scale effect on rock strength

Pierce et al. (2009) used the *SRM* approach to simulate rock blocks larger than standard core size (i.e., > 50 mm diameter) and investigated the influence of specimen size on the strength of heavily defected quartzite from the Bingham Canyon Mine near Salt Lake City, Utah. Figure 5-8a and b show examples of quartzite with minor and heavy defect intensities. Figure 5-8c illustrates the way that the strength of defected quartzite is strongly dependent on the size of specimen (i.e., diameter).

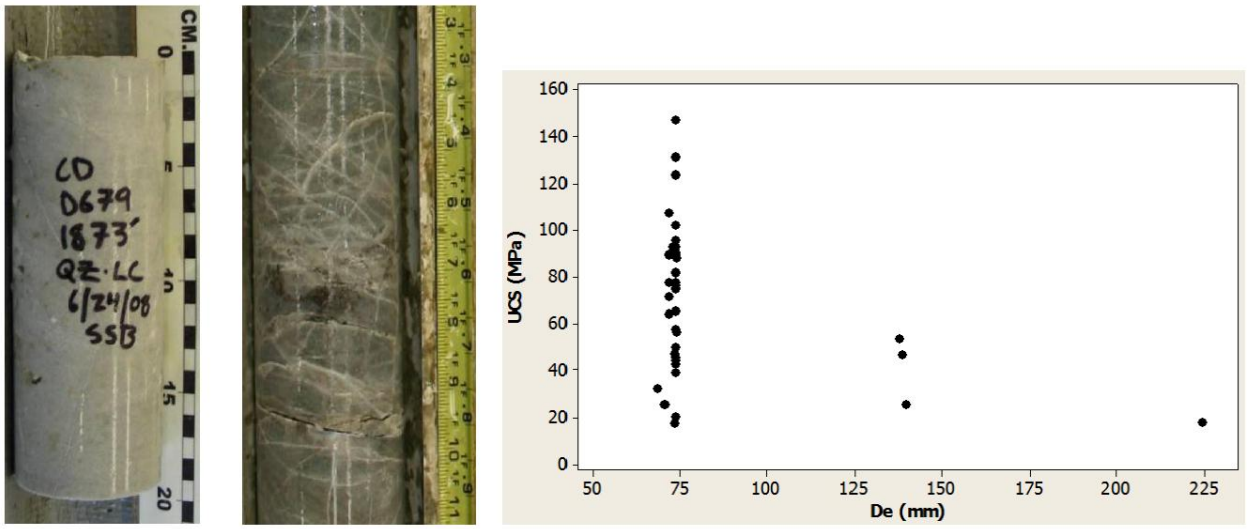

(a) (b) (c)

Figure 5-8: Quartzite cores with: a) no defect; and b) heavy defect intensity. c) Influence of specimen diameter on the strength of defected quartzite (after Pierce et al., 2009).

In generating the *SRM* specimens, an isotropic network of fully persistent veins was generated with a vein frequency of 20/m. The vein network was embedded into the 1 m cube *PFC* model, and the vein structure was replaced with smooth-joint contacts. The scale effect on rock strength was examined by subdividing the 1 m cube specimens into smaller prismatic specimens with a height-to-width ratio of 2. The results of these artificial scale effect tests are presented in Figure 5-9a for vein strengths equal to 50%, 33% and 25% of the baseline strength. The strengths in this figure are normalized to the mean value obtained for the smallest diameter specimens with equivalent lengths of 78.7 mm. An overall power-law trend of decreasing relative strength and its variability with increasing specimen scale can be seen.

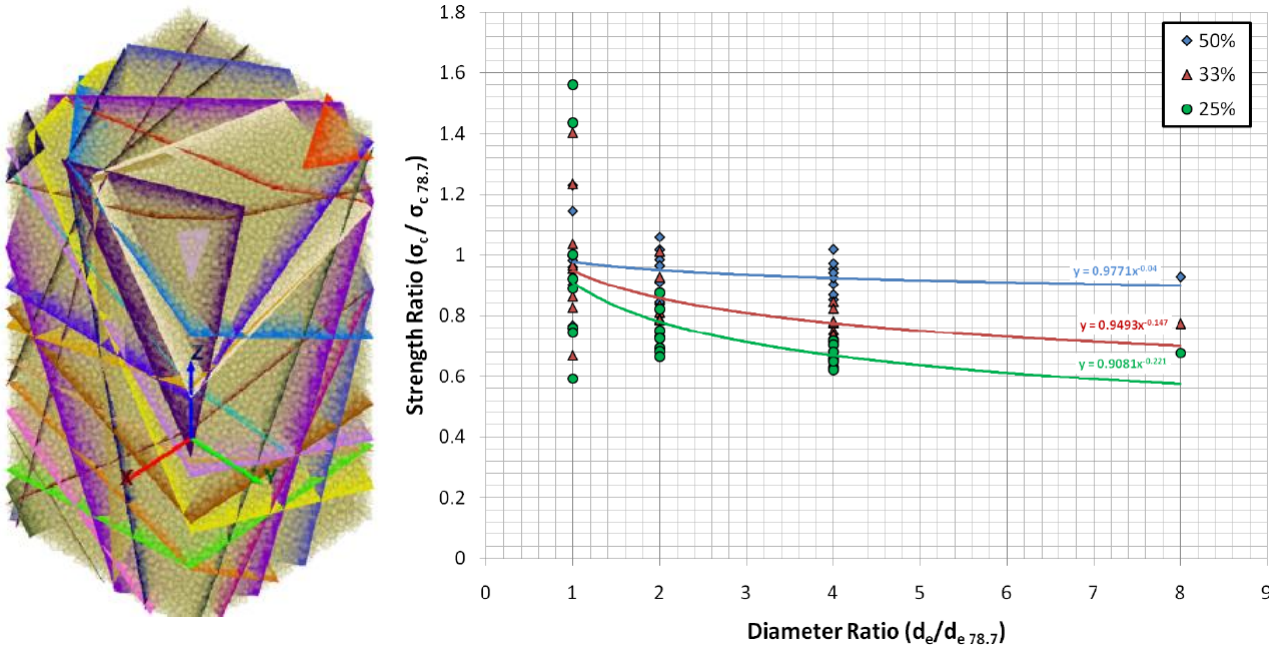

(a) (b)

Figure 5-9: a) *SRM* specimen to simulate veined quartzite. b) Results of *UCS* tests on *SRM* specimens representing veined quartzite (after Pierce et al., 2009).

Esmaieli et al. (2010) collected structural data from Brunswick Mine in Canada and generated a 40 m × 40 m × 40 m *DFN* model. The *DFN* model was sampled to produce 40 cubic specimens with widths ranging from 0.05 to 10 m and a constant height-to-width ratio of 2. The cubic specimens were introduced to *PFC3D* to generate *SRM* specimens (Figure 5-10). A statistical analysis of the results of the *UCS* tests simulated on the *SRM* specimens was used to estimate the *REV* size of the rockmass.

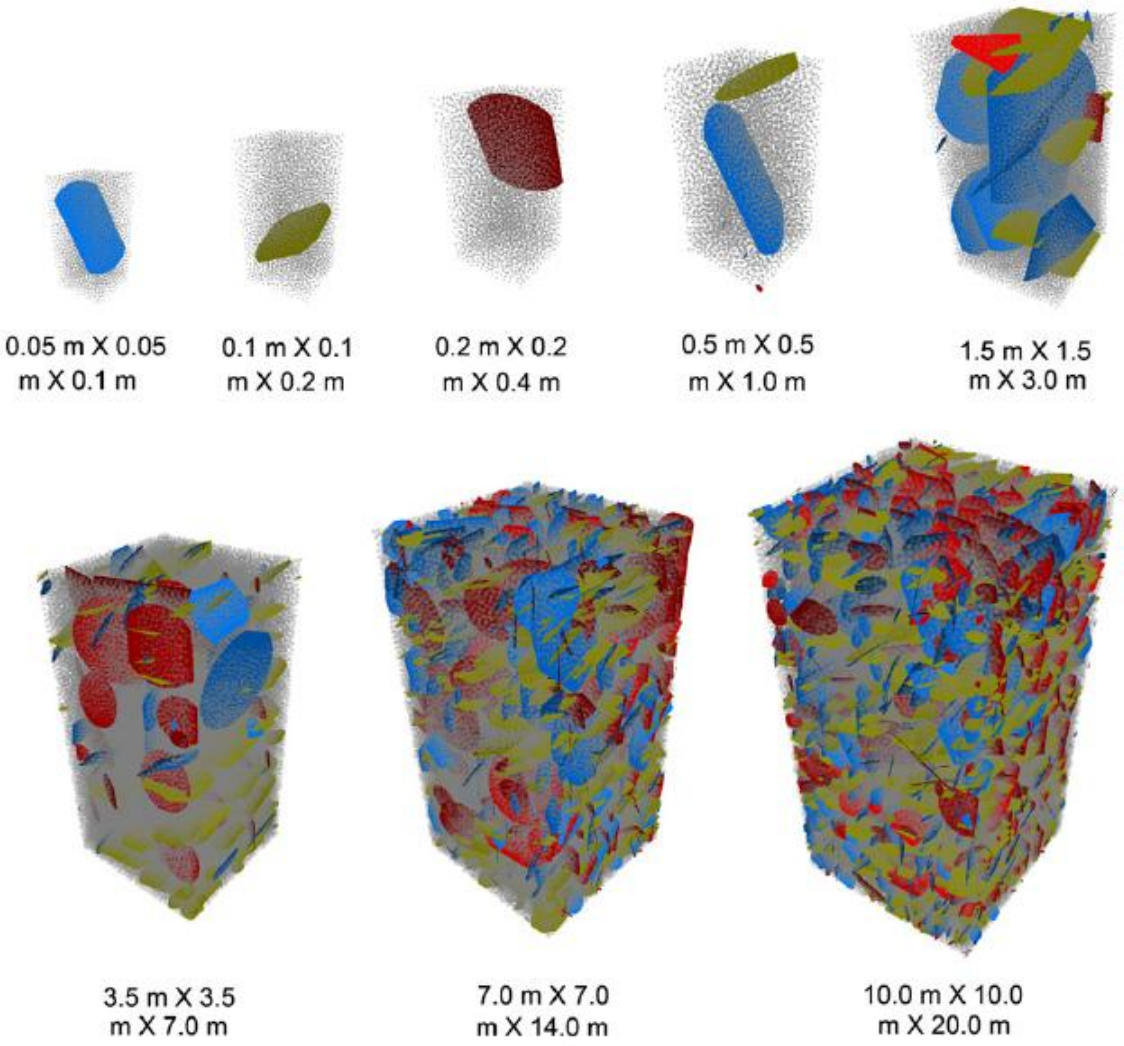

Figure 5-10: *SRM* specimens generated by integrating *PFC3D* and *DFN* models (after Esmaieli et al., 2010).

The relationship between specimen size and the *UCS* of the *SRM* specimens normalized to the intact rock *UCS* is illustrated on a logarithmic scale in Figure 5-11. The results once again indicate that the *UCS* decreases as the size of the *SRM* specimens increases. The very low *UCS* values found in Figure 5-11 could be attributed to the through-going and critically oriented joints (Figure 5-10), whose presence caused the *SRM* specimens to fail along them.

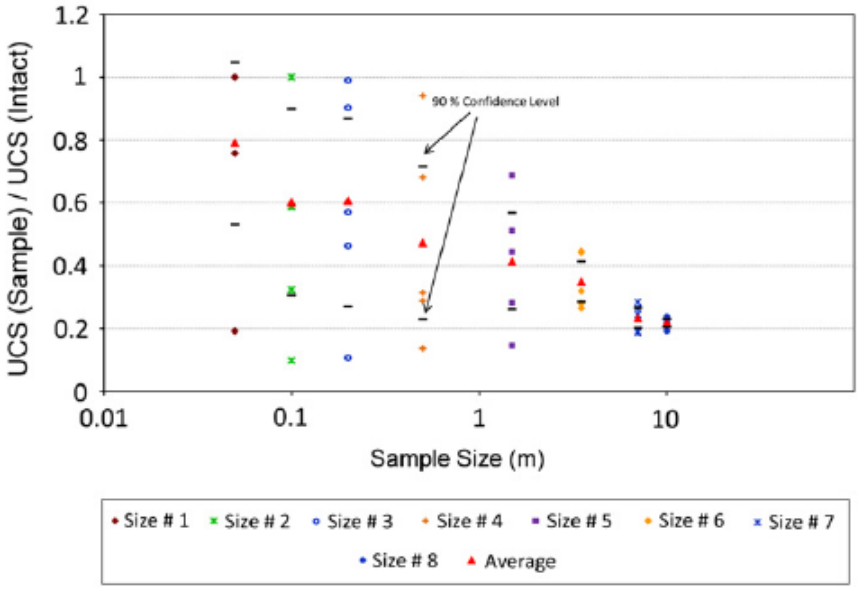

Figure 5-11: Influence of scale on the strength of *SRM* specimens (after Esmaieli et al., 2010).

Mas Ivars et al. (2011) simulated uniaxial compression tests on 1 m × 2 m cylindrical specimens in *PFC3D* and matched their strengths to the mean strength of *in situ* rock blocks at Rio Tinto's Northparkes mine. They then generated an 80 m cubic specimen in *PFC3D* with the parameters obtained from the calibration. The *DFN* generated from the borehole and tunnel scanline mapping information of the Northparkes mine was applied to the 80 m cubic specimen to generate an *SRM* specimen. The *SRM* specimen was carved into smaller specimens with heights of 80 m, 40 m and 20 m and a height-to-width ratio of 2:1 (Figure 5-12). The *SRM* specimens were then subjected to unconfined and confined compression tests.

The numerical simulation results showed a decrease in strength with increasing specimen size (Figure 5-13). Furthermore, the *SRM* specimens carved in different orientations exhibited different rates of strength reduction with increasing specimen scale. Again, the very low strength of *SRM* specimens is interpreted to be due to the presence of critically oriented joints, which intersects the specimen boundaries.

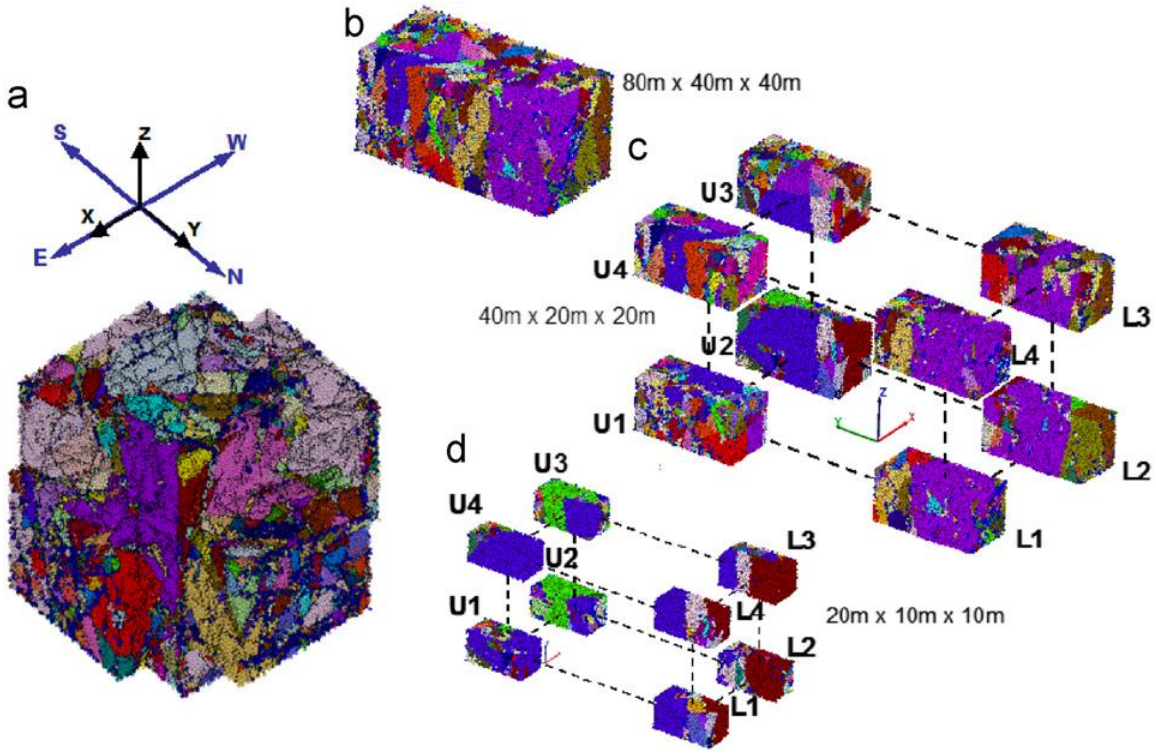

Figure 5-12: 3D cluster plots for: a) three concentric 80 m × 40 m × 40 m parallelepiped specimens in three axial directions; b) the 80 m × 40 m × 40 m parallelepiped specimen in the y-direction (N–S); c) the 80 m × 40 m × 40 m parallelepiped specimen in the y-direction subdivided into eight parallelepiped samples of 40 m × 20 m × 20 m; and d) the 40 m × 20 m × 20 m parallelepiped specimens, subdivided into eight smaller 20 m × 10 m × 10 m subsamples (after Mas Ivars et al., 2011).

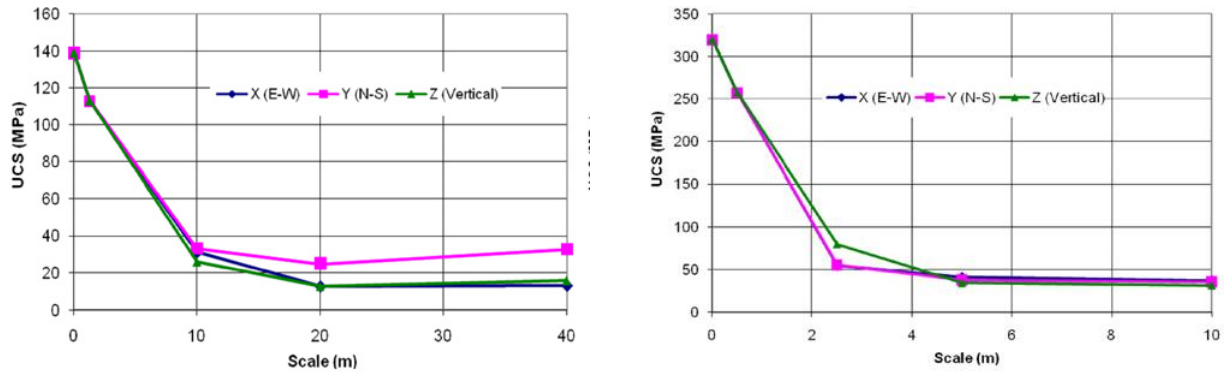

(a) (b)

Figure 5-13: Numerically obtained values of unconfined compressive strength for: a) carbonatite; and b) dolerite, versus specimen size for three orientations of the applied axial stress (after Mas Ivars et al., 2011).

Zhang et al. (2011) investigated the influence of specimen size on rock strength using *PFC3D*. They first calibrated the *PFC* models to the strength of Yamaguchi marble. To simulate rock specimens with increasing scale, models with heights of 40 mm, 60 mm, 80 mm and 120 mm and a height-to-width ratio of 2 were generated in *PFC3D* (Figure 5-14a-e). They used smooth-joint contacts to simulate pre-existing fractures inside the specimens and observed that, when the fracture size included in the specimens of various sizes is constant or proportional to the specimen size, the predicted scale effect trend is contrary to the experimental results; *UCS* increases with increasing specimen scale.

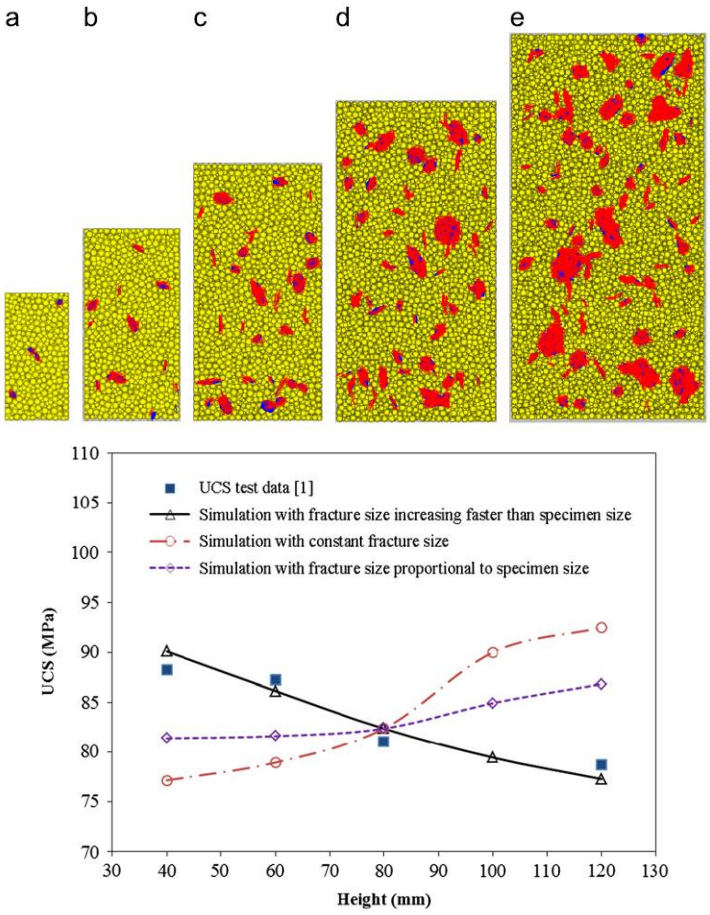

(f)

Figure 5-14: *PFC* specimens for: a) 40 mm; b) 60 mm; c) 80 mm; d) 100 mm; and e) 120 mm height specimens. f) *UCS* versus specimen height for different fracture size patterns (after Zhang et al., 2011).

They also found that the laboratory observed scale effect on rock strength could only be captured by introducing fractures whose sizes increased exponentially with the specimen size, as shown in Figure 5-14f. It will be shown later in this chapter that the observed increase in the strength of *PFC* specimen with increasing size is due to the adopted loading rate.

Poulsen and Adhikary (2013) attempted to numerically reproduce the scale effect in coal strength and its variability at the laboratory scale, as was observed by Medhusrt and Brown (1998), and at the rock block scale, as was observed by Bieniawski and Van Heerden (1975). Furthermore, to simulate a realistic tensile to compressive strength ratio and a non-linear failure envelope for rock like materials, Poulsen and Adhikary (2013) used *PFC2D* and its recently developed bond model, which is called the flat-joint contact model (Potyondy, 2012). The diameters of the synthetic specimens used to simulate the laboratory observed scale effect were 61 mm, 101 mm, 146 mm and 300 mm. The height-to-width ratio of these synthetic specimens was 2.5.

It is mentioned by Poulsen and Adhikary (2013), that when frictionless walls are used as platens in *PFC*, the strength results are independent of specimen size. To simulate the observed scale effect in *PFC* a random distribution of broken bonds was introduced to the models. Similar to the investigation by Zhang et al. (2011), the percentage of broken bonds present in *PFC* specimens had to be increased as the specimen size increased in order to reproduce the observed scale effect. No defects (i.e., broken bonds) were introduced into the models with diameters of 61 mm and 101 mm and the amount of defects in the models with diameters of 146 mm and 300 mm were 7% and 22.5%, respectively.

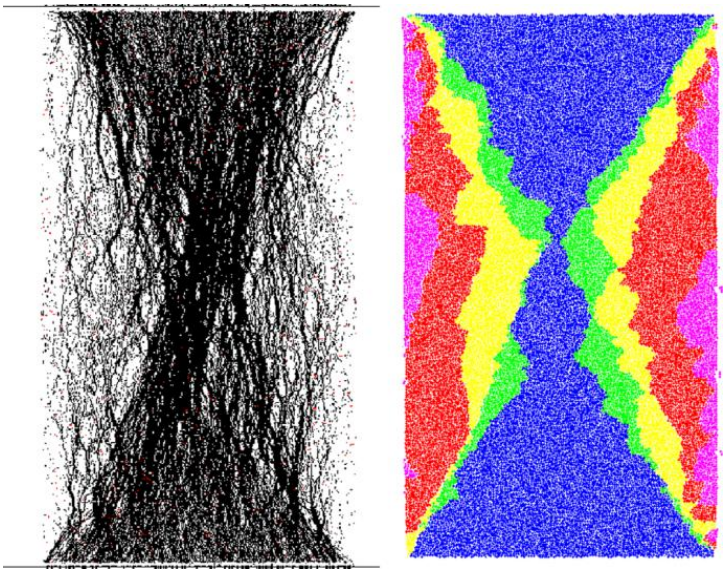

Figure 5-15: The synthetic specimen with a width of 0.5 m. Hour glass shaped force chains (left) and horizontal ball displacement (right) are the result of highly frictional end constraints (after Poulsen and Adhikary, 2013).

Poulsen and Adhikary (2013) also simulated a large scale block (0.5 m × 1.0 m) to capture the lower strength of the coal block. They used boundary conditions representative of the *in situ* conditions, which presented highly frictional end constrains. Using this approach, they were able to reproduce the reduction in the strength observed by Bieniawski and Van Heerden (1975). The frictional end constraints of this synthetic specimen resulted in its non-uniform displacement and force chain distributions within it. As shown in Figure 5-15, little force is carried by the boundary particles at mid-specimen height, while a distinctive hour glass shape is formed by the force carried in the core and from the constrained end boundaries. Boundary particles at mid-specimen height are horizontally displaced and the final specimen has the distinctive hour glass shape observed underground in over-stressed pillars.

The results of numerical analyses reported by Pierce et al. (2009), Esmaieli et al. (2010), Mas Ivars et al. (2011), Zhang et al. (2011) and Poulsen and Adhikary (2013) suggest that it is not

only the size of the specimen that acts as the primary reason for the observed scale effect in rock strength. Other factors such as the change in the density of defects and joints and boundary conditions with increasing specimen scale are also considered as main contributing factors that encourage the occurrences of the observed scale effects in rock strengths. In the following sections, an approach similar to that of *SRM* is used to investigate more systematically the scale effect on the strength of intact and defected rocks.

5.3 Investigation of Scale Effect on Rock Strength using PFC2D

Previous attempts to simulate veined rocks or jointed rockmasses using the *SRM* approach considered the ball model (bonded with parallel bonds) to represent the intact rock and the *DFN* model to represent structures such as veins or joints (e.g., Pierce et al., 2007; Pierce et al., 2009; Hadjigeorgiou et al., 2009; Esmaeili et al., 2010; Mas Ivars et al., 2011; Bahaaddini et al., 2011; Zhang and Stead, 2015). Recently, Turichshev and Hadjigeorgiou (2015) made a step forward to more realistically simulate rock specimens and their fracturing process by combining a 3D clumped model (instead of ball model) and a *DFN* model to generate an *SRM* specimen. In their modified *SRM* approach, the clumps represented irregular shaped grains that are unbreakable and the *DFN* was used to simulate veins. A visual representation of the result of numerical simulations, including the final fracture developed through the *SRM* specimen and its comparison with actual failure mode of the veined rock specimen, is presented in Figure 5-16. This example shows failure along a critically oriented vein, which means that the measured strength is not truly representative of a veined specimen, but that of the vein.

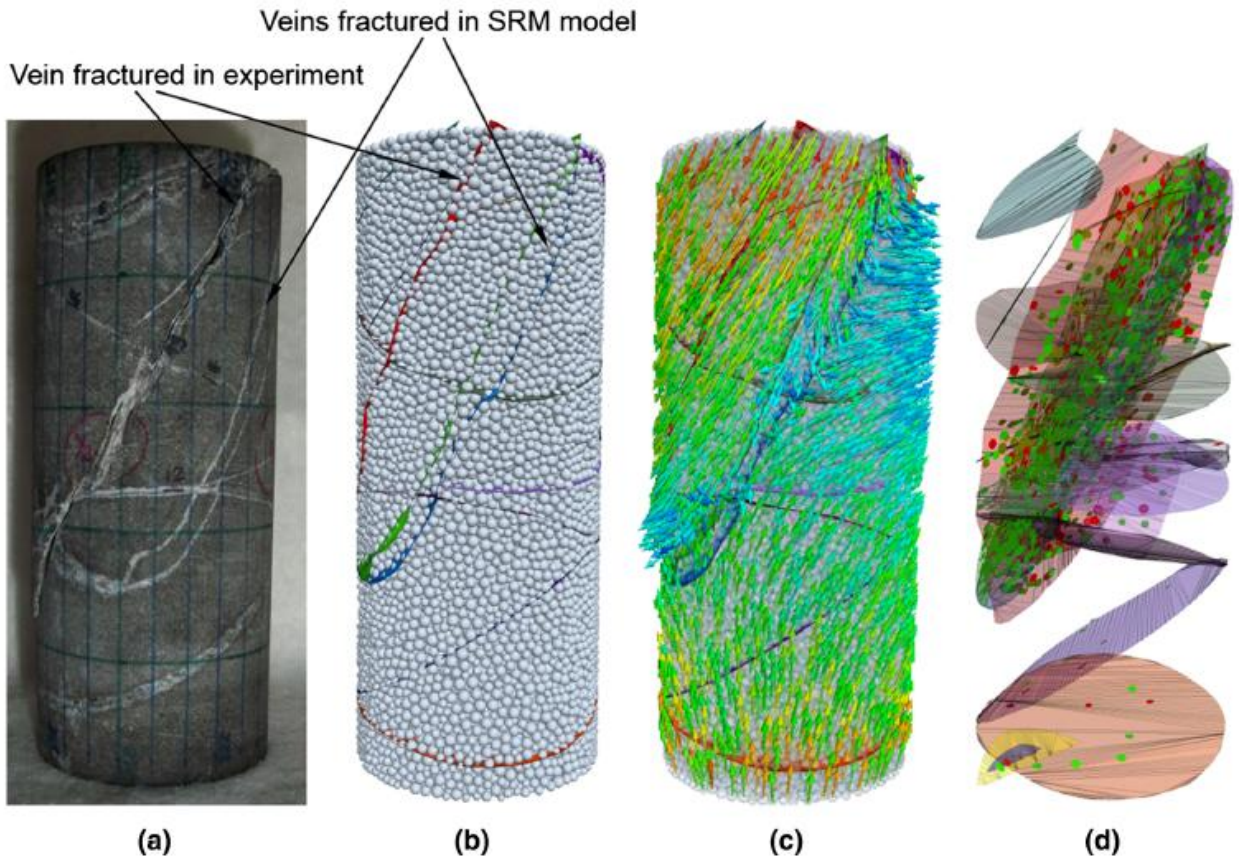

Figure 5-16: Illustration of: a) a fracture developed in the veined specimen; and b) *SRM* specimen of the veined specimen; c) displacement vectors; and d) smooth-joint contacts broken in tension (red disks) and in shear (green disks) (after Turichshev and Hadjigeorgiou, 2015).

It was mentioned in *Chapter 2* that one of the main limitations of the clumped model is that clumps representing mineral grains are rigid and unbreakable and it was concluded that the grain-based model provides a more realistic simulation of rock fracturing process as the grains are simulated as deformable and breakable objects. Hence, in an effort to arrive at more realistic simulations of laboratory scale defected rock specimens and their failure modes, the grain-based model with breakable grains and the *DFN* model representing defects are combined in *PFC2D*. The following describes modeling assumptions and strategies used to simulate intact and defected rock specimens and investigate the influence of specimen size on their strengths.

5.3.1 Influence of specimen size on strength of intact rock

Five grain-based specimens with widths of 1 to 5 cm and a height-to-width ratio of 2.5 were generated (Figure 5-17) following the procedure described in *Chapter 3* with the micro-properties of intact (undamaged) grain-based specimen given in Table 3-2 and Table 3-3. Table 5-1 compares the grain-based specimens in terms of the numbers and densities of smooth-joint contacts and parallel bonds. As can be seen, the numbers of smooth-joint contacts and parallel bonds increase rapidly with increasing specimen size, while their densities remain relatively constant.

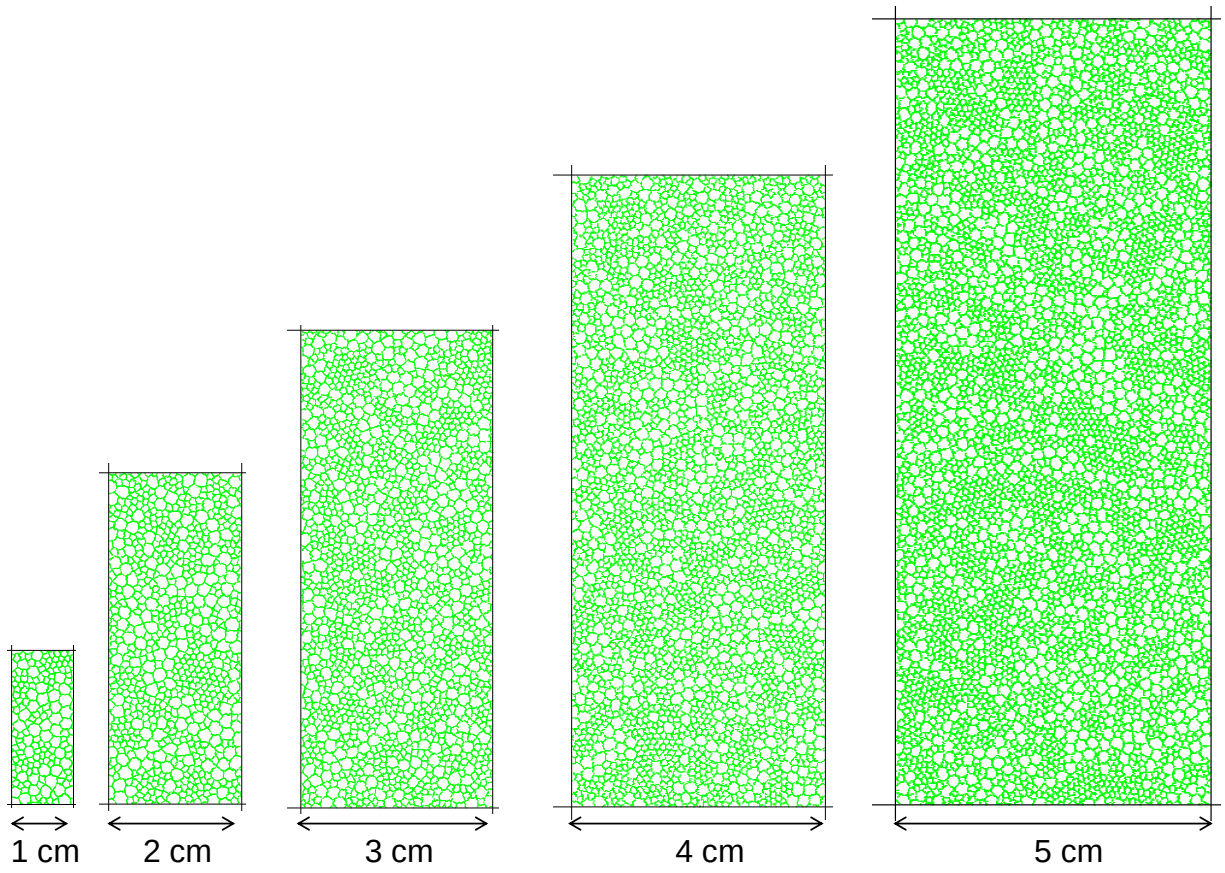

Figure 5-17: Undamaged grain-based specimens used to investigate the influence of specimen size on the strength of intact rock. Green lines refer to the undamaged smooth-joint contacts representing undamaged grain boundaries.

Table 5-1: Numbers and densities of parallel bonds (*Pb*) and smooth-joint contacts (*Sj*).

Specimen width (cm)	# of *Pb*	# of *Sj*	*Pb* density	*Sj* density
1	3986	2085	1594	834
2	16457	8286	1646	829
3	36967	18923	1643	841
4	65763	34430	1644	861
5	103382	57717	1645	923

Five grain-based specimens with different realizations for the grain structure and ball arrangement were generated for each specimen size and the average, maximum and minimum strengths were used in the analysis. A series of *UCS* tests were conducted with the strain rate of 1.0, which is the same as that used for the grain-based specimen with the width of 2 cm calibrated to the properties of intact Wombeyan marble in *Chapter 3*.

Figure 5-18 shows that the strength of undamaged grain-based specimens increases with increasing specimen size. This is contrary to the results of most of laboratory scale effect tests reviewed earlier in this chapter, but consistent with the results of numerical simulations obtained by Zhang et al. (2011). This is interpreted to be due to the adopted strain rate at which the uniaxial compression tests were simulated. Therefore, it was decided that it was necessary to conduct a sensitivity analysis on the influence of strain rate on the *UCS* of differently-sized grain-based specimens.

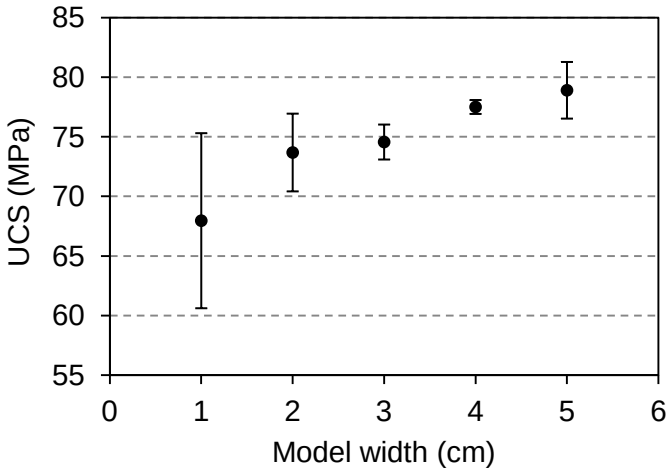

Figure 5-18: Influence of specimen size on the *UCS* of undamaged grain-based specimens simulated with the strain rate of 1.0.

Figure 5-19 shows the influence of strain rates on the *UCS* of differently-sized specimens. In general, the strength decreases as the strain rate decreases. The strengths of the synthetic specimens with the widths of 5 cm and 4 cm are highly dependent on the strain rate. The strain rate dependency of the strength decreases with the decrease of the specimen size; the strengths of specimens with the widths of 1 and 2 cm are only slightly influenced by the strain rate. This sensitivity analysis suggests that, in order to investigate the influence of specimen size on the rock strength, the grain-based specimens should be tested with a strain rate of less than 0.1.

Figure 5-20 shows the results of unconfined compression tests conducted with the strain rate of 0.05 on differently-sized grain-based specimens. This figure suggests that the average strength is independent of the specimen size. Note that these tests were simulated with frictionless platens (walls in *PFC*), which means that no decrease with increasing size was expected. The variability of the strength tends to decrease with increasing size, except for the specimen with the width of 5 cm. Note that all the numerical simulations discussed in the rest of this chapter were run with the strain rate of 0.05.

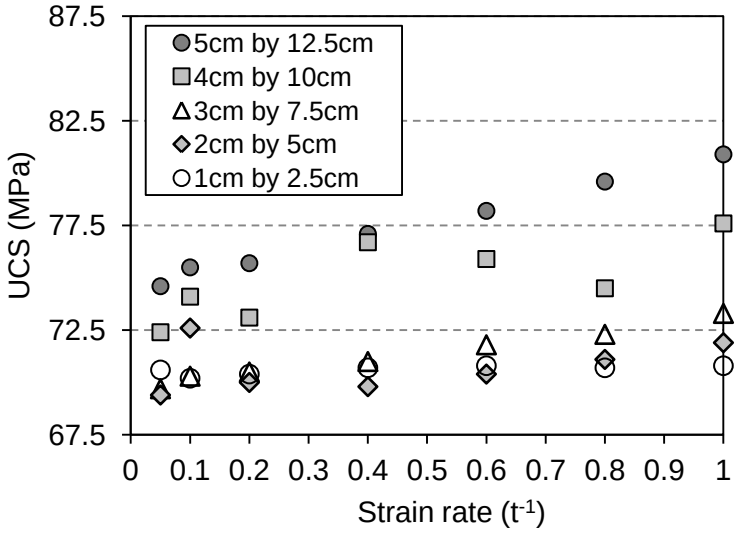

Figure 5-19: Influence of strain rate on the *UCS* of differently-sized grain-based specimens.

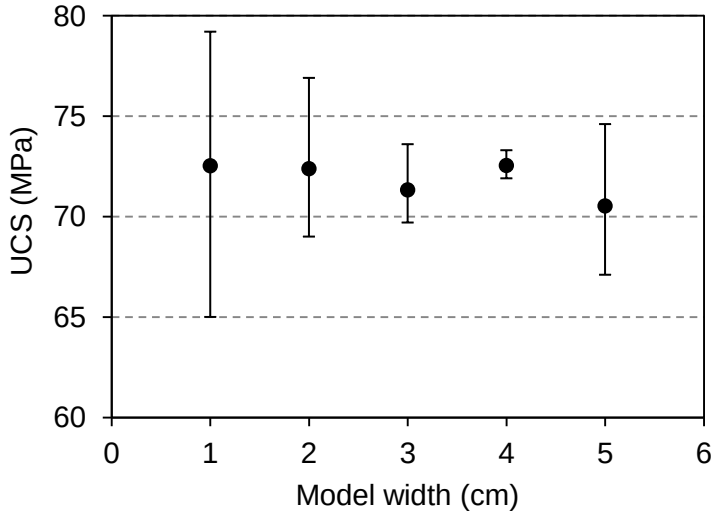

Figure 5-20: Influence of specimen size on the *UCS* of grain-based specimens simulated with the strain rate of 0.05. Error bar indicates minimum and maximum strengths.

Figure 5-21a shows that the stress-strain responses of differently sized grain-based specimens behave very similarly, which is in agreement with the findings of Exadaktylos and Vardoulakis (2001) and Lan et al. (2010). The failure mode of differently sized grain-based specimens is shown in Figure 5-21b.

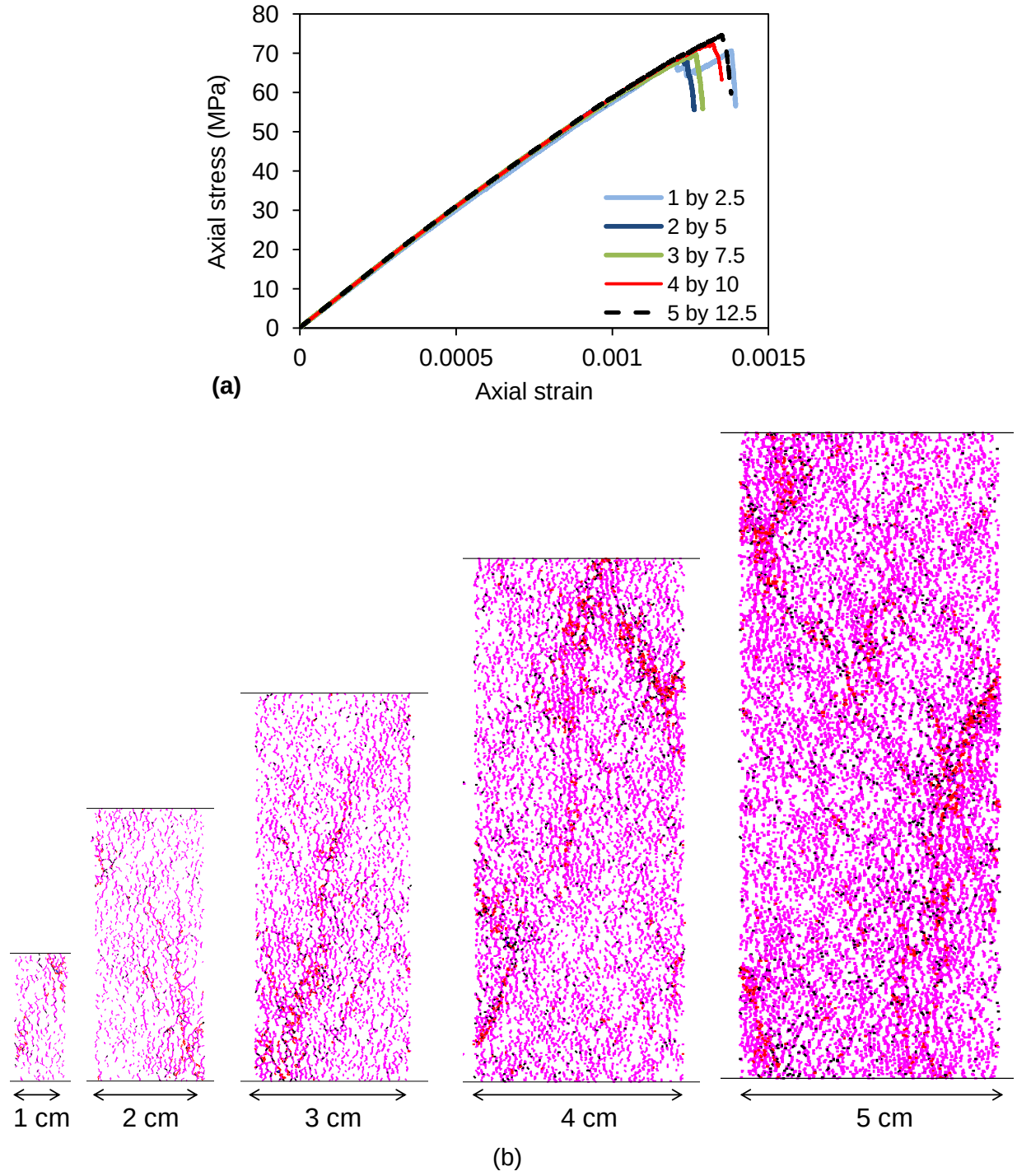

Figure 5-21: a) Stress-strain curves of differently sized undamaged grain-based specimens; b) failure modes of differently sized undamaged grain-based specimens. Pink and black refer to inter-grain tensile and shear cracks, respectively, and red and blue refer to intra-grain tensile and shear cracks.

It can be seen from Figure 5-21b that the specimen size has little influence on the failure mode. The failure mode of all the specimens is dominated by the grain boundary tension cracks that are oriented in a manner that is approximately parallel to the loading direction. These tension cracks are randomly located within the specimens. The interaction between these tension cracks generates relatively long axial fractures. These axial fractures interact with inter- and intra-grain shear cracks to generate macroscopic shear fractures close to the boundaries of the specimens and drive them to failure.

5.3.2 Influence of specimen size on strength of defected rock

5.3.2.1 Generation of Discrete Fracture Network (DFN) models

The influence of specimen size on the strength of defected rocks is investigated in this section. The *DFN* was used to simulate the defect geometries. The *DFN* generator scheme in *Phase2* (Rocscience, 2010) was used for this purpose. Prior to generating a *DFN* model, statistical parameters for each defect (i.e., the joint element in *Phase2*) needed to be defined. These include the mean, the standard deviation and the statistical distribution (normal distribution, in this study) for defect orientation, length, and persistence. A defect intensity (joints/area) of 0.2 was used in all the *DFN* models. The generated *DFN* models consisted of two sets with different orientations for defects. In total, six $12\,\text{cm} \times 24\,\text{cm}$ *DFN* models presenting the defect configurations listed in Table 5-2 were generated. The geometries of all the six *DFN* models are shown in Figure 5-22. Note that *DFN1* to *DFN3*, and *DFN4* and *DFN5* were generated using the same input parameters, which means that the differences in their geometries noticeable in Figure 5-22 are due to stochastic sampling during *DFN* generation.

Table 5-2: Configuration of defects (joint elements in *Phase2*) in *DFN* models.

DFN #	Joint set #	Dip angle (°)		Length (cm)		Persistence (cm)	
		Mean	S.Dev.	mean	S.Dev.	mean	S.Dev.
1, 2 & 3	1	0	5	2	0.5	0.5	0.1
	2	90	5	2	0.5	0.5	0.1
4 & 5	1	40	5	2	0.5	0.5	0.1
	2	130	5	2	0.5	0.5	0.1
6	1	20	5	2	0.5	0.5	0.1
	2	110	5	2	0.5	0.5	0.1

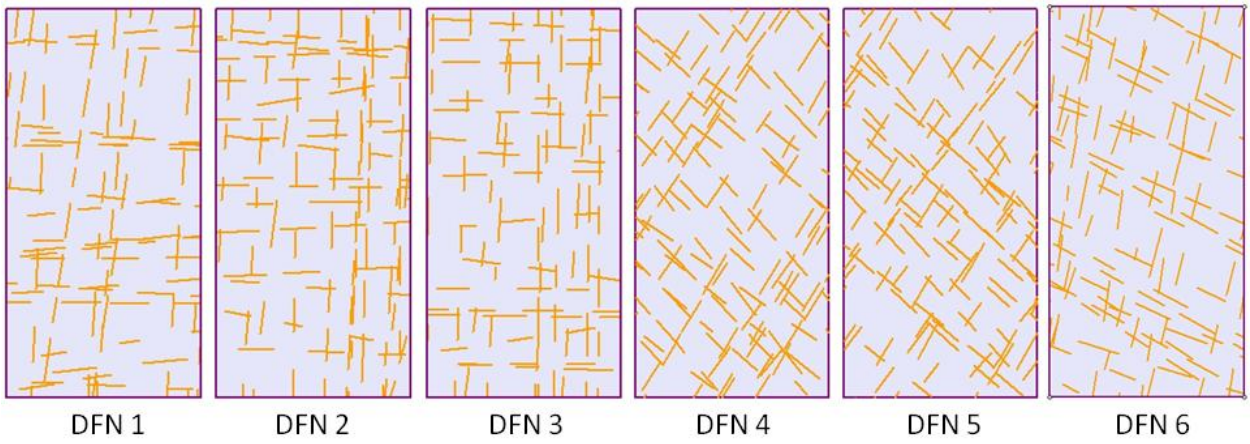

Figure 5-22: Six 12 cm × 24 cm *DFN* models generated using *Phase2*.

5.3.2.2 Integration of GBM and DFN

In this section, the grain-based specimens are combined with the *DFN* models described above in order to more realistically simulate a defected rock and investigate the influence of specimen size on its strength. The defected grain-based specimens are called *GBM-DFN*x, wherein x refers to the number of the *DFN* model shown in Figure 5-22 (e.g., *GBM-DFN5*).

The following describes the steps undertaken to generate a defected grain-based specimen. The defect structure (obtained from the *DFN* models in Figure 5-22) is first overlaid on the ball specimens according to the properties listed in Table 3-2. The defect structure is replaced by the

smooth-joint contacts with the properties listed in Table 5-3. Next, the grain structure is overlaid on the ball specimens consisting of defects. The grain structure is replaced by the smooth-joint contacts. The properties of the smooth-joints used to simulate the grain boundaries are the same as those of undamaged grain-based specimens calibrated to the properties of the intact Wombeyan marble in *Chapter 3* (see Table 3-3).

The properties of the smooth-joints used to simulate the defects are listed in Table 5-3. The defects were simulated to be cohesive yet weaker and softer than the grain boundaries; the tensile strength and cohesion of the smooth-joints representing the defects are 10% of those representing the grain boundaries and the stiffness of the smooth-joints representing the defects are 2.5 times smaller than those representing the grain boundaries. Similar to the grain boundaries, a zero friction angle (peak frictional component) and a non-zero friction coefficient (residual frictional component) was chosen for the defects. However, the smooth-joints representing the defects were assigned a lower friction coefficient of 0.7, which corresponds to the friction angle of 35°.

Five samples were taken from the center of each *DFN* model to generate five smaller *DFN* models with widths ranging from 1 to 5 cm and a height to width ratio of 2.5 (Figure 5-23). Each *DFN* model was combined with differently sized grain-based specimens following the procedure described above. Figure 5-24 shows an example of differently sized *GBM-DFN1* specimens. A series of uniaxial compressive strength tests were simulated on the *GBM-DFN* specimens and the results in terms of peak strength were used to investigate the influence of specimen size on the strength of defected rocks.

Table 5-3: Properties of smooth-joint contacts representing defects.

Parameters	Values
smooth-joint normal (tensile) strength	1 MPa
smooth-joint cohesion	6.5 MPa
smooth-joint friction angle	0°
smooth-joint friction coefficient	0.7
smooth-joint normal to shear stiffness ratio	2.5
smooth-joint stiffness factor	0.08

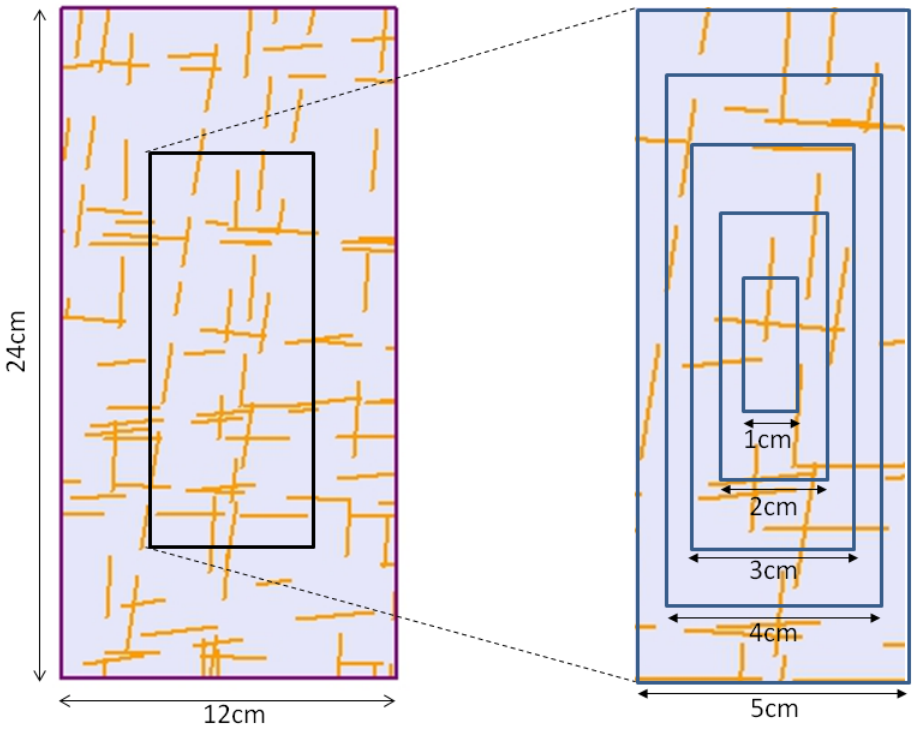

Figure 5-23: Samples taken from the *DFN1* model.

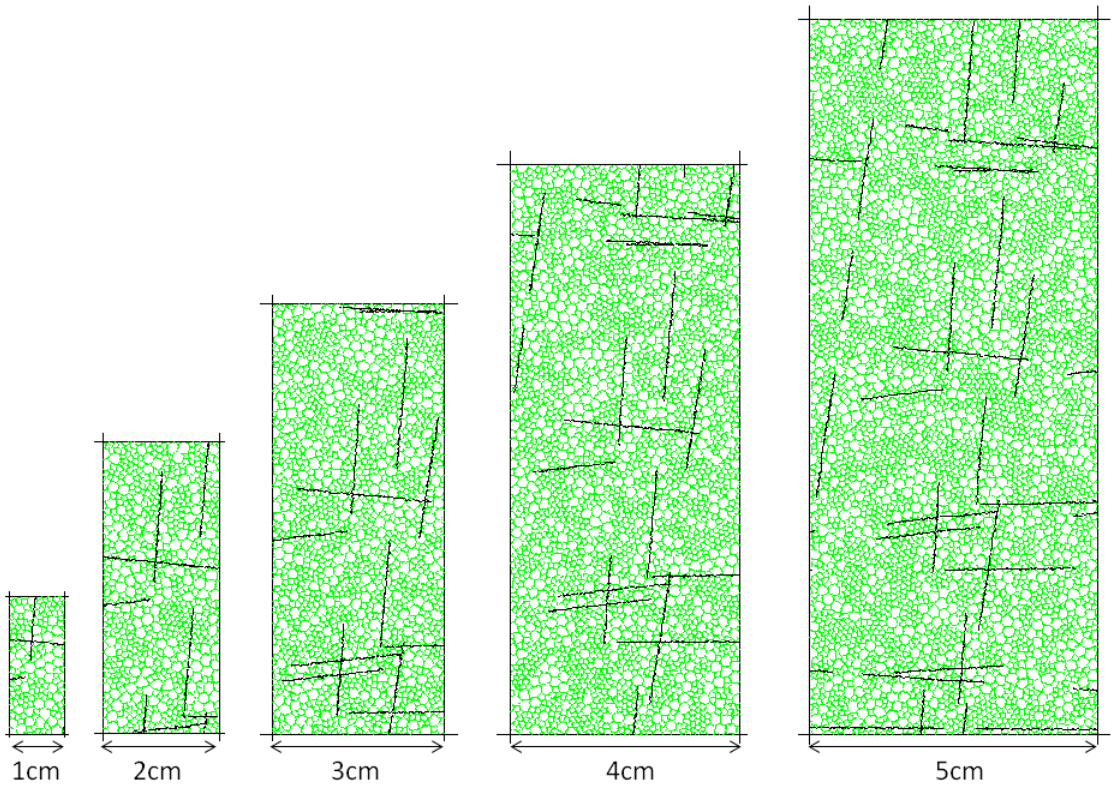

Figure 5-24: Five *GBM-DFN1* specimens with widths ranging from 1 to 5 cm and a height-to-width ratio of 2.5. Green lines refer to the undamaged grain boundaries and black lines refer to the defects.

5.3.2.3 Results of scale effect simulations on GBM-DFN specimens

The stress-strain curves and failure modes of three of the *GBM-DFN* specimens are investigated in this section. Figure 5-25 presents the stress-strain curves and failure modes of differently sized *GBM-DFN3* specimens. The defects in these specimens are nearly parallel and perpendicular to the loading direction. The stress-strain curves of all the specimens are similar up to close to the peak stress (Figure 5-25a). The stress-strain curves close to the peak stress and in the post-peak region include fluctuations in the axial stress until the specimens fail following an abrupt stress drop. Figure 5-25a illustrates how the strength of *GBM-DFN3* specimens tends to decrease with increasing specimen size and levels off at larger specimen sizes.

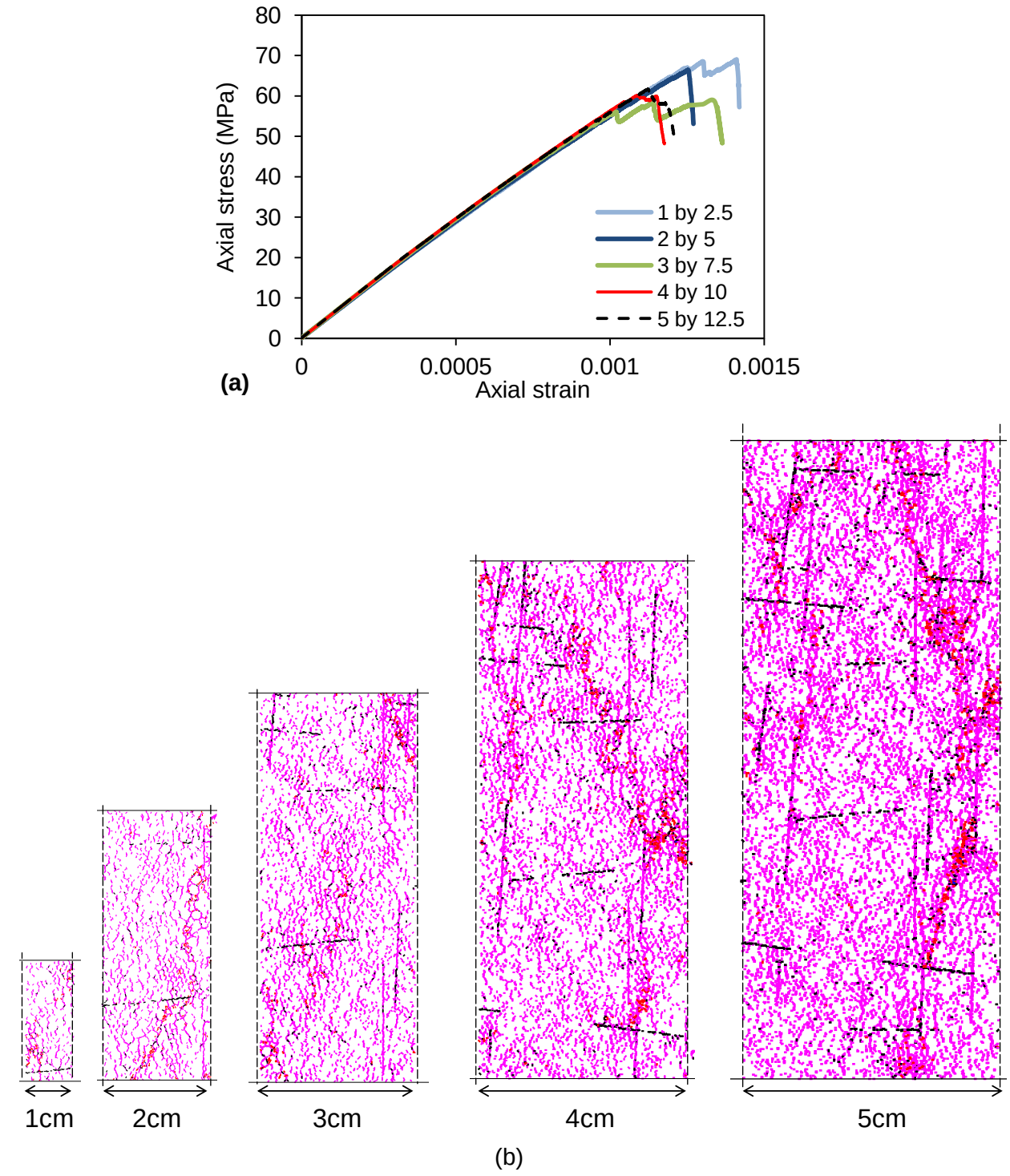

Figure 5-25: a) Stress-strain curves; and b) failure modes of differently sized *GBM-DFN3* specimens. The dashed lines in (b) indicate the specimen boundaries. Pink and black refer to inter-grain and defect tensile and shear cracks (smooth-joint), respectively, and red and blue refer to intra-grain tensile and shear cracks (parallel bond).

The failure modes shown in Figure 5-25b are similar. Two types of failure can be observed for defects; tensile failure of defects that are nearly parallel to the loading direction, and shear failure of defects that are nearly perpendicular to the loading direction. The failure modes of the intact part of the specimens is similar to the undamaged grain-based specimens described in *Section 3.4.5* and *Section 5.3.1*; the interaction of axial inter-grain tensile micro-cracks leads to the formation of macroscopic axial fractures and the interaction of inter-grain shear micro-cracks and intra-grain tensile micro-cracks leads to the formation of macroscopic shear fractures.

The behavior of *GBM-DFN2* specimens (not shown) is very similar to that of *GBM-DFN3* specimens in terms of the stress-strain curves and failure modes and is therefore not reviewed here. The behavior of *GBM-DFN1* specimens is also very similar to those of *GBM-DFN3* specimens in terms of its stress-strain curves and failure modes. The strength of *GBM-DFN1* specimens, however, decreases more rapidly than that of *GBM-DFN3* specimens due to the localized failure of steep defects intersecting the boundaries of the larger specimens.

Figure 5-26 presents the stress-strain curves and failure modes of differently sized *GBM-DFN4* specimens. Two sets of defect in these specimens have the mean dip angles of 40° and 130°. This means that the set with the dip angle of 130° ± 5° is nearly parallel to the direction of critical shear stress for a defect with the friction angle of 35°.

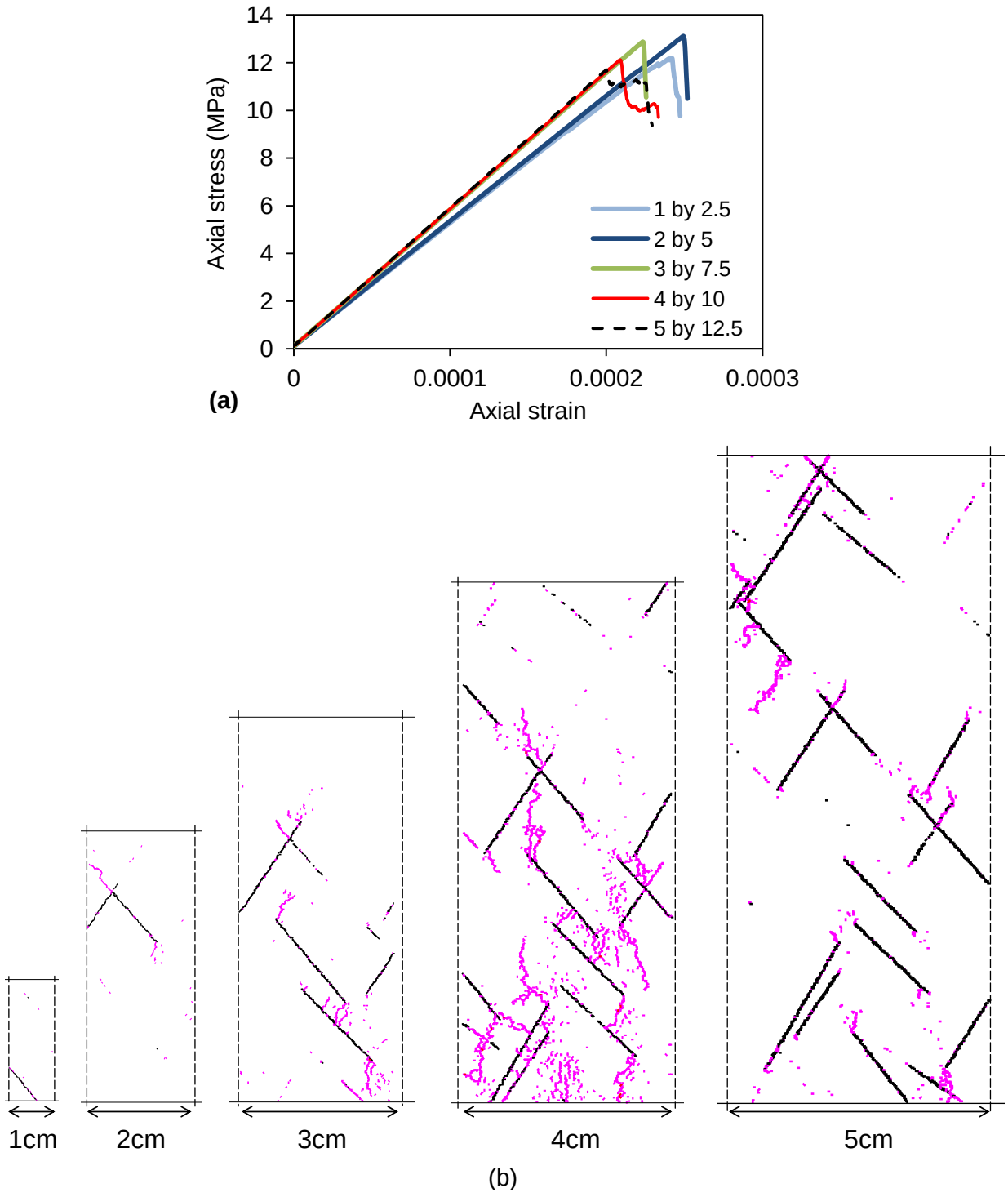

Figure 5-26: a) Stress-strain curves; and b) failure modes of different sized *GBM-DFN4* specimens. The dashed lines indicate the specimen boundaries. Pink and black refer to inter-grain and defect tensile and shear cracks (smooth-joint), respectively, and red and blue refer to intra-grain tensile and shear cracks (parallel bond).

Figure 5-26a shows that the stress-strain curves of differently sized *GBM-DFN4* specimens are very similar at all of the three loading stages, including pre-peak, peak and post-peak regions. As expected, the peak strength was found to be much lower than other specimens. This is interpreted to be due to the failure mode of these specimens, which is dominated by the shear failure of the defects that are critically oriented (as shown in Figure 5-26b). In some cases, especially in that of the specimen with the width of 4 cm, tensile crack propagation from the tips of the defects can be observed. The behaviors of *GBM-DFN5* specimens are very similar to those of *GBM-DFN4* specimens in terms of stress-strain curves and failure modes and, therefore, are not reviewed here.

Figure 5-27 illustrates the stress-strain curves and failure modes of differently sized *GBM-DFN6* specimens. The smallest *GBM-DFN6* specimen is the weakest specimen and behaves differently from the other four specimens in terms of its stress-strain curve and failure mode (Figure 5-27a). Its strength is comparable to those of the *GBM-DFN4* and *GBM-DFN5* specimens as the failure occurs by shearing along a defect. The other four specimens, whose widths range from 2 to 5 cm, behave in an elastic manner until an axial stress of about 15 MPa occur, whereupon a slight reduction in axial stress occurred due to slip along defects. This reduction is followed by a stress build-up as shear failure of the defects cannot be propagated into the rock bridge. Such steps in the stress-strain curves occur a few times prior to the peak stress. A few stress drops and build-ups can also be seen in the post-peak region. The failure modes of these specimens include defects that have mainly failed in shear as well as rock bridges whose failures were dominated by inter-grain tensile cracks propagated from the tips of their defects (Figure 5-27b).

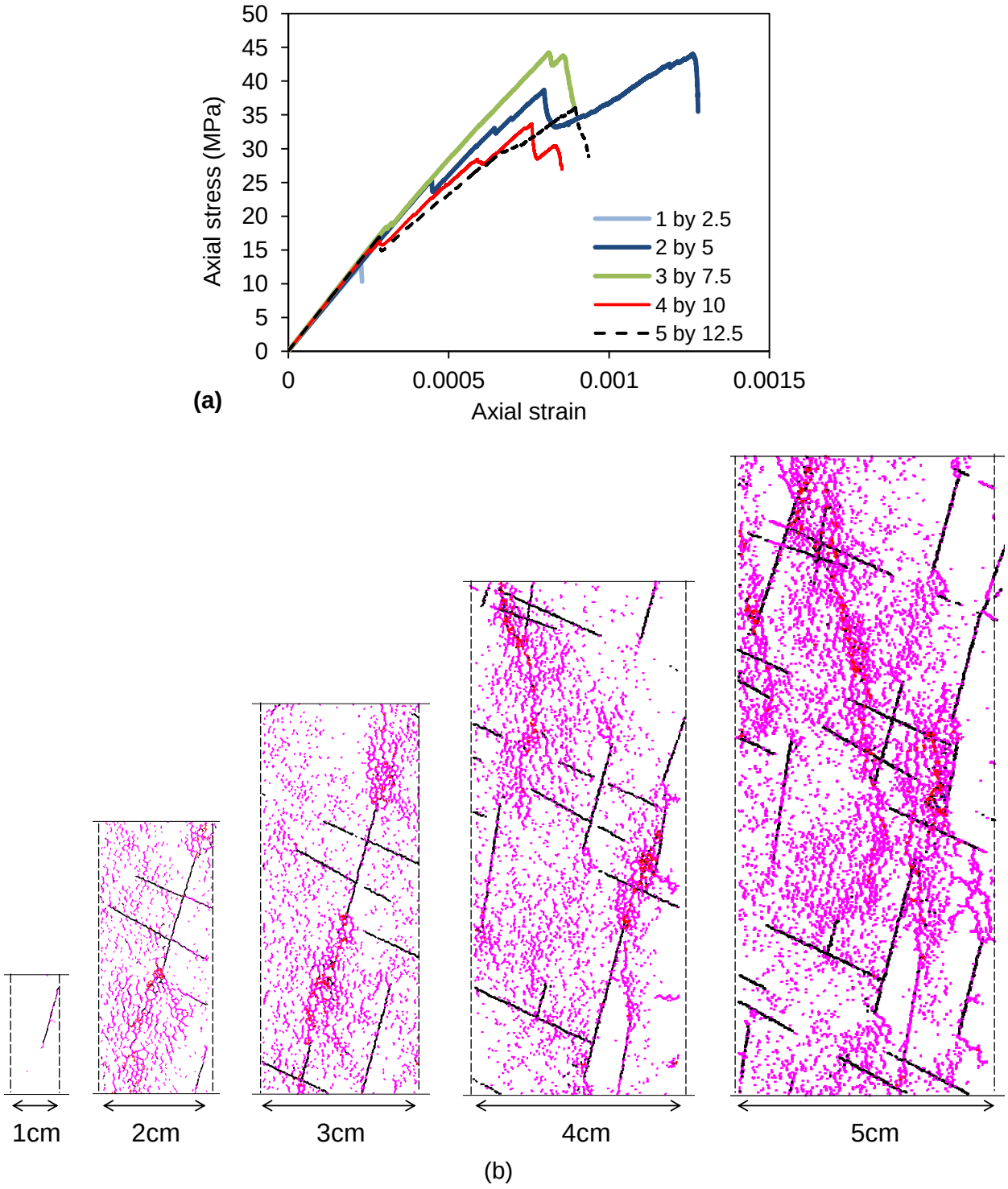

Figure 5-27: a) stress-strain curves; and b) failure modes of differently sized *GBM-DFN6* specimens. The dashed lines show the specimen boundaries. Pink and black refer to inter-grain and defect tensile and shear cracks (smooth-joint), respectively, and red and blue refer to intra-grain tensile and shear cracks (parallel bond).

The results of scale effect tests simulated on defected grain-based specimens are summarized in Figure 5-28. This figure plots the peak strength versus specimen width. It can be seen from Figure 5-28 that, on one hand, the strength of intact grain-based specimen with no defects is independent of scale, as is expected for tests conducted with frictionless platens. On the other hand, the specimens with defects oriented parallel and perpendicular to the loading direction (*GBM-DFN2* and *GBM-DFN3*) show a small reduction in strength with the increase in specimen size. The rapid reduction in the strength of *GBM-DFN1* specimens is due to the presence of discrete defects that intersect their boundaries and causing them to fail prematurely. The specimens with critically oriented defects (*GBM-DFN4* and *GBM-DFN5*) exhibit the lowest strengths and the strength they do possess is independent of specimen size. The *GBM-DFN6* specimen with the width of 1 cm has a low strength of 13 MPa. This low strength is due to its failure along a discrete defect. An increase in the specimen size results in an increase and then a decrease in the strength. The strength of the maximum sized specimen is close to 50% of the intact strength.

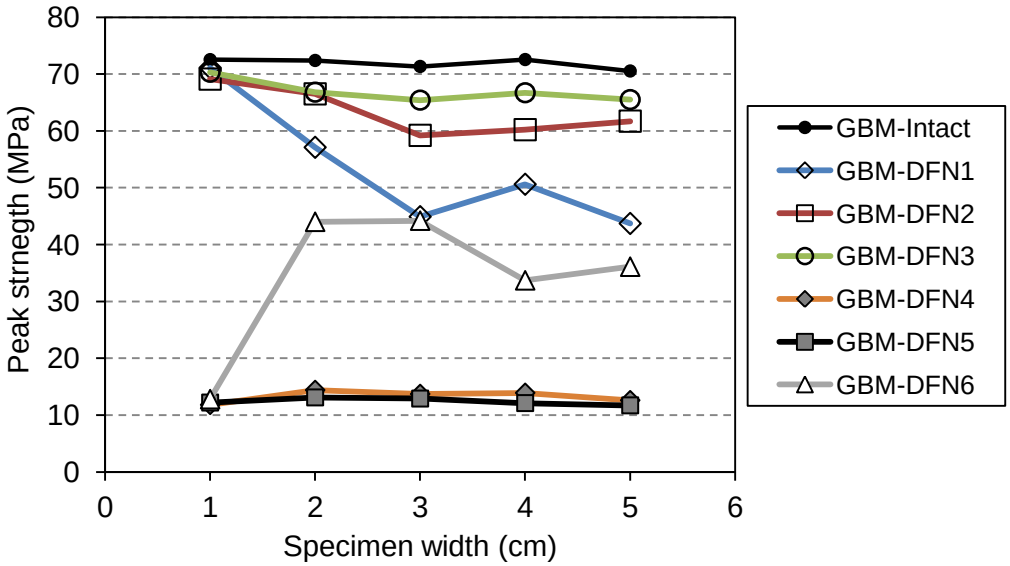

Figure 5-28: Results of numerical analysis on different sized intact and defected grain-based specimens.

In summary, the results presented in this section are consistent with those of previous studies that used the *SRM* modeling approach. This consistency clearly demonstrates the nature of the dominant effect of the defect orientation and properties on the strength of defected rocks. In this research, the defects were simulated using the smooth-joint contact logic in *PFC2D* with strength properties (i.e., peak: $\phi_j = 0°$, $c_j = 6.5$ MPa, $\sigma_{tj} = 1$ MPa, residual: $\phi_j = 35°$, $c_j = 0$ MPa, $\sigma_{tj} = 0$ MPa) that are much lower than the strength of the intact part of the host rock. In reality, the defects may actually prove to be stronger or weaker than the adopted strength values, which may result in a lower or higher strength reduction as the specimen size is increased. Therefore, it should not be expected that all defected rocks will present similar behaviours.

5.3.2.4 Integration of BM and DFN specimens

As the *GBM-DFN* specimens with a width of 5 cm would take between 10 and 15 days to run, which was beyond the abilities of available computing resources, further increase in the size of grain-based specimens was not feasible. This is due to the large number of balls and bonds required to generate larger *GBM-DFN* specimens. As such, it was decided that it would be the conventional ball model rather than the grain-based model that would serve as the intact material for larger specimens. The smooth-joint contacts were used to simulate defects, similar to the standard *SRM* approach.

This required the generation of a ball model with a reasonable number of balls and its calibration to the properties of undamaged grain-based specimen under unconfined condition (i.e., *UCS*). Figure 5-29 compares the ball and grain-based specimens in terms of the number of balls each possesses and the size of balls and grains. As can be seen from this figure, the balls in the ball model are smaller than the grains but larger than the balls in the grain-based model. In fact, the

number of balls in the ball model is about 8 times less than that in the grain-based model. The calibration was simply conducted by reducing the parallel bond strength until the unconfined strength of the ball model became comparable to that of undamaged grain-based specimens. The micro-properties of the calibrated ball model are listed in Table 5-4. Figure 5-30 illustrates how the *UCS* of the ball model is comparable to that of grain-based specimens.

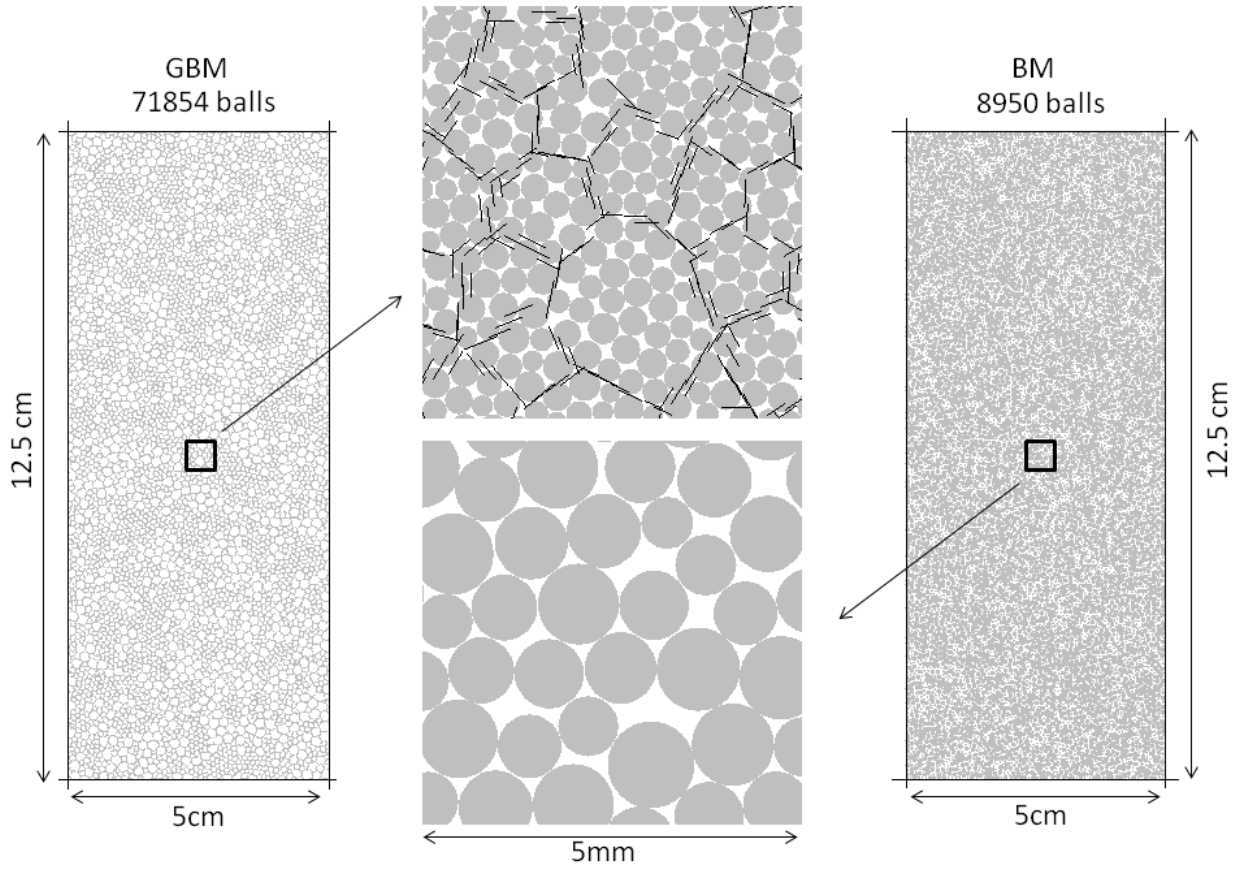

Figure 5-29: The *BM* used to replace the *GBM*, and comparison between the ball and grain sizes in the *BM* and the *GBM*.

Table 5-4: Micro-properties of the calibrated ball model.

Micro-parameters	Values
minimum particle (ball) radius	0.34 mm
ratio of maximum to minimum ball radius	1.66
contact normal to shear stiffness ratio	2.5
parallel bond normal to shear stiffness ratio	2.5
contact modulus	50 GPa
parallel bond modulus	50 GPa
ball friction coefficient	0.5
parallel bond radius multiplier	1
parallel bond normal (tensile) strength	55 MPa
parallel bond cohesion	55 MPa
parallel bond friction angle	0°

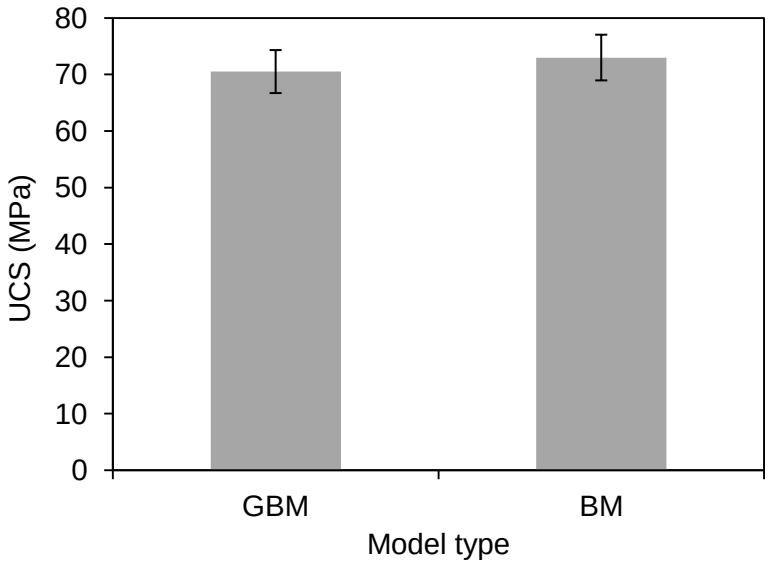

Figure 5-30: Comparison between the strengths of 5 cm by 12.5 cm ball and grain-based specimens.

Once the ball model was calibrated, the *BM-DFN* specimens were generated by overlaying the *DFN* structure on the ball models and replacing the defect structures with smooth-joint contacts using the properties listed in Table 5-3. The *UCS* test was simulated on the *BM-DFN* specimens and their strengths, failure modes and stress-strain curves were compared with those of *GBM-DFN* specimens.

Table 5-5 provides a comparison between the strengths of *GBM-DFN* and *BM-DFN* specimens and suggests that the two model types are very similar in terms of their strength values. The failure modes and stress-strain responses of *GBM-DFN* and *BM-DFN* specimens were also found to be comparable with one another. As an example, the failure modes of *GBM-DFN1* and *BM-DFN1* as well as *GBM-DFN4* and *BM-DFN4* specimens are compared in Figure 5-31. It can be seen from this figure that the *BM-DFN* specimens capture the macroscopic fractures observed in the *GBM-DFN* specimens, including the failure along defects and their interactions with the intact part that drive the specimens to failure.

However, they do not capture the grain boundary micro-cracks randomly located in the *GBM-DFN* specimens that mainly occur in the pre-peak stage of loading. This is due to the relatively high parallel bond tensile strength of 50 MPa used in the ball model compared to the smooth-joint tensile strength of 10 MPa used in the grain-based specimen that was required for the calibration of the ball model. The stress-strain curves of *GBM-DFN1* and *BM-DFN1* are shown in Figure 5-32. The intact and defected ball specimens (*BM* and *BM-DFN*) exhibit stress-strain responses, including reductions in Young's modulus and strength that are similar to those of intact and defected grain-based (*GBM* and *GBM-DFN*) specimens.

Table 5-5: Comparison of the unconfined strengths of *GBM-DFN* and *BM-DFN* specimens with a width of 5 cm.

Model type	*DFN1* (MPa)	*DFN2* (MPa)	*DFN3* (MPa)	*DFN4* (MPa)	*DFN5* (MPa)	*DFN6* (MPa)
GBM-DFN	43.7	61.7	65.5	12.6	11.7	36.1
BM-DFN	48.8	63	61.2	16	13.5	26.6

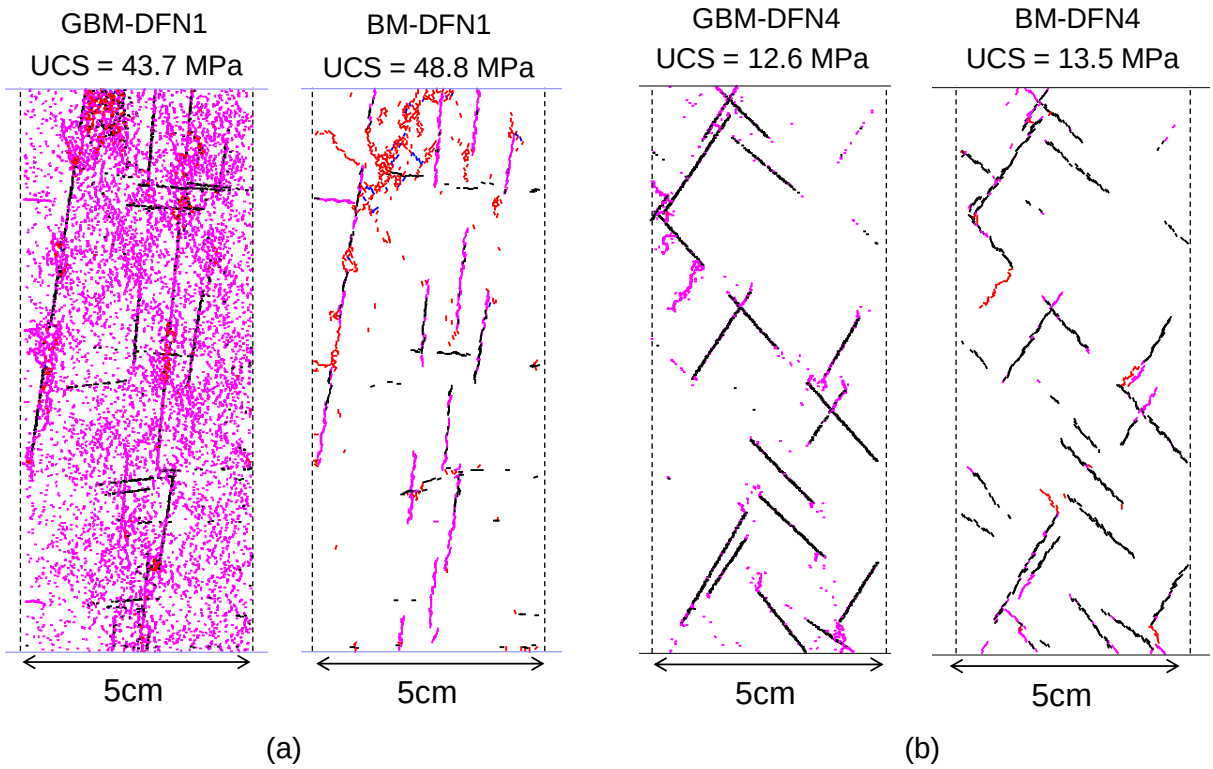

Figure 5-31: Comparison of the failure modes of 5 cm by 12.5 cm: a) *GBM-DFN1* and *BM-DFN1* specimens; and b) *GBM-DFN4* and *BM-DFN4* specimens. The dashed lines indicate the specimen boundaries. Pink and black refer to tensile and shear smooth-joint cracks (grain boundary or defect), respectively, and red and blue refer to parallel bond tensile and shear cracks (grain or intact part of the specimen).

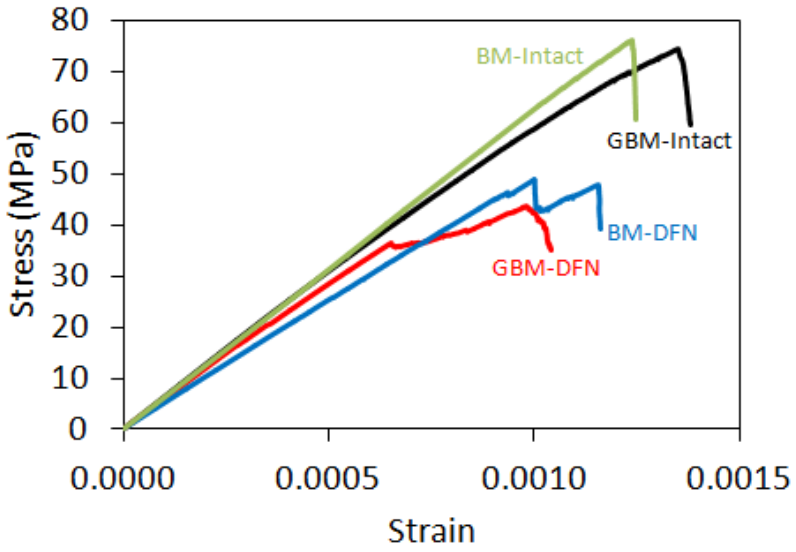

Figure 5-32: Comparison between stress-strain curves of 5 cm by 12.5 cm intact and defected ball (*BM* and *BM-DFN*) and grain-based (*GBM* and *GBM-DFN*) specimens.

In summary, the defected ball specimens were found to be reasonable models of the defected grain-based specimens in terms of strength, macroscopic failure modes and stress-strain responses under unconfined condition. The results of scale effect simulations using the calibrated ball model are presented next.

5.3.2.5 Results of scale effect simulations on BM-DFN specimens

Once the *BM-DFN* specimens with the width of 5 cm were confirmed to behave similarly to the *GBM-DFN* specimens of the same size in terms of strength, failure modes and stress-strain responses, the scale effect investigation was continued on two larger defected ball specimens (*BM-DFN*) with widths of 8 and 12 cm and a height-to-width ratio of 2. An example of two larger samples taken from the *DFN1* model is shown in Figure 5-33. The *BM-DFN* specimens were generated following the approach described earlier and *UCS* tests were simulated on the *BM-DFN1* to *BM-DFN6* specimens.

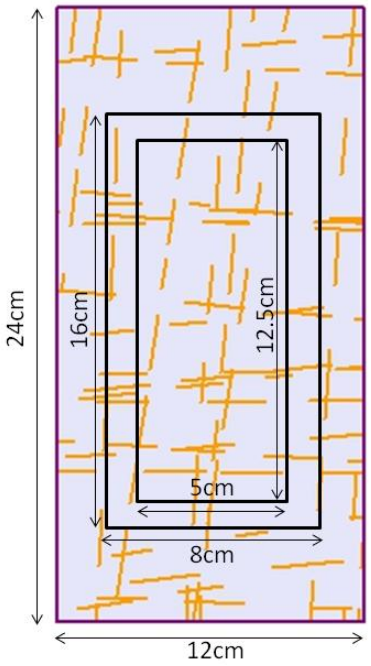

Figure 5-33: Samples taken from *DFN1* model.

Figure 5-34 presents the stress-strain curves and failure modes of the *BM-DFN3* specimens with widths ranging from 5 to 12 cm. It is seen that the specimens' strengths are independent of their sizes. The specimens all behaved in a linear elastic manner until the peak stress, which followed by a rapid stress drop in the post-peak region (Figure 5-34a). The failure modes of the differently-sized *BM-DFN3* specimens are shown in Figure 5-34a. As can be seen from this figure, prior to reaching the peak stress, failure involves the tensile cracking of the defects oriented nearly parallel to the applied load and minor shear cracking of the defects orientated nearly perpendicular to the applied load. This is followed by the tensile fracturing of the intact part of the specimen, which is formed from the tips of defects and propagates towards adjacent ones. This process begins to occur when the axial load is near the peak stress and continues in the post-peak region.

Figure 5-35 presents the stress-strain curves and failure modes of *BM-DFN4* specimens, respectively. The specimens' strengths seem to be independent of their size. Furthermore, the presence of defects oriented parallel to the critical shear stress direction resulted in a ductile behavior of the specimens under unconfined condition. As can be seen in Figure 5-35a, all three of the *BM-DFN4* specimens behave in a linearly elastic manner until they are close to the peak stress. Upon reaching this stress level, the stress-strain curves begin to include a few stress increases and decreases as the specimens continue to strain until an abrupt stress drop occurs. The failure modes include shear failure of defects, which are connected to each other through the tensile fracturing of the intact part of the specimens. Such an interaction results in the generation of continuous shear planes in the specimens, as is shown in Figure 5-35b.

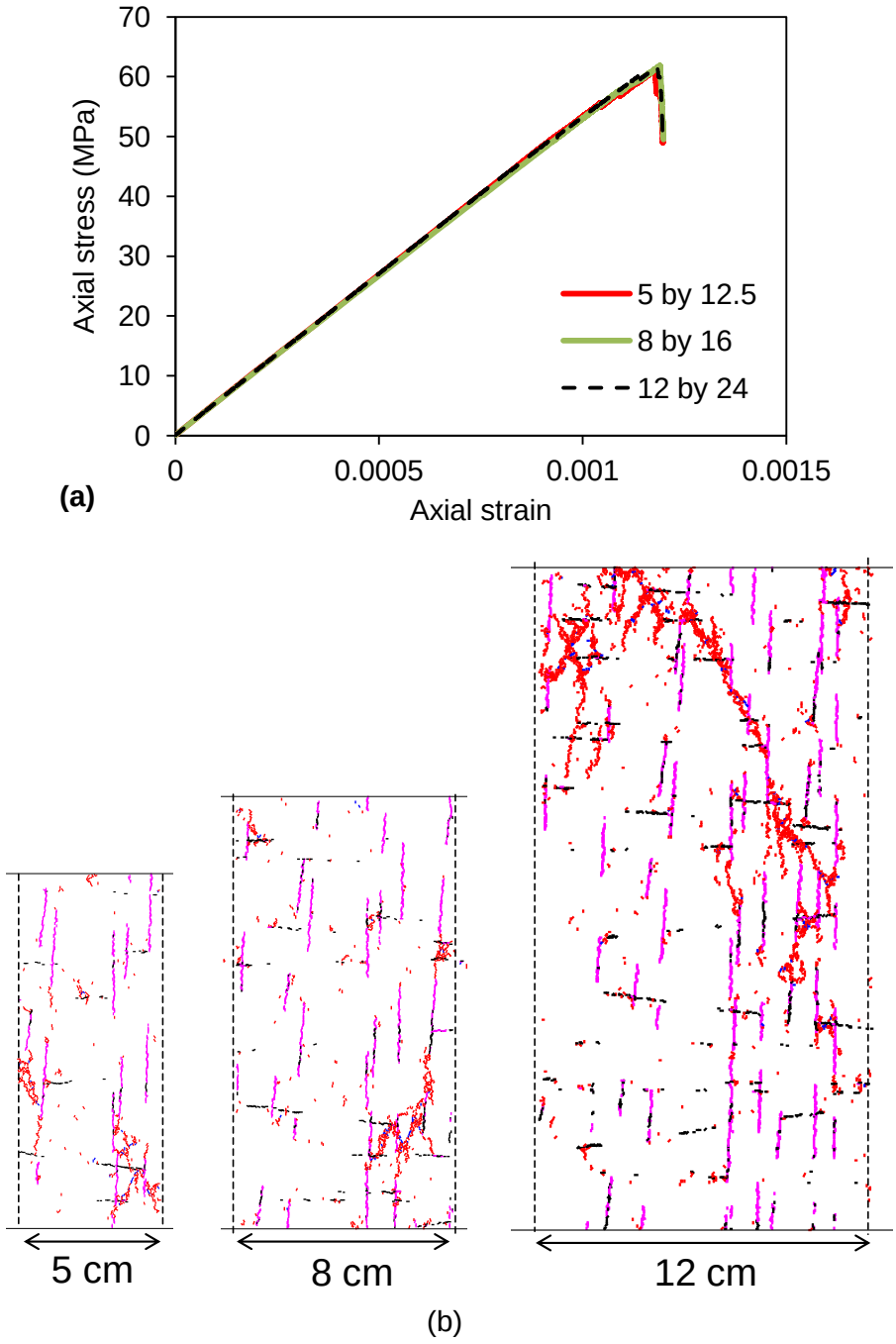

Figure 5-34: a) Stress-strain curves; and b) failure modes of differently sized *BM-DFN*3 specimens. The dashed lines indicate the specimen boundaries. Pink and black refer to tensile and shear smooth-joint (defect) cracks, respectively, and red and blue refer to parallel bond tensile and shear cracks.

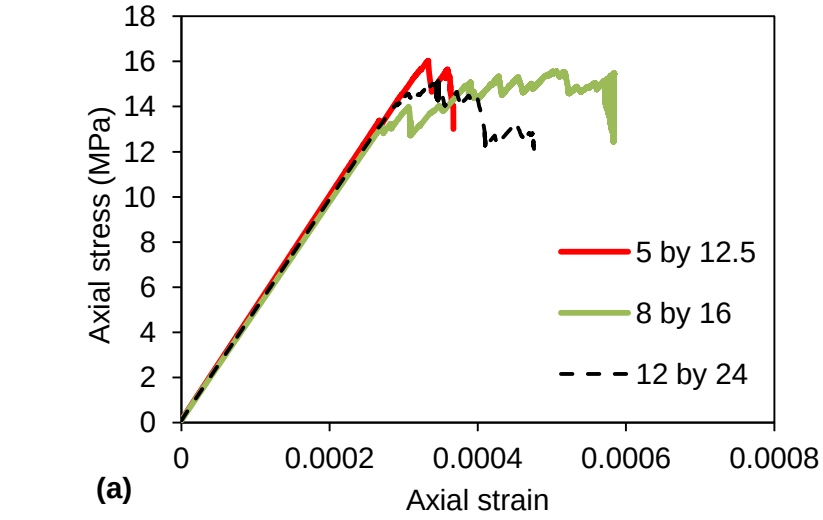

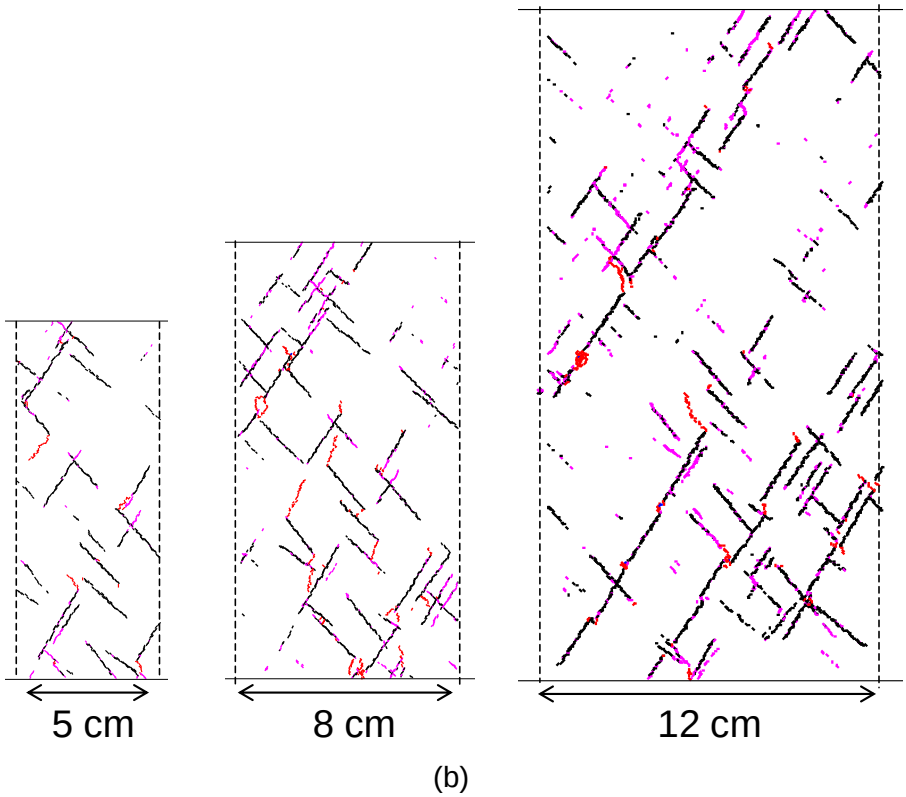

Figure 5-35: a) Stress-strain curves; and b) failure modes of differently sized *BM-DFN*4 specimens. The dashed lines indicate the specimen boundaries. Pink and black refer to tensile and shear smooth-joint (defect) cracks, respectively, and red and blue refer to parallel bond tensile and shear cracks.

The stress-strain curves and failure modes of the *BM-DFN6* specimens are presented in Figure 5-36. An increase in their strengths with increasing specimen size is observed. All of the three specimens studied behave in a linear elastic manner until an axial load of about 17 MPa (Figure 5-36a) is reached. From that point onward until the reaching of the peak stress, a few steps (i.e., stress decrease and increase) result in the reduction of the slope of the stress-strain curves. The specimens with the widths of 5 and 12 cm show a sudden stress drop in the post-peak region, whereas the specimen with the width of 8 cm shows a gradual reduction in the axial stress in the post-peak region. Figure 5-36b illustrates how the defects fail either in shear or tension. The failure also involves the tensile fracturing of the intact part of the specimens, which is propagated from the tips of the defects.

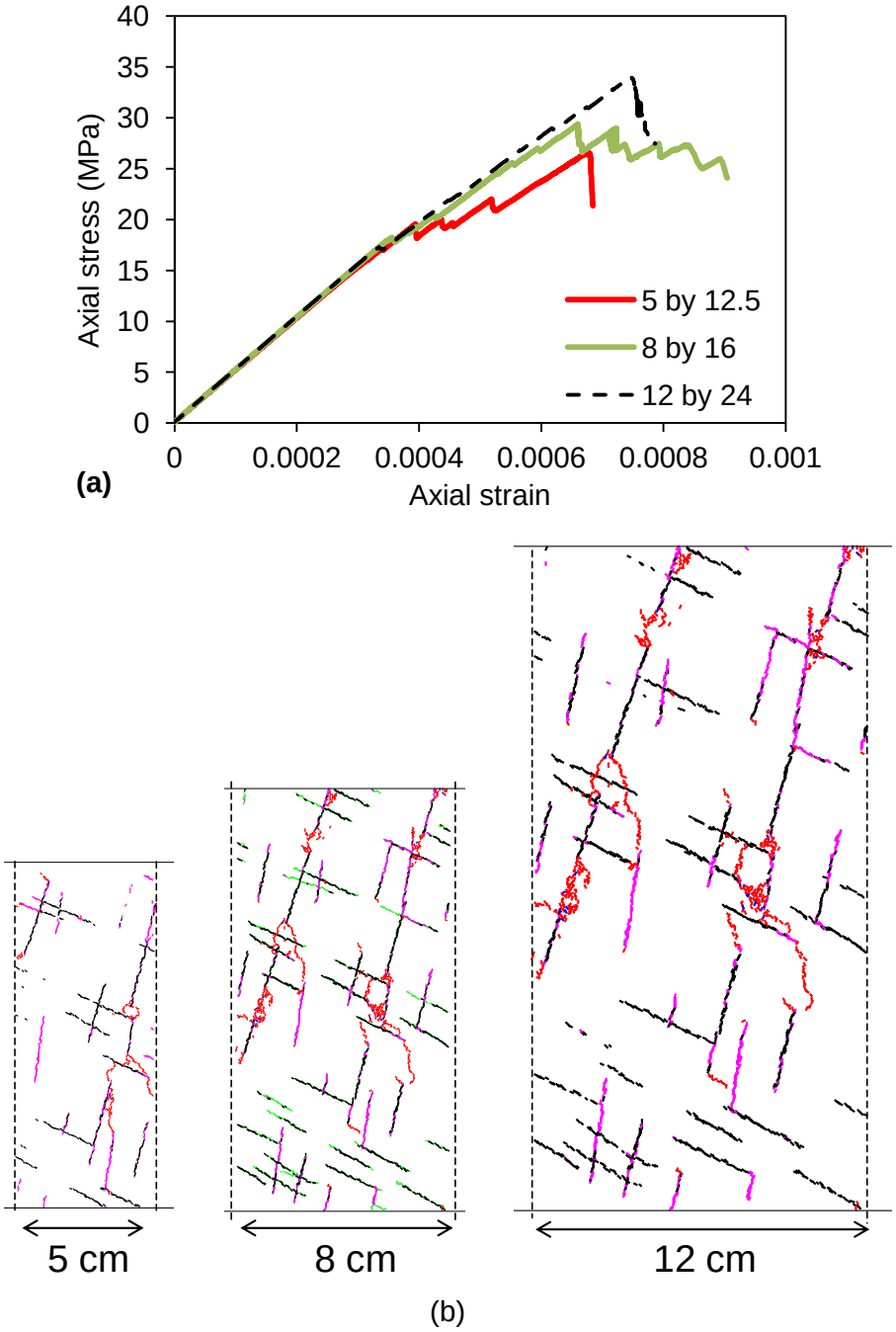

Figure 5-36: a) Stress-strain curves; and b) failure modes of differently sized *BM-DFN6* specimens. The dashed lines indicate the specimen boundaries. Pink and black refer to tensile and shear smooth-joint (defect) cracks, respectively, and red and blue refer to parallel bond tensile and shear cracks.

The results of scale effect tests simulated on defected grain-based and ball specimens are summarized in Figure 5-37. In terms of the strength values, the specimens can be divided into four groups:

- *Intact specimens*: The strength of intact rock tested with frictionless platens is independent of specimen size.
- *Defected specimens with the defect structures DFN1 to DFN3*: These specimens show a slight reduction in strength with increasing specimen size followed by a convergence to about 75% of the intact strength at their largest size.
- *Defected specimens with the defect structures DFN4 and DFN5*: The strength of these specimens is independent of specimen size and is directly influenced by the defect properties (which represent a lower limit in defect strength in these models).
- *Defected specimens with the defect structure DFN6*: The strength changes rapidly with size and tends to converge to about 45% of the intact strength at its largest specimen size.

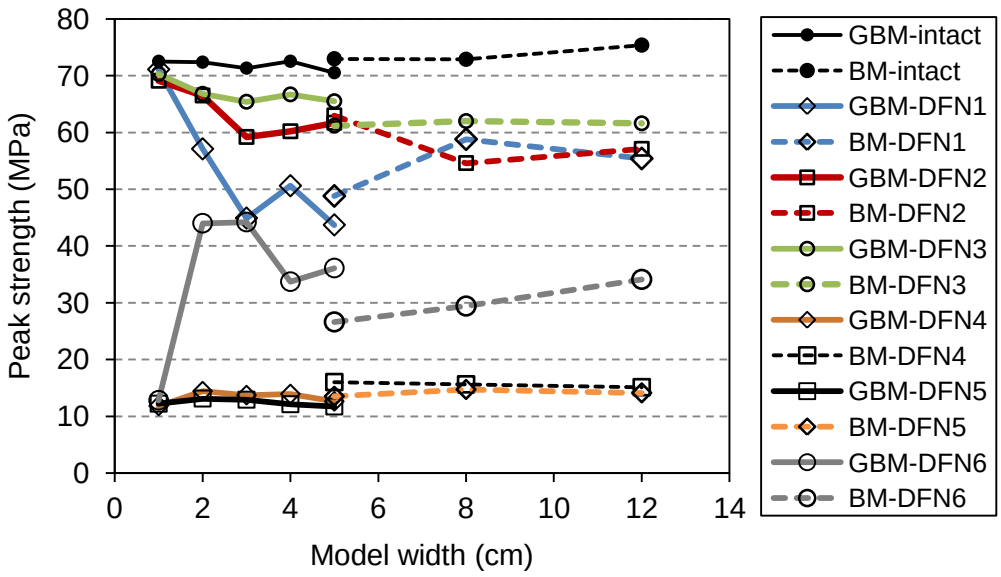

Figure 5-37: Influence of specimen scale on rock strength. Note that the results of grain-based model and conventional ball model are combined in this figure.

In terms of macroscopic failure mode, the specimens can be divided into three groups:

- *Intact specimens and defected specimens with the defect structures DFN1 to DFN3*: The macroscopic failure mode is mainly axial fracturing through intact rock.
- *Defected specimens with the defect structures DFN4 and DFN5*: The failure mode is mainly shear failure along discrete defects.
- *Defected specimens with the defect structure DFN6*: The failure involves a combination of axial fracturing though intact rock and shear failure along discrete defects.

5.4 Application of SD Approach for Estimation of Confined Strength of Defected Rock

In *Chapter 4*, the *SD* approach was developed to facilitate the estimation of the confined strengths of micro-defected rocks. In this section, the applicability of this approach for estimating the confined strength of defected rocks is investigated. For this purpose, the analysis was conducted on the results of laboratory experiments on large-sized coal specimens by Medhurst and Brown (1998), naturally defected limestone reported by Ribacchi (2000) and artificially slotted marble reported by Yang et al. (2008). The details of these experiments were reviewed in *Chapter 2* and are not repeated here.

5.4.1 Large-sized coal

The results of laboratory tests on the 61 mm, 146 mm and 300 mm diameter coal specimens reported by Medhurst and Brown (1998) are used to investigate the applicability of the *SD* approach for the estimation of the confined strengths of large-sized coal specimens.

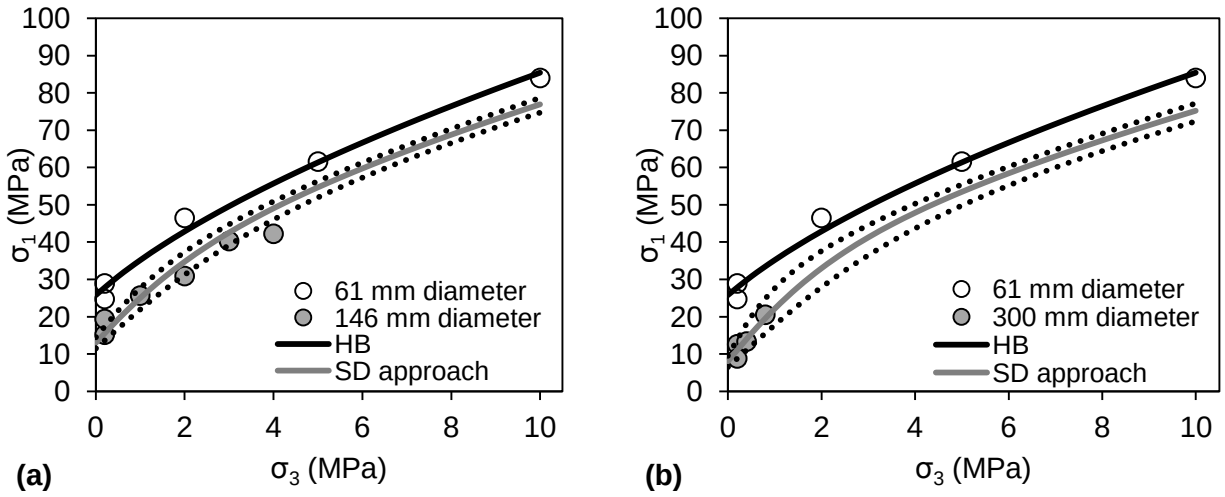

Figure 5-38: Laboratory data of 61 to 300 mm diameter coal specimens and the estimation of confined strength of: a) 146 mm diameter; and b) 300 mm diameter specimens using the *SD* approach (data from Medhurst and Brown, 1998). The dotted curves show the strength variability estimated using the *SD* approach.

In this analysis, the 61 mm diameter specimen is considered an intact specimen and the 146 mm and 300 mm diameter specimens are considered to be defected specimens. The UCS_d values for the 146 mm and 300 mm specimens, required in the *SD* approach, were estimated from projecting the linear strength envelope fitted to the peak strengths of these specimens at low confinement (see Figure 5-7). It can be seen from Figure 5-38 that the confined strengths of both large-sized specimens and their variability are reasonably captured using the *SD* approach for the range of confinement under which these tests were conducted.

5.4.2 Fractured limestone

The results of laboratory tests on intact (*IN*) and defected (*IF*, *FR*, and *SH*) limestone specimens reported by Ribacchi (2000) along with the confined strengths estimated using the *SD* approach are presented in Figure 5-39 (a, c and d). As a reminder, the specimens were divided into the following four groups:

- *IN*: seemingly intact specimens;
- *IF*: specimens with rare and mostly healed fractures;
- *FR*: specimens with diffused fracturing;
- *SH*: specimens having multiple shear surfaces.

It was indicated in *Chapter 2* that there is a wide scatter even in the intact data (likely due to failure on weakness planes), which means that it would be unreasonable to expect a perfect fit to the defected data. Nevertheless, as can be seen from Figure 5-39a, the *SD* approach provides a reasonable estimate of the confined strength of the *IF* specimens, which were described as containing healed fractures. The upper and lower bounds obtained from approximating the ± 95% *CI* (dotted lines) indicate the estimated variability in the test data. Clearly, many weaker tests fall outside of the estimated upper and lower strength envelopes (dotted curves), but this is not unexpected as they are likely dominated by the presence of through-going and/or critically oriented defects.

It must be noted that the *SD* approach is not applicable when assessing the strengths of *SH* specimens as failure in these specimens is dominated by shearing along defects and, therefore, their strengths are not representative of the strength of defected rocks but rather that of the weakness plane. The scatter in the strength values is derived from deviations from the critical plane (i.e. minimum only if the weakness is parallel to the plane of critical shear stress). This is evident in Figure 5-39c, where the strength envelope is indicated for an equivalent friction angle of 30°. The mismatch of the *SD* approach is therefore expected and understood as the *SH* data basically provide the defect strength.

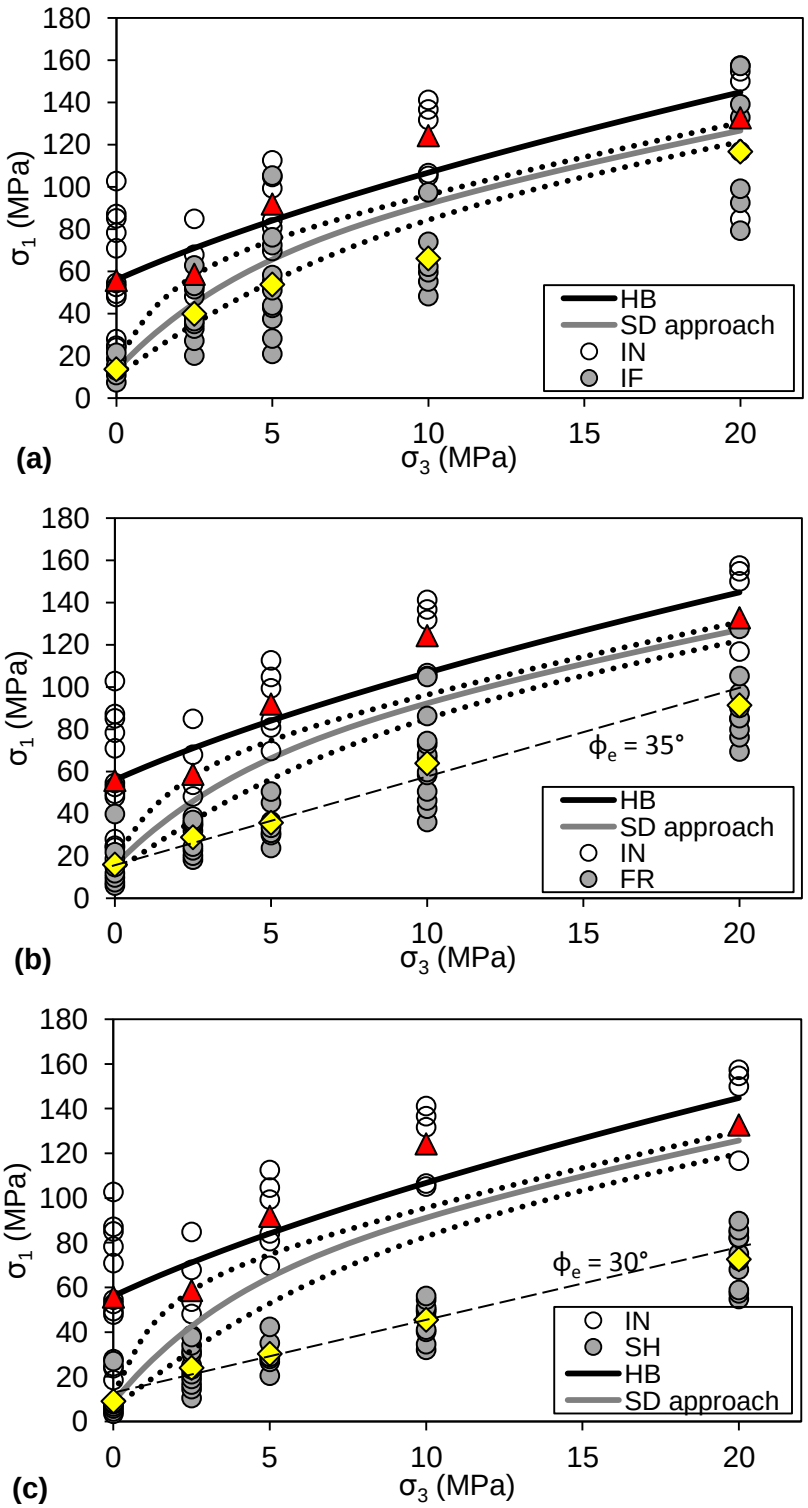

Figure 5-39: Laboratory data of intact (*IN*) and defected (*IF*, *FR* and *SH*) limestone, and estimation of confined strength of defected limestone using the *SD* approach (laboratory data from Ribacchi, 2010). The dotted curves show the strength variability estimated using the *SD* approach. Red triangles and yellow diamonds refer to average intact and defected strengths, respectively.

The strengths of *FR* specimens are thus expected to fall between those of the *IF* and *SH* specimens (i.e., near residual strength if defects are through-going and critically oriented, and near the strength estimated by the *SD* approach if defects are discontinuous and not critically oriented). Keeping this in mind, it becomes understood that, though Figure 5-39b shows that the *SD* approach systematically overestimates the confined strength of *FR* specimens, its strength estimations actually match the upper range of the *FR* data (which was described by Ribacchi (2000) to contain diffused fractures) quite well.

5.4.3 Slotted marble

The results of laboratory tests on intact and slotted fine- and coarse-grained marble are shown in Figure 5-40 (a-f), along with the confined strengths estimated by the *SD* approach. As a reminder, the slotted specimens contained two discrete slots filled with gypsum and were divided into four types depending on their slot orientation: Type A is intact with no slots, while Types B, C and D are slotted with angles of 30°, 45° and 60° to the specimen axis, respectively.

The observed rapid increase in the strength of slotted specimens with increasing confining pressure is interpreted to be due to the properties and geometry of the slots; they were created to be discontinuous, and cohesive. It can be seen from Figure 5-40 that the *SD* approach reasonably estimates the rapid increase in the strength of slotted marble with increasing confinement (with one outlier in the fine grained rock of Type B) as well as the variability in the test data.

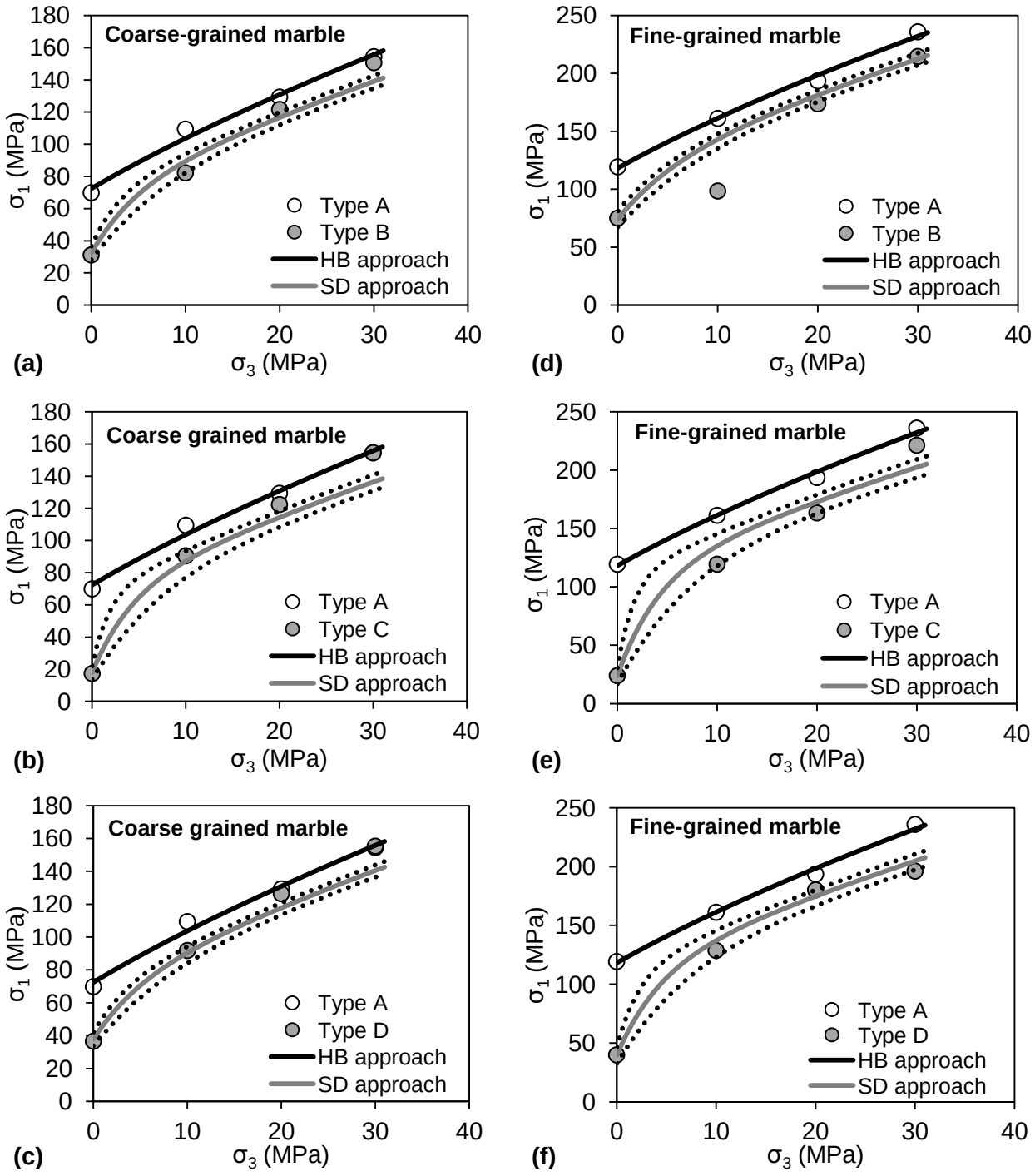

Figure 5-40: Laboratory data of intact and slotted coarse-grained (a-c) and fine-grained (d-f) marble, and the estimation of the confined strength of slotted marble using the *SD* approach (laboratory data from Yang et al., 2008). The dotted curves show the strength variability estimated using the *SD* approach.

Table 5-6 compares the percentage of data points located between the upper and lower strength envelopes estimated using the *SD* approach described in *Chapter 4*. In most cases (except for that of the defected limestone for reasons explained earlier) over 50% of the data points fall within the estimated upper and lower bounds.

In summary, the *SD* approach can be applied when estimating the confined strength of defected rocks consisting of cohesive defects but not with through-going and critically oriented surfaces. The *SD* approach tends to overestimate the confined strength of specimens, in which critically oriented defects dominate the failure of the specimen. Therefore, when failure along weakness planes is allowed, the strength can be lower than that predicted by the *SD* approach. In practice, this can only happen near excavations and not when the excavation boundaries are remote from tips of defects as is the case, for example, in the core of a wide pillar.

Table 5-6: Percentage of laboratory data falling between the upper and lower strength envelopes.

Rock type		Percentage of data
Large-sized coal (Medhurst and Brown, 1998)	146 mm diameter	50%
	300 mm diameter	100%
Fine grain slotted marble (Yang et al., 2008)	Type B	50%
	Type C	75%
	Type D	50%
Coarse grain slotted marble (Yang et al., 2008)	Type B	25%
	Type C	50%
	Type D	50%
Defected Limestone (Ribacchi, 2000)	*IF*	30%
	FR	9%*
	SH	11%*

* attributed to shear slip

Thus, it is concluded that the *SD* approach provides representative strength results for estimating the confined strength representative for a pillar core. This is of high practical relevance as there is a tendency to underestimate the strength when defects dominate the laboratory test results. It is suggested that the applicability of the *SD* approach for estimating the confined strength of defected rocks should be further investigated on naturally defected rock specimens with varying defect geometries (i.e., persistence and orientation) and frictional properties (i.e., roughness).

5.5 Summary and Conclusions

The undamaged grain-based specimen previously calibrated to the laboratory properties of intact Wombeyan marble was used to investigate the influence of scale on intact and defected rock strength. Hypothetical *DFN* models were used to simulate defects. A total of six *DFN* models, each consisting of two sets for defects and varying defect set orientations relative to the loading direction were generated using the *DFN* generator scheme in *Phase2*. The *DFN* models were combined with the grain-based models with widths ranging from 1 to 5 cm and a height-to-width ratio of 2.5. The same *DFN* models were also combined with the ball models with widths ranging from 5 to 12 cm and a height-to-width ratio of 2. Uniaxial compressive tests were simulated on the defected grain-based and ball specimens.

The following can be concluded from the analysis of failure modes:

- The failure mode of defected rocks in which the defects are perpendicular and parallel to the applied loading direction is axial splitting and the majority of fractures propagate through the intact part of the specimens.
- The failure mode of defected rocks in which the defects are critically oriented; these test results should be excluded for the determination of *UCS*, but can be used to determine the properties of defects.

- The failure mode of defected rocks in which the defects are inclined but not critically oriented (not parallel to the direction of critical shear stress) is a combination of failure through intact rock and shearing of discrete defects.

The following can be concluded from the numerical simulations with respect to the strength determination of defected rocks:

- The strength of intact rock (with no defects) is independent of scale (i.e., when smooth and frictionless platens are used).
- The strength of defected rock in which defects are perpendicular and parallel to the applied loading direction decreases with increasing specimen size and reaches about 75% of the intact strength at its largest size.
- When sample failure is dominated by defects that are inclined and oriented parallel to the criticial shear stress direction, the resulting strength is not representative of the rock but can be used to obtain the defect properties.
- The strength of defected rock, in which defects are inclined but not critically oriented (not parallel to the direction of critical shear stress), rapidly changes (increase/ decrease) with increasing specimen size and approaches about 45% of the intact strength at its largest size.
- The strength of defected rocks under unconfined condition is largely influenced by the proximity of the defects to the specimen boundary, especially when critically oriented. Such a condition is not representative of rock strength properties when the rock is confined such as the core of wide pillars.

The Strength Degradation (*SD*) approach originally developed for the estimation of confined strength of micro-defected rocks was tested on the results of laboratory tests on naturally and artificially defected rocks. The *SD* approach was found to be capable of estimating the confined strength of rocks consisting of cohesive discrete defects with rough surfaces (or high equivalent friction angles) as well as those where the defects are oriented perpendicular to the loading

direction. However, this approach was also found to overestimate the confined strength of rocks with critically oriented and continuous defects when failure along defects is allowed.

In the next chapter, the grain-based specimens calibrated to the properties of granulated Wombeyan marble are used to simulate jointed rockmasses with various degrees of interlock.

Chapter 6

6 Influence of Degree of Interlock on Rockmass Strength

6.1 Introduction

In this chapter, the results of numerical simulation of granulated Wombeyan marble, considered to be an analogue for a highly interlocked jointed rockmass, are used to investigate the influence of the degree of block interlock on the peak strength of such rockmasses. The simulations are conducted to investigate:

- the influence of block geometric interlock on the rockmass strength; and
- the influence of block boundary interlock on the rockmass strength.

For this purpose, the influence of joint roughness (i.e., friction angle) and joint persistence are explored. The numbers of intra-block shear and tensile cracks, the failure mechanism including the fracture type and particle velocity vectors, and the stress-strain curves as a function of confinement are used to better understand the influence of the degree of block interlock on the rockmass strength.

6.2 Consideration of Degree of Interlock on Hoek-Brown (HB) Failure Criterion

Hoek (1994) and Hoek et al. (1995) considered the degree of interlock between rock blocks for the characterization and estimation of jointed rockmasses only as far as it affects the freedom of the rock blocks, defined by open joints, to slide and rotate under different confining stress conditions.

This interlock is controlled by the geometrical shape of the rock blocks, the condition of the surfaces separating the blocks (e.g., joint roughness), and the joint persistence. The latter was not considered by them as it was basically the block volume and joint conditions that were used to characterize the rockmass. In the original *GSI* chart, Hoek (1994) and Hoek et al. (1995) classified rockmasses based on the degree of interlock between rock blocks, as illustrated in Table 6-1. The most interlocked rockmass in this classification is a blocky rockmass that consists of undisturbed cubical rock blocks formed by three orthogonal joint sets, and the least interlocked rockmass is a poorly interlocked, disintegrated rockmass that consists of a mixture of angular and rounded rock pieces.

Table 6-1: Different rockmass structures used in the original *GSI* chart (Hoek and Brown, 1997)

Blocky rockmass	Very blocky rockmass	Blocky/disturbed rockmass	Disintegrated rockmass
---------->	Decreasing degree of interlock between rock blocks		---------->
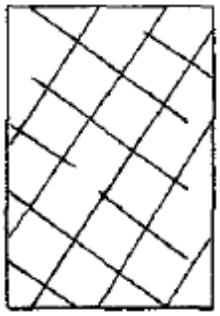	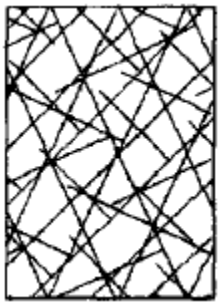		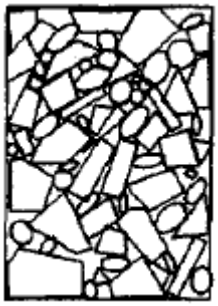
Very well interlocked undisturbed rockmass consisting of cubical blocks formed by three orthogonal discontinuity sets.	Interlocked, partially disturbed rockmass with multifaceted angular blocks formed by four or more discontinuity sets.	Folded and/or faulted rockmass with angular blocks formed by many intersecting discontinuity sets.	Poorly interlocked, heavily broken rockmass with a mixture of angular and rounded rock pieces.

The *HB* criterion's early development was based on the laboratory test results of Westerly granite (Wawersik and Brace, 1971), and intact and heavily jointed and weathered Panguna andesite from slopes of the Bougainville Mine in Papua New Guinea. Hoek and Brown (1980a) used the post-peak progressive failure and fracturing stages of Westerly granite tested under unconfined and confined conditions by Wawersik and Brace (1971) (Figure 6-1a) as an analogue for a jointed rockmass to understand the strength degradation of a jointed rockmass from the intact rock. Figure 6-1b shows the complete stress-strain curves obtained from these tests. The following fracturing stages were used by Hoek and Brown (1980a) for the strength analysis of jointed rockmasses:

- stage IV: formation of large number of small fractures parallel to the direction of loading;
- stage VI: formation of small steeply inclined shear fractures;
- stage VII: growth of small steeply inclined fractures into an open fault; and
- stage VIII: ultimate strength of loose broken material held together by friction between particles.

Hoek and Brown (1980a) plotted the failure envelopes in the normal-shear stress space for these stages and determined the values of *m* and *s* as shown in Figure 6-2. As can be seen, the values of the constants *m* and *s* decrease as fracturing of these specimens progresses; the value of *m* is reduced by a factor of approximately 2, whereas the value of *s* decreases from 1.0 to 0.0 as the strength of the rock specimens reduces from peak to ultimate.

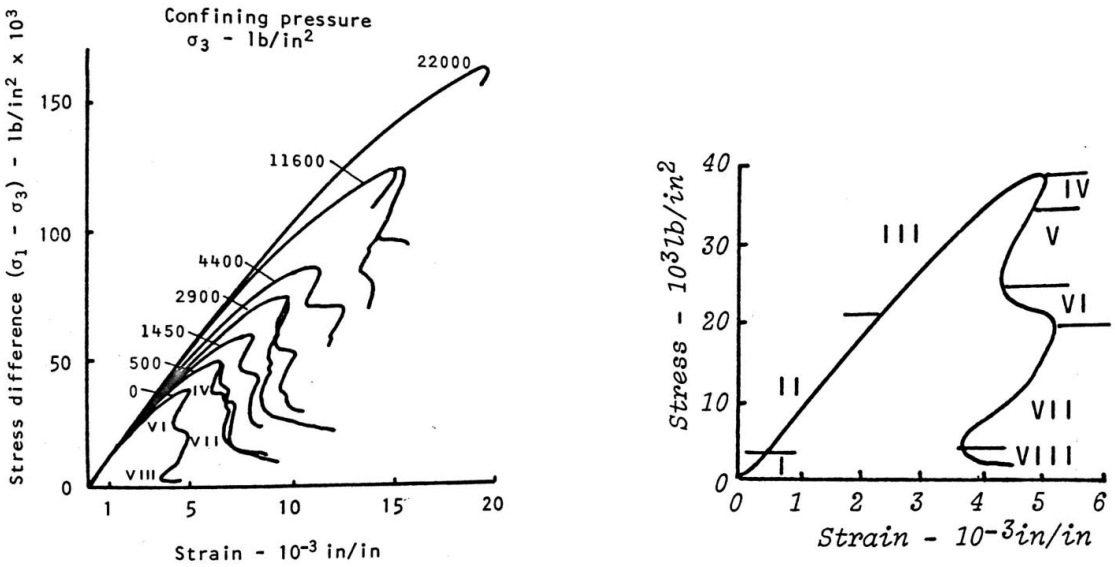

Figure 6-1: a) Complete stress-strain curves for Westerly granite under unconfined and confined conditions tested by Wawersik and Brace (1971); b) fracturing stages in a uniaxial stress-strain curve for Westerly Granite.

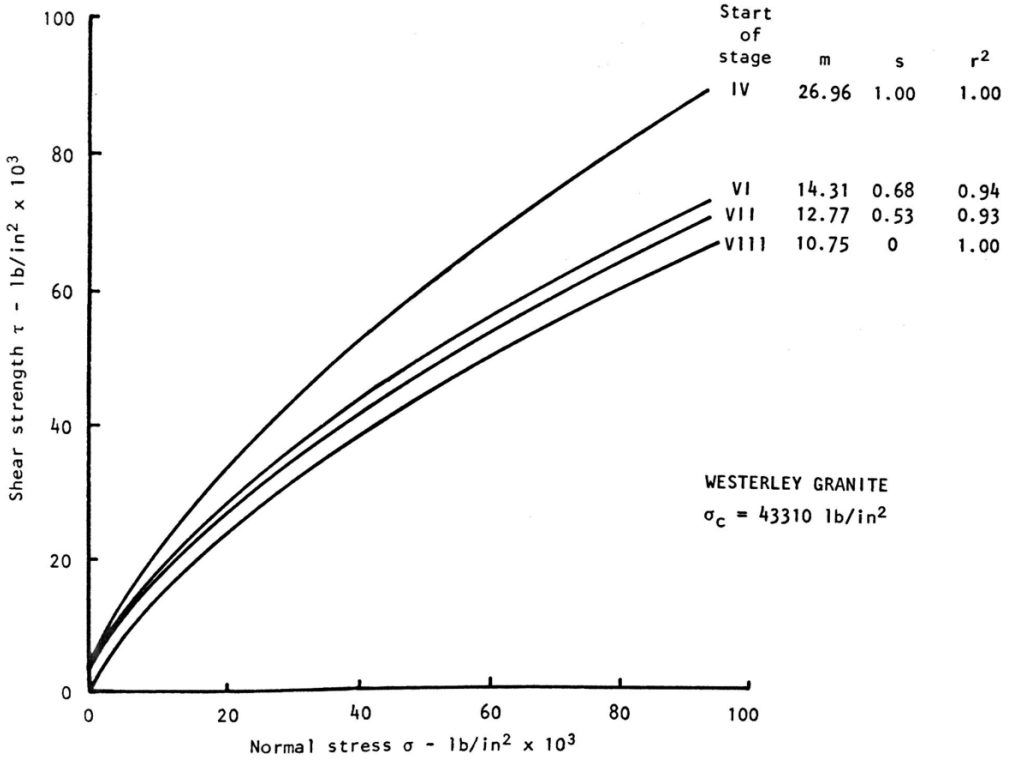

Figure 6-2: Mohr envelopes for Westerly granite at various post-peak fracturing stages along with their *HB* strength parameters *m* and *s* (after Hoek and Brown, 1980a).

Figure 6-3 shows the laboratory strength data (not in principal stress space) of intact and 150 mm diameter undisturbed cores of heavily jointed and weathered Panguna andesite. First, the *HB* envelope with a *GSI* of 100 was fitted to the intact data. The *GSI* was then reduced in increments of 10 from 90 until the strength of jointed andesite is matched (Figure 6-3a). This figure shows that both the unconfined and the confined strengths of the jointed rockmass decrease as the *GSI* value decreases from 100 to 10. The minimum and maximum strengths of heavily jointed andesite are bound with the *GSI* values of 10 and 30, respectively (Figure 6-3b).

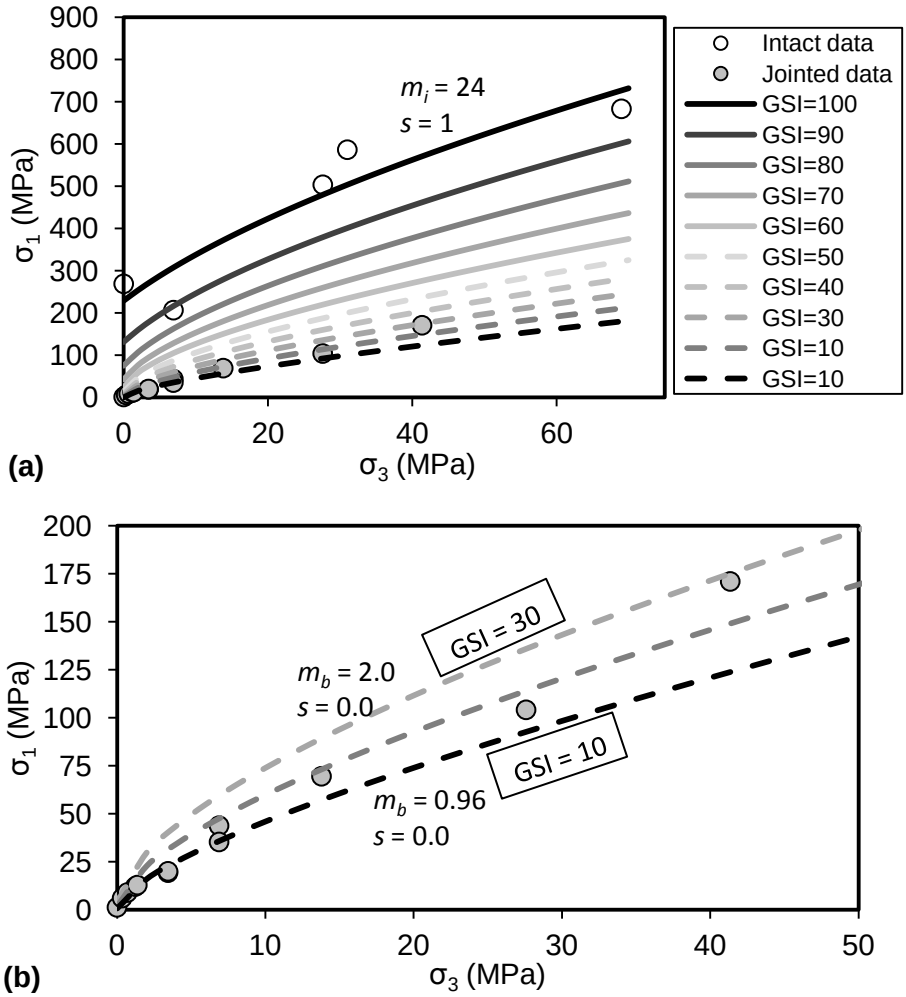

Figure 6-3: a) Strengths of intact and jointed andesite and the *HB* failure envelopes for *GSI* values ranging from 100 to 10; b) closer view of the strength of jointed andesite bound with *GSI* values of 10 and 30.

It can be seen from Figure 6-3 that, similar to the results of analysis on Westerly granite, the values of the constants *m* and *s* decrease from the intact andesite (i.e., m_i = 24 and *s* = 1 for *GSI* = 100) but more significantly to those of jointed andesite (i.e., m_b = 0.96 and *s* = 0.0 for *GSI* = 10). Based on the results of these two series of tests, Hoek and Brown (1980a) concluded that the presence of discontinuities in a rock specimen (i.e., jointed rockmass) results in a reduction in the values of both constants *m* and *s* from intact rock.

Hoek and Brown (1980b) plotted the *HB* parameter *s* and the ratio m/m_i (on a log scale) against the rockmass classification systems *RMR* and *Q* for various categories of Panguna andesite specimens (Figure 6-4). They fitted a straight line to the strengths of intact and jointed Panguna andesite to provide approximate relationships between *s* and m/m_i and the classification ratings.

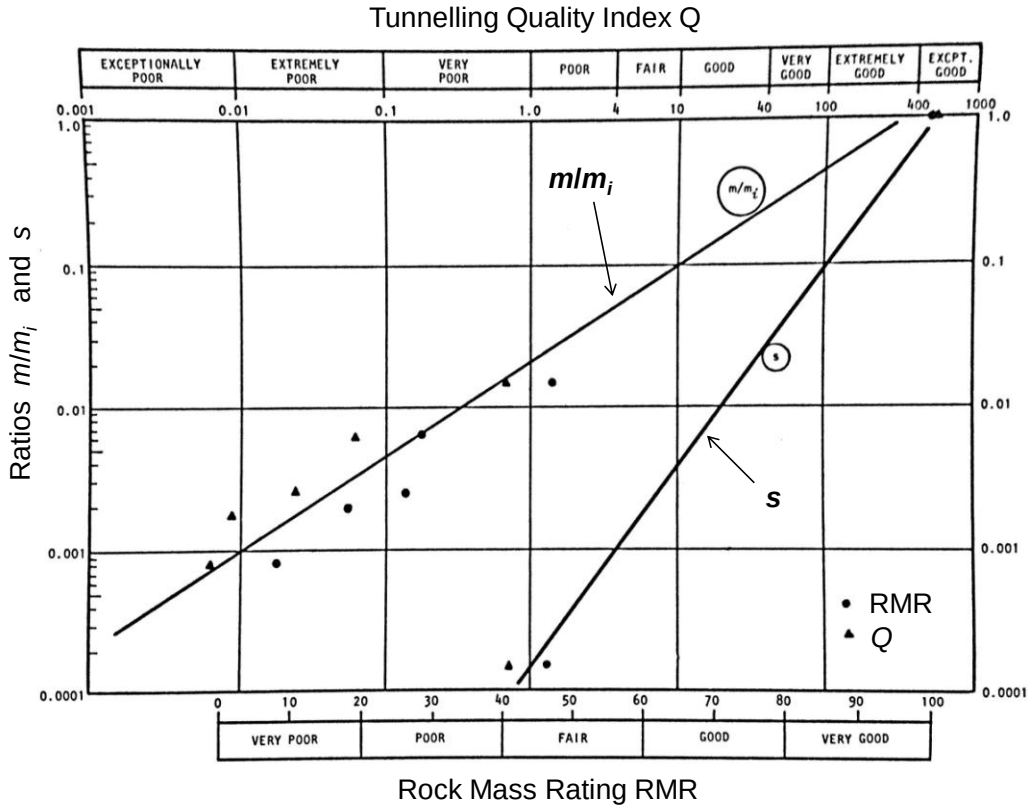

Figure 6-4: Plots of *s* and m/m_i for Panguna andesite against rockmass classification systems *RMR* and *Q* (after Hoek and Brown, 1980b)

As can be seen from Figure 6-4, the jointed andesite covers low *RMR* and *Q* values (i.e., weak and poorly interlocked rockmasses) and there is a lack of data for *RMR* values greater than 50 or *Q* values greater than 4 (i.e., fair to extremely good rockmasses).

Hoek and Brown (1980a) also conducted a similar analysis on the laboratory test results of intact and granulated Wombeyan marble tested by Rosengren and Jaeger (1969). They found that the value of the constant *s* drops from 1.0 for the intact marble to 0.19 for the granulated marble. However, the value of the constant *m* increases from m_i = 4.0 for the intact marble to m_b = 5.26 for the granulated marble. Hoek and Brown (1980a) mentioned that after granulation, the basic unit of the granulated marble became a calcite crystal or grain, which would be expected to have a higher value of σ_{ci} than the intact marble. They hypothesized that if the unconfined and confined strengths of calcite crystals could be measured and applied in the analysis, the value of m_b would have reduced below 5.26.

Hoek and Brown (1980a) further discussed that the observed increase in the value of *m*, which is against the trend of the results of Western granite and Panguna andesite, could likely be due to the high degree of geometric interlock caused by the shape of calcite grains, and rough surfaces of the grain boundaries. For these reasons, Hoek and Brown (1980b) suggested that the granulated marble would be a reasonable analogue for a highly interlocked jointed rockmass, but not for lower interlocked jointed rockmasses, such as heavily jointed and weathered Panguna andesite. Therefore, they intentionally did not use the results of laboratory tests on intact and granulated Wombeyan marble, neither those of plaster models reviewed in *Chapter 2*, for the development of the *HB* failure criterion. These data are used here to establish the degradation in

strength for highly interlocked rockmasses as typically encountered at great depths in hard, brittle rockmasses.

It should be noted that Hoek and Brown (1980b) strongly emphasized that the *HB* failure criterion is based on very sparse data and is an approximate, and should be used as rough guides in preliminary design calculations. They suggested that every attempt should be made to determine the required strength parameters by laboratory and *in situ* testing and by observations of the full-scale performance of the rockmass around trial excavations.

6.3 Strength of Interlocked Jointed Rockmasses

Block shape, joint roughness and joint persistence are considered as the main factors that define the degree of freedom of the rock blocks to slide and rotate under different stress conditions (i.e., degree of interlock) in a jointed rockmass. These factors were briefly reviewed in *Chapter 1*. In this section, the influence of these factors on the strength of jointed rockmasses under unconfined and confined conditions is investigated, by extending the fully damaged grain-based specimen (i.e., model of granulated Wombeyan marble), described in *Chapter 3*, to a highly interlocked jointed rockmass.

6.3.1 Influence of block shape

Two structures were considered to investigate the influence of block shape (i.e., block geometric interlock) on the strength of jointed rockmasses:

- Highly interlocked jointed rockmass with polygonal blocks (called RM_{HI}); and
- Interlocked jointed rockmass with cubical blocks (called RM_{I}).

These two rockmasses are shown in Figure 6-5. As can be seen, the structure in the RM_{HI} specimen is the same as that of the grain-based specimen calibrated to the properties of granulated Wombeyan marble. Due to the polygonal shape of the rock blocks, the RM_{HI} specimen is considered to be a representative for a highly interlocked jointed rockmass, as suggested by Hoek and Brown (1980a). The structure in the RM_I specimen is similar to that of blocky rockmass in the *GSI* chart (Table 6-1). Due to the cubical shape of the rock blocks, the RM_I specimen is considered to represent a jointed rockmass with standard interlock.

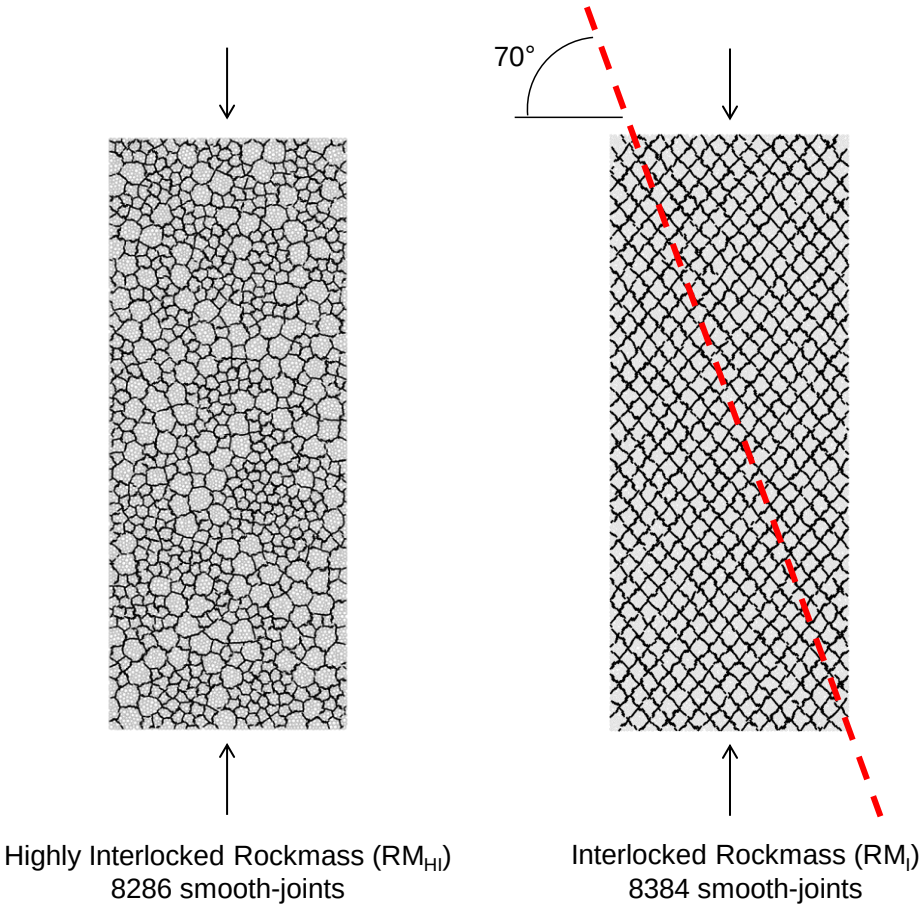

Figure 6-5: Two rockmass structures representing: a) highly interlocked jointed rockmass (RM_{HI}); and b) interlocked jointed rockmass (RM_I). The direction of critical shear stress is shown with the dashed red line.

Table 6-2: Properties of blocks and joints is RM_{HI} and RM_I.

Properties	Intact and granulated marble
contact modulus	50 GPa
parallel bond modulus	50 GPa
ball friction coefficient	0.5
parallel bond normal (tensile) strength	110 MPa
parallel bond cohesion	110 MPa
parallel bond friction angle	0°
smooth-joint normal (tensile) strength	0 MPa
smooth-joint cohesion	0 MPa
smooth-joint friction angle	0°
smooth-joint friction coefficient	1.2
smooth-joint stiffness factor	0.2

The properties of the intact rock and joints in these two rockmasses are identical to those of the fully damaged grain-based specimen calibrated to the properties of granulated Wombeyan marble (Table 6-2). Note that the joints are simulated as frictional features with no tensile strength and cohesion. Moreover, the blocks in these two rockmasses are breakable (with $UCS_i >$ 100 MPa). The spacing between the joints in the RM_I specimen was chosen so that the number of smooth-joint contacts is close to that of the RM_{HI} specimen. Therefore, by choosing the same properties for the intact rock and joints and the same number of smooth-joint contacts in these two synthetic rockmass specimens, the block shape is the only variable and its influence on the rockmass strength can be investigated. The dip angles of the joint sets in the RM_I specimen were chosen so that the joints are not parallel to the direction of critical shear stress on joints (i.e., 70° for the given friction angle of 50° for the joints).

Figure 6-6a compares the unconfined and confined strengths of the RM_{HI} and RM_I specimens. The unconfined strength of the RM_{HI} specimen is about 20 MPa. Its strength increases non-linearly with increasing confinement up to about 10.3 MPa confining pressure, and then linearly increases beyond this limit until the maximum applied confining pressure of 34.4 MPa. On the

other hand, the strength of the RM_I specimen under unconfined condition is about zero. Its strength rapidly increases linearly up to about 10.3 MPa confining pressure, and then linearly increases with a smaller slope beyond this limit. As can be seen in Figure 6-6a, the main difference between these two rockmasses is their strength and strength development at low confinement (σ_3 < 10 MPa).

Figure 6-6b illustrates the strength deference between these rockmasses as a function of confinement. The strength difference is about 20 MPa under unconfined condition. It then increases to just below 30 MPa at the confining pressure of 3.5 MPa and then deceases linearly down to about 7 MPa at the confining pressure of about 10.3 MPa. Beyond this confining pressure the strength difference is about 6 MPa. Beyond 25 MPa confinement it tends to drop further with increasing confinement and reaches zero at 34.7 MPa confining pressure. This is due to the intra-block fracturing in the two rockmasses at high confining pressures, which will be discussed next.

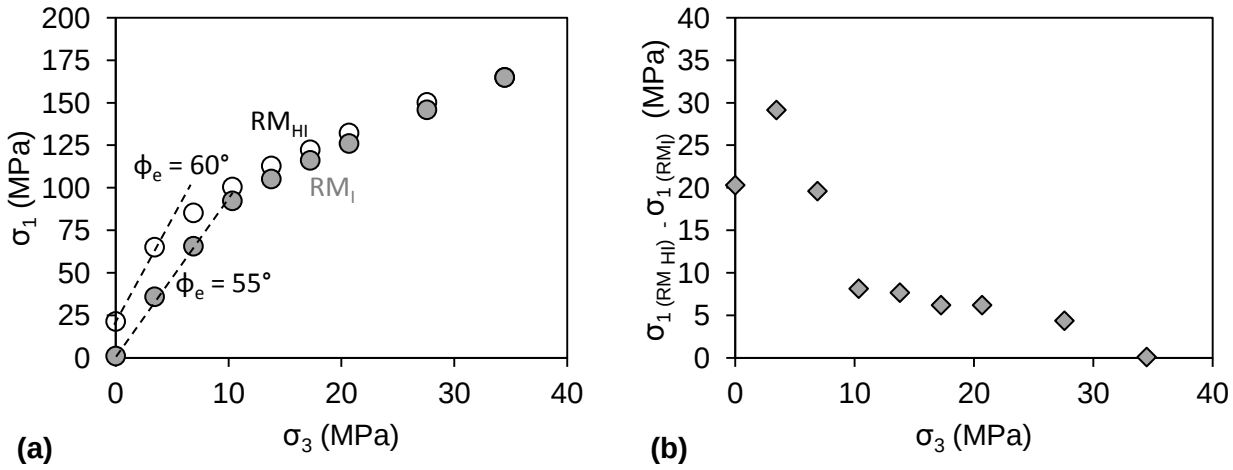

Figure 6-6: a) Comparison between the strengths of RM_{HI} and RM_I specimens; b) strength difference between RM_{HI} and RM_I specimens as a function of confinement.

Figure 6-7a and b compare the numbers of tensile and shear intra-block fractures up to the peak stress in both rockmasses. In the RM_{HI} specimen, intra-block tensile fracturing occurs at all confining pressures (i.e., from zero to 34.5 MPa). In this rockmass, intra-block shear fracturing occurs at all confinement levels except for zero confining pressure. The number of fractures (shear or tensile) prior to the peak stress increases with increasing confinement. In the RM_I specimen, intra-block tensile fracturing starts from the confining pressure of 10.3 MPa, while shear fracturing occurs at very high confining pressures (i.e., 20.7, 27.6 and 34.5 MPa).

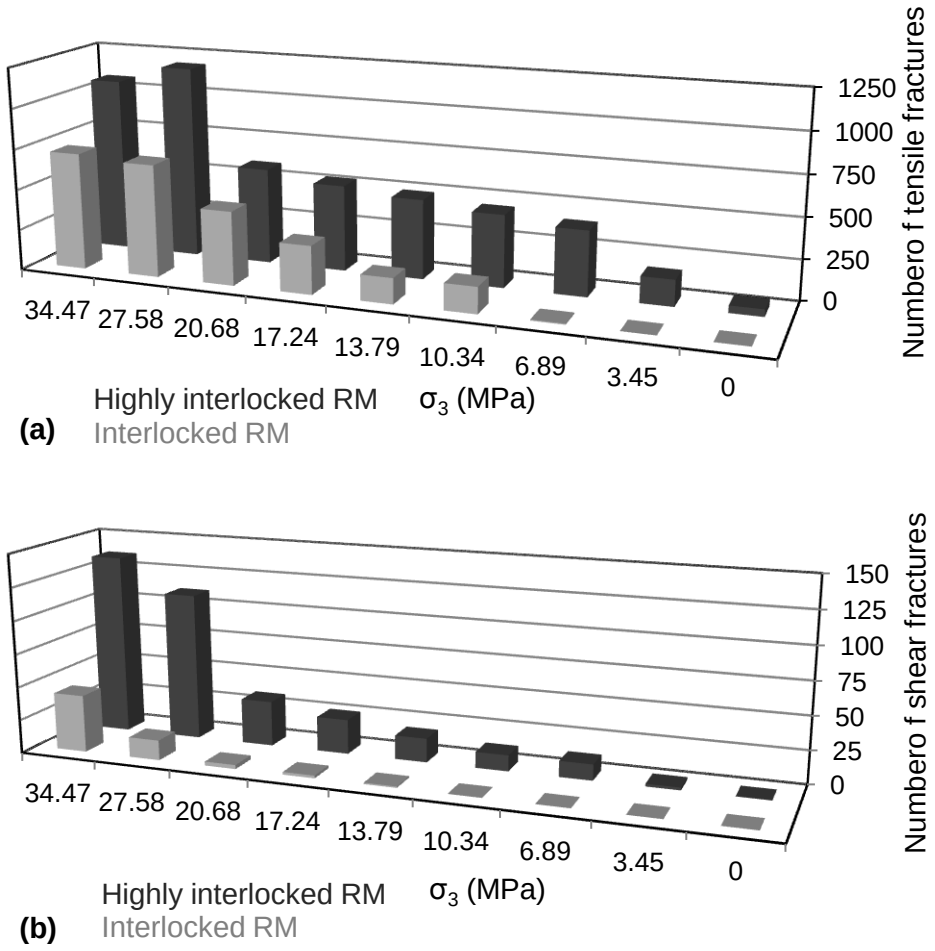

Figure 6-7: Comparison between the numbers of intra-block: a) tensile fractures; and b) shear fractures, prior to the peak stress in the RM_{HI} and RM_I specimens.

Figure 6-8 illustrates the fracture patterns in the RM_{HI} and RM_I specimens at their peak strengths for all values of confining pressure. In this figure, the frictional joints are shown with green lines. Red and blue lines represent intra-block tensile and shear fractures (i.e., broken parallel bonds), respectively. In the RM_{HI} specimens, the failure mode cannot be distinguished from fracture pattern until the confining pressure of 13.8 MPa. Beyond this confining pressure, a shear plane generated from the interaction of intra-block tensile fractures can be seen. In the RM_I specimens, such a shear plane can only be distinguished at very high confining pressures of 27.6 and 34.5 MPa. This suggests that opening or sliding along frictional joints dominates the failure of both rockmasses at low confinement. This was further investigated by analyzing the particle velocity vectors in both rockmasses.

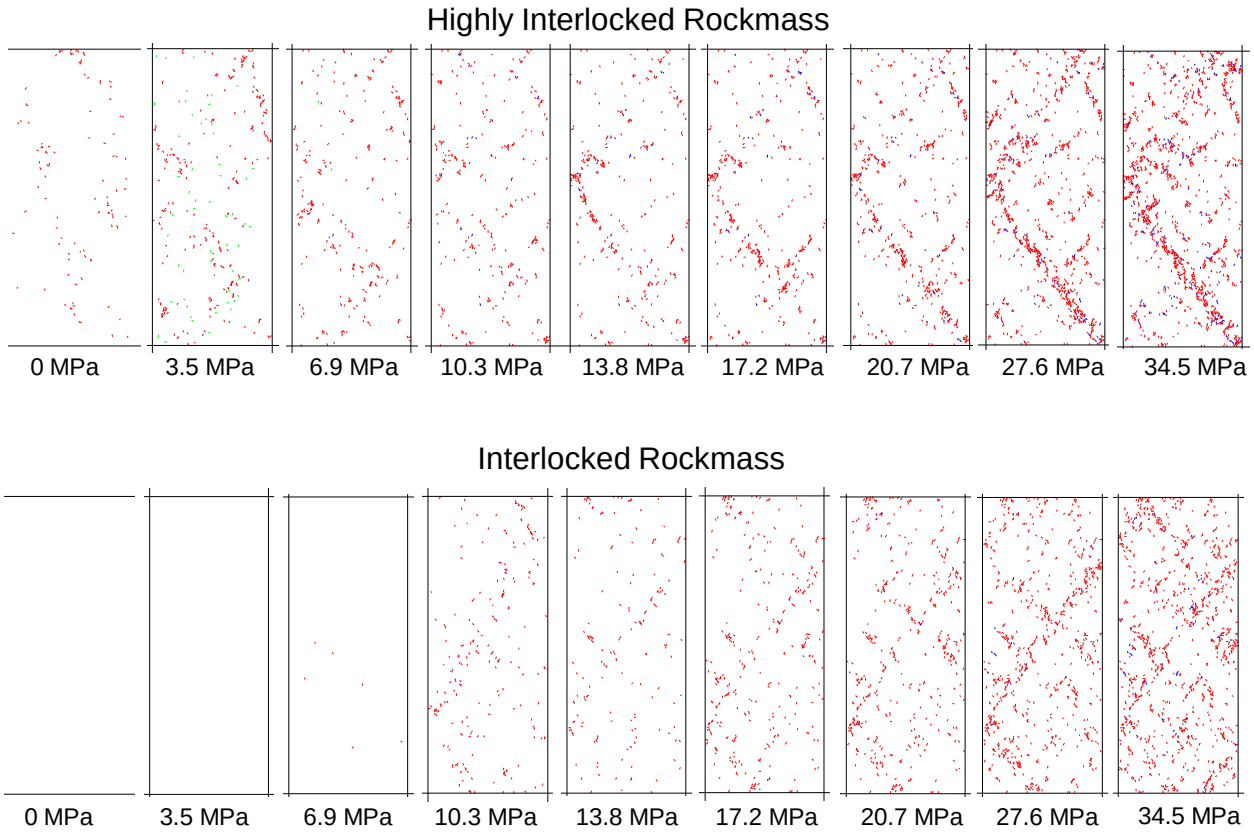

Figure 6-8: Comparison between intra-block fracturing patterns of the RM_{HI} and RM_I specimens up to the peak stress for different values of confining pressures.

The failure modes in terms of particle velocity vectors and block fracturing in the highly interlocked (RM_{HI}) and interlocked (RM_I) rockmass specimens at various confinement levels are shown in Table 6-3.

Low confinement (i.e., σ_3 < 10.3 MPa):

At confining pressures of 0 MPa and 3.5 MPa, failure involves opening of block boundaries and minor block rotation in the RM_{HI} specimen, with the direction of block movements being mainly parallel and perpendicular to the loading direction. In the RM_I specimen, failure mainly involves a combination of sliding along block boundaries and block rotation. In the RM_{HI} specimen, minor intra-block fracturing results in the generation of small shear planes at 3.5 MPa confining pressure. No intra-block fracturing occurs in the RM_I specimen at this confining pressure.

High confinement (i.e., σ_3 > 10.3 MPa):

At confining pressures of 17.4 MPa and 34.5 MPa, the accumulation and interaction of intra-block tensile and shear fractures results in the formation of a major shear plane in the RM_{HI} specimen. In the RM_I specimen, a combination of sliding along frictional joints and tensile fracturing through the blocks drives the rockmass to failure. At 34.5 MPa confining pressure, the direction of velocity vectors in both rockmasses is mainly dictated by the intra-block fractures than the frictional joints.

Table 6-3: Comparison between failure modes of the RM_{HI} and RM_I specimens at low and high confinements; black lines are frictional joints, and red and dark blue lines are intra-block tensile and shear fractures, respectively. Velocity vectors are shown with black arrows.

	σ_3 (MPa)	RM_{HI}	RM_I
Low confinement	0.0	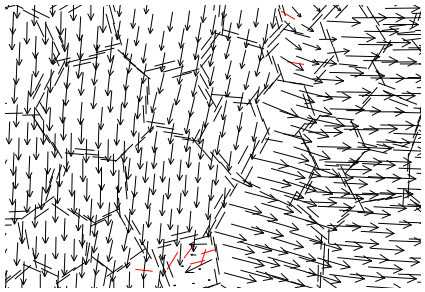	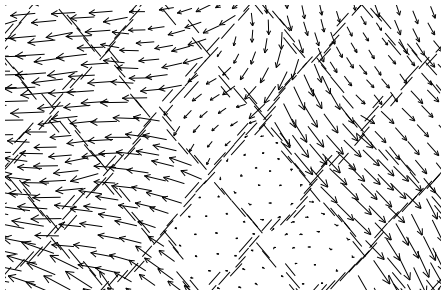
	3.5	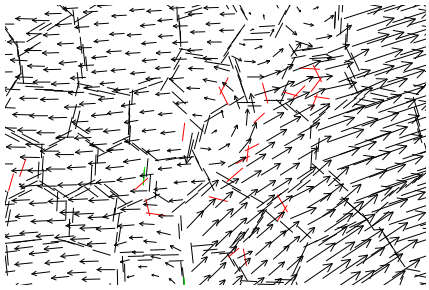	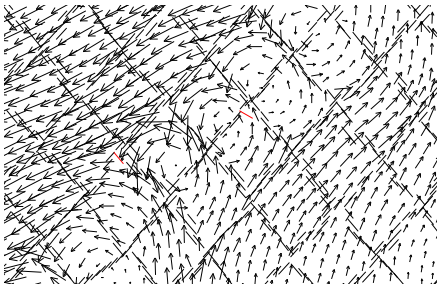
High confinement	17.4	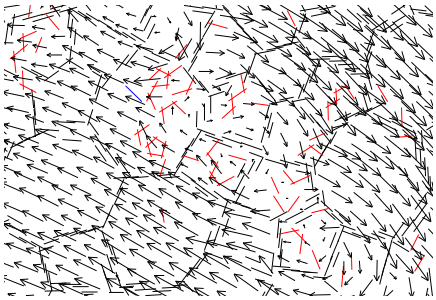	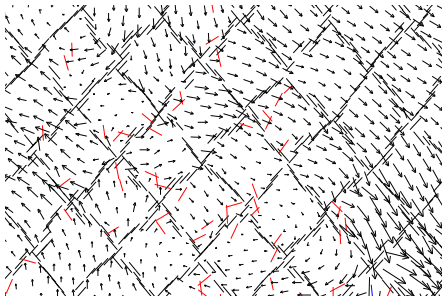
	34.5	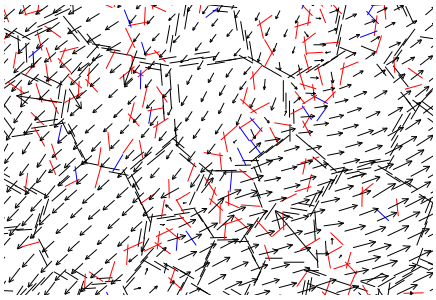	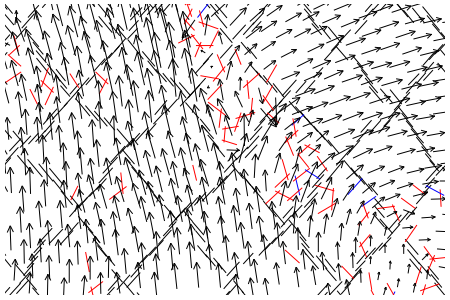

6.3.2 Influence of joint roughness

Joint roughness has a fundamental influence on the development of dilation (i), therefore on the strength of a joint during shearing under various levels of normal stress, and consequently on the strength of a jointed rockmass at various levels of confinement. Joint roughness influences the degree of block boundary interlock, as it defines the freedom of rock blocks to slide along joints; the degree of block boundary interlock increases with increasing joint roughness.

In simulations of jointed rockmasses, the joint roughness was not explicitly simulated, as the smooth-joint logic used in *PFC* considers joints as smooth surfaces. Therefore, the smooth-joint friction angle was increased from its basic friction angle (ϕ_j) to that of "equivalent" friction angle ($\phi_j + i$) to account for joint roughness. For example, the joints in the RM_{HI} and RM_I specimens were assigned an equivalent joint friction angle of 50°. This represents a rough joint, which has a basic friction angle of 35° and a dilation angle of 15°. Strictly speaking, however, this only takes a part of the effect of joint roughness into account (i.e., the increase in strength), but not the actual normal deformation, as it still is a smooth joint. Hence, the actual effect of joint roughness is higher than what is simulated here.

The influence of equivalent joint friction angle ($\phi_j + i$) on the strengths of the RM_{HI} and RM_I specimens are investigated in this section. The results of sensitivity analyses are shown in Figure 6-9, which illustrates the influence of joint friction angle on the strengths of the RM_{HI} specimen (Figure 6-9a), the RM_I specimen (Figure 6-9b), and their strength difference as a function of confinement. Figure 6-9a shows that a reduction of joint friction angle from 50° to 20° results in a reduction of the *UCS* of the RM_{HI} specimen from about 20 MPa to close to zero. This strength reduction is not dependent on the confinement, which means that the strength envelope of the

RM_{HI} specimen remains non-linear independent of the joint friction angle. This is interpreted to be due to the complex shapes of rock blocks in the RM_{HI} specimen, which prevents the rock blocks to slide along joints and causes intra-block fracturing even at very low values of joint friction angle.

It can be seen from Figure 6-9b that the unconfined strength of the RM_I specimen is close to zero for all values of joint friction angle. However, the confined strength of the RM_I specimen is heavily dependent on the joint friction angle, and decreases more rapidly with decreasing the joint friction angle compared to the RM_{HI} specimen. The non-linearity of the strength envelope also decreases with decreasing the joint friction angle; the strength envelopes of the RM_I specimen with the joint friction angle of 40° to 50° are non-linear, and become linear for the joint friction angles of 35° and lower. The linearity of the strength envelope in the RM_I specimen with low joint friction angles is interpreted to be due to the rock blocks that slide along these joints, independent of the value of confining pressure.

The results presented in Figure 6-9a indicate that the inter-block joint condition (J_c) has much less effect on the confined strength of highly interlocked rockmasses. The strength degradation is only slightly influenced with increasing confinement. This is one aspect that points towards the reason for the validity of the hypothesis presented in *Chapter 1*.

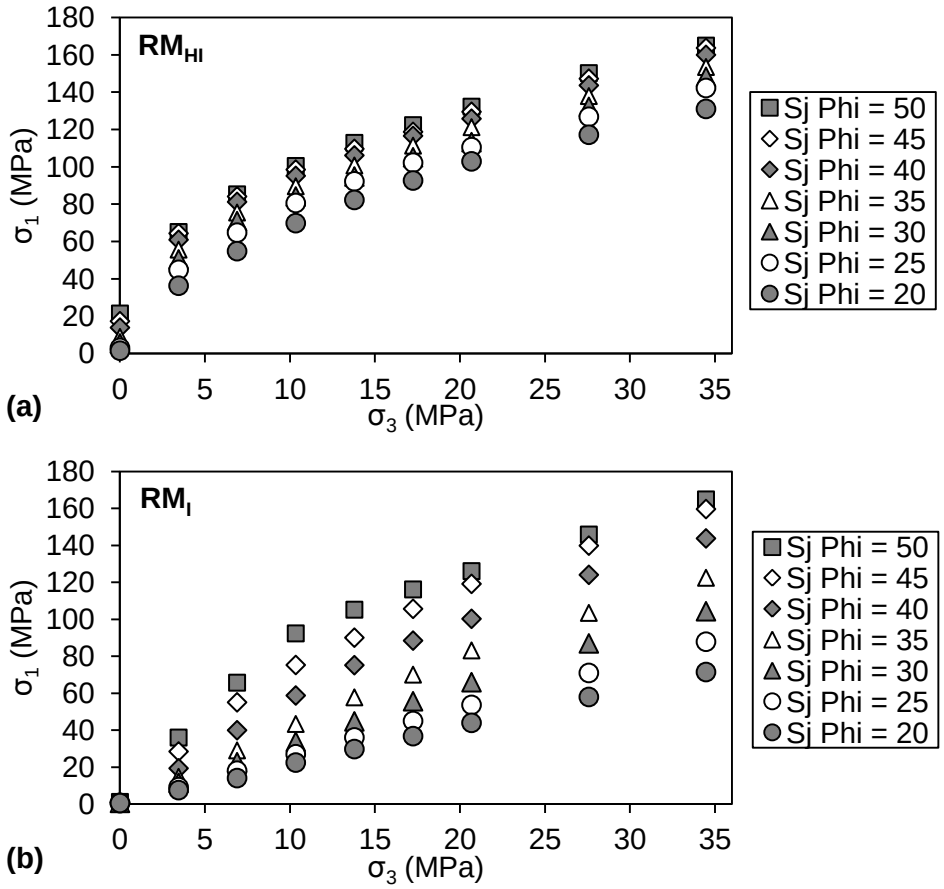

Figure 6-9: Influence of joint friction angle on: a) the strength of RM_{HI}; and b) the strength of RM_I.

The reason for the difference between the strength behavior of the RM_{HI} and RM_I specimens was further investigated by comparing the numbers of intra-block fractures formed up to the peak stress for different values of confining pressure (Figure 6-10 and Figure 6-11). In the RM_{HI} specimen, intra-block fracturing occurs even under unconfined condition. This is due to the complex shapes of rock blocks and therefore their high degree of interlock, which prevents block sliding along joints. Therefore, blocks accept more and more load until intra-block fracturing drives the rockmass to failure. In the RM_I specimen, intra-block fracturing occurs only at high confinement. This is due to the fact that sliding along joints occurs before intra-block fracturing and this causes failure of the RM_I specimen at a lower axial stress than the RM_{HI} specimen.

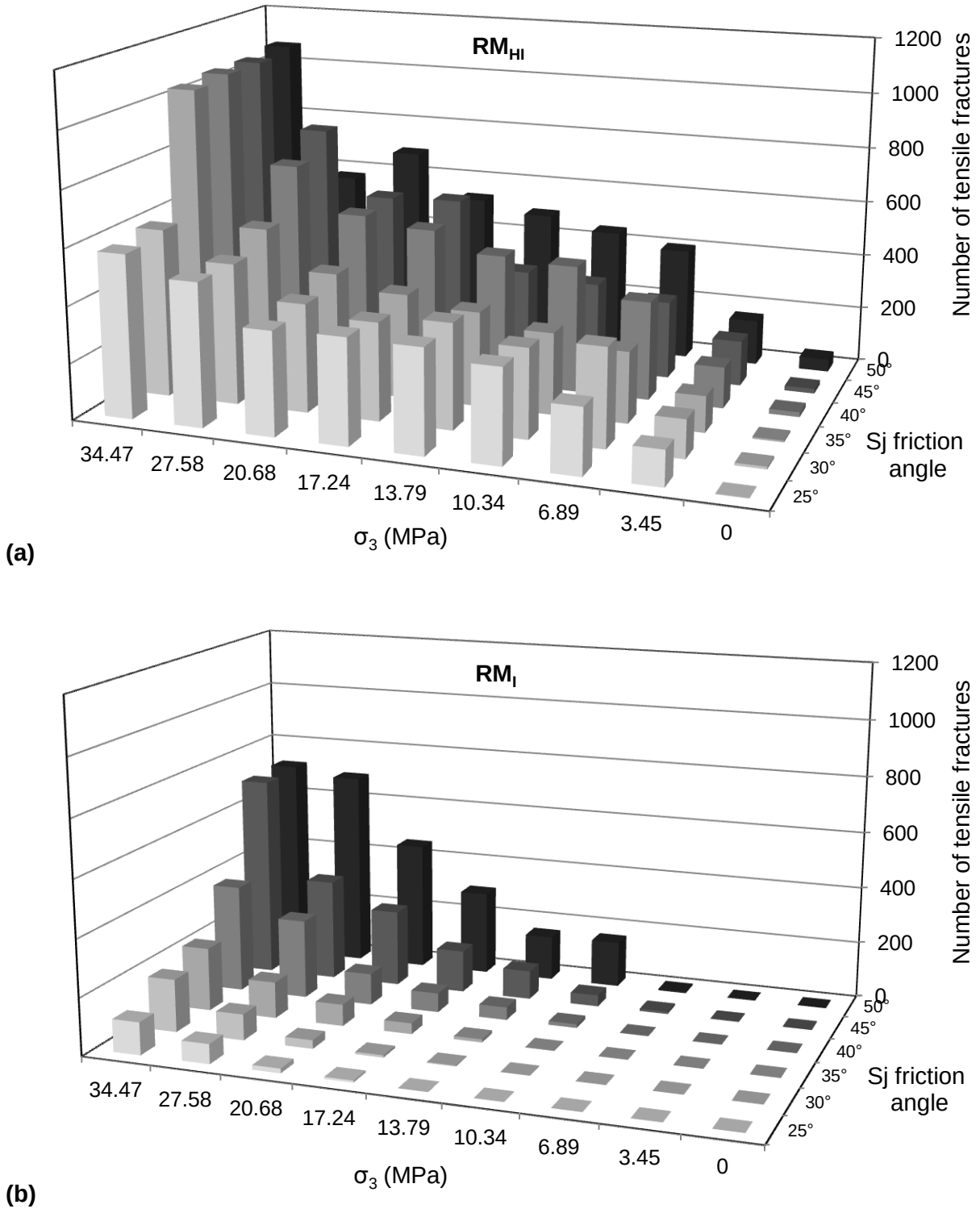

Figure 6-10: Number of intra-block tensile fractures as a function of joint friction angle and confinement in: a) RM_{HI}; and b) RM_I specimens.

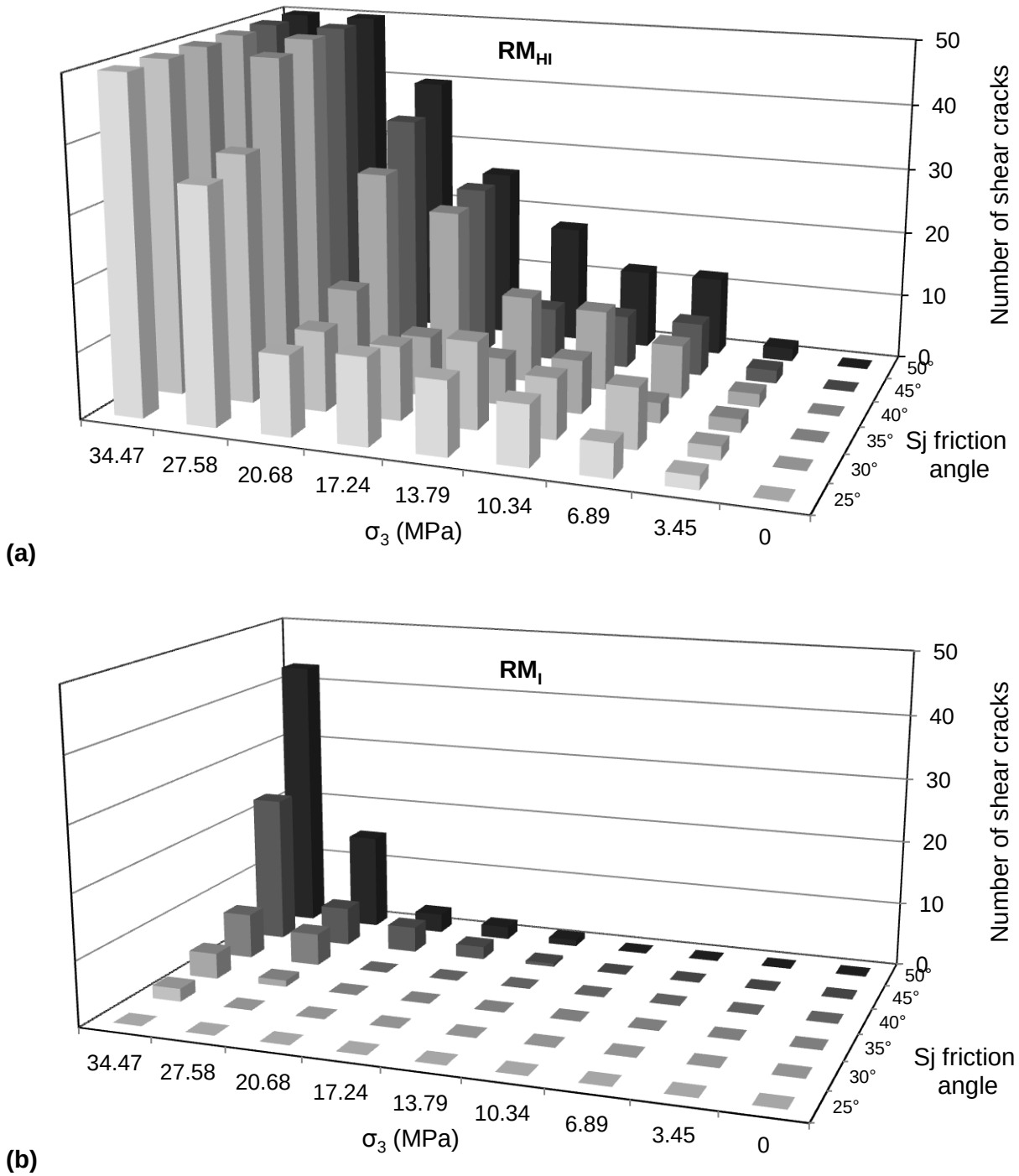

Figure 6-11: Number of intra-block shear fractures as a function of joint friction angle and confinement in: a) RM_{HI} ; and b) RM_I specimens.

The comparison between Figure 6-10 and Figure 6-11 indicates that tensile fracturing is the dominant mode of intra-block failure in both rockmasses. The numbers of tensile and shear intra-block fractures increase with increasing joint friction angle in both rockmasses.

The stress-strain curves of the RM_{HI} and RM_I specimens at low confinement (σ_3 = 3.5 MPa) for different values of joint friction angle are presented in Figure 6-12a and b. As can be seen from this figure, the RM_{HI} specimen behaves in a more ductile manner for all the values of joint friction angle, and its pre-peak ductility increases with decreasing joint friction angle due to plastic deformation before the peak stress (Figure 6-12a). However, the RM_I specimen behaves in a more brittle manner for high values of joint friction angle, and tends to become slightly more ductile (i.e., a flatter post-peak slope) as the joint friction angle decreases from 50° to 25° (Figure 6-12b). The strain at which the peak stress is reached in the RM_{HI} specimen increases with decreasing joint friction angle, whereas it decreases in the RM_I (as would be expected).

The difference between the stress-strain curves of these two rockmasses is due to the difference in their degrees of interlock and their failure modes. As mentioned before, in the RM_{HI} specimen, sliding along joints is prevented early on during loading due to the complex shapes of the blocks. Therefore, the blocks accept higher loads until intra-block fracturing close to the peak stress, at the peak stress and in the post-peak region causes the failure of the highly interlocked rockmass. In the RM_I specimen, sliding along frictional joints occurs at lower axial stresses before any significant block fracturing occurs.

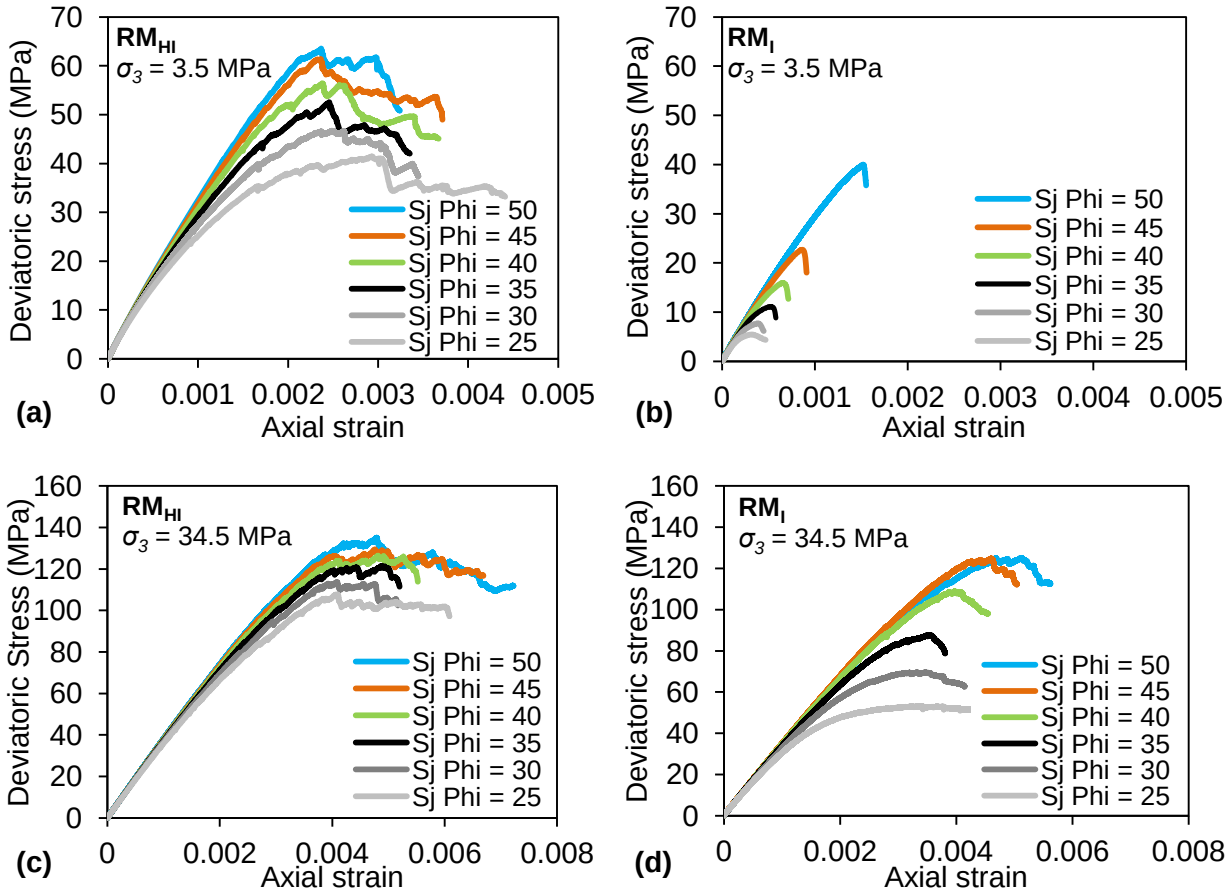

Figure 6-12: Influence of joint friction angle on stress-strain curves of: a) RM_{HI} at 3.5 MPa confining pressure; b) RM_I at 3.5 MPa confining pressure; c) RM_{HI} at 34.5 MPa confining pressure; and d) RM_I at 34.5 MPa confining pressure.

At high confinement (σ_3 = 34.5 MPa), both rockmasses show more ductility, although this is more pronounced in the RM_{HI} specimen. At this confining pressure, the strength of the RM_{HI} specimen is much less influenced by the value of joint friction angle, compared to that of the RM_I specimen (Figure 6-12c and d). This is interpreted to be due to the higher degree of interlock forcing rock block failure in the RM_{HI} specimen. The strain at which the peak stress is reached in the RM_{HI} specimen is almost independent of confinement. In the RM_I specimen, however, this value decreases with decreasing joint friction angle from 50° to 35°, and then becomes constant for lower values of joint friction angle.

6.3.3 Influence of joint persistence

As discussed in *Chapter 1*, the joint persistence is used to describe the areal extent or size of a discontinuity within a plane. The joint persistence influences the strength and failure modes of a jointed rockmass under different stress conditions. As discussed by Einstein (1993), instability is much more likely to occur if joints are fully persistent. The presence of rock bridges in a non-persistently jointed rockmass prevents the rock blocks from sliding or falling from an excavation or slope until the rock bridge fails (Kim et al., 2007). Therefore, the joint persistence influences the degree of interlock between rock blocks; the degree of interlock decreases with increasing the joint persistence.

The influence of joint persistence on the strength of the RM_{HI} and RM_I specimens are investigated in this section. The non-persistently jointed rockmass was simulated by randomly removing a number of smooth-joint contacts from the RM_{HI} and RM_I specimens and replacing them with parallel bonds with the same properties used to bond the particles inside the blocks. Figure 6-13 shows a massive rockmass where all the contacts are bonded using parallel bonds (blue circles), a fully persistently jointed rockmass where the block boundaries are simulated using smooth-joint contacts (black line) and a non-persistently jointed rockmass where 50% of smooth-joint contacts are replaced with parallel bonds. In this document, *K'* refers to the ratio of the number of smooth-joint contacts in a non-persistently jointed synthetic rockmass specimen to the number of smooth-joint contacts in a fully persistently jointed synthetic rockmass specimen. The *K'* ratio corresponds with the joint persistence, *K*, described in *Chapter 1* (Equation 1-1). Various levels of joint persistence in a jointed rockmass were simulated by varying the *K'* ratio from 0.0 to 1.0 in increments of 0.1. Figure 6-14 shows examples of RM_{HI} and RM_I specimens

with non-persistent and persistent joints. It was discussed in *Chapter 2* that the structure of the RM_{HI} specimen with $K' = 1.0$ is a non-persistently jointed rockmass as the joints are of limited length, although they are open and form blocks without rock bridges.

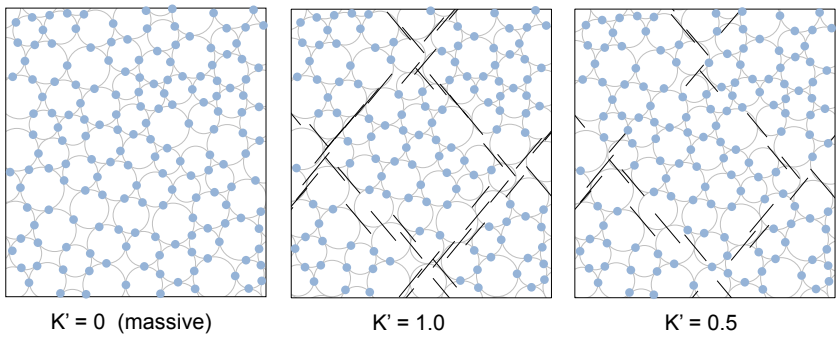

Figure 6-13: Examples of massive jointed rockmass ($K' = 0.0$), fully persistently jointed rockmass ($K' = 1.0$) and non-persistently jointed rockmass ($K' = 0.5$). Blue circles and black lines refer to parallel bonds and frictional smooth-joint contacts, respectively.

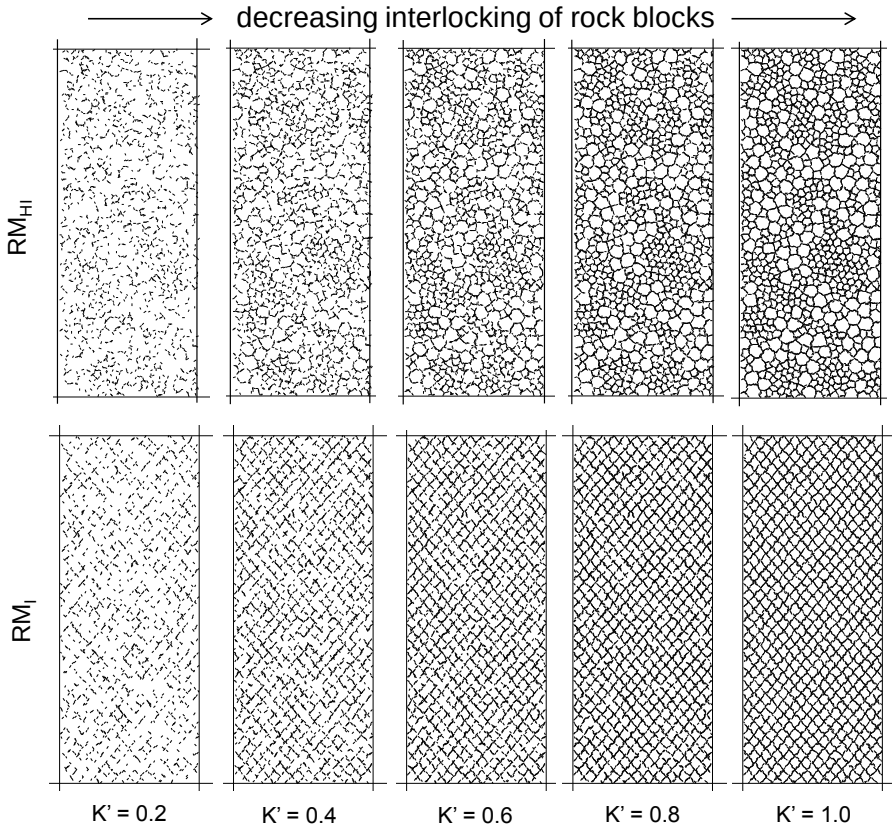

Figure 6-14: Examples of RM_{HI} and RM_I specimens with persistent and non-persistent joints. Black lines are smooth-joint contacts. Note that parallel bonds inside the blocks are not shown in these figures.

Figure 6-15a plots the unconfined compressive strengths of the RM_{HI} and RM_I specimens as a function of K' ratio. As can be seen from this figure, the strength of massive rockmass ($K' = 1$) is about 120 MPa. This is close to the lower bound strength of calcite grain suggested by Lama and Vutukuri (1978) to range between 120 MPa and 150 MPa. The *UCS* of both rockmasses decreases non-linearly with increasing the K' ratio. The strengths of both rockmasses are comparable for K' ratios ranging from 0.1 to 0.5. For higher K' ratios, the strength of the RM_I specimen decreases more rapidly with increasing the K' ratio compared to that of the RM_{HI} specimen, as slip along joints occurs easily as the structure of the RM_I specimen becomes closer to that of a fully persistent jointed rockmass ($K' = 1$).

It is clear from Figure 6-15a that when $K' = 1$ the *UCS* of the RM_{HI} is about 20 MPa higher than that of the RM_I. This has an implication when estimating the unconfined compressive strength of a RM_{HI} using the currently available empirical approaches; the empirical approaches, which were mainly developed based on experiences from and in situ tests on interlocked or poorly interlocked rockmasses, underestimate the unconfined compressive strength of highly interlocked rockmasses.

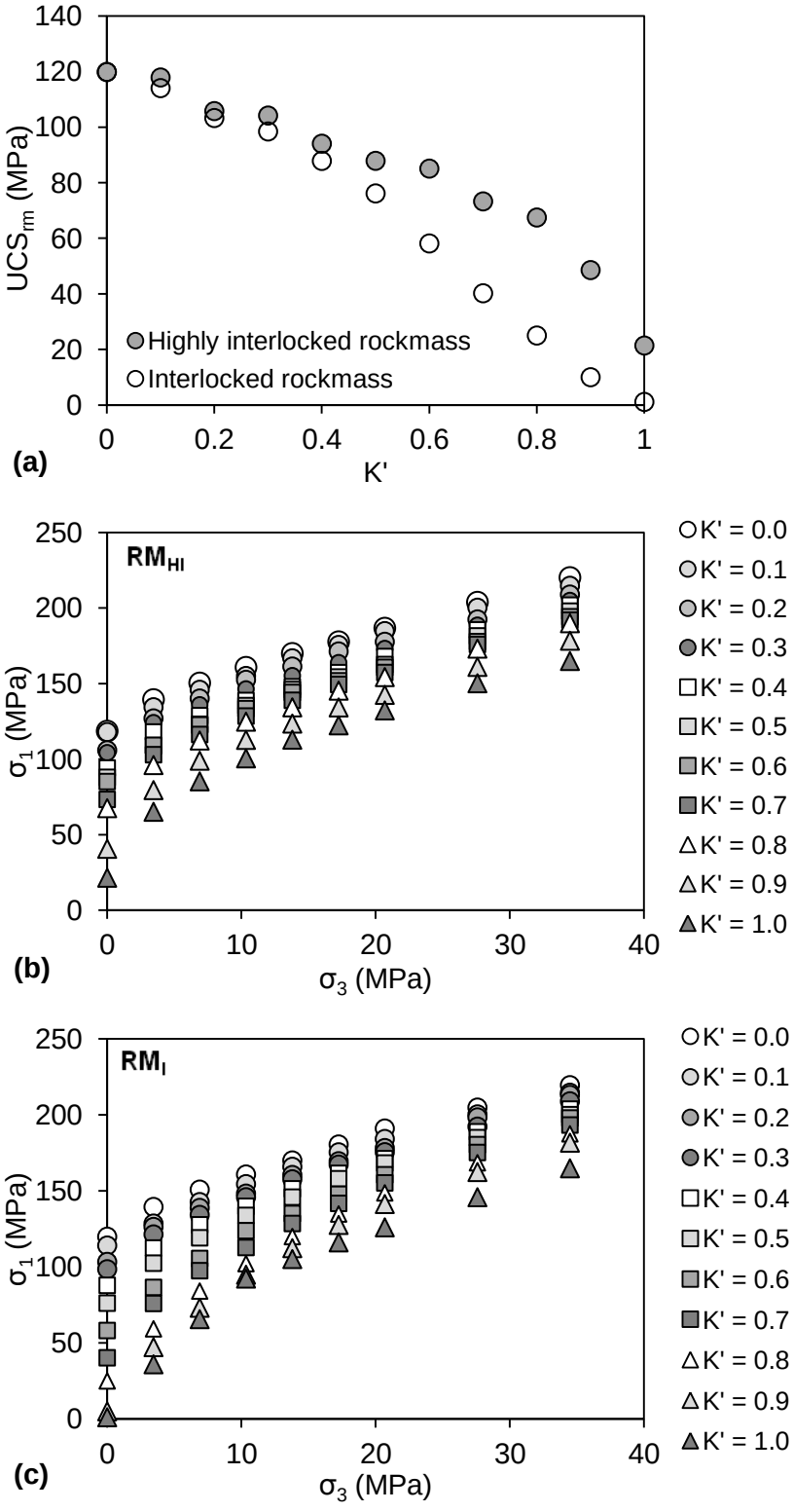

Figure 6-15: Influence of *K'* on: a) unconfined compressive strengths of highly interlocked and interlocked rockmass specimens; b) strength envelopes of highly interlocked rockmass specimens; and c) strength envelopes of interlocked rockmass specimens.

The influence of persistence (*K'* ratio) on the strength envelopes of the RM_{HI} and RM_I specimens are shown in Figure 6-15b and c. The main difference between these two rockmasses is their strengths for *K'* ratios greater than 0.5 (Figure 6-15c). For *K'* ratios greater than 0.5, the RM_{HI} specimen exhibits higher strengths, especially at low confinement (σ_3 < 10.4 MPa), when much more dilatant. As the structure becomes closer to a persistently jointed rockmass (*K'* = 1), the influence of slip along joints become more and more dominant on the strength of the RM_I specimen. The strengths of the RM_{HI} and RM_I specimens become comparable at high confinement and for *K'* ratios greater than 0.5. As discussed earlier, this is due to the intra-block fracturing in both rockmasses, as slip along joints is inhibited due to the combined influence of confinement and high degree of block boundary interlock, which arises from the relatively high friction angle of joints.

6.4 Evaluation of GSI approach for estimating the strength of interlocked rockmasses

The application of equations based on the *GSI* system (Equation 2-16 to Equation 2-18) for estimating the confined strength of highly interlocked (RM_{HI}) and interlocked (RM_I) rockmasses is investigated in this section. For this purpose, the *HB* failure criterion (Equation 2-15) with the *GSI* of 100 was first fitted to the strength of a massive rockmass (i.e., *PFC* specimen where all particles are bonded with parallel bonds; *K'* = 0 in Figure 6-13). The *GSI* was then lowered until the reduced unconfined compressive strength matched those of RM_{HI} and RM_I specimens with fully persistent joints (*K'* = 1). This analysis was conducted for different values of smooth-joint friction angle for each rockmass.

Figure 6-16 (a-d) presents the results of analysis for the highly interlocked rockmass (RM_{HI}) for various values of joint friction angle (50° to 20°). As can be seen in these figures, the *GSI* approach, if anchored at the UCS_{rm}, consistently underestimates the confined strengths of highly interlocked rockmasses by as much as a factor of two, independent of the value of joint friction angle (grey envelopes). This was expected, as the *HB* failure criterion and the *GSI*-based equations for the determination of the *HB* strength parameters were not developed for the estimation of the confined strength of highly interlocked rockmasses (Hoek and Brown, 1980a; 1997).

It was discussed in the previous section and shown in Figure 6-15a that even under unconfined condition the empirical approaches including the *GSI* system tend to underestimate the strength of highly interlocked jointed rockmasses. In the analysis conducted in this section and shown in Figure 6-16 (a-d), it was assumed that the *GSI* approach reliably estimates the *UCS* of the RM_{HI} specimen. However, underestimation of the unconfined strength of the highly interlocked rockmass by the inappropriate use of empirical approaches including the *GSI* system leads to a further underestimation of the confined strength of the highly interlocked rockmass. This is demonstrated in Figure 6-16a for the case of the RM_{HI} specimen with a joint friction angle of 50° (dashed black envelope). For this reason, it is suggested that the empirical approaches be used only when there is no access to the rockmass. Once the mine is in its development stage and access to the rockmass is possible, back analysis of the unconfined strength from monitoring of the rockmass behavior near excavation boundaries will provide a more reliable estimate of the highly interlocked rockmass strength.

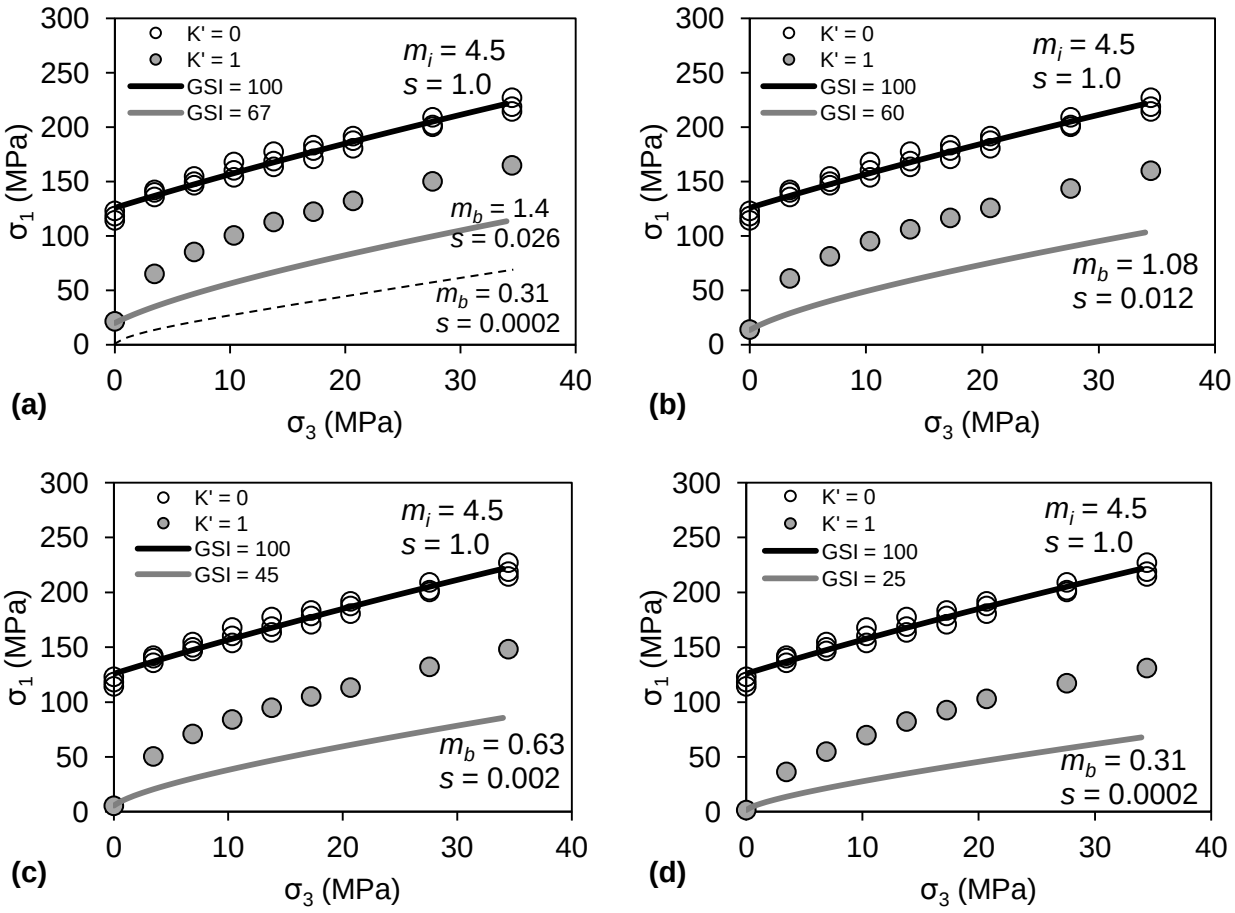

Figure 6-16: Comparison between the confined strengths estimated using the *GSI* approach and those of RM_{HI} specimens for different values of joint friction angle: a) $\emptyset_j = 50°$; b) $\emptyset_j = 40°$; c) $\emptyset_j = 30°$; d) $\emptyset_j = 20°$.

Figure 6-17(a-d) shows the results of analyses conducted on the strength data of interlocked rockmass specimens (RM_I) with fully persistent joints for various values of joint friction angle (50° to 20°). It was found that the unconfined compressive strength of the RM_I specimen could be matched with the *GSI* of 20 for all the cases, since its strength is independent of joint friction angle under unconfined condition. However, it can also be seen that when the joint friction angle is 50° (Figure 6-17a), the *GSI* approach underestimates the confined strength of the RM_I specimen. The confined strength of the RM_I specimen decreases and approaches that estimated by the *GSI* approach as the joint friction angle decreases to 30° (Figure 6-17b and c). Only when

the joint friction angle is 20° does the confined strength estimated by the *GSI* approach match that of the RM_I specimen (Figure 6-17d).

This was not expected, as the *HB* failure criterion and the *GSI*-based equations were developed for poorly interlocked rockmasses such as that of Panguna andesite. The main difference between the Panguna andesite rockmass and the simulated RM_I specimen is the rock block and joint surface conditions. The Panguna andesite rock blocks are heavily disturbed and have strengths that are much less than 100 MPa. The joint surfaces in this rockmass are heavily weathered and therefore not dilatant and have low equivalent friction angles. The consistency between the strength envelope estimated using the *HB* criterion and that of the RM_I specimen occurs only when the joints in the RM_I specimen are assigned a very low friction angle of 20° (Figure 6-17d). Therefore, in interlocked jointed rockmasses consisting of hard brittle rock blocks, only when block boundaries are smooth and free to move does the *GSI* approach seem to predict the confined rockmass strength accurately.

It is concluded from the analyses conducted in this section that the equations based on the *GSI* system used to determine the *HB* strength parameters are not applicable to highly interlocked jointed rockmasses, or interlocked jointed rockmasses consisting of hard brittle rock blocks (with strength greater than 100 MPa). Moreover, the *GSI* system can only be used to estimate the confined strength of interlocked jointed rockmasses made up of persistent joints with relatively smooth surfaces (i.e., low “equivalent” joint friction angle).

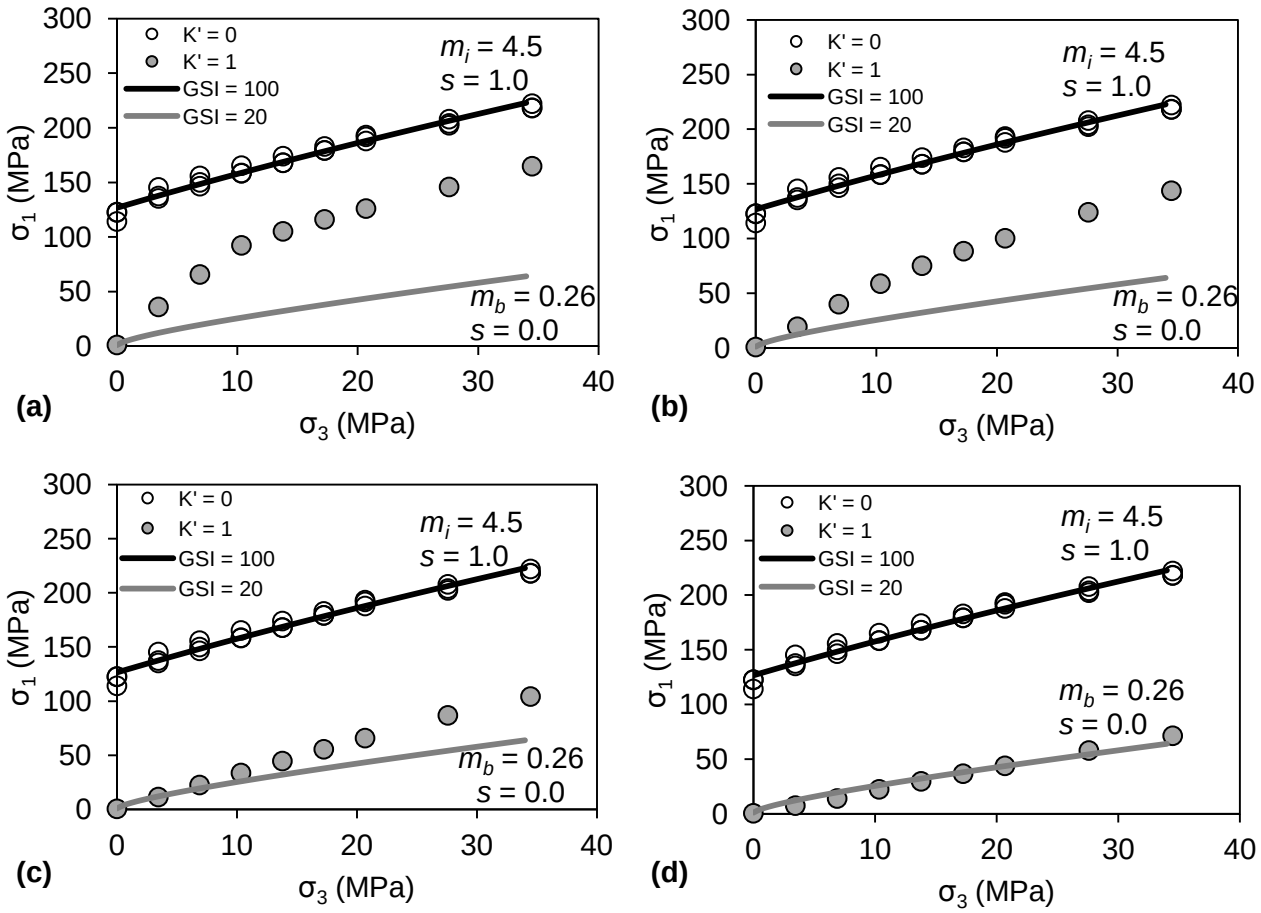

Figure 6-17: Comparison between the confined strengths estimated using the *GSI* approach and those of RM_I for different values of joint friction angle: a) $\emptyset_{sj} = 50°$; b) $\emptyset_{sj} = 40°$; c) $\emptyset_{sj} = 30°$; d) $\emptyset_{sj} = 20°$.

6.5 Summary and Conclusions

The results of laboratory test simulations on the fully damaged grain-based specimen previously calibrated to the laboratory properties of granulated Wombeyan marble (in *Chapter 3*), were expanded to a highly interlocked jointed rockmass to investigate the influence of the degree of interlock on rockmass strength. Three main factors controlling the degree of interlock, including block shape, joint roughness and joint persistence were numerically investigated in this chapter.

First, two synthetic rockmass specimens with structures representative for a highly interlocked jointed rockmass (i.e., fully damaged grain-based specimen) and a standard interlocked jointed rockmass made up of nearly two orthogonal joint sets were considered to investigate the influence of block shape on the rockmass strength. These rockmasses consist of hard brittle rock blocks (UCS_i > 100 MPa) and joints with zero tensile strength and cohesion, and a relatively high "equivalent" friction angle of 50° for joints. It was found that the main difference between these two rockmasses is their strength and failure mechanisms at low confinement:

- Under unconfined condition, the highly interlocked rockmass fails at an axial stress of about 20 MPa. The strength of interlocked jointed rockmass is nearly zero under unconfined condition.
- The highly interlocked rockmass represents a higher strength at low confinement (σ_3 < 10 MPa) compared to the interlocked rockmass. However, their strengths become comparable at high confinement (σ_3 > 10 MPa) especially at the very high confining pressure of 34.5 MPa, as slip along joints is inhibited and failure occurs due to intra-block fracturing.
- At low confinement (σ_3 < 10 MPa), the failure of highly interlocked rockmass involves opening of blocks along their boundaries as well as some intra-block fracturing. At this confinement level, the interlocked rockmass fails due to sliding of blocks along their frictional boundaries.
- At high confinement (σ_3 > 10 MPa), the failure of both highly interlocked and interlocked rockmasses involves intra-block fracturing, although this is more dominant in the highly interlocked rockmass.

The influence of joint roughness on rockmass strength was investigated by varying the joint friction angle from 50° representing a very rough and dilatant joint (without dilation effect consideration), to 20° representing a smooth and non-dilatant joint. It was found that the strength of highly interlocked rockmass under unconfined and confined conditions is not very sensitive to

the value of joint friction angle, and the strength envelope remains non-linear for different values of joint friction angle (20° to 50°). The confined strength of interlocked rockmass, however, decreases rapidly with decreasing joint friction angle. Moreover, the joint friction angle influences the non-linearity of the strength envelope in the interlocked rockmass; the strength envelope is linear for the joint friction angle of 35° and lower.

Various levels of joint persistence were simulated by randomly removing smooth-joint contacts and replacing them with parallel bonds. It was found that the strengths of highly interlocked and interlocked rockmasses made up of hard brittle rock blocks and rough joints, under unconfined and confined conditions decrease as the level of joint persistence increases. Moreover, the non-linearity of the strength envelopes increases with increasing persistence level (K') in both rockmasses.

The results of analyses reported in this chapter showed that the strength of a jointed rockmass is strongly dependent on the degree of interlock between rock blocks and in general higher than that predicted by the *GSI* approach. Therefore, more accurate estimation of rockmass strength under unconfined and confined conditions can be achieved only if factors that influence the degree of interlock including the shape of rock blocks, joint roughness and persistence are considered in the estimation of the rockmass strength. It was demonstrated that the *HB* failure criterion originally developed on data from persistently and weathered, therefore poorly interlocked, jointed rockmasses, should not be used to estimate the strength of highly interlocked jointed rockmasses. Moreover, the *HB* failure criterion can be used to estimate the strength of interlocked jointed rockmasses consisting of strong rock blocks, only if the joints are smooth and non-dilatant.

In the next chapter, the results of analysis of the highly interlocked jointed rockmass presented in this chapter will be used to develop semi-empirical approaches that can be used to estimate the confined strength of such rockmasses.

Chapter 7

7 Estimation of Confined Strength of Highly Interlocked Jointed Rockmasses

7.1 Introduction

In this chapter, the results of numerical simulations of the highly interlocked rockmass specimens (RM_{HI}), presented in the previous chapter, are used to develop semi-empirical approaches that can be used to estimate the confined strength of such rockmasses. Two approaches are proposed in this regard: The first approach is similar to the Strength Degradation (*SD*) approach developed for micro-defected rocks in *Chapter 4*, and the second approach is based on the *HB* failure criterion by adjusting its strength parameters m_b, a and s so that this criterion can be applied to highly interlocked jointed rockmasses. The assumptions in these approaches are:

- the *UCS* and triaxial test results of intact rock are available and fall into the class of "high rock strength" according to the classification by Bieniawski (1973), thus $UCS_i > 100$ MPa;
- the unconfined compressive strength of the jointed rockmass (UCS_{rm}) can be estimated using one of the empirical methods reviewed in *Chapter 2* (e.g., empirical equations by Aydan and Dalgic, 1998; Kalamaras and Bieniawski, 1993; Sheorey, 1997; or the empirical chart by Carter et al., 2008);
- the rockmass is randomly and non-persistently jointed; and
- joints have zero tensile strength and cohesion, and are dilatant (e.g., with equivalent joint friction angle greater than 40°).

These approaches are then tested on the results of published laboratory tests on jointed rockmasses and their estimated confined rockmass strengths are compared with those of the

generalized *HB* failure criterion with strength parameters determined using the *GSI*-based equations suggested by Hoek et al. (2002).

7.2 Strength Degradation (SD) Logic for Highly Interlocked Jointed Rockmasses

The results of laboratory test simulations on the highly interlocked rockmass (RM_{HI}) specimens presented in Figure 6-15b are used in this section to develop a Strength Degradation (*SD*) logic for jointed rockmasses. This logic can be used to estimate the confined strength of a highly interlocked jointed rockmass in a situation where the unconfined and confined strengths of the intact rock and the unconfined strength of the rockmass are known.

7.2.1 Determination of degradation parameters

The degradation parameter (*DP*), which is the percent difference between the strengths of the intact (σ_{1i}) specimen and that of the jointed rockmass (σ_{1rm}), was calculated for the RM_{HI} specimens, according the following equation:

$$DP = \left(\frac{\Delta\sigma_1}{\sigma_{1i}}\right) \times 100 = ((\sigma_{1i} - \sigma_{1rm})/\sigma_{1i}) \times 100 \qquad \text{Equation 7-1}$$

Figure 7-1 plots the *DP* as a function of confinement for the RM_{HI} specimens with *K'* ratios ranging from 0.1 to 1.0. As can be seen, the *DP* under unconfined condition ranges between 0% and 80%. With increasing confinement, the *DP* decreases and approaches an asymptotic value or plateau beyond the confining pressure of about $UCS_i/10$ = 12 MPa.

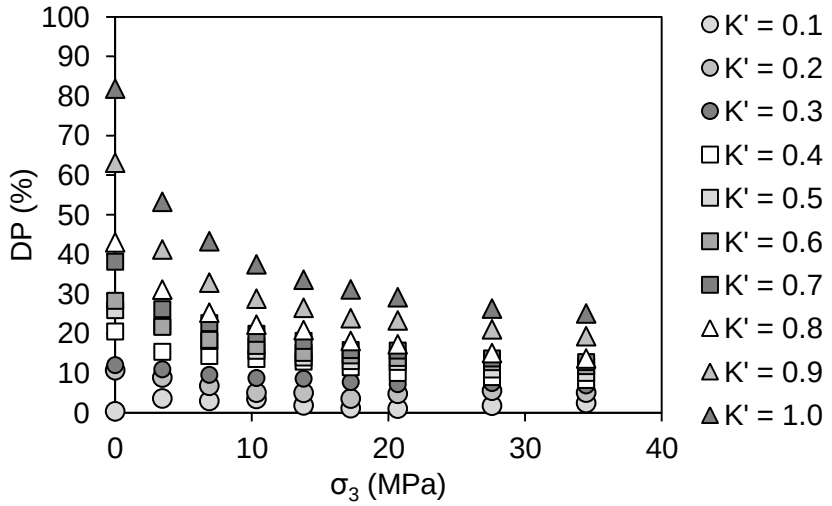

Figure 7-1: Degradation parameter versus confinement determined for RM_{HI} specimens with *K'* ratios ranging from 0.1 to 1.0.

The decrease in the *DP* with increasing confinement is more pronounced in rockmasses with higher *K'* ratios (more persistent joints). The maximum strength degradation at high confinement (i.e., σ_3 = 34.5 MPa) is about 25% of the intact strength, which corresponds to the RM_{HI} specimen with the *K'* ratio of 1.0, and less than 10% for *K'* < 0.5.

An exponential function with the general form given in Equation 4-2 was used to fit to the results of numerical simulations presented in Figure 7-1. The least square regression analysis was conducted to determine the fitting parameters. A negative exponential function was used to correlate the *DP* to confinement. This function is similar to that used in the development of the *SD* approach for micro-defected rocks:

$$DP = (Du - Dc)e^{[100(-\sigma_3/\sigma_{ci})/c]} + Dc \qquad \text{Equation 7-2}$$

where, as before, *Du* (unconfined degradation) is the value of *DP* under unconfined condition, *Dc* (confined degradation) is the value of *DP* at high confinement where *DP* becomes

independent of confinement and *c* is the curvature parameter. *c* corresponds to the dilation angle of the rockmass; the higher the dilation angle the lower the *c*-value. Figure 7-2 shows the best fit curve and the ± 95% confidence intervals (*CI)* for the RM_{HI} specimen with *K'*= 0.5. Table 7-1 lists the degradation parameters *Du*, *Dc* and *c*, obtained from the least square regression analysis for *K'* ratios ranging from 0.1 to 1.0.

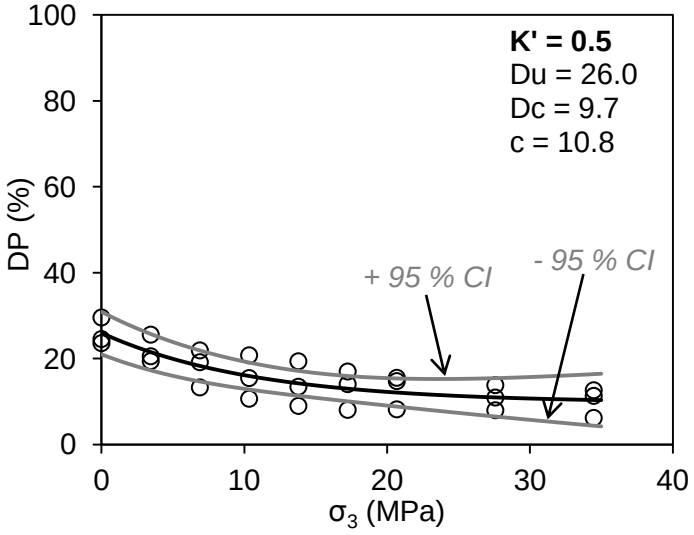

Figure 7-2: Plot of *DP* versus confinement showing the best fit and ± 95% *CI* curves along with the values of *Dc*, *c* and *Du* obtained from the least square regression analysis for the RM_{HI} specimen with *K'* = 0.5.

Table 7-1: Degradation parameters of the RM_{HI} specimens obtained from the least square regression analysis.

K' (%)	*Du* (%)	*Dc* (%)	c
10	2.2	1.9	25
20	11.1	4.6	4.8
30	12.1	6.7	9.6
40	19.6	7.5	11.8
50	26.0	9.7	9.1
60	27.9	12.3	6.6
70	37.2	13.6	6.0
80	42.2	14.6	6.7
90	57.9	17.4	4.7
100	80.7	27.1	4.9

Note that *K'* is a numerical parameter, and therefore not measurable in practice. It is related to the degree of jointing in a rockmass and its strength under unconfined condition (UCS_{rm}), and therefore the unconfined degradation *Du*. Since *Du* is a known parameter in the *SD* approach, *Dc* and *c* were plotted against *Du*, to obtain relationships between *Dc* and *Du* and between *c* and *Du*. Figure 7-3a and b show the best fit curves that correlate *Dc* to *Du*, and *c* to *Du*, respectively.

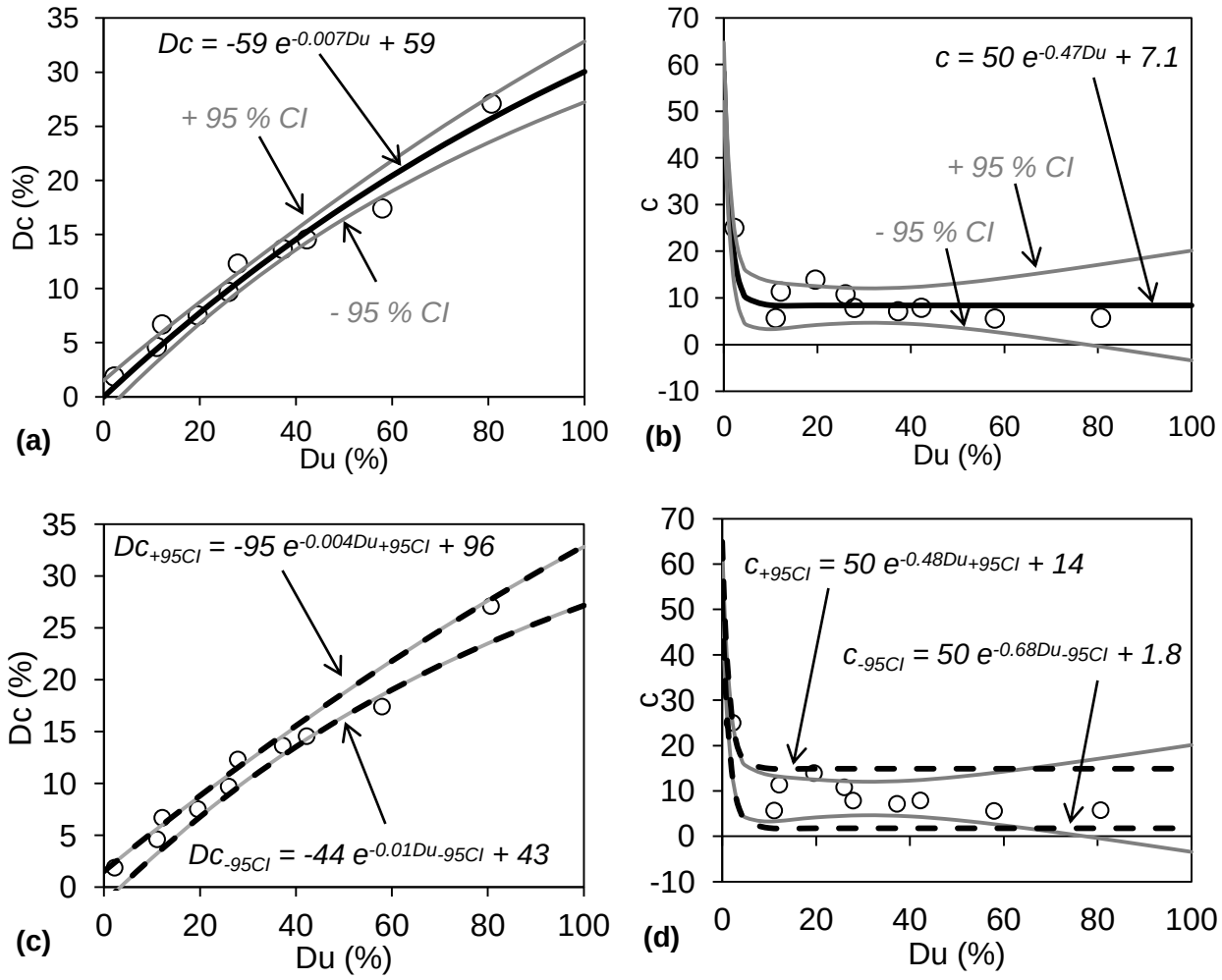

Figure 7-3: Relationships between a) D_c and D_u; and b) *c* and D_u. Approximation of ± 95% confidence intervals of degradation parameters for: c) *Dc*; and d) *c*. Solid grey and dashed black curves are actual and approximated ± 95% confidence intervals, respectively.

The confined degradation *Dc* and the curvature parameter *c* were found to be related to *Du* according to the following equations:

$$Dc = -59\, e^{-0.007Du} + 59 \quad \text{Equation 7-3}$$

$$c = 50\, e^{-0.47Du} + 7.1 \quad \text{Equation 7-4}$$

Exponential functions similar to Equation 7-3 and Equation 7-4 were used to approximate the ± 95% *CI* curves. The approximated ± 95% *CI*s are presented with the dashed black curves in Figure 7-3c and d. The average 95% confidence interval for *Du* was calculated to be 5.4. Therefore, the unconfined degradation for the + 95% (Du_{+95}) and - 95% (Du_{-95}) confidence intervals can be approximated by adding 5.4 to and subtracting 5.4 from the unconfined degradation (*Du*).

Equation 7-5 to Equation 7-8 are used to approximate the upper confidence intervals (+ 95% *CI*) of the degradation parameters.

$$Du_{+95CI} = Du + 5.4 \quad \text{Equation 7-5}$$

$$Dc_{+95CI} = -95\, e^{-0.004Du_{+95CI}} + 96 \quad \text{Equation 7-6}$$

$$c_{+95CI} = 50\, e^{-0.48Du_{+95CI}} + 14 \quad \text{Equation 7-7}$$

$$DP_{+95CI} = (Du_{+95CI} - Dc_{+95CI})e^{[100(-\sigma_3/\sigma_{ci})/c_{+95CI}]} + Dc_{+95CI} \quad \text{Equation 7-8}$$

Equation 7-9 to Equation 7-12 can be used to approximate the lower confidence intervals (-95% *CI*) of the degradation parameters.

$$Du_{-95CI} = Du - 5.4 \quad \text{Equation 7-9}$$

$$Dc_{-95CI} = -44\, e^{-0.01 Du_{-95CI}} + 43 \quad \text{Equation 7-10}$$

$$c_{-95CI} = 50\, e^{-0.68 Du_{-95CI}} + 1.8 \quad \text{Equation 7-11}$$

$$DP_{-95CI} = (Du_{-95CI} - Dc_{-95CI}) e^{[100(-\sigma_3/\sigma_{ci})/c_{-95CI}]} + Dc_{-95CI} \quad \text{Equation 7-12}$$

7.2.2 Approach to estimate confined rockmass strength

Now that the strength degradation of highly interlocked jointed rockmasses can be estimated as a function of confinement, the peak strength of such rockmasses can be estimated after rearranging Equation 7-1:

$$\sigma_{1rm} = \sigma_{1i} \times [1 - (DP/100)] \quad \text{Equation 7-13}$$

The following steps are to be followed to estimate the confined strength of a highly interlocked jointed rockmass using the *SD* approach:

Step 1: The *HB* criterion is used to fit to the unconfined and confined strengths of intact rock following the procedure suggested by Hoek and Brown (1997).

Step 2: The unconfined degradation *Du* is determined from the unconfined compressive strength of intact rock (σ_{ci}) obtained from triaxial compression strength tests and the unconfined jointed rockmass strength (UCS_{rm}) according to Equation 7-14. Note that it is assumed in the *SD* approach that the magnitude of UCS_{rm} can be reliably estimated using one of the available empirical approaches reviewed in *Chapter 2* (e.g., empirical equations by Aydan and Dalgic, 1998; Kalamaras and Bieniawski, 1993; Sheorey, 1997; or the empirical chart by Carter et al.,

2008), or from back analysis based on observation of and monitoring rockmass behavior near underground excavations (e.g., tunnel wall failure).

$$Du = [(\sigma_{ci} - UCS_{rm})/\sigma_{ci}] \times 100 \qquad \text{Equation 7-14}$$

Step 3: The values of *Dc*, *c* and *DP* are determined from Equation 7-3, Equation 7-4, and Equation 7-2, respectively.

Step 4: The confined strength of the highly interlocked jointed rockmass is then estimated using Equation 7-13.

Step 5: Equation 7-5 to Equation 7-8 are used to approximate the upper confidence intervals (+ 95%) of the degradation parameters, and Equation 7-9 to Equation 7-12 are used to approximate the lower confidence intervals (- 95%) of the degradation parameters.

Step 6: DP_{-95} determined from step 5 replaces *DP* in Equation 7-13 to obtain the upper bound confined strength of the rockmass, and DP_{+95} determined from step 5 replaces *DP* in Equation 7-13 to obtain the lower bound confined strength of the damaged rock.

7.3 Adjusted HB Strength Parameters for Highly Interlocked Jointed Rockmasses

Bahrani and Kaiser (2013) discussed how block boundary dilation and geometric bulking of the block assembly contribute to the rapid strengthening effect with increasing confinement in a highly interlocked jointed rockmass:

Block boundary dilation: Analogous to Patton (1966) for rough joints, it is evident that a high joint dilation, which is controlled by the asperity geometry, and friction, which is a rock property, lead to a steep initial slope of the joint shear strength envelope. Therefore, rough block boundaries in a jointed rockmass result in elevated dilation at low confinement and a rapid increase in the shear strength of the block boundary as confinement increases. Consequently, one contributor to the initially steep slope of the strength envelope is the block boundary dilation (represented by J_c in the *GSI* system according to Cai et al., 2004).

Geometric bulking of block assembly: Since failure at low confinement mainly occurs along block boundaries, the geometry of the block assembly directly influences the volumetric response of a rock assembly. Therefore, geometric incompatibilities of rock blocks in a highly interlocked rockmass with randomly oriented joints lead to a bulking process with a high volume gain and thus provide a second contributor to the steep initial slope of the strength envelope. Both factors together can typically add some 25° or more to the friction angle of a smooth joint (e.g., see laboratory test results on analogues of jointed rockmasses reviewed in *Chapter 2*).

As mentioned earlier, the constant m_b in the *HB* failure criterion corresponds to the rockmass internal friction angle. Based on Equation 2-17, m_b is always less than m_i; it decreases for decreasing *GSI* values. However, in a highly interlocked jointed rockmass, where a steep rise in the failure envelope at low confinement is to be anticipated (due to the boundary dilation and geometric bulking effects described above), m_b must be higher than m_i.

Beyond a critical confinement level, when geometric bulking of block assembly and block boundary dilation are suppressed, the slope of the failure envelope decreases before the rockmass strength exceeds the intact rock strength. This implies that the curvature, represented by the

parameter *a* in the *GSI*-based equations has to differ for highly interlocked rockmasses; the value of *a* has to be less than 0.5. The results of laboratory test simulations on the highly interlocked rockmass (RM_{HI}) specimens were analyzed to investigate this concept and to obtain representative values for m_b and *a* for such hard, brittle and highly interlocked rockmasses.

7.3.1 Determination of HB strength parameters

It was shown in the previous chapter that when the unconfined compressive strength in the *HB* failure criterion is matched with the average UCS_{rm} of the synthetic rockmass specimens (by lowering the *GSI* value), its confined strength (estimated by the *HB* failure criterion using the strength parameters determined from Equation 2-16 to Equation 2-18) underestimates that of RM_{HI} specimens. A series of least square regression analyses were thus conducted and values of *s*, m_b and *a* were adjusted to match the results from the *SD* approach for *K'* ratios ranging from 0.1 to 1.0. The adjusted *HB* strength parameters are called s^{α}, m_b^{α} and a^{α}.

Figure 7-4a shows that the adjusted s^{α} decreases at an almost linear trend with increasing *K'* ratio from 0.1 to 1.0. The constant s^{α}, which is related to the rockmass cohesive strength, is considered to be a known parameter in this approach.

Figure 7-4b shows how the original (*GSI*-based) m_b and adjusted m_b^{α} values change with increasing *K'* ratio from 0.1 to 1.0. The value of m_i is shown as a dashed line for reference. As can be seen from this figure, the *GSI*-based m_b is always less than m_i and initially decreases in a linear fashion with increasing *K'* from 0.1 to 0.8 and then drops more rapidly when *K'* approaches unity. However, m_b^{a}, obtained from the least square regression analysis, is greater than m_i until *K'* exceeds 0.8.

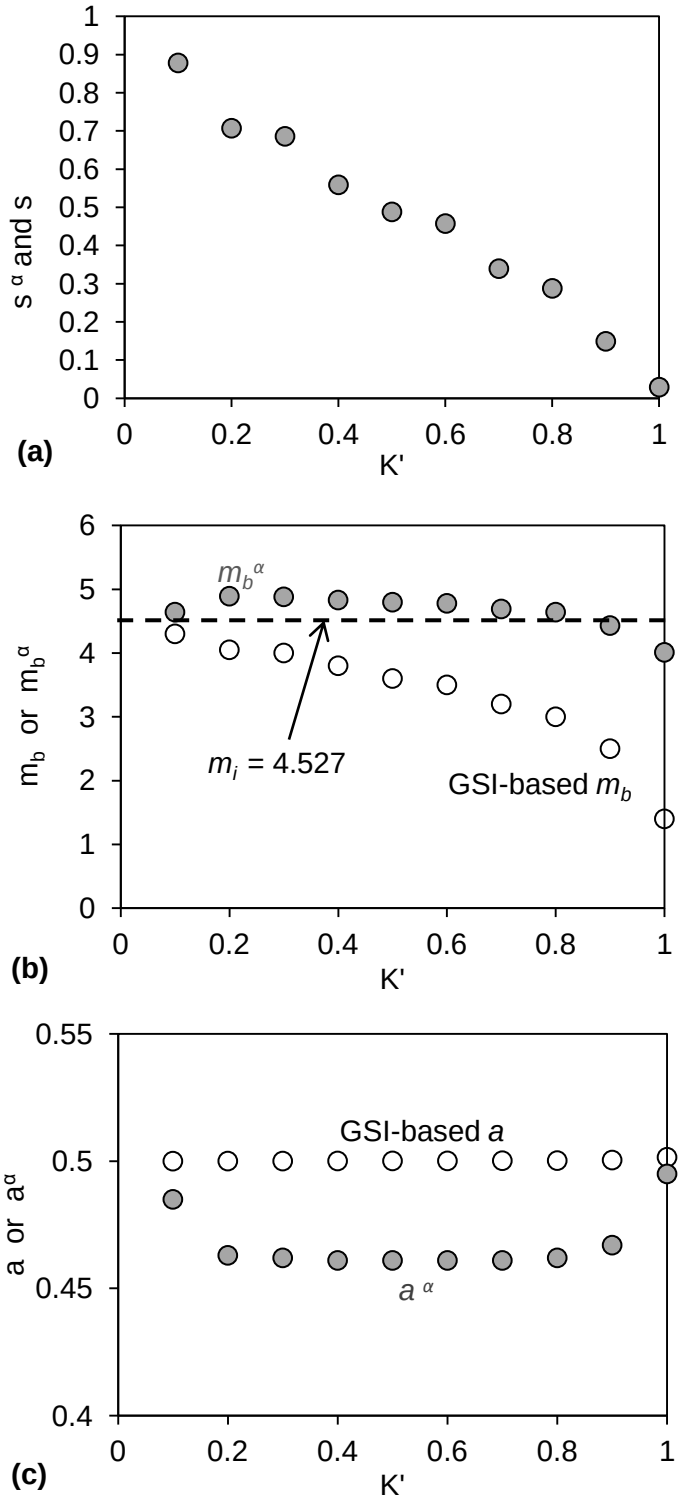

Figure 7-4: Influence of *K'* on: a) s^a; b) m_b and m_b^a; and c) a and a^a.

Figure 7-4c illustrates how the original (*GSI*-based) a and adjusted a^{α} values change with increasing K' from 0.1 to 1.0. It can be seen from this figure that the *GSI*-based a is independent of K', whereas a^{a} decreases from 0.5 for $K' = 0$ to about 0.46 for $K' = 0.2$, remains relatively constant for K' between 0.2 and 0.8, and then increases back to 0.5 for $K' = 1.0$.

As mentioned earlier, the unconfined degradation Du is a known parameter and therefore the correlations between Du and s^{a}, $m_b{}^{a}$ and a^{a} have to be defined. Figure 7-5 (a-c) plot the s^{a}, $m_b{}^{a}/m_i$ ratio, and a^{a} versus Du. Polynomial functions were found to be suitable to fit the data. The functions were forced to intersect $s^{a} = 1$ for $Du = 0$, and $s^{a} = 0$ for $Du = 100$ in Figure 7-5a, $m_b{}^{a}/m_i = 1$ for $Du = 0$ in Figure 7-5b, and $a^{a} = 0.5$ for $Du = 0$ in Figure 7-5c, so that the unconfined and confined strengths of a rockmass become equal to those of the intact rock when the degradation is zero (i.e., $Du = 0$).

Based on the least-square regression analysis, which resulted in relatively high correlation coefficients ($R^2 > 0.8$), the following equations were obtained and suggested for the adjusted *HB* strength parameters s^{a}, $m_b{}^{a}$ and a^{a}, when dealing with highly interlocked jointed rockmasses:

$$s^{\alpha} = [0.01Du^2 - 2Du + 100]/100 \qquad \text{Equation 7-15}$$

$$m_b{}^{\alpha} = m_i \times [-0.007Du^2 + 0.4Du + 100]/100 \qquad \text{Equation 7-16}$$

$$a^{\alpha} = [0.002Du^2 - 0.2Du + 50]/100 \qquad \text{Equation 7-17}$$

From the type of function (polynomial fit) used to fit the data in Figure 7-5, it is suggested that the end members near $Du > 0.9$ be assessed with care.

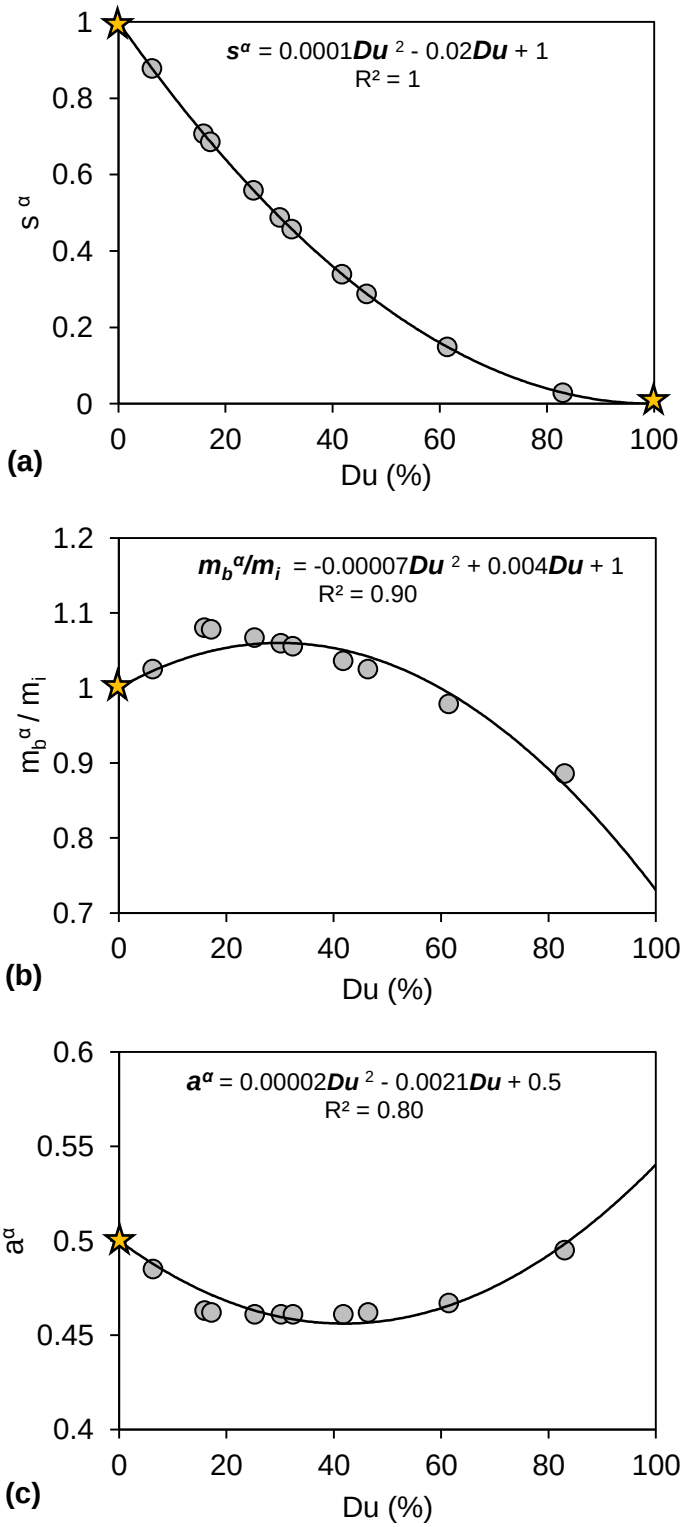

Figure 7-5: Correlations between: a) ratio of m_b^a to m_i and s^a; and b) a^a and s^a with anchor points for regression analysis at locations indicated by star.

In summary, the strength of a highly interlocked, non-persistently jointed rockmass can be estimated using the *HB* failure criterion with an adjusted m_b^a value, which is higher than that of the *GSI*-based m_b, and an adjusted *a* value, which is lower than that of the *GSI*-based *a*.

7.3.2 Approach to estimate confined rockmass strength

The following four steps are to be taken to estimate the confined strength of a highly interlocked jointed rockmass with high block strength (UCS_i >100 MPa) using the adjusted *HB* strength parameters:

Step 1: The *HB* failure envelope is fitted to the unconfined and confined strengths of intact rock to obtain the intact rock strength parameters m_i and σ_{ci}, following the procedure suggested by Hoek and Brown (1997) and Hoek et al. (2002).

Step 2: The unconfined degradation *Du* is determined from the unconfined compressive strength of intact rock (σ_{ci}) obtained from triaxial compression strength tests and the unconfined jointed rockmass strength (UCS_{rm}) using Equation 7-14. Note that it is assumed in this approach that the magnitude of UCS_{rm} can be reliably estimated using one of the available empirical approaches reviewed in *Chapter 2* (e.g., empirical equations by Aydan and Dalgic, 1998; Kalamaras and Bieniawski, 1993; Sheorey, 1997; or the empirical chart by Carter et al., 2008), or from back analysis based on observation of and monitoring rockmass behavior near underground excavations (e.g., tunnel wall failure).

Step 3: Equation 7-15, Equation 7-16 and Equation 7-17 are used to determine the values of s^a, m_b^a and a^a, respectively.

Step 4: The generalized *HB* failure criterion (Equation 2-15) is used to estimate the confined strength of the highly interlocked jointed rockmass.

7.4 Case Examples

In this section, the *SD* approach and the *HB* failure criterion using the adjusted *HB* strength parameters (Equation 7-15 to Equation 7-17) are first examined on the results of numerical simulations from which these approaches were developed. This of course is a circular argument as the inputs were obtained from the eventual outputs, but is presented here to demonstrate and verify the approach. The applicability of these approaches is then investigated on the published laboratory test data, which are considered to be analogues for jointed rockmasses.

Figure 7-6a to c show the results of numerical test simulations on the synthetic intact rock and highly interlocked rockmass specimens (with *K'* of 0.1, 0.5 and 1.0). This figure illustrates the correspondence between the confined strengths of the RM_{HI} specimens and those estimated by the *SD* approach and the *HB* failure criterion using the adjusted strength parameters. As was expected, the *HB* failure criterion based on the *GSI*-based equations (Equation 2-16 to Equation 2-18) tends to underestimate the confined strength of the highly interlocked rockmass specimens. The amount of underestimated confined strength increases with decreasing the unconfined rockmass strength (or increasing the unconfined strength degradation in the *SD* approach or decreasing the *s*-value).

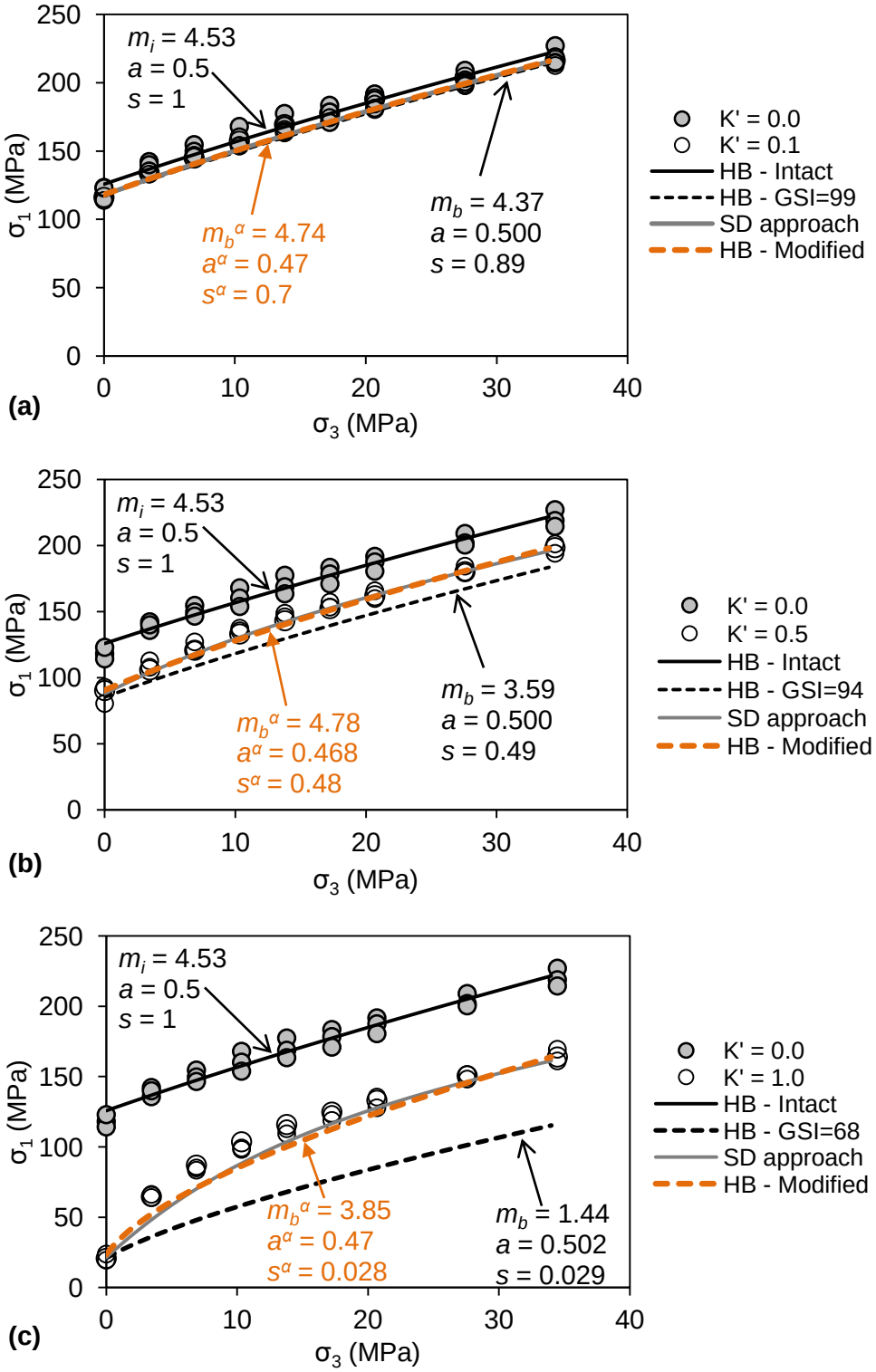

Figure 7-6: Comparison between the confined strengths of RM_{HI} specimens for three different *K'* values (a to c) and those estimated using the *SD* approach and the *HB* failure envelopes based on the adjusted and *GSI*-based strength parameters.

The applicability of the *SD* approach and the *HB* failure criterion using the adjusted strength parameters for estimating the confined strength of jointed rockmasses was further investigated on the published laboratory test data on the fractured rock specimens reviewed in *Chapter 2*.

Unfortunately, no published case examples that truly reflect the unconfined and confined strengths of both intact rock and highly interlocked jointed rockmass are available. The granulated Wombeyan and Carrara marble tested by Gerrogiannopoulos (1976) and Rosengren and Jaeger (1968) are relevant examples of a highly interlocked jointed rockmass. However, as discussed by Hoek and Brown (1980a), the calcite grain in the granulated marble is representative for the intact rock and unfortunately its strength is not known. Another relevant example of a highly interlocked rockmass is the plaster models (i.e., *H30*, *H45*, and *H60* specimens) tested by Brown (1970). The unjointed plaster model in these experiments, however, cannot be considered as the intact specimen, as its strength at high confinement is less than that of jointed plaster models.

Therefore, the results of the remaining laboratory experiments on fractured rocks, considered to be analogues for jointed rockmasses (but not necessarily highly interlocked jointed rockmasses), including the damaged *LdB* granite by Martin (1993), the fractured limestone by Ribacchi (2000) and the artificially jointed granite by Arzua et al. (2014) are used to investigate the applicability of the proposed approaches for the estimation of confined strength of jointed rockmasses.

7.4.1 Damaged LdB Granite

The damaged *LdB* granite is representative for a non-persistently jointed rockmass, as the drilling-induced cracks terminate within the intact rock. Figure 7-7 (a-c) shows that although the *SD* approach underestimates the confined strength of damaged *LdB* granite, it very well captures

the strength variability (by the upper and lower bounds shown with dotted lines), as over 90% of the data are between the estimated strength limits.

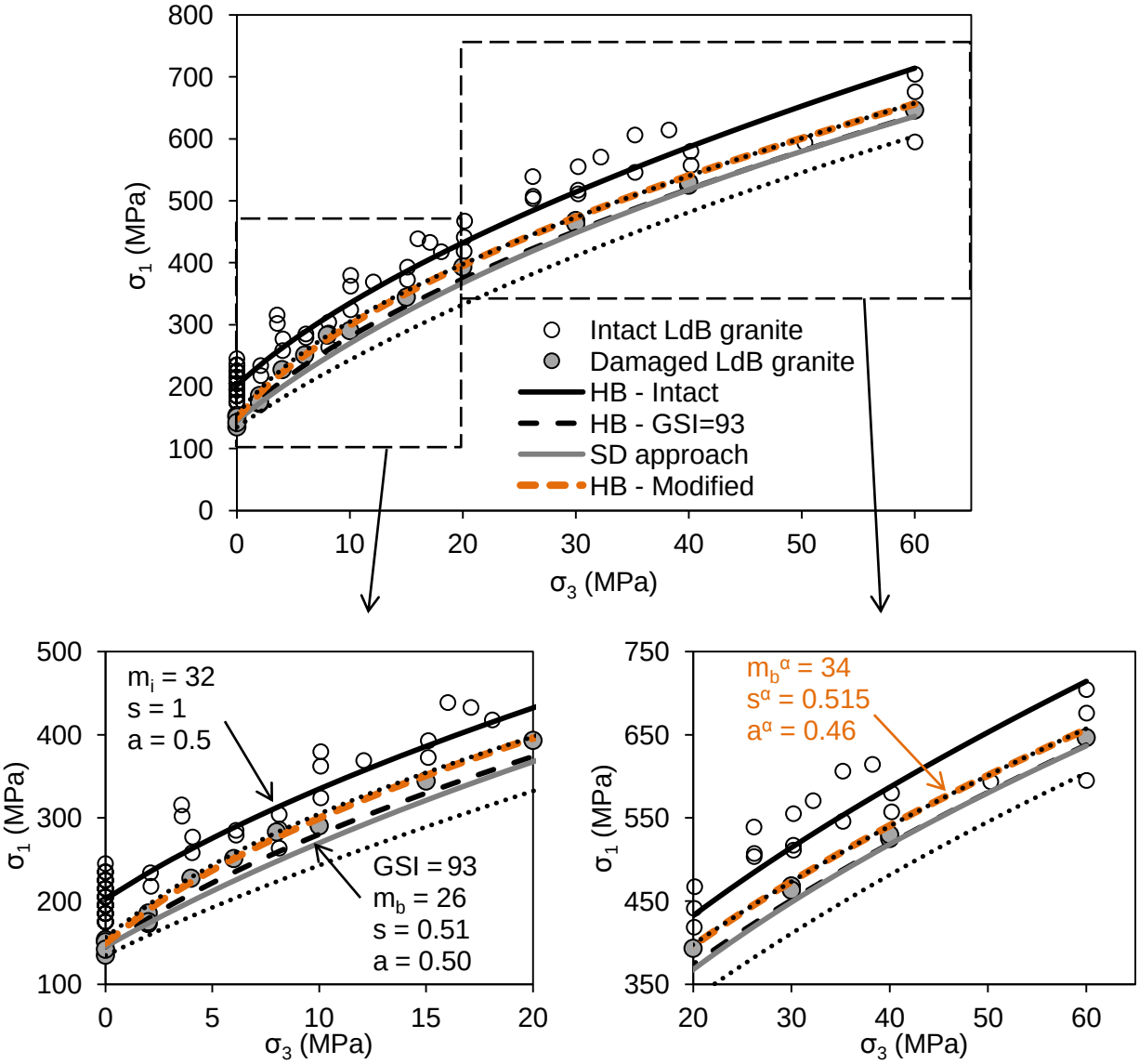

Figure 7-7: Estimation of the confined strength of damaged *LdB* granite using the *SD* approach and the *HB* failure criterion using the *GSI*-based and adjusted strength parameters. The dotted lines show the strength variability estimated using the *SD* approach.

On the other hand, the confined strength of the damaged granite, especially the rapid increase in the strength at low confinement, is very well captured by the *HB* criterion using the adjusted

strength parameters (Figure 7-7). This is mainly due to the higher adjusted m_b^a and lower a^a values compared to the those of m_b and a obtained from the *GSI*-based equations. As shown in this figure, the *HB* criterion based on the *GSI*-based strength parameters consistently underestimates the confined strengths of damaged granite.

7.4.2 Fractured Limestone

The results of triaxial tests on fine-grained limestone made up of various degrees of fracturing tested by Ribacchi (2000) are presented in Figure 7-8 (a-c), along with the strength envelopes estimated using the *SD* approach and the *HB* strength envelopes based on the adjusted and *GSI*-based strength parameters. Ribacchi (2000) mentioned that the fractured limestone can be considered as a small scale model of a jointed rockmass. However, it is not possible to comment whether the fractured limestone is an analogue for a highly interlocked jointed rockmass, as very little information on the geometry and properties of the fractures or the failure modes of the specimens is available. The average UCS_i value is less than 100 MPa, although the average is not meaningful as some of the intact specimens failed along defects which could not be seen before the tests (Ribacchi, 2000). On the other hand, some UCS_i values of the intact specimens are as high as 100 MPa. Therefore, these specimens are considered as hard brittle rocks. Ribacchi (2000) classified the limestone specimens into four groups. The description of each group is repeated here for convenience:

- *IN*: seemingly intact specimens;
- *IF*: specimens with rare and mostly healed fractures;
- *FR*: specimens with diffused fracturing; and
- *SH*: specimens having multiple shear surfaces.

As discussed in *Chapter 2*, only the *IF* specimens are representative of an interlocked rockmass. As can be seen in Figure 7-8a, both the *SD* approach and the *HB* criterion based on the adjusted strength parameters reasonably estimate the confined strength of *IF* limestone. The *HB* envelope based on the *GSI*-based strength parameters, however, represents the lower strength of the *IF* specimens and consistently underestimates the average confined strengths shown with the diamonds. Due to the very high variability of the strength of *IN* and *IF* specimens, only 44% of the data points are between the upper and lower bounds estimated using the *SD* approach. However, this is not considered as a deficiency of the *SD* approach, as it is likely that the weaker *IF* specimens were dominated by the presence of through-going defects.

As shown in Figure 7-8b and c, the *HB* envelope based on the *GSI*-based strength parameters provides a better estimate of the confined strengths of the *FR* and *SH* specimens, compared to the proposed approaches. This is more pronounced in the case of *SH* specimens, which were described by Ribacchi (2000) as specimens containing multiple shear surfaces. The *SD* approach and the *HB* criterion based on the adjusted strength parameters consistently overestimate the confined strength of these specimens. This is consistent with the findings presented in *Chapter 5*. The *SH* specimens were probably dominated by shear failure along joints and thus satisfy the *HB* criterion with the strength parameters determined using the *GSI*-based equations. Figure 7-8b, for the *FR* specimens, shows that some of the specimens are highly interlocked and their strengths are captured by the *SD* approach and the *HB* criterion based on the adjusted strength parameters.

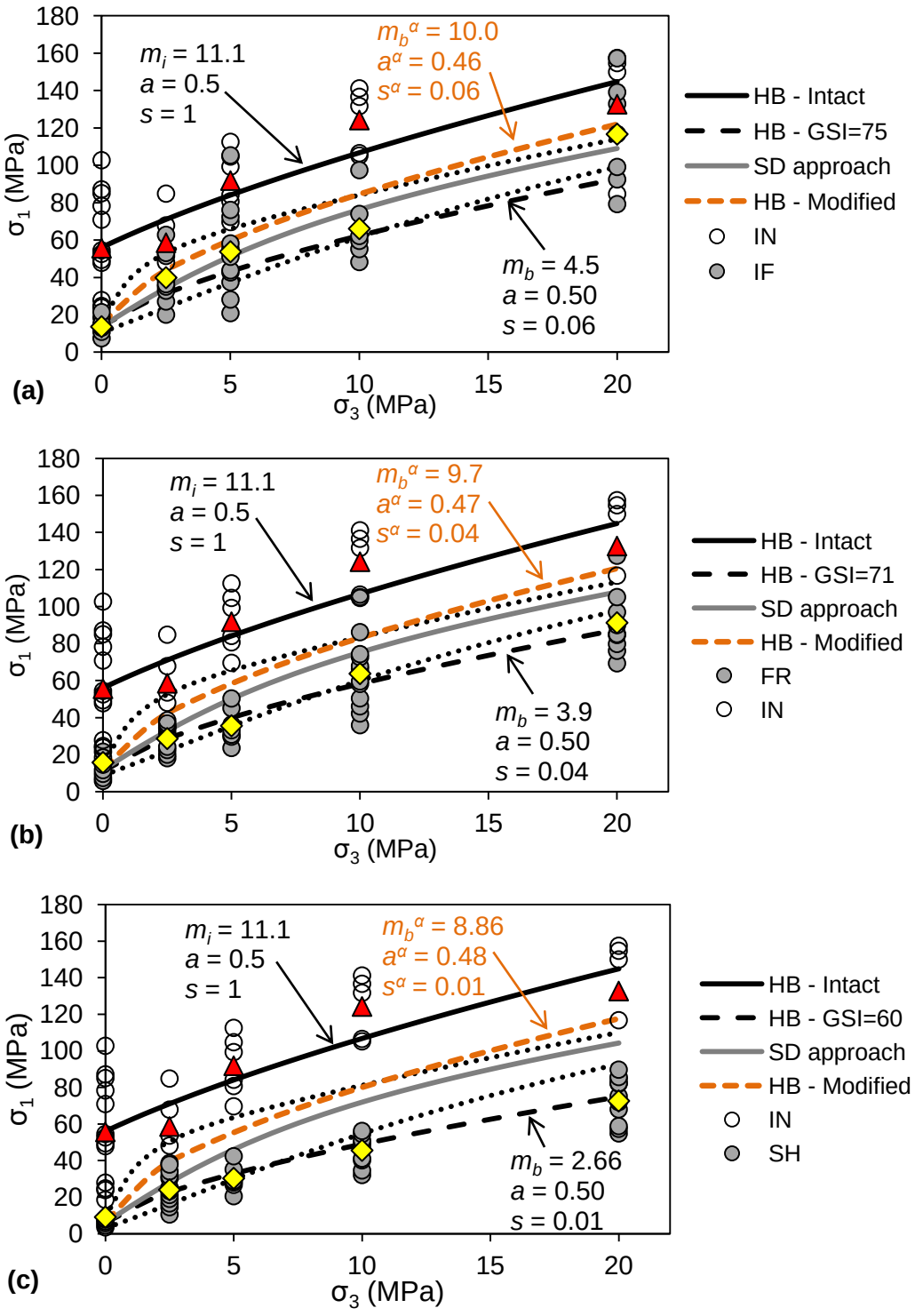

Figure 7-8: Estimation of the confined strength of fractured limestone (Ribacchi, 2000) using the *SD* approach and the *HB* failure criterion using the *GSI*-based and adjusted strength parameters: a) *IN* and *IF* specimens; b) *IN* and *FR* specimens; and c) *IN* and *SH* specimens. The dotted lines show the strength variability estimated using the *SD* approach. Triangles and diamonds indicate average strengths of intact and defected specimens, respectively.

These two approaches, however, overestimate the strength of weaker *FR* specimens, which were probably failed by shearing along joints. It can be concluded that the *GSI*-based approach would significantly underestimate the confined strength of highly interlocked rockmasses, even though it does provide a good fit to the lowest rockmass strength, in which the failure is dominated by shearing along joints. Thus, it follows that the *GSI*-based approach does not provide a representative strength envelope for highly interlocked hard rockmasses.

7.4.3 Jointed Granite

The results of laboratory experiments on intact and artificially jointed granite conducted by Arzua et al. (2014) are shown in Figure 7-9, along with the failure envelopes estimated using the *SD* approach and the *HB* criterion based on the adjusted and *GSI*-based strength parameters.

It should be noted that the conditions of the joints in the jointed granite do not meet with the assumptions on which the proposed approaches are based. The joints in these specimens are persistent and smooth and have a relatively low friction angle of 26° (Alejano et al., 2012). Furthermore, the maximum confinement in these tests is 12 MPa, which is about 10% of the intact rock UCS_i. According to Hoek and Brown (1997), triaxial tests to obtain the failure envelope should be conducted up to a maximum confining pressure of half of the intact rock UCS_i. When this condition is not met, it is likely that the statistically determined m_i value overestimates the true m_i of the intact rock. The m_i value of the intact granite based on the limited confining pressure range was determined to be about 40.

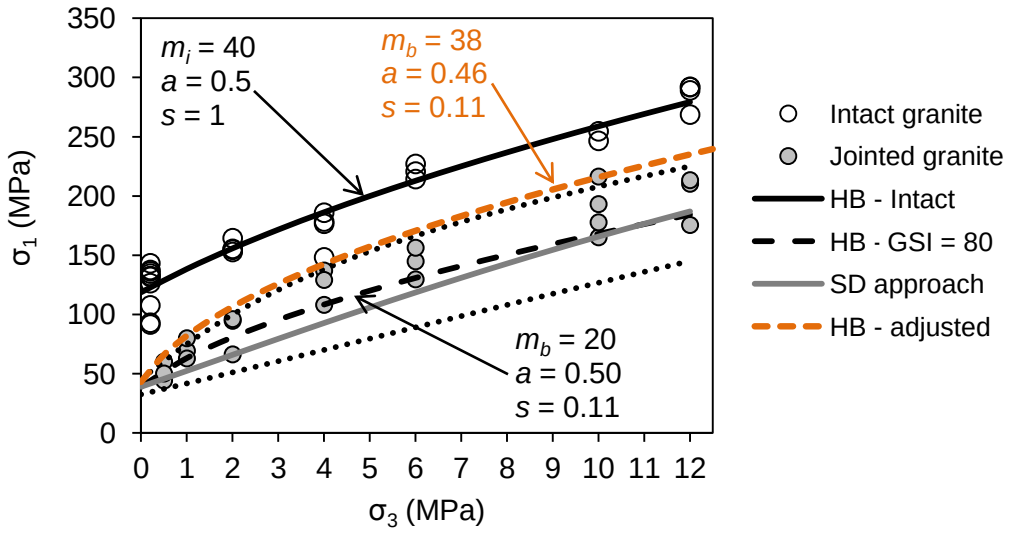

Figure 7-9: Estimation of the confined strength of fractured limestone (Arzua et al., 2014) using the *SD* approach and the *HB* failure criterion using the *GSI*-based and adjusted strength parameters. The dotted lines show the strength variability estimated using the *SD* approach.

Figure 7-9 shows that the *HB* criterion using the *GSI*-based strength parameters reasonably estimate the confined strength of the jointed rockmass. Although the *SD* approach fits to the lower strength limit, the strength variability is very well captured as over 90% of the data points are between the upper and lower bounds.

As can be seen from Figure 7-9, the *HB* criterion using the adjusted strength parameters, however, slightly overestimates the confined strength of the jointed granite. This is interpreted to be due to the overestimation of m_i as a result of conducting triaxial tests up to the low confining pressure of 12 MPa. Had the triaxial tests been conducted up to $UCS_i/2$ = 60 MPa, the m_i value would have been less than 40 and m_b^{α} value would have calculated to be less than 38, and this would have brought the estimated failure envelope closer to the confined strengths of the jointed granite. For example, the *HB* envelope with m_i = 36 and thus a rockmass strength envelope based

on the adjusted m_b^{α} = 34 would fall into the confidence range given by the *SD* approach (dotted lines).

7.5 Discussion on the use of SD approach and adjusted HB strength parameters

In this chapter, two semi-empirical approaches for the estimation of confined strength of highly interlocked jointed rockmasses were developed: 1. the *SD* approach; and 2. the *HB* criterion based on the adjusted *HB* strength parameters. In both approaches, the intact rock triaxial test data and the unconfined compressive strength of the jointed rockmass are assumed to be the known parameters.

While these two approaches were developed based on regression analysis through the same data (as shown in Figure 7-6), they may lead to slightly different estimates of the strength values (as shown in Figure 7-7, Figure 7-8, and Figure 7-9) due to their inherent differences. The *SD* approach is based on the percentage difference between the strengths of intact rock and jointed rockmass, whereas the approach based on the adjusted *HB* strength parameters is related to the the slope of the failure envelope of the intact rock (m_i).

The advantage of the approach based on the adjusted *HB* strength parameters over the *SD* approach is that it can be directly used in the currently available continuum codes, which provide the users with the *HB* failure criterion as one of the criteria for the materials. The *SD* approach, however, can only be used in codes that provide the users with the option of adding user-defined constitutive models. The advantage of the *SD* approach over the approach based on the *HB*

strength parameters is that it can be used for probabilistic analysis and reliability-based design, whereas the approach based on the *HB* strength parameters is purely deterministic.

The concurrent use of both approaches when estimating the confined strength of highly interlocked jointed rockmasses is suggested. In fact, one can use the *SD* approach first to obtain the upper and lower strength limits, and then conduct a series of regression analysis to obtain their representative *HB* strength parameters. This would then allow for probabilistic analysis and reliability-based design of underground excavations using the currently available continuum codes with the *HB* strength parameters adjusted for highly interlocked jointed rockmasses.

7.6 Summary and Conclusions

The results of numerical simulations of highly interlocked rockmass specimens were used and two semi-empirical approaches for the estimation of confined strengths of such rockmasses were developed:

- The first approach is based on the strength degradation of rockmass from intact rock as a function of confinement. This approach, called the Strength Degradation (*SD*) approach for jointed rockmasses, is similar to the *SD* approach previously developed for micro-defected rocks.
- In the second approach, the values of the *HB* strength parameters s, m_b and a were adjusted to s^{α}, m_b^{α} and a^{α} and equations that relate these parameters to the unconfined degradation *Du* were suggested.

These two approaches were examined on the results of published laboratory tests on fractured rocks, which are considered to be analogues for jointed rockamsses. It was found that the confined strengths of jointed rockmasses estimated using the proposed approaches are as good as

and often much better than those estimated using the *HB* criterion with the strength parameters determined using the *GSI*-based equations.

Based on these verifications and the extensive model studies presented in the previous chapters, it can be concluded that both approaches, the *SD* and adjusted *HB* approaches, offer more realistic failure envelopes for confined, highly interlocked, hard rockmasses. Unfortunately, no field data was available to examine the proposed strength envelopes on the failure of confined rockmasses (e.g., highly confined pillars). However, discussions of indirect evidence supporting this conclusion are offered in *Chapter 8* along with some recommendations for future work.

Chapter 8

8 Conclusions, Implications and Future Research

8.1 Summary

In *Chapter 1*, the thesis of this research, that the existing empirical and analytical approaches for strength determination tend to underestimate the confined strength of jointed rockmasses made up of highly interlocked, hard brittle rock blocks and with non-persistent and dilatant joints, is presented. Based on this hypothesis, the primary objective of the research was to develop an approach to estimate the confined strength of such rockmasses and to study the influence of the degree of block interlock on the strength of jointed rockmasses at low and high confinement. For this purpose, the two-dimensional numerical code *PFC2D* with its embedded grain-based model (*GBM*) was used to reproduce the behaviour of a rock specimen with a polygonal grain structure (i.e., grains that are deformable and breakable). The *GBM* was also used to study the influence of various parameters affecting the strength as well as the rock response to loading. Although the focus was on the peak strength of rocks, the immediate post-peak behavior was also simulated.

The main objective of this research was to develop a more reliable but semi-empirical approach to estimate the confined strength of highly interlocked, non-persistently jointed rockmasses. The practical relevance of such an improved method for strength estimation was explained to relate to engineering questions involving strong confined rockmasses, as is often encountered when designing relatively wide (W/H > 1.5) pillars in deep mines or at high extractions ratios.

The following steps were taken to achieve this objective:

- simulation of intact rocks;

- simulation of micro-defected rocks;
- estimation of the confined strength of micro-defected rocks with new semi-empirical equations;
- simulation of defected rocks;
- simulation of jointed rockmasses; and
- estimation of the confined strength of highly interlocked, non-persistently jointed rockmasses with new semi-empirical equations.

The initial numerical analyses conducted for this research were designed to reproduce the results of laboratory experiments on intact and heat-treated (called granulated) Wombeyan marble as reported by Gerrogiannopoulos (1976). It was hypothesized that the granulated marble is an analogue for a highly interlocked, non-persistently jointed rockmass. Based on this hypothesis, a *GBM* was generated and calibrated to the properties of intact and granulated Wombeyan marble. The calibrated grain-based specimens were used to simulate micro-defected rocks, defected rocks and jointed rockmasses. The results of these laboratory test simulations were then used to develop semi-empirical approaches to estimate the confined strength of micro-defected rocks, defected rocks and jointed rockmasses.

In a *GBM*, the smooth-joint contacts are used to simulate grain boundaries and the parallel bonds are used to bond the grain particles together. In calibrating the *GBM* to the properties of Wombeyan marble, the following assumptions were made:

- heating the intact marble affected the mechanical properties of the grain boundaries but not the grains themselves;
- the grain boundaries in the granulated marble have zero tensile strength and cohesion; and

- heating the intact marble had no impact on the frictional properties of the grains and grain boundaries.

Based on these assumptions, all the smooth-joint contacts in the model of intact marble were considered to be cohesive and all the smooth-joint contacts in the model of granulated marble were considered to be purely frictional. Accordingly, the model of intact marble was called the undamaged grain-based specimen and the model of granulated marble was called the fully damaged grain-based specimen. Partially damaged specimens were then simulated by assigning the properties of damaged grain boundaries (frictional smooth-joint contacts) to a number of smooth-joint contacts. The influence of pre-existing damage (frictional grain boundaries) on the failure mode and fracturing processes at the grain and specimen scales were investigated and yielded the following outcomes:

- the amount of pre-existing damage in a rock specimen does not influence the overall failure mode at various levels of confinement;
- at the specimen scale, the failure mode changes from axial splitting at low confinement to shear band formation at high confinement and this is independent of micro-defect density;
- at the grain scale, three modes of failure are opening, combined opening-shearing and direct shearing;
- opening, which occurs along the grain boundaries, is the dominant mode under unconfined condition, while combined opening-shearing occurs at low to medium confinement and direct shearing (which occurs through the grains) is the dominant mode at high confinement;
- as was found by others (e.g., Diederichs, 1999), rock fracturing due to axial loading is initiated by tensile cracking and continued by shear cracking close to the peak stress and in the post peak region;

- grain or grain-boundary tensile cracks are always initiated before grain or grain-boundary shear cracks; and
- the number of shear cracks increases with increasing confinement.

The results of triaxial test simulations on undamaged, partially damaged and fully damaged grain-based specimens were then used to develop a semi-empirical approach for the estimation of the confined strength of micro-defected rocks. In this approach, the strength degradation between intact and micro-defected rocks is related to the level of confinement and the various rock structural characteristics described above. The applicability of this approach was investigated and confirmed on a number of published laboratory tests conducted on intact and damaged rocks.

Next, the size of the calibrated undamaged grain-based specimen was increased and a number of Discrete Fracture Network (*DFN*) models were used to simulate defects. The following conclusions emerged from the analysis of the influence of specimen size on defected rock strength under unconfined condition:

- three known modes of failure of defected rocks (defined as axial splitting, shear failure along discrete defects and combined failure, which includes intact rock and shear on discrete defects) were reproduced and thus shown to be consistent with laboratory observations:
    - axial splitting is the main mode of failure when the defects are nearly perpendicular and parallel to the direction of applied load;
    - shear failure is the main mode of failure when the defects are critically oriented (i.e., parallel to the direction of critical shear stress);
    - combined failure occurs when the defects are inclined but not critically oriented;
- the strength of intact rocks (with no defects) is independent of the specimen size when simulated with frictionless platens;

- the strength of defected rocks where defects are critically oriented is independent of the specimen scale and directly influenced by the defect properties
- the strength of defected rocks with defects that are not critically oriented varies between 45% and 75% of the intact strength.

The fully damaged grain-based specimen, as a model of highly interlocked jointed rockmass, was modified to simulate an interlocked rockmass made up of nearly cubical hard rock blocks (with $UCS_i > 100$ MPa and with two joint sets). The comparison between the results of laboratory test simulations on the highly interlocked and regularly interlocked jointed rockmasses (simply referred to as "interlocked" jointed rockmasses) lead to the following conclusions:

- under unconfined condition, the highly interlocked rockmass exhibits some amount of cohesive strength (i.e., UCS_{rm} = 20 MPa), whereas the unconfined strength of the interlocked rockmass is nearly zero (i.e., UCS_{rm} = 0 MPa);
- the strength of the highly interlocked rockmass increases more rapidly with confinement and exhibits a higher strength at low confinement ($\sigma_3 < \sim UCS_i/10$) than that of the interlocked rockmass;
- at high confinement ($\sigma_3 > \sim UCS_i/10$), the strengths of the two rockmasses formed by hard rock blocks become comparable, especially at very high confining pressures (i.e., 34.5 MPa for the examples shown);
- at low confinement ($\sigma_3 < \sim UCS_i/10$), the failure of highly interlocked rockmass with strong rock blocks involves the opening of blocks at their boundaries as well as some intra-block fracturing. At this confinement level, the interlocked rockmass fails because the blocks along their frictional boundaries begin to slide with no intra-block fracturing; and
- at high confinement ($\sigma_3 > \sim UCS_i/10$), the failure of both rockmasses involves intra-block fracturing, although this is more pronounced in the highly interlocked rockmass.

The results of the triaxial test simulations on the highly interlocked rockmass specimens with various degrees of joint persistence mentioned above were then used to develop two semi-empirical approaches for estimating the confined strength of such rockmasses. The first approach is based on the strength degradation of the jointed rockmass from the intact rock. This approach, called the Strength Degradation (*SD*) approach for jointed rockmasses, is similar to that developed for micro-defected rocks. The second approach is based on adjusting the *HB* strength parameters (called s^{α}, a^{α} and $m_b{}^{\alpha}$) to extend the applicability of the *HB* criterion to highly interlocked, non-persistently jointed rockmassess. In this approach, the adjusted $m_b{}^{\alpha}$ exceeds the original m_b and the adjusted a^{α} is less than the original a obtained from the *GSI*-based equations.

These two approaches can be used in situations where the unconfined and confined strengths of the intact rock are known and the unconfined strength of the jointed rockmass can be estimated using one of the currently available empirical approaches or by back-analysis from the rock behaviour at low confinement (near excavation walls). The application of these approaches is constrained to highly interlocked, non-persistently jointed rockmasses made up of hard brittle rock blocks and joints that are dilatant (e.g., when the equivalent joint friction angle is typically greater than 40°).

8.2 Conclusions

This section includes a brief description of the major findings and key contributions:

- The currently available empirical methods, mainly developed from civil engineering cases at relatively shallow depths (< 1000 m) and from observations of rockmass behavior near excavation boundaries (i.e., low confinement), cannot be used to estimate the confined strength of highly interlocked, non-persistently jointed rockmasses.

- The *HB* failure criterion, which can be used to estimate both the unconfined and confined strengths of jointed rockmasses were originally developed for the design of underground openings in poorly interlocked, persistently jointed and weak rockmasses.
- The analysis of the results of laboratory experiments on damaged and defected rocks showed that the strengths of these specimens under unconfined condition are lower than those of intact specimens. This strength can be as little as 10% or as high as 80% of UCS_i, depending on the density and orientation of defects relative to the direction of applied load.
- The strengths of damaged and defected specimens increase more rapidly than those of intact rock as confinement increases. In fact, in the principal stress space, the initial equivalent friction angle of damaged and defected rocks (i.e., $\phi_e = \phi_b + i$) can be as high as 50° to 60° when $\sigma_3 < \sim UCS_i/10$. At high confinement, when $\sigma_3 > \sim UCS_i/10$, the failure envelope tends to approach the equivalent friction angle of the intact rock, which typically ranges between 10° and 35°.
- The *GBM* can be used to simulate brittle failing rocks with very low tensile to compressive strength ratios (i.e., $\sigma_t/UCS_i < 0.05$), non-linear strength envelopes and high friction angles. The *GBM* can also be used to simulate highly interlocked, non-persistently jointed rockmasses.
- The rapid increase in the rock strength with increasing confinement, observed in the laboratory experiments conducted on damaged and defected rocks can be simulated using the *GBM*.
- The *SD* approach for micro-defected rocks can be used to estimate the confined strength of such rocks in situations where the unconfined and confined strengths of the intact rock (σ_{ci} and σ_{1i}) and the unconfined strength of the micro-defected rock (UCS_d) are known. The following equations are applicable within the limitations described above (refer to *Chapter 4* for the description of the parameters):

$$\sigma_{1d} = \sigma_{1i} \times [1 - (DP/100)]$$ Equation 8-1

$$DP = (Du - Dc)e^{[100(-\sigma_3/\sigma_{ci})/c]} + Dc$$ Equation 8-2

$$Du = [(\sigma_{ci} - UCS_d)/\sigma_{ci}] \times 100$$ Equation 8-3

$$Dc = -17.3e^{-0.017D_u} + 17.3$$ Equation 8-4

$$c = 10.8e^{-0.055D_u} + 4.5$$ Equation 8-5

- The *SD* approach for micro-defected rocks (above equations) can also be used to estimate the confined strength of moderately defected rocks consisting of cohesive and rough defects.
- The strength of rock specimen with no defects is independent of scale. The strength of defected rocks may increase or decrease depending on the defect orientation relative to the applied loading direction when the size of the specimen is increased.
- The interlock is defined as the constraints limiting the kinematic freedom of rock blocks, which reduces the ability of the blocks to rotate and slide along each other. Factors influencing the degree of interlock in a jointed rockmass include block shape, block boundary (joint) roughness and persistence.
- The *SD* approach for jointed rockmasses can be used to estimate the confined strength of highly interlocked, non-persistently jointed rockmasses made up of hard brittle rock blocks and joints that are rough and dilatant, in situations where the unconfined and confined strengths of the intact rock (σ_{ci} and σ_{1i}) and the unconfined strength of the jointed rockmass (UCS_{rm}) are known. The following equations are applicable within the limitations described above (refer to *Chapter 7* for the description of the parameters):

$$\sigma_{1rm} = \sigma_{1i} \times [1 - (DP/100)]$$ Equation 8-6

$$DP = (Du - Dc)e^{[100(-\sigma_3/\sigma_{ci})/c]} + Dc$$ Equation 8-7

$$Du = [(\sigma_{ci} - UCS_{rm})/\sigma_{ci}] \times 100$$ Equation 8-8

$$Dc = -59\, e^{-0.007Du} + 59$$ Equation 8-9

$$c = 50\, e^{-0.47Du} + 7.1$$ Equation 8-10

- The equations based on the *GSI* system for determining the *HB* strength parameters *a* and m_b should not be used to estimate the confined strength of highly interlocked, non-persistently jointed rockmasses.
- The *HB* strength parameters were adjusted for highly interlocked, non-persistently jointed rockmasses and labeled s^a, ${m_b}^a$ and a^a. It was found that in such rockmasses, the value of ${m_b}^a$ is greater than that of the *GSI*-based m_b and that the value of a^a is lower than that of the *GSI*-based *a*. The following equations are suggested to obtain the *HB* strength parameters for highly interlocked, non-persistently jointed rockmasses:

$$s^\alpha = [0.01Du^2 - 2Du + 100]/100$$ Equation 8-11

$${m_b}^\alpha = m_i \times [-0.007Du^2 + 0.4Du + 100]/100$$ Equation 8-12

$$a^\alpha = [0.002Du^2 - 0.2Du + 50]/100$$ Equation 8-13

8.3 Implications for Pillar Design

With the hypothesis advanced in this thesis, it follows that the confined strength of highly interlocked rockmasses is underestimated by the inappropriate use of the *GSI*-based equations (Equation 2-16, Equation 2-17 and Equation 2-18) that were developed for poorly interlocked, persistently jointed and weak rockmasses. The results of this research therefore suggest that the confined rockmass strength may be higher when the rockmass in question is highly interlocked

and confined. The specific implications for the estimation of pillar strength in such conditions are briefly discussed next with the elaboration on the findings presented by Kaiser et al. (2011).

Based on the hypothesis that the strength degradation of a jointed rockmass at high confinement is less than that estimated using the original *GSI* approach, Kaiser et al. (2011) proposed an *s*-shaped failure criterion for massive to moderately jointed rockmasses, based on a degradation logic that is a function of confinement. They introduced a confinement-dependent *GSI'*, which replaces *GSI* in Equation 2-16, Equation 2-17 and Equation 2-18 to produce confinement-dependent values of *s*, m_b and *a*. The value of *GSI'* is obtained using the following equation:

$$GSI' = f(\sigma_3, GSI, \sigma_{ci}) = \frac{M - \frac{M}{100}GSI}{1 + e^{(-\sigma_3 + \sigma_{ci}/10)}} + GSI \qquad \text{Equation 8-14}$$

where, *M* is a constant that controls the strength degradation at high confinement ($\sigma_3 > \sim UCS_i/10$). Kaiser and Kim (2008) used an *M* value of 80 in their analysis, although they mentioned that such a value is hypothetical and was chosen in the absence of supporting data. Figure 8-1a and b compare the strength envelopes obtained from the *GSI*- and *GSI'*-based equations for *GSI* values ranging from 40 to 100. As can be seen from this figure, at low confinement ($\sigma_3 < \sim UCS_i/10$), the two approaches provide identical strength envelopes. However, at high confinement ($\sigma_3 > \sim UCS_i/10$), the rockmass strength estimated using the *GSI'*-based equation (*s*-shaped criterion) is less degraded from the intact rock strength with a *GSI* of 100 when compared to that estimated using the original *GSI*-based equations.

Kaiser et al. (2011) investigated the impact of the *s*-shaped criterion over the original *GSI*-based equations on the estimated pillar strength in massive to moderately jointed rockmasses. They

simulated pillars with various width-to-height ratios (0.2 to 3) using a software based on the Boundary Element Method with elastic properties and calculated the stresses inside the pillars. They plotted the calculated elastic stresses on the principal stress space along with the *HB* failure criterion for the intact rock and the rockmass strength envelopes determined using the *GSI*- and *GSI'*-based equations (for *GSI* = 40). An example of this analysis for a pillar with a width-to-height ratio of 0.5 is shown in Figure 8-2a.

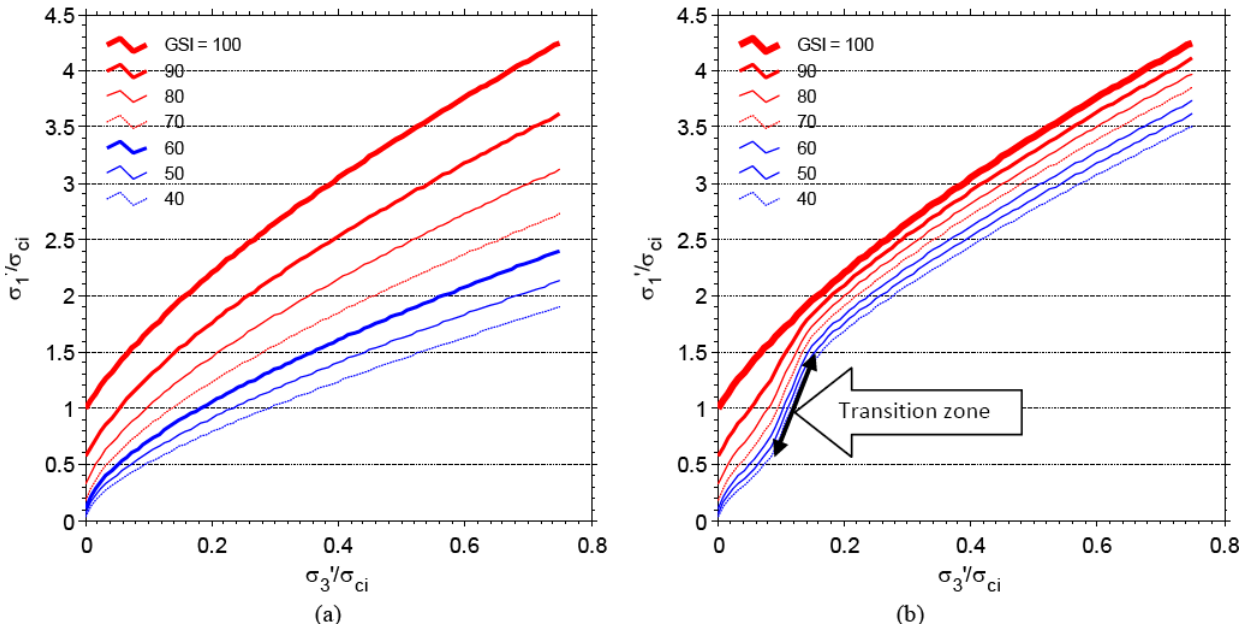

Figure 8-1: Strength envelopes for rockmasses calculated based on: a) the original *GSI*-based equations; b) the *GSI'*-based equation (*s*-shaped criterion).

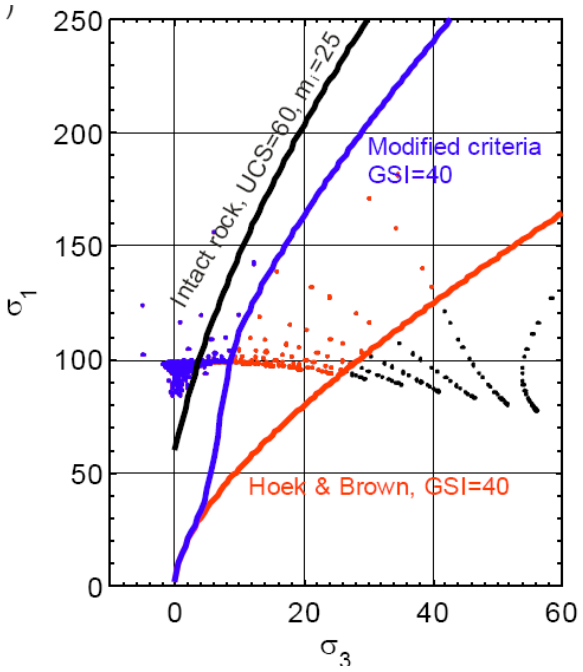

(a)

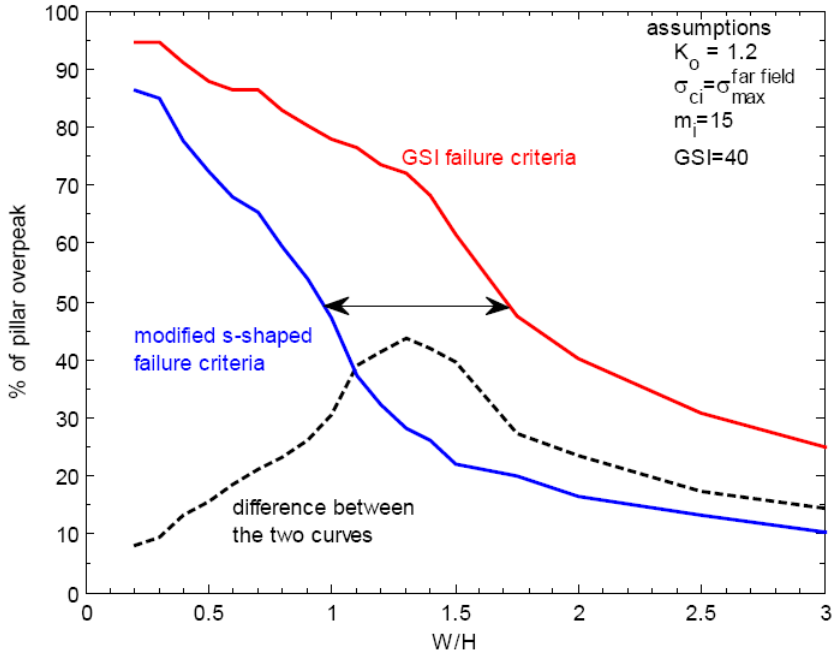

(b)

Figure 8-2: a) Failure envelopes of intact rock and rockmass and calculated stresses inside the pillar with a width-to-height ratio of 0.5; b) comparison of the percentage of pillar stresses over the peak for the two criteria as a function of pillar width-to-height ratio.

Kaiser et al. (2011) then calculated the percentage of the stresses over the peak strength envelopes obtained from the two approaches for all the pillar cases. The summary of this analysis is presented in Figure 8-2b, which plots the percentage of the stresses over the peak for pillar width-to-height ratios of 0.2 to 3. It can be seen that the results of the two failure criteria are significantly different, particularly in pillars with the width-to-height ratios of 1.0 to 1.8. Kaiser et al. (2011) elaborate that if the percentage of stresses over the peak envelope is considered as a proxy for pillar stability, a pillar with a width-to-height ratio of 1.0 analyzed while considering the *s*-shaped failure criterion would be found to be in the same relative state of stability as a pillar with a width-to-height ratio of 1.7, considering the *GSI*-based equations (see arrow in Figure 8-2b).

The analysis performed in *Chapter 7* is summarized in Figure 8-3. As can be seen in this figure, when the *GSI*-based equations are used to match the strength of the highly interlocked synthetic rockmass specimen at zero confinement, the confined strength of the highly interlocked synthetic rockmass specimen is underestimated by a factor of up 1.5, depending on the level of confinement. The use of $m_b^{\alpha} = 4.75$ instead of $m_b = 1.46$ and $a^{\alpha} = 0.46$ instead of $a = 0.5$ was required to fit the strength of highly interlocked synthetic rockmass. This is consistent with the approach suggested by Kaiser et al. (2011).

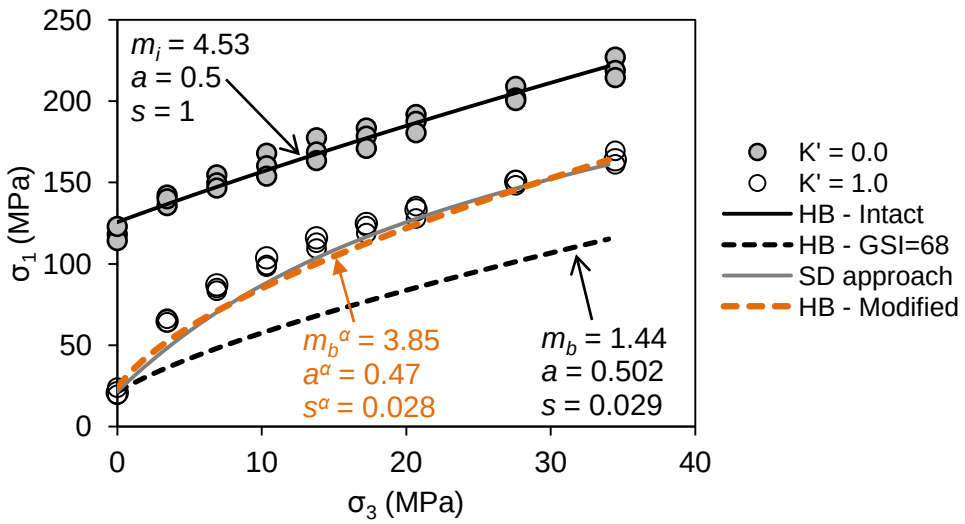

Figure 8-3: Comparison between the *HB* strength envelopes determined using the *GSI*-based and adjusted strength parameters.

In Figure 8-3, the strength differences between the *HB* strength envelope obtained using the *GSI*-based equations (i.e., black dashed line) and the envelope for the highly interlocked rockmass (i.e., red dashed line) obtained using the adjusted strength parameters becomes most relevant for the design of wide pillars and abutments at great depths (e.g., > 1500 m). As discussed by Valley et al. (2011) and Kaiser et al. (2011), using a strength envelope that properly captures the strength increase with confinement will lead to an optimized design of pillars. On the other hand, if the strength of a pillar core is underestimated (i.e., by applying the *GSI*-based equations developed for poorly interlocked, persistently jointed and weak rockmasses), they may not yield and accumulate stress, which will make them more prone to bursting.

For pillar design in highly interlocked jointed rockmasses, it was necessary to develop the means to obtain the failure envelope that better captures their rapid strengthening effect due to confinement. The strength degradation logic inherent in the *SD* approach and the adjusted *HB* strength parameters is consistent with those suggested by Kaiser et al. (2011) and seem to be

suitable to assess the strength of pillar cores. Further calibration studies need to be carried out with the use of these approaches to investigate their impact on mine pillar stability in such rockmasses, as is suggested in the next section. The discussion and analysis presented above suggest that pillar design based on current empirical approaches may be adversely conservative and thus not optimal from an economic perspective. This aspect is of particular interest for block caves where drawpoint spacing may have a significant impact on cave propagation, and economics.

8.4 Future Research

Three main areas need additional research to enhance the understanding of factors influencing the strength of jointed rockmasses and to more realistically simulate brittle fracturing and failure of rocks at various scales (i.e., laboratory specimen, rock block and rockmass scales):

- field mapping and rockmass behavior monitoring;
- laboratory experiments including triaxial tests on defected rocks and physical models of jointed rockmasses; and
- numerical simulations including triaxial tests on jointed rockmasses.

8.4.1 Field Mapping and Rockmass Behavior Monitoring

The following specific recommendations are offered for field mapping and rockmass behavior monitoring:

- *Rockmass characterization using conventional and novel field mapping techniques*: Face mapping, photogrammetry and 3D laser scanning can be used to extract information such as joint roughness, joint persistence and block shape. Such information is relevant as it will make it possible to determine the degree of interlock between rock blocks, and can

be used to generate appropriate *DFN* models of jointed rockmasses for numerical modeling.

- *Back analysis of rockmass strength by monitoring the deformation, fracturing process and failure of jointed rockmasses*: Various instruments and techniques can be used to monitor slender and wide pillars to investigate the influence of confinement on rockmass strength. Some of these techniques include logging holes drilled into the pillars (e.g., borehole camera or optical and acoustic televiewers) to identify joint conditions and pillar fracturing processes. Installing stress cells to monitor stress changes inside the pillar cores and monitoring strain changes within the pillars (e.g., borehole extensometer, inclinometer, fiber optics) are also valid monitoring techniques. For this purpose, it is extremely important to have a sound understanding of the stress paths the pillars experience. Because of the difficulties inherent to making point measurements from stress change cells, a combination of deformation and stress back-analysis may have to be adopted to allow for optimal understanding of the stress paths.

8.4.2 Laboratory Testing

Laboratory tests to investigate the influence of degree of interlock on rockmass strength are:

- *Direct shear tests on intact rock and rock joints*: The purpose of direct shear tests is to investigate the factors influencing the rapid shear strengthening effect that comes with increasing the normal stress (such as joint roughness and persistent) and the shear strength degradation of a rock joint from an intact rock as a function of normal stress.
- *Triaxial tests on physical models of jointed rockmasses*: The 3D printing technology (Jiang and Zhao, 2014) can be used to build physical models of rockmasses with various degrees of interlock (i.e., block shape, joint persistent and joint roughness) and to investigate the influence of these parameters on the confinement-dependent strength degradation of jointed rockmasses.

However, before proceeding with further modeling, it will be necessary to develop a material that truly reflects hard, brittle rocks. Most of the cemented or porous model materials (such as

plaster of Paris) are not suitable because they tend to collapse under hydrostatic conditions. Consequently, the intact material behaviour tends to be weaker than that of the individual model blocks, thus leading to conflicting results at high confinement.

8.4.3 Numerical Modeling

It is suggested that numerical modeling be used as a tool to confirm the results of field mapping and rockmass behavior monitoring, to develop a systematic approach for back analyses of rockmass strength and to improve the pillar design chart. The specific recommendations for future research in this regard are as follows:

8.4.3.1 Model tool improvements

- *Verification of the dilation angle in the smooth-joint contact in PFC*: It is possible to consider a dilation angle for the smooth-joint contacts in *PFC*, although such an option has not widely used by numerical modelers. It is therefore suggested to systematically investigate the applicability of the smooth-joint dilation angle for simulating rough joints.
- *Simulation of direct shear tests on intact rock and rock joints*: Similar to the proposed laboratory tests, the goal of these simulations would be to investigate the influence of joint roughness and persistence on the shear strength degradation of rock joints from intact rocks. For this purpose, rough joints can be explicitly simulated using the smooth-joint contact in *PFC*.
- *Simulation of the rock fracturing process using the flat-jointed contact model in PFC*: Recently, Potyondy (2012) developed a bond model in *PFC* called the flat-jointed contact and was able to overcome the shortcomings of conventional bond models such as contact and parallel bonds in *PFC*. It is recommended to use this bond model instead of the parallel bond inside the grains in the *GBM* and investigate its applicability in simulating the fracturing processes of brittle rocks and the strength of jointed rockmasses.

8.4.3.2 Numerical modeling for further development of the *SD* approach:

- *Three-dimensional simulation of jointed rockmasses*: Fracture initiation and propagation is a three-dimensional phenomenon. It is suggested that the findings of this research can be improved by simulating jointed rockmasses using a 3D *DEM* code (e.g., *PFC3D*). This would allow for a more realistic simulation of rock block shape and, therefore, their 3D interlocking effects on the rockmass strength.
- *Explicit simulation of rock block defects in a jointed rockmass*: As investigated in this research, the defects can reduce the strength of rock blocks and can therefore have a significant impact on the strength of jointed rockmasses under different stress conditions. It is desirable to explicitly simulate rock block defects in models of jointed rockmasses and expand the *SD* approach so that the strength degradation of a jointed rockmass is not only a function of confinement but also a function of rock block defects.
- *Consideration of joint friction angle in semi-empirical approaches*: In this thesis, the semi-empirical approaches developed for the estimation of rockmass strength were based on the simulation of jointed rockmasses with a constant joint friction angle (i.e., 50° degrees). It is desirable to conduct similar analyses with various joint friction angles and expand the *SD* approach so that the strength degradation of a rockmass is not only a function of confinement but also a function of joint friction angle.
- *Investigation of the influence of defects on the confined strength of rock blocks*: In this research, the strength of defected rock blocks was only investigated under unconfined condition. This was mainly due to the extensive computation time required to simulate confined tests on models of defected rock blocks. The most recent version of *PFC* (v.5) allows for parallel processing and this can significantly reduce the computation time. It is therefore suggested to use the most recent version of *PFC* and investigate the influence of defects and their roughness on the confined strength of rock blocks and their strength degradation from intact rocks.
- *Determination of degree of interlock for jointed rockmasses*: In this research, two rockmasses with different joint systems were simulated to demonstrate the influence of degree of interlock on rockmass strength under unconfined and connfined conditions. Dershowitz and Einstein (1988) described various joint system models in jointed

rockmasses such as orthogonal model, Baecher disk model, Veneziano model and Dershowitz model. In fact, these joint system models are the basis for most of the *DFN* codes, and may represent different degrees of interlock in a jointed rockmass. It is suggested that the influence of these joint system models and therefore their degrees of interlock on rockmass strength be investigated by the integrating three-dimensional *DFN* and *DEM* codes. Further research on the quantification of the degree of interlock for rockmasses with various joint system models based on the results of field mapping and borehole logging would be desirable.

- *Investigation of the application of fractal theory for the estimation of rockmass strength*: A fractal is a natural phenomenon or a mathematical set that exhibits a repeating pattern that displays at every scale. The concept of fractals has proven to be a usefull way of describing the statistics of naturally occurring geometrics (Xie, 1993). Future research is suggested to include an investigation on the application of the fractal theory for the estimation of the strength of jointed rockmasses at the field scale from the strengths of laboratory scale rock specimens.

8.4.3.3 Simulation of rock pillars:

- *Investigations concerning the influence of block interlock on pillar strength*: *PFC2D* and *PFC3D* (or any *DEM* code) can be used to simulate rock pillars of various width-to-height ratios. The objective is to investigate the influence of the degree of interlock (joint roughness, joint persistence and block shape) and rock block defects on the pillar strength. The results of such analyses can be used to improve the pillar stability chart.
- *Investigations concerning the influence of excavation-induced damage on pillar strengths*: The excavation-induced damage can be simulated in *PFC2D* and *PFC3D* by first excavating the drifts on the two sides of the future pillar under stress to allow for stress redistribution and damage accumulations inside the pillars, and then loading the pillars axially until failure. Such simulations can be conducted on pillars with various width-to-height ratios and under various *in situ* stress ratios.

References

AASHTO. 1996. Standard Specifications for Highway Bridges. American Association of State Highway and Transportation Officials, Washington, DC.

Alejano L.R., Gonzalez J. & Muralha J. 2012. Response by the authors to S.R. Hencher's discussion of the paper "Comparison of different techniques of tilt testing and basic friction angle variability assessment", *Rock Mechanics and Rock Engineering*, 45(6): 1141-1143.

Amadei B. 1988. Strength of a regularly jointed rock mass under biaxial and axisymmetric loading conditions. *International Journal of Rock Mechanics and Mining Science*, 25: 3-13.

Arzua J., Alejano L.R. & Walton G. 2014. Strength and dilation of jointed granite specimens in servo-controlled triaxial tests. *International Journal of Rock Mechanics and Mining Science*, 69: 93-104.

Aydan O. & Dalgic S. 1998. Prediction of deformation behavior of 3-lanes Bolu tunnels through squeezing rock of North Anatolian fault zone (NAFZ). In: *Proc. of regional symposium on sedimentary rock engineering*, Taipei, 228-233.

Bahaaddini M., Sharrock G. & Hebblewhite B.K. 2011. A comparison of physical and numerical experiments on artificial jointed rock masses using PFC3D. In: *Proc. Continuum and Distinct Element Numerical Modeling in Geomechanics*, Australia, 10p.

Bahrani N. & Kaiser P.K. 2013. Strength degradation of non-persistently jointed rockmass. *International Journal of Rock Mechanics and Mining Science*, 62: 28-33.

Bahrani N., Kaiser P.K. & Valley B. 2014. Distinct element method simulation of an analogue for a highly interlocked, non-persistently jointed rockmass. *International Journal of Rock Mechanics and Mining Science*, 71: 117-130.

Bahrani N., Potyondy D.O. & Pierce M. 2012c. Simulation of Brazilian test using PFC2D grain-based model. In: *Proc. 21st Canadian Rock Mechanics Symposium*, Edmonton, Canada, 9p.

Bahrani N., Purvance M. & Emam S. 2013. A comparison between 2D and 3D bonded-particle models for rock. In: *Proc. 47th US Rock Mechanics/Geomechanics Symposium,* San Francisco, USA.

Bahrani N., Valley B. & Kaiser P.K. 2011b. Discrete element modeling of drilling induced core damage and its influence on laboratory properties of Lac du Bonnet granite, In: *Proc. 45th US Rock Mechanics Symposium*, San Francisco, 9p.

Bahrani N., Valley B. & Kaiser P.K. 2012b. Influence of borehole orientation on in-situ stress estimation using the Kaiser effect. *Proc. 6th International Conference on Mass Mining*, Sudbury, Canada, 9p.

Bahrani N., Valley B., Kaiser P.K. & Pierce M. 2011a. Evaluation of PFC2D grain-based model for simulation of confinement-dependent rock strength degradation and failure processes. In: *Proc. 45th US Rock Mechanics Symposium*, San Francisco, 11p.

Bahrani N., Valley B., Maloney S. & Kaiser P.K. 2012a. Numerical investigation of the influence of borehole orientation on drilling-induced core damage. In: *Proc. EUROCK2012*, Sweden, 13p.

Barton N. & Pandey S.K. 2011. Numerical modeling of two stopping methods in two Indian mines using degradation of c and mobilization of ϕ based on Q-parameters, *International Journal of Rock Mechanics and Mining Science*, 48: 1095-1112.

Barton N. 1973. Review of a new shear strength criterion for rock joints. *Engineering Geology*, (7): 287-332.

Barton N. 2002. Some new Q-value correlations to assist in site characterization and tunnel design. *International Journal of Rock Mechanics and Mining Science,* 39(2): 185-216.

Barton N.R., Lien R. & Lunde J. 1974. Engineering classification of rock masses for the design of tunnel support. *Rock Mechanics*, 6: 189-239.

Bewick R.P., Amann F., Martin C.D. & Kaiser P.K. 2015a. Interpretation of UCS test results for engineering design. In: *Proc. 13th International ISRM Congress*, Montreal.

Bewick R.P., Kaiser P.K. & Bawden W.F. 2015c. DEM simulation of direct shear: 2. Grain boundary and mineral grain strength component influence on shear rupture. *Rock Mechanics and Rock Engineering*, DOI: 10.1007/s00603-013-0494-4.

Bewick R.P., Kaiser P.K. & Valley B. 2011. Interpretation of triaxial testing data for estimation of the Hoek-Brown strength parameters m_i. In: *Proc. 45th US Rock Mechanics Symposium*, San Francisco.

Bewick R.P., Kaiser P.K., Bawden W.F. & Bahrani N. 2015b. DEM simulation of direct shear: 1. Rupture under constant normal stress boundary conditions. *Rock Mechanics and Rock Engineering*, DOI 10.1007/s00603-013-0490-8.

Bieniawski Z. & Vanheerden W. 1975. The significance of in situ tests on large rock specimens. *International Journal of Rock Mechanics and Mining Science & Geomechanics Abstract*, 12(4): 101-113.

Bieniawski Z. T. 1973. Engineering classification of jointed rock masses. *Transaction of South African Institute for Civil Engineers*, 15: 335-344.

Bieniawski Z. T. 1976. Rock mass classifications in rock engineering. In: *Proc. of Symposium on Exploration for Rock Engineering*, 1: 97-106.

Bieniawski Z.T. 1967. Mechanism of brittle fracture of rock: Part 1 – theory of the fracture process. *International Journal of Rock Mechanics and Mining Science & Geomechanics Abstract*, 4(4): 395-404.

Bieniawski Z.T. 1968. The effect of specimen size on compressive strength of coal. *International Journal of Rock Mechanics and Mining Science*, 5: 325-335.

Bieniawski Z.T. 1979. The geomechanics classification in rock engineering applications, In: *Proc. of Fourth Congress of the International Society for Rock Mechanics*, 2: 41-48.

Bieniawski Z.T. 1988. The rock mass rating (RMR) system (geomechanics classification) in engineering practice. *Rock Classification Systems for Engineering Purposes*, ASTM STP 984, Louise Kirkaldie, Ed., American Society for Testing and Materials, Philadelphia, pp. 17-34.

Bieniawski Z.T. 1989. Engineering Rock Mass Classification. New York: Wiley.

Bieniawski ZT & Bernede MJ. 1979. Suggested methods for determining the uniaxial compressive strength and deformability of rock materials. *International Journal of Rock Mechanics and Mining Science & Geomechanics Abstract*, 16: 138-40.

Blanks R.F. & McNamara C.C. 1935. Mass concrete tests in large cylinders. *Journal of American Concrete Institute*, 31: 280-303.

Brace W.F., Paulding B.W. & Scholz C.H. 1966. Dilatancy in the fracture of crystalline rocks, *Journal of Geophysical Research*, 71(16): 3939-3953.

Brady B.H.G. & Brown E.T. 2007. Rock Mechanics for Underground Mining, Springer Science & Business Media, 628p.

Brown E.T. & Trollope D.H. 1970. Strength of a model of jointed rock. *Journal of the Soil Mechanics and Foundation Division*, 96: 685-704.

Brown E.T. 1970. Strength of models of rock with intermittent joints. *Journal of the Soil Mechanics and Foundation Division*, 96: 1935-1949.

Brown W.S. & Swanson S.R. 1970. Influence of load path and state of stress on failure strength and stress-strain properties of rocks, Report UTEC 70-025, University of Utah, Mechanical Engineering Department.

Cai M. 2011. Rock mass characterization and rock property variability considerations for tunnel and cavern design, *Rock Mechanics and Rock Engineering*, 44(4): 1-21.

Cai M., Kaiser P.K., Tasaka Y. & Minami M. 2007. Determination of residual strength parameters of jointed rock masses using the GSI system. *International Journal of Rock Mechanics and Mining Science*, 44(2): 247-265.

Cai M., Kaiser P.K., Uno H., Tasaka Y. & Minami M. 2004. Estimation of rock mass deformation modulus and strength of jointed hard rock masses using the GSI system. *International Journal of Rock Mechanics and Mining Science*, 41(1): 3-19.

Carter T.G., Diederichs M.S. & Carvalho J.L. 2008. Application of modified Hoek-Brown transition relationships for assessing strength and post yield behavior at both ends of the rock competence scale. *The Journal of The Southern African Institute of Mining and Metallurgy*, 108: 325-338.

Chiu C., Wang T., Weng M. & Huang T. 2013. Modeling the anisotropic behavior of jointed rock mass using a modified smooth-joint model. *International Journal of Rock Mechanics and Mining Science*, 62: 14-22.

Cho N., Martin C.D. & Sego D.C. 2007. A clumped particle model for rock. *International Journal of Rock Mechanics and Mining Science*, 44: 997-1007.

Cundall P.A. & Strack O.D.L. 1979. A discrete numerical model for granular assemblies. *Geotechnique,* 29(1): 47-65.

Cundall P.A. 1971. A computer model for simulating progressive, large scale movements in blocky rock systems. In: *Proc. Symposium of International Society for Rock Mechanics*, Nancy, No. 8.

Darlington W.J., Ranjith P.G. & Choi S.K. 2011. The effect of specimen size on strength and other properties in laboratory testing of rock and rock-like cementitious brittle materials. *Rock Mechanics and Rock Engineering*, 44: 513-529.

Deere D.U. 1964. Technical description of rock cores for engineering purposes. *Rock Mechanics & Rock Engineering*, 1: 107-116.

Dershowitz W.S. & Einstein H.H. 1988. Characterizing rock joint geometry with joint system models, *Rock Mechanics and Rock Engineering*, 21: 21-51.

Di S.j., Xu W.Y. & Ning Y. 2011. Macro-mechanical properties of columnar jointed basaltic rock masses. *Journal of Central South University of Technology*, 18 (6): 2143-2149.

Diederichs M.S. 1999. Instablity of hard rock masses; the role of tensile damage and relaxation, PhD thesis, University of Waterloo, 617p.

Diederichs M.S. 2003. Manuel Rocha Medal Recipient: Rock Fracture and Collapse under Low Confinement Conditions. *Rock Mechanics & Rock Engineering*, 36 (5): 339-381.

Dinc O.S., Sonmez H., Tunusluoglu C. & Kasapolgu K.E. 2011. A new general empirical approach for the prediction of rock mass strengths of soft to hard rock masses. *International Journal of Rock Mechanics and Mining Science*, 48: 650-665.

Dusseault M.B. & Morgenstern N.R. 1978. Shear strength of Athabasca Oil Sands, *Canadian Geotechnical Journal*, 15: 16-38.

Dusseault M.B. & Morgenstern N.R. 1979. Locked sands, *Quarterly Journal of Engineering Geology and Hydrogeology*, 12: 117-31.

Eberhardt E. 2001. Numerical modeling of three-dimensional stress rotation ahead of an advancing tunnel face. *International Journal of Rock Mechanics and Mining Science*, 38: 499-518.

Eberhardt E., Stead D. & Stimpson B. 1999. Effects of sample disturbance on the stress-induced microfracturing characteristics of brittle rock. *Canadian Geotechnical Journal*, 36: 239-250.

Einstein H.H. & Hirschfeld R.C. 1973. Model studies in mechanics of jointed rock. *Journal of the Soil Mechanics and Foundation Division*, 99: 229-48.

Einstein H.H. 1993. Modern developments in discontinuity analysis, the persistence-connectivity problem. *Comprehensive rock engineering*. Pergamon Press, Oxford, 193-213.

Einstein H.H., Veneziano D., Baecher G.B., & O'Reilly K. J. 1983. The effect of discontinuity persistence on rock slope stability. *International Journal of Rock Mechanics and Mining Sciences & Geomechanics Abstracts*. 20 (5): 227-236.

Elmo D. and Stead D. 2009. An integrated numerical modeling-discrete fracture network approach applied to the characterization of rock mass strength of naturally fractured pillars. *Rock Mechanics & Rock Engineering*.

Erarsalan N. & Williams D.J. 2012. Investigating the effect of cyclic loading on the indirect tensile strength of rocks. *Rock Mechanics & Rock Engineering*, 45: 327-40.

Esmaieli K., Hadjigeorgiou J. & Grenon M. 2010. Estimating geometrical and mechanical REV based on synthetic rock mass models at Brunswick Mine, *International Journal of Rock Mechanics and Mining Science,* 47: 915-26.

Exadaktylos G.E. & Vardoulakis I. 2001. Microstructure in linear elasticity and scale effects: A reconsideration of basic rock mechanics and rock fracture mechanics, *Tectonophysics*, 335: 81-109.

Fang Z. & Harrison J.P. 2001. A mechanical degradation index for rock. *International Journal of Rock Mechanics and Mining Science,* 38: 1193-1199.

Gatelier N., Pellet F., Loret B. 2002. Mechanical damage of an anisotropic porous rock in cyclic triaxial tests, *International Journal of Rock Mechanics and Mining Science,* 39: 335-54.

Gerogiannopoulos N.G. & Brown E.T. 1978. The critical state concept applied to rock. *International Journal of Rock Mechanics and Mining Science*, 15: 1-10.

Gerogiannopoulos N.G. 1976. A critical state approach to rock mechanics. PhD thesis, University of London, 325p.

Goricki A., Rachaniotis N., Hoek E., Marinos P., Tsotsos S. & Schubert W. 2006. Support design criteria for tunnels in fault zone. In: *Proc. of the 55th geomechanics colloquium*. Salsberg. 14p.

Griffith A.A. 1921. The phenomena of rupture and flow in solids. *The Philosophical Transactions of the Royal Society London (Series A)*, 221: 163-198.

Grimstad E. & Barton N. 1993. Updating of the Q-system for NMT. In: *Proc. of the International Symposium on Sprayed Concrete*, Norwegian Concrete Association, Oslo, pp. 46-66.

Grimstad E., Barton N., Lien R., Lunde J. & Loset F. 1986. Classification of rock masses with respect to tunnel stability – new experiences with the Q-system. In Norwegian in Fjellsprengningsteknikk, Bergmekanikk, Geoteknikk, p. 30.1 – 3.18, Tapir Press.

Hadjigeorgiou J., Esmaieli K. & Grenon M. 2009. Stability analysis of vertical excavations in hard rock by integrating a fracture system into a PFC model. *Tunnelling & Underground Space Technology*, 24: 296-308.

Hajiabdolmajid V., Kaiser P. K. & Martin C.D. 2002. Modelling brittle failure of rock. *International Journal of Rock Mechanics and Mining Science*, 39(6): 731-741.

Halakatevakis N. & Sofianos A.I. 2010. Strength of a block rock mass based on an extended plane of weakness theory. *International Journal of Rock Mechanics and Mining Science*, 47(8): 568-582.

Harrison J.P. Hudson J.A. 2000. Engineering Rock Mechanics – An Introduction to the Principles, Pergamon.

Hawkins A.B. 1998. Aspect of rock strength. *Bulletin of Engineering Geology and the Environment*, 57: 17-30.

Hedley D.G.F. & Grant F. 1972. Stope-and-pillar design for the Elliot Lake Uranium Mines. *Bulletin of Canadian Institute of Mining and Metallurgy*, 65: 37-44.

Hoek E. & Bieniawski Z.T. 1965. Brittle rock fracture propagation in rock under compression. *International Journal of Fracture Mechanics*, 1: 137-155.

Hoek E. & Brown E.T. 1980a. Underground Excavations in Rock. Institution of Mining and Metallurgy, London.

Hoek E. & Brown E.T. 1980b. Empirical strength criterion for rock masses, *Journal of Geotechnical Engineering - ASCE*, 106: 1013-35.

Hoek E. & Brown E.T. 1988. The Hoek-Brown failure criterion – a 1988 update, In: *Proc. 15th Canadian Rock Mechanics Symposium*, Toronto, 31-38.

Hoek E. & Brown E.T. 1997. Practical estimates of rock mass strength. *International Journal of Rock Mechanics and Mining Science*, 34(8): 1165-86.

Hoek E. & Marinos P. 2007. A brief history of the development of the Hoek-Brown failure criterion. *Soils and Rocks*, 2: 1-13.

Hoek E. 1983. Strength of jointed rock masses. *Géotechnique*, 33(3): 187-223.

Hoek E. 1994. Strength of rock and rock masses, *ISRM News Journal*, 2(2): 4-16.

Hoek E. 1999. Putting Numbers to Geology – an Engineer's Viewpoint. *Quarterly Journal of Engineering Geology*, 32(1): 1-19.

Hoek E. 2002. Carranza-Torres C. Corkum B. Hoek-Brown failure criterion – 2002 edition. In: *Proc. NARMS-TAC Conference*, Toronto, 1: 267-273.

Hoek E., Carranza-Torres C., Diederichs M. & Corkum B. 2008. The Kersten lecture: Integration of geotechnical and structural design in tunneling. In: *Proc. of the University of Minnesota 56th annual geotechnical engineering conference*, Minneapolis. p. 1-53.

Hoek E., Kaiser P.K. & Bawden W.F. 1995. Support of Underground Excavations in Hard Rock. Rotterdam, Balkema.

Hoek E., Wood D. & Shah S. 1992. A modified Hoek-Brown criterion for jointed rock masses, In: *Proc. of Rock Characterization Symposium*, EUROCK 92, London, 209-213.

Holcomb D. J. & Costin L.S. 1987. Damage in brittle materials: experimental methods. In: Lamb JP, editor. *Proc. of the 10th U.S. National Congress of Applied Mechanics*.

Holt R.M., Brignoli M. & Kenter C.J. 2000. Core quality: quantification of coring-induced rock alteration. *International Journal of Rock Mechanics and Mining Sciences,* 37: 889-907.

Hoskins J.R. & Horino F.G. 1969. Influence of spherical head size and specimen diameters on the uniaxial compressive strength of rocks. US Department of the Interior, Bureau of Mines, Washington.

Hudson J.A. and Harrison J.P. 1997. Engineering Rock Mechanics. Oxford: Elsevier.

ISRM 1978. Suggested methods for the quantitative description of discontinuities in rockmasses. *International Journal of Rock Mechanics and Mining Sciences & Geomechanics Abstracts*, (15) 6: 319-368.

Itasca 2008a. Itasca Consulting Group Inc., Particle Flow Code in 2 dimensions (PFC2D), Ver. 4.0., Minneapolis, USA; 2008.

Itasca 2008b. Itasca Consulting Group Inc., Particle Flow Code in 3 dimensions (PFC3D), Ver. 4.0., Minneapolis, USA; 2008.

Jaeger J.C. 1970. The behavior of closely jointed rock. In: *Proceedings of 11th Symposium on Rock mechanics*, Berkeley, California, 57-68.

Jaeger JC., Cook N.G.W. & Zimmerman R. 2007. Fundamentals of Rock Mechanics, Wiley-Blackwell, 488p.

Jahns H. 1966. Measuring the strength of rock in situ at an increasing scale. In: *Proc. 1st ISRM Congress*, Lisbon, 1: 477-482.

Jiang C. & Zhao G. 2015. A preliminary study of 3D printing on rock mechanics. *Rock Mechanics and Rock Engineering*, DOI: 10.1007/s00603-014-0612-y.

Kaiser P.K. & Kim B. 2008. Rock mechanics challenges in underground construction and mining, In: *Proc. 1st Southern Hemisphere International Rock Mechanics Symposium*, 1: 3-38.

Kaiser P.K. & Kim B. 2015. Characterization of strength of intact brittle rock considering confinement-dependent failure processes. *Rock Mechanics and Rock Engineering*, 48(1): 107-119.

Kaiser P.K., Kim B., Bewick R.P. & Valley B. 2011. Rock mass strength at depth and implications for pillar design, *Mining Technology*, 120(3): 170-179.

Kaiser PK., Diederichs MS., Martin CD., Sharp J. & Steiner W. 2000. Underground works in hard rock tunneling and mining. In: *Proc. of GeoEng 2000*, Melbourne, 841-926.

Kalamaras G.S. & Bieniawski Z.T. 1993. A rock mass strength concept for coal seams. In: *Proc. of 12th Conference on Ground Control in Mining*, Morgantown, 274-283.

Kim B., Cai M., Kaiser P.K. & Yang H.S. 2007. Estimation of block sizes for rock masses with non-persistent joints, *Rock Mechanics and Rock Engineering*, 40(2): 169-192.

Kulhawy F.H. & Goodman R.E. 1987. Foundations in rock. In: *Ground engineer's reference book*, Butterworths, London, 55: 1-13.

Ladanyi B. & Archambault, G. 1972. Simulation of shear behavior of jointed rock mass. In: *Proc. 11th Symposium on Rock Mechanics*, New York, 105-125.

Lan H., Martin C.D. & Hu B. 2010. Effect of heterogeneity of brittle rock on micromechanical extensile behavior during compression loading. *Journal of Geophysical Research*. 115: B01202.

Lan H., Martin D. & Hu B. 2010. Effect of heterogeneity of brittle rock on micromechanical extensile behavior during compression loading. *Journal of Geophysical Research*, 115: B01202.

Lanaro F., Sato T. & Nakama S. 2009. Depth variability of compressive strength test results of Toki granite from Shobasama and Mizunami Construction Sites, Japan. *Rock Mech and Rock Engineering*, 42: 611-629.

Langford J.C. & Diederichs M.S. 2015. Quantifying uncertainty in Hoek-Brown intact strength envelopes. *International Journal of Rock Mechanics and Mining Science,* 74: 91-102.

Laubscher D.H. & Jakubec J. 2000. The MRMR rock mass classification for jointed rock masses, In: *Underground Mining Methods: Engineering Fundamentals and International Case Studies*, SMME, p. 475-481.

Laubscher D.H. 1975. Class distinction in rock masses. *Coal, Gold, Base minerals S. Afr.* 23.

Laubscher D.H. 1990. A geomechanics classification system for the rating on rock mass in mine design. *Journal of the Southern African Institute of Mining and Metallurgy*, 90: 257-273.

Laubscher D.H. 1993. Planning mass mining operations. In: *Comprehensive Rock Engineering*, Vol. 2, Pergamon Press.

Lauffer H. 1958. Gebirgsklassiferung fur den Stollenbau. *Geologie und Bauwesen*, 24: 46-51.

Lim S.S. & Martin C.D. 2010. Core disking and its relationship with stress magnitude for Lac du Bonnet granite, *International Journal of Rock Mechanics and Mining Science*, 47: 254-264.

Lockner D.A. Byerlee J.D. Kuksenko V. Ponomarev A. Sidorin A. 1992. Observation of quasi-static fault growth from acoustic emissions. In: Evans B, Wong T., editors. *Fault mechanics and transport properties of rocks*. New York: Academic press, p.3-31.

Lunder P.J. & Pakalnis R. 1997. Determination of the strength of hardrock mine pillars. *Bulletin of Canadian Institute of Mining and Metallurgy*, 90: 51-5.

Marinos V., Marinos P. & Hoek E. 2005. The geological strength index: applications and limitations. *Bulletin of Engineering Geology and the Environment*, 64: 55-65.

Martin C. 1993. The strength of massive Lac du Bonnet granite around underground openings. PhD thesis, University of Manitoba, 278p.

Martin C.D. & Maybee W.G. 2000. The strength of hard rock pillars. *International Journal of Rock Mechanics and Mining Sciences*, 37: 1239-46.

Martin C.D. 1997. Seventeenth Canadian Geotechnical Colloquium: The effect of cohesion loss and stress path on brittle rock strength, *Canadian Geotechnical Journal*, 34: 698-725.

Martin C.D., Kaiser P. K. & McCreath D. R., 1999. Hoek-Brown parameters for predicting the depth of brittle failure around tunnels. *Canadian Geotechnical Journal*, 36 (1): 136-151.

Martin CD, Chandler NA. 1994. The progressive fracture of Lac du Bonnet granite. *International Journal of Rock Mechanics and Mining Science & Geomechanics Abstract*, 31: 643-59.

Martin, C.D. & Stimpson, B. 1994. The effect of sample disturbance on laboratory properties of Lac du Bonnet granite. *Canadian Geotechical Journal*, 31(5): 692–702.

Mas Ivars D. 2010. Bonded particle model for jointed rock mass. PhD Thesis, Royan Institute of Technology (KTH), 94p.

Mas Ivars D., Pierce M.E., Darcel C., Reyes-Montes J., Potyondy D.O., Young R.P. & Cundall PA. 2011. A synthetic rock mass approach for jointed rock mass modeling, *International Journal of Rock Mechanics and Mining Science*, 48: 219-44.

Medhurst T.P. & Brown E.T. 1998. A study of the mechanical behavior of coal for pillar design. *International Journal of Rock Mechanics and Mining Science*, 35(8): 1087-1105.

Mosher S., Berger R.L. & Anderson D.E. 1975. Fracture characteristics of two granites. *Rock Mech.*, 7: 167-176.

NGI. 2013. Using the Q-system, Handbook of rock mass classification and support design. 57p.

Nicksiar M. & Martin C.D. 2013. Crack initiation stress in low porosity crystalline and sedimentary rocks, *Engineering Geology*, 154: 64-76.

Ortlepp W.D. 1997. Rock Fracture and Rockbursts; an Illustrative Study, The South African Institute of Mining and Metallurgy, Johannesburg, 98p.

Palmström A. 1982. The volumetric joint count - a useful and simple measure of the degree of jointing. In: *Proc. International Congress IAEG,* New Delhi, pp. V.221 - V.228.

Pariseau W., Puri S. & Schmelter S. 2008. A new model for effects of impersistent joint set on rock slope stability. *International Journal of Rock Mechanics and Mining Science*, 45: 122-31.

Paterson MS. 1958. Experimental deformation and faulting in Wombeyan marble, *Geological Society of American Bulletin*, 69: 465-76.

Patton FD. 1966. Multiple mode of shear failure in rock. In: *1st International Conference in Rock Mechanics*, Lisbon, 509-511.

Pierce M., Gaida M. & DeGagne D. 2009. Estimation of rock block strength. In : *Proc. 3rd CanUS Rock Mechanics Symposium*, Toronto, Paper 4360.

Pierce M., Mas-Ivars D., Cundall P. & Potyondy D. 2007. A synthetic rock mass model for jointed rock, In: *Proc. 1st CanUS Rock Mechanics Symposium*, Vancouver, pp 341-349.

Potvin Y., Hudyma M.R. & Miller H.D.S. 1989. Design guidelines for open stope support. *Bulletin of Canadian Institute of Mining and Metallurgy*, 82:53-62.

Potyondy D.O. & Cundall P.A. 2004. A bonded particle model for rock. *International Journal of Rock Mechanics and Mining Science*, 41: 1329-1364.

Potyondy D.O. 2012. A flat-jointed bonded-particle material for hard rock. In: *Proc. of the 46th US Rock Mechanics Symposium*, Chicago, Paper ARMA12-501.

Potyondy DO. 2010. A grain-based model for rock: approaching the true microstructure. In: *Proc. Rock Mechanics in the Nordic Countries*, 10p.

Potyondy DO. 2015. The bonded-particle model as a tool for rock mechanics research and application: current trends and future directions. *Geosystem Engineering,* 18(1): 1-28.

Poulsen B.A. & Adhikary D.P. 2013. A numerical study of the scale effect in coal strength. *International Journal of Rock Mechanics and Mining Science*, 63: 62-71.

Pratt H., Black A., Brown W. & Brace W. 1972. The effect of specimen size on the mechanical properties of unjointed diorite. *International Journal of Rock Mechanics and Mining Science & Geomechanics Abstract*, 9(4): 513-529.

Prudencio M. & Van Sin Jan M. 2007. Strength and failure modes of rock mass models with non-persistent joints. *International Journal of Rock Mechanics and Mining Science*, 44: 890-902.

Ramamurthy T. & Arora V.K. 1994. Strength predictions for jointed rocks in confined and unconfined states. *International Journal of Rock Mechanics and Mining Sciences & Geomechanics Abstracts*, 31(1): 9-22.

Ramamurthy T. 1993. Strength and modulus response of anisotropic rocks. In: *Compressive rock engineering – principle, practice and projects*, Pergamon Press, Oxford, 1: 313-329.

Ramamurthy T., Rao G.V. & Rao K.S. 1985. A strength criterion for rocks, In: *Proc. of Indian geotechnical conference*, Roorkee, 1: 59-64.

Read R.S., Chandler N.A. & Dzik E.J. 1998. In situ strength criteria for tunnel design in highly-stressed rock masses, *International Journal of Rock Mechanics and Mining Sciences,* 35(3): 261-278.

Ribacchi R. 2000. Mechanical tests on pervasively jointed rock material: insight into rock mass behavior. *Rock mechanics & Rock Engineering*, 33(4): 243-266.

Rockfield, 2007. Rockfield Software Ltd. Technium, Kings Road, Prince of Wales Dock, Swansea, SA1 8PH, UK. http://www.rockfield.co.uk/

Rocscience 2010. Phase2 v.9, Finite element analysis for excavations and slopes. www.rocscience.com

Rocscience 2013. Roclab v.1.0: Rock mass strength analysis using the Generalized Hoek-Brown failure criterion, www.rocscience.com.

Rosenblueth, 1981 Rosenblueth E. Two-point estimates in probabilities. *Journal of Applied Mathematical Modelling*, 5: 329-35.

Rosengren K.J. & Jaeger J.C. 1969. The mechanical properties of a low-porosity interlocked aggregate. *Geothecnique*, 18(3): 317-326.

Schultz R. 1995. Limits on strength and deformation properties of jointed basaltic rock masses, *Rock Mechanics & Rock Engineering*, 28:1-15.

Sheorey P.R. 1997. Empirical Rock Failure Criteria, Balkema, Rotterdam.

Singh B., Geol R.K., Mehrotra V.K., Garg S.K. & Allu M.R. 1998. Effect of intermediate principal stress on strength of anisotropic rock mass. *Tunnelling & Underground Space Technology*, 13(1): 71-79.

Singh B., Viladkar M.N., Samadhiya N.K. & Mehrotra V.K. 1997. Rock mass strength parameters mobilized in tunnels, *Tunnelling & Underground Space Technology*, 12(1): 47-54.

Singh M. & Rao K.S. 2005. Empirical methods to estimate the strength of jointed rock masses. *Engineering Geology*, 77(1-2): 127-137.

Sonmez H. & Ulusay R. 1999. Modification to the geological strength index (GSI) and their applicability to stability of slopes. *International Journal of Rock Mechanics and Mining Science*, 36: 743-760.

Symons I.F. 1970. The effect of size and shape of specimen upon the unconfined compressive strength of cement-stabilized materials. *Magazine of Concrete Research*, 22: 45-50.

Terzaghi K. 1946. Rock defects and loads on tunnel support. In: *Rock Tunneling with Steel Supports*. Proctor and White (eds.), pp. 15-99.

Thuro K., Plinninger R.J., Zah S. & Schutz S. 2001. Scale effects in rock strength properties. Part1: Unconfined compressive test and Brazilian test. In: *Rock mechanics-a challenge for society*, June 3-7 2001. ISRM, Espoo, pp. 169–174.

Turichshev A. & Hadjigeorgiou J. 2015. Experimental and numerical investigations into the strength of intact veined rock. *Rock Mechanics and Rock Engineering*, DOI: 10.1007/s00603-014-0690-x.

Valley B., Kaiser P.K. & Duff D. 2010. Consideration of uncertainty in modeling the behavior of underground excavations. In: *5th International Seminar on Deep and High Stress Mining*, 423-436.

Valley B., Kim B-H., Suorineni F.T., Bahrani N., Bewick R. & Kaiser P.K. 2011. Influence of confinement dependent failure processes on rock mass strength at depth. In: *Proc. ISRM Congress*, China.

Valley B., Suorineni F.T. & Kaiser P.K. 2010. Numerical analyses of the effect of heterogeneities on rock failure process. In: *Proc. of 44th U.S. Rock Mechanics Symposium*, paper-648, 10p.

Walsh J. B., Brace W. F. & Wawersik W. R. 1970. Attenuation of Stress Waves in Cedar City Quartz Diorite, Report AFWL-TR-70-8 Air Force Weapons Laboratory, Kirtland AFB, New Mexico.

Wang Y. & Tonon F. 2009. Modeling Lac du Bonnet granite using a discrete element model. *International Journal of Rock Mechanics and Mining Science*, 46: 1124-1135.

Wang Y. and Tonon F. Calibration of a discrete element model for intact rock up to its peak strength. *International Journal of Numerical & Analytical Methods in Geomechanics*, 2010; 34: 447-469.

Watson B.P., Kuijpers J.S., Henry G., Palmer C.E. & Ryder J.A. 2009. Nonlinear rock behaviour and its implications for deeper level platinum mining. *Journal of the Southern African Institute of Mining and Metallurgy*. 108: 5-13.

Wawersik W.R. & Brace W.F. 1971. Post-failure behavior of a granite and a diabase. *Rock Mechancis*, 3(2): 61-85.

Xie H. 1993. Fractals in Rock Mechanics, CRC Press, 464 p.

Yang S.Q. Jing H.W. Li Y.S. Han L.J. 2011. Experimental investigation on mechanical behavior of coarse marble under six different loading paths. *Experimental mechanics*, 51:315-334.

Yang S.Q., Jiang Y.Z., Xu W.Y. and Chen X.Q. 2008. Experimental investigation on strength and failure behavior of pre-cracked marble under conventional triaxial compression, *International Journal of Solids and Structures*, 45: 4796-4819.

Yoon J. 2007. Application of experimental design and optimization to PFC model calibration in uniaxial compression simulation. *International Journal of Rock Mechanics and Mining Science*, 44: 871-889.

Yoon J.S., Jeon S., Zang A. & Stephansson O. 2011. Bonded particle model simulation of laboratory rock tests for granite using particle clumping and contact unbonding. In: *Continuum and Distinct Element Numerical Modeling in Geomechanics*, Minneapolis, USA, paper: 08-05.

Yoon J.S., Zang A. & Stephansson O. 2012. Simulating fracture and friction of Aue granite under confined asymmetric compressive test using clumped particle model. *International Journal of Rock Mechanics and Mining Science*, 49: 68-83.

Yoshinaka R., Osada M., Park H., Sasaki T. & Sasaki K. 2008. Practical determination of mechanical design parameters of intact rock considering scale effect. *Engineering Geology*, 96: 173-186.

Yudhbir W.L. & Prinzl F. 1983. An empirical failure criterion for rock masses. In: *Proc. of 5th international congress on rock mechanics*, Melbourne, 1: B1-B8.

Zhang L. & Einstein H.H. 2004. Using RQD to estimate the deformation modulus of rock masses. *International Journal of Rock Mechanics and Mining Science*, 41: 337-341.

Zhang L. 2011. Estimating the strength of jointed rock masses. *Rock Mechanics & Rock Engineering*, 43: 391-402.

Zhang Q., Zhu H., Zhang L. & Ding X. 2011. Study of scale effect on intact rock strength using particle flow modeling. *International Journal of Rock Mechanics and Mining Science*, 48: 1320-1328.

Zhang Y. & Stead D. 2015. Modeling 3D crack propagation in hard rock pillars using a synthetic rock mass approach. *International Journal of Rock Mechanics and Mining Science*, 72: 199-213.